Dissertation
submitted to the
Combined Faculty of Mathematics, Engineering, and Natural Sciences
of Heidelberg University, Germany
for the degree of
Doctor of Natural Sciences

Put forward by
Moritz Schöne
born in: Backnang, Germany
Oral examination: 1 February 2023

Tropospheric BrO plumes in Arctic spring – A comparison of TROPOMI satellite observations and model results

Referees: **Prof. Dr. Ulrich Platt**
Prof. Dr. Thomas Leisner

Zusammenfassung

Halogenradikale können die Chemie der polaren Atmosphäre drastisch verändern. Dies wird durch die wiederholte Zerstörung von Ozon in der Grenzschicht im polaren Frühling deutlich, welche man als Ozonzerstörungsereignisse (engl. Ozone Depletion Events, ODEs) bezeichnet. Diese ODEs werden durch erhöhte Konzentrationen von reaktiven Halogenen, insbesondere von Brommonoxidradikalen (BrO), verursacht. Messungen deuten daraufhin, dass es zwei verschiedene Arten von Umweltbedingungen gibt, die die Emission von Brom in die Atmosphäre begünstigen, namentlich kalte und stabile meteorologische Bedingungen einerseits und weniger stabile Bedingungen im Zusammenhang mit Tiefdruckgebieten andererseits. Um die Bedeutung dieser unterschiedlichen Umweltbedingungen auf einer pan-arktischen Skala zu untersuchen, vergleicht diese Dissertation TROPOMI Satellitenbeobachtungen von BrO mit den Ergebnissen eines Modells für die atmosphärische Chemie und Meteorologie für den arktischen Frühlings 2019. Für die Bestimmung von troposphärischem BrO aus Satellitenmessungen wird ein Algorithmus entwickelt, welcher die Einschätzung der troposphärischen Teilsäule ohne Zuhilfenahme externer Eingangsdaten erlaubt. Im Vergleich mit anderen Algorithmen ermöglicht dies die volle Nutzung von TROPOMIs hoher räumlicher Auflösung ($7 \times 3.5\,\mathrm{km}^2$), während es zugleich Verzerrungen durch die Nutzung von Modelldaten vermeidet.
Bei der Validation des Modells mittels der Satellitenmessungen konnte gezeigt werden, dass ein Mechanismus für die Bromfreisetzung aus der Schneedecke, welcher von vielen Modellen verwendet wird, ungeeignet ist, um ODEs im frühen Februar für hohe Sonnenzenithwinkel vorherzusagen. In Fallstudien wurde weiterhin demonstriert das die beobachteten räumlichen Muster sowie die großen BrO Säulen im späten Frühling in Assoziation mit polaren Zyklonen durch die Einmischung von Brom in die freie Troposphäre erklärt werden können. Auch konnte demonstriert werden dass die Größenordnung von Bromemissionen aus Flugschnee in polaren Zyklonen wahrscheinlich überschätzt wird. Eine saisonale Abhängigkeit der Umweltbedingungen, welche die Bromfreisetzung begünstigen, konnte etabliert werden. Ruhige meteorologische Bedingungen begünstigen das Auftreten von ODEs zu Beginn des polaren Frühlings. Während des späten März und April konnte Ozon als limitierender Faktor für die BrO Bildung identifiziert werden und Ergebnisse deuteten darauf hin, dass hohe Windgeschwindikeiten die Bromfreisetzung begünstigen. Eine statistische Auswertung der räumlichen Ausdehnung und Form von ODEs ergab einen Maßstab zwischen 40 km und 1000 km für die typischen Luftmassen mit erhöhtem Bromgehalt.

Abstract

Halogen radicals can drastically alter the polar atmospheric chemistry. This is made evident by a recurrent destruction of boundary layer ozone during polar springs called ozone depletion events (ODEs). ODEs are caused by enhanced concentrations of reactive halogens, in particular bromine monoxide (BrO) radicals. Measurements suggest that there are two distinct sets of environmental conditions favoring the emissions of bromine to the atmosphere, namely cold and stable meteorological conditions on one side and less stable conditions associated with low-pressure systems on the other. This thesis investigates the importance of these differing environmental conditions on a pan-Arctic scale by comparing TROPOMI satellite observations of BrO with the results of an meterology model coupled with atmospheric chemistry (WRF-CHEM) for the Arctic spring of 2019. For the retrieval of tropospheric BrO from satellite measurements an algorithm is developed which allows to assess the tropospheric partial column without reliance on external input. Compared to other retrieval algorithms, it enables the full utilization of TROPOMI's high spatial resolution ($7 \times 3.5\,\mathrm{km}^2$) while also avoiding biases from the use of model data.
Satellite observations are used to validate model assumptions. It was demonstrated that a bromine release mechanism from the snow-pack employed in numerous models is unfit to predict ODEs in early February at high solar zenith angles. Case studies demonstrated that the observed spatial patterns and large BrO columns observed during late polar spring in association with polar cyclones can be explained by the intrusion of bromine into the free troposphere. It was shown that the magnitude of bromine emissions from blowing snow in polar cyclones is likely overestimated. A seasonal dependence in the environmental conditions favoring bromine release was established. Calm meteorological conditions favor the occurrence of ODEs during early polar spring. During late March and April, ozone was identified as limiting factor for BrO formation and results indicated high wind speeds as favorable meteorological parameter for bromine release. A statistical analysis of spatial extent and shape of ODEs was conducted, showing a scale of 40 km to 1000 km for bromine enhanced air masses.

Contents

Part I

Motivation and Scientific Background

1 | Introduction

The prediction of global stratospheric ozone depletion in the 1970s and the discovery of the ozone hole in 1985 heralded a shift in public awareness of humanity's relationship with the Earth's atmosphere. From the realization that anthropogenic emissions are capable of destroying the ozone layer, one of the foundations of complex life on Earth, it became evident that human actions could radically influence something as fundamental as the relevant constituents of the atmospheric composition itself.

The scientific efforts which gradually led to this insights were spearheaded by Paul Crutzen, Mario Molina, Frank Sherwood Rowland, and colleagues. Crutzen proposed that nitrous oxide (N_2O) emitted from the expected fleet of supersonic jets directly into the stratosphere could be converted to nitric oxide (NO) and serve as a catalyst for the formation of oxygen from ozone, thereby depleting the overall abundance of ozone (Crutzen, 1970, 1974). Built on this proposition, the famous *Rowland-Molina hypothesis* suggests a similar mechanism of a catalytic destruction of ozone from long-lived organic halogen compounds (Rowland and Molina, 1974). The predominant source of such compounds was represented by anthropogenic emissions of chlorofluorocarbons (CFCs). It was also shown that the effectiveness of halogens as catalyst for ozone destruction is even larger than of NO, in particular for chlorine (Cl) (Cicerone et al., 1974) and bromine (Br) (Wofsy et al., 1975; McElroy et al., 1986). For their work on stratospheric ozone formation and depletion, Crutzen, Molina and Rowland were awarded the Nobel Prize in Chemistry in 1995.

These discoveries demonstrated beyond doubt that human activity could affect the stratospheric ozone layer. This became even clearer with the discovery of the Antarctic "ozone hole", a strong depletion of polar stratospheric ozone far larger than anyone had anticipated (Farman et al., 1985). In their seminal work, Solomon et al. (1986) proposed that the localized formation of polar stratospheric clouds (PSCs) at the low temperatures in the Antarctic stratosphere provides additional surfaces for halogen recycling from heterogeneous reactions, which in turn increases ozone depletion.

The insights gained by the scientific community sparked international environmental cooperations that culminated in the Montreal Protocol, one of the most successful agreements in international environmental politics. It effectively banned ozone-depleting substances such as CFCs worldwide and its success is already visible in the slow recovery of the ozone layer over Antarctica (Chipperfield et al., 2017; Fang et al., 2019; Banerjee et al., 2020). The realization that human activity began to destroy the protective layer of ozone in the

stratosphere signals a woeful turning point in human history. At the same time, the fact that human action also enabled the ongoing recovery of the ozone layer serves as an outstanding example of humanity's ability to solve problems when science, the public and policy-makers share a common goal. Although the emerging changes in Earth's climate caused by anthropogenic greenhouse gas emissions delay the ozone layer recovery, this nevertheless provides a gleam of hope for the challenge of climate change and global warming, respectively. As an opinion piece in the *The New York Times* described it in 2019, "The world solved the ozone problem. It can solve climate change." (The New York Times Editorial Board, 2019).

While awareness for stratospheric ozone destruction was rising, tropospheric ozone was regarded more as a nuisance by the general public, in form of harmful concentrations of ozone produced during conditions of high pollution (a phenomenon broadly denoted as "smog"). Yet tropospheric ozone also provides an important source of the hydroxyl radical (OH), arguably the most important oxidizing agent which controls the atmospheric lifetime of most gases in the troposphere. In this sense, it is sometimes referred to as "the detergent of the atmosphere" (Crutzen and Zimmermann, 1991).

Discussions surrounding measures to combat stratospheric ozone destruction were still ongoing when observations in the Arctic troposphere revealed a frequent, almost complete depletion of ozone near the surface (e.g. Oltmans, 1981; Bottenheim et al., 1986). Similar findings were later also reported in the Antarctic troposphere (Kreher et al., 1996). These events are referred to as *ozone depletion events* (ODEs) (Oltmans et al., 1989). It was found that these naturally occurring events were mainly driven by halogen compounds and in particular inorganic bromine radicals (Hausmann and Platt, 1994).

An important mechanism proposed to explain the strong correlation of ozone depletion and the increase of atmospheric bromine is a sequence of hetereogeneous reactions denoted as *bromine explosion* (Platt and Janssen, 1995; Platt and Lehrer, 1996; Wennberg, 1999). During these events an autocatalytic release of bromine from halide laden surfaces to the gas phase occurs, leading to an exponential increase of bromine radicals in the atmosphere which can result in the destruction of near-surface ozone over the course of a few hours. Subsequent studies provided a huge body of observational evidence, for both the influence of bromine on tropospheric ozone depletion but also for its important role for several other chemical cycles in the near-surface atmosphere. As an example, the frequently observed depletion of atmospheric mercury (Steffen and deMaria, 1996; Schroeder et al., 1998, 2003) was linked to oxidation of gaseous mercury from bromine monoxide in parallel with ODEs. It was proposed that this can lead to a deposition of poisonous mercury compounds into the biosphere (Angot et al., 2016). Furthermore, the marine sulphur cycle can be altered by the presence of halogen radicals, which can affect cloud condensation nuclei and the formation of aerosol particles (Von Glasow and Crutzen, 2004; Chen et al., 2018).

The primary source of bromine most likely is the sea ice surface. In particular first-year (FY) sea ice, i.e. sea ice less than one year old, with its increased salinity is suspected to play a major role (e.g. Wagner et al., 2001). It is expected that a changing climate accompanied by surface warming in the Arctic region will decrease the area covered by the

so-called multi-year (MY) sea ice, i.e. the sea ice not melting during Arctic summer (Kwok et al., 2009, 2020). This is partially compensated by an increase of FY sea ice. Studies have shown that this increase in FY ice is correlated to an increasing frequency and intensity of ODEs and the associated release of activated bromine compounds (e.g. Hollwedel et al., 2004; Bougoudis et al., 2020). Consequently, it is assumed that climate change will also significantly affect the occurrence and strength of ODEs. However, accurate predictions of future halogen release rates and changes in the overall oxidation capacity in the Arctic troposphere require a precise understanding of the way in which changing environmental conditions are affecting tropospheric halogen chemistry. As an example, it is speculated that the frequency of ODEs could increase due to a rising occurrence of extreme Arctic cyclones (Blechschmidt et al., 2016) from climate change (e.g. Vavrus, 2013). Then again, near-surface temperature is inversely correlated to the frequency of bromine activation, e.g. because of a temperature dependence in the release mechanisms (e.g. Sander et al., 2006) or because it impedes upon the formation of temperature inversions favoring the formation of high bromine mixing ratios (Swanson et al., 2020), which would imply a decline in the frequency of ODEs from climate change.

Despite intense research efforts, many central aspects of the interactions between different environmental conditions and polar tropospheric halogen chemistry remain unclear. This ranges from the relevant properties of the surface (Bartels-Rausch et al., 2014), favorable meteorological conditions for bromine release such as wind speed or near-surface temperature (e.g. Simpson et al., 2007a; Swanson et al., 2020) and the importance of aerosol particles for the recycling and release of activated bromine (e.g. Yang et al., 2008; Peterson et al., 2017) to the role of synoptic scale weather events and frontal systems (e.g. Sihler, 2012; Blechschmidt et al., 2016). Closely related to this is the understanding of the mechanisms responsible for the initial release of gaseous bromine. It is well accepted by now that the bromine explosion is the main driver for ODEs, yet a sufficiently fast bromine explosion explaining the observed timescale of ozone depletion requires an initial mixing ratio as "jumpstart" for the reaction sequence. While there are many possible candidates able to provide such a mixing ratio, the exact mechanism remains unclear (e.g. Bognar et al., 2020; Swanson et al., 2022). The extensive literature surrounding these topics will be reviewed in the next chapter. For the reasons mentioned, a more accurate understanding of the influence of climate change on the phenomenon of ODEs requires a deeper understanding of polar atmospheric bromine chemistry and its relation to different environmental conditions.

Satellite missions provide distinct advantages for the observation of ODEs and the study of polar halogen chemistry. Satellite instruments are able to probe areas which are difficult to access for in-situ measurements due to the hostile environmental conditions in polar regions. Furthermore, satellite observations can provide a quasi-continuous monitoring on a pan-Arctic or even global scale, which can facilitate the identification of spatial structures, e.g. in relation to meteorology on a synoptic scale. Studies using satellite instruments have made substantial contributions to the understanding of the phenomenon of ODEs and polar halogen chemistry (e.g. Wagner and Platt, 1998; Hollwedel et al., 2004; Sihler et al., 2012;

Blechschmidt et al., 2016; Choi et al., 2018). The next chapter discusses these in more detail.

The goal of this thesis is to contribute to an improvement of the understanding of Arctic atmospheric bromine chemistry and its relation to different environmental conditions. To this end, a combination of satellite observations and predictions of an atmospheric chemistry and meteorology model are utilized. One of the main aspects of this work was the update and improvement of a satellite retrieval algorithm capable of estimating the tropospheric contribution of bromine radicals to the observed total column without reliance on external input. This allows for an assessment of the model performance based on satellite observations without the introduction of other model biases used for the retrieval. From discrepancies between model predictions and satellite measurements it is possible to validate model assumptions and examine the chemistry mechanisms implemented in the model with a focus on bromine emission mechanisms and their influence by environmental and meteorological parameters. Furthermore, the updated retrieval enables the full utilization of the high spatial resolution of the TROPOspheric Monitoring Instrument (TROPOMI) aboard ESA's Sentinel-5P satellite. This allows a fine-grained study of the spatial extent of bromine enhancements and ODEs to investigate if conditions favoring the occurrence of ODEs might emerge on a localized small scale.

The work presented here is divided into four parts. In the first part, the scientific background of the phenomenon of ozone depletion events is discussed. This includes the underlying chemical reactions and the environmental and physical factors influencing halogen chemistry as well as a review of existing algorithms for the retrieval of tropospheric BrO from satellite (Chapters 2 and 3). The second part describes the methods and instruments utilized within this work. An emphasis is put on the improvement and implementation of the tropospheric BrO retrieval algorithm. Furthermore a description of the atmospheric chemistry model used for this thesis is given (Chapters 4 to 7). In the third part the results of this thesis are presented. This includes a comparison of the model results with ground based measurements as well as satellite retrievals together with an analysis of temporal trends in the bromine release predicted by the model (Chapter 8), an exploration of the relationship between bromine activation and environmental parameters in the context of case studies (Chapter 9) and a statistical analysis of the size and shape of enhanced BrO plumes measured from satellite (Chapter 10). The thesis closes with conclusions and an outlook (Chapters 11 and 12).

2 | Tropospheric ozone depletion events: principles of chemical and physical processes

After a winter in complete darkness, the air in the boundary layer over Arctic sea ice and surrounding coastal areas frequently experiences reductions of ozone concentrations from their typical background levels (around 30 nmol mol^{-1} to 40 nmol mol^{-1}) to below 5 nmol mol^{-1} and sometimes even below observational detection limits (Oltmans, 1981; Bottenheim et al., 1986; Solberg et al., 1996; Hopper et al., 1998; Bottenheim et al., 2002, 2009). Measurements of atmospheric compounds using filter packs revealed that these so-called Ozone Depletion Events (ODEs) are generally accompanied by a significant increase of gaseous bromine concentrations (Barrie et al., 1988; Oltmans et al., 1989) (see Figure 2.1).

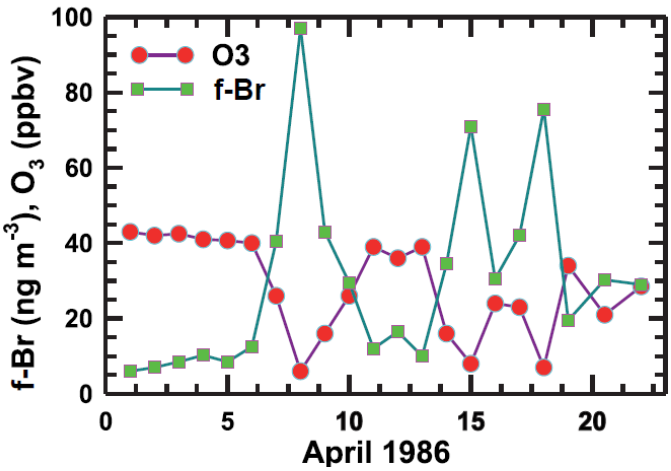

Figure 2.1: *Comparison of daily mean ground level ozone and filterable bromine concentrations at Alert, Canada in April 1986. Figure adapted from Barrie et al. (1988).*

The assumed correlation between bromine radical chemistry and ozone depletion was made evident by the detection of atmospheric BrO mixing ratios as high as 30 pmol mol^{-1} in the near-surface air (Hausmann and Platt, 1994; Tuckermann et al., 1997). It is now reasonably certain that sea salt sourced bromine species are key drivers of the depletion of

polar boundary layer ozone (e.g. Fan and Jacob, 1992; McConnell et al., 1992; Tang and McConnell, 1996; Platt and Hönninger, 2003). The existence of ODEs in the Antarctic troposphere is also established by now (Kreher et al., 1996). Interestingly, ODEs seem to occur almost exclusively in polar spring (e.g. Simpson et al., 2007a; Nasse et al., 2019). There are also a number of observations reporting similar levels of ozone depletion and halogen activation outside the polar region, for example over the Dead Sea (e.g. Matveev et al., 2001; Holla et al., 2015).

This chapter serves as an introduction of the main mechanisms responsible for ozone depletion. In section 2.1, the most important aspects of the chemistry surrounding ODEs are summarized. This is followed by a description of different hypotheses regarding the initial release mechanisms of reactive bromine compounds in section 2.1.1 while section 2.2 discusses the influence of different environmental factors on ODEs and the release and reactivation of bromine.

2.1 Chemistry

Halogen radicals can act as a catalyst for the depletion of ozone (O_3). During an ODE, the destruction of ozone is largely driven by the following reaction cycle (Hausmann and Platt, 1994; Barrie et al., 1988):

$$\mathrm{Br} + \mathrm{O_3} \longrightarrow \mathrm{BrO} + \mathrm{O_2} \tag{R1}$$

$$\mathrm{BrO} + \mathrm{BrO} \longrightarrow 2\,\mathrm{Br} + \mathrm{O_2} \tag{R2}$$

$$\mathrm{BrO} + \mathrm{BrO} \longrightarrow \mathrm{Br_2} + \mathrm{O_2} \tag{R3}$$

$$\mathrm{Br_2} + \mathrm{h}\nu \longrightarrow 2\,\mathrm{Br} \tag{R4}$$

In this sequence, a bromine radical can react with O_3 to produce bromine monoxide. The BrO produced in Reaction (R1) rapidly photolyses. This leads to the regeneration of O_3 and Br_2 in a null cycle:

$$\mathrm{BrO} + \mathrm{h}\nu \longrightarrow \mathrm{O} + \mathrm{Br} \tag{R5}$$

$$\mathrm{O} + \mathrm{O_2} \longrightarrow \mathrm{O_3} \tag{R6}$$

To irreversibly remove ambient ozone, BrO must react with BrO or another halogen oxide. The rate limiting steps for the ozone depletion are therefore typically the BrO self-reactions (R2) and (R3), which leads to the rate of O_3 loss being quadratic in the BrO concentration. If these reactions take place, this results in a net destruction of ozone:

$$2\,\mathrm{O_3} \longrightarrow 3\,\mathrm{O_2} \tag{R7}$$

Enhanced BrO levels photolytically decay within hours (Platt and Hönninger, 2003). During conditions of sufficient ozone concentrations a bromine atom can destroy around 100 O_3

molecules via Reactions (R1 – R4) before being removed from the atmosphere itself. This occurs mainly via one of two pathways: (i) Br may react with OH or aldehydes (such as formaldehyde, HCHO) to form the chemically inert HBr:

$$\mathrm{Br} + \mathrm{HCHO} + \mathrm{O_2} \longrightarrow \mathrm{HBr} + \mathrm{CO} + \mathrm{HO_2} \tag{R8}$$

or (ii) BrO may react with the hydroperoxil radical (HO_2) to form hypobromous acid:

$$\mathrm{BrO} + \mathrm{HO_2} \longrightarrow \mathrm{HOBr} + \mathrm{O_2} \tag{R9}$$

Both bromine compounds are then either photolysed and produce reactive bromine again, or, far more likely, are deposited to the surface or to aerosols.

Without any kind of mechanism to re-activate these deposited bromine compounds, which are somewhat imprecise termed as "recycling", the atmospheric lifetime of BrO is approximately 100 s because of Reaction (R5) (Lehrer et al., 2004). The observed strong correlation between bromine activation and ozone depletion therefore heavily implies the existence of such recycling mechanism capable of producing activated gaseous bromine from deactivated and dissolved bromine (Platt and Hönninger, 2003). The most accepted candidate for this mechanism is a heterogeneous cycle of reactions proposed soon after the first observation of ODEs (Fan and Jacob, 1992; McConnell et al., 1992; Abbatt, 1994; Platt and Janssen, 1995; Platt and Lehrer, 1997) following the uptake of gaseous HOBr by a halide containing surface:

$$\mathrm{HOBr} \longrightarrow \mathrm{HOBr\,(aq)} \tag{R10}$$

$$\mathrm{HOBr\,(aq)} + \mathrm{H^+\,(aq)} + \mathrm{Br^-\,(aq)} \longrightarrow \mathrm{Br_2} + \mathrm{H_2O} \tag{R11}$$

$$\mathrm{Br_2} + \mathrm{h}\nu \longrightarrow 2\,\mathrm{Br} \tag{R12}$$

$$\mathrm{Br} + \mathrm{O_3} \longrightarrow \mathrm{BrO} + \mathrm{O_2} \tag{R13}$$

$$\mathrm{BrO} + \mathrm{HO_2} \longrightarrow \mathrm{HOBr} + \mathrm{O_2} \tag{R14}$$

The reaction cycle begins with the uptake of HOBr, e.g. on an ice surface or the aqueous phase of an aerosol particle, which then reacts with bromide to form molecular bromine (R11). This then degases to the atmosphere, where it can be photolysed if sufficient radiation is available (R12). The bromine radicals then act as a catalyst in the ozone destruction cycle (R1 – R4) before being deactivated again in a reaction with hydroperoxyl, forming HOBr. This and other important mechanisms affecting the bromine chemistry and ozone depletion are sketched in Figure 2.2.

The autocatalytic sequence (R10 – R14) provides a recycling mechanisms for deactivated bromine, both in the form of HBr, which provides Br^- in the liquid phase as well as in the form of HOBr. Furthermore it allows for an amplification of the gaseous bromine concentration, i.e. the release of additional amounts of bromine previously dissolved in the liquid

phase, as can be seen in the following net reaction:

$$\mathrm{Br} + \mathrm{Br^-(aq)} + \mathrm{H^+(aq)} + \mathrm{HO_2} + \mathrm{O_3} + \mathrm{h}\nu \longrightarrow 2\,\mathrm{Br} + \mathrm{H_2O} + 2\,\mathrm{O_2} \tag{R15}$$

In principle, the concentration of atmospheric bromine partaking in this reaction cycle doubles after each cycle. Consequently, if more than 50 % of activated bromine compounds go through this sequence of reactions, the amount of reactive bromine in the atmosphere increases exponentially. For that reason, the heterogeneous reaction cycle (R10 – R14) was named *bromine explosion* (Platt and Janssen, 1995; Platt and Lehrer, 1996; Wennberg, 1999). Because there are also other reactions of the bromine radical, for example the production of HBr or the formation of BrCl in the liquid phase, the actual factor by which bromine increases is $\alpha \leq 2$:

$$\mathrm{Br} \longrightarrow \alpha\,\mathrm{Br} \tag{R16}$$

This reaction sequence enables the "explosive" increase of the BrO concentration in the lower troposphere if the following conditions are met:

(i) There exists an initial "seed" mixing ratio of gas-phase bromine, which can be deposited as HOBr to the surface or the aqueous phase.

(ii) The surface provides both $\mathrm{Br^-}$ and $\mathrm{H^+}$ in sufficient amounts for Reaction (R11). This requires a surface with a sufficient bromide density, which is currently believed to be mainly sourced by sea salt (Fan and Jacob, 1992; McConnell et al., 1992; Simpson et al., 2015) as well as a low enough pH value (Fickert et al., 1999). As discussed in section 2.2.1, sea ice surfaces seem to be especially suited for this due to its potential high salinity and concentration of bromides at the surface (Abbatt et al., 2012; Bartels-Rausch et al., 2014).

(iii) Sufficient radiation (sunlight) is available for an efficient photolysis of molecular bromine.

(iv) A sufficiently large ozone mixing ratio is present, which is needed as direct reaction partner as well as source of HOx radicals from photolysis (Simpson et al., 2015).

Other halogen compounds are less influential in the chemistry of ODEs. The role of fluorine is completely negligible due to its reaction with water vapor to the very stable hydrogen fluoride (Cady, 1935). Activated iodine (I) was only found in small quantities (Saiz-Lopez et al., 2007; Atkinson et al., 2012; Zielcke, 2015; Raso et al., 2017). This is likely due to significantly smaller concentrations of iodide in sea water in comparison to bromide (Grebel et al., 2010). However, recent measurements by Benavent et al. (2022) suggest that the impact of iodine on the Arctic ozone destruction might be underestimated. The concentration of chloride (Cl) in sea water on the other hand is approximately 600 times larger than the concentration of bromide and approximate 500-fold larger than the bromide concentration in the snow-pack (Pratt et al., 2013). This means that the availability of chloride is inherently higher than that of bromide. Yet, in contrast to bromine and iodine, chlorine can react with

hydrocarbons such as methane forming hydrogen chloride (denoting the hydrocarbon chain with R) due to its higher reactivity and the increased bond strength of HCl (compared to HBr and HI):

$$\mathrm{Cl} + \mathrm{RH} \longrightarrow \mathrm{HCl} + \mathrm{R}^{\bullet} \tag{R17}$$

As a result of the high abundance of methane and the large reaction rate constant, activated chlorine will quickly produce chemically inert HCl, leading to an α below 1 (cf. (R16)). Therefore no mechanism exists analogous to the bromine explosion for chlorine.

The predominant influence of chlorine and iodine is stemming from interhalogen reactions, in particular with bromine. These can occur in the gas phase similar to Reaction (R2) by substitution of one BrO molecule (with X denoting either Cl or I):

$$\mathrm{BrO} + \mathrm{XO} \longrightarrow \mathrm{BrX} + \mathrm{O_2} \tag{R18}$$

$$\mathrm{BrX} + \mathrm{h}\nu \longrightarrow \mathrm{Br} + \mathrm{X} \tag{R19}$$

Because the rate constant of these reactions are approximately one order of magnitude larger compared to Reactions (R2) and (R3) (Atkinson et al., 2007), these can further increase ozone depletion. Likewise, the interhalogenic reactions can occur via heterogeneous reactions in the liquid phase of aerosols or the surface. In particular, this can increase the speed of bromine release from the surface via the reaction of HOBr with chlorine in the liquid phase:

$$\mathrm{HOBr\,(aq)} + \mathrm{H^+\,(aq)} + \mathrm{Cl^-\,(aq)} \longrightarrow \mathrm{BrCl} + \mathrm{H_2O} \tag{R20}$$

Under typical $\mathrm{Cl^-/Br^-}$ ratios (between 40 to 600), this reaction is occurring at speeds two or three magnitudes larger than the reaction with bromide (R11). If the BrCl produced in this reaction would subsequently be released to the gas phase, this would actually slow down the bromine explosion, since it does not increase the amount of bromine in the gas phase (i.e. $\alpha = 1$ compared to $\alpha \leq 2$, cf. (R16)). However, there is an equilibrium reaction which can lead to the release of $\mathrm{Br_2}$ from this reaction:

$$\mathrm{BrCl} + \mathrm{Br^-} \rightleftharpoons \mathrm{Br_2Cl^-} \tag{R21}$$

This equilibrium is shifted towards $\mathrm{Br_2Cl^-}$ for colder temperatures, see also section 2.2.2. For temperatures below $-15\,^{\circ}\mathrm{C}$, the reaction of HOBr with chloride strongly increases the reaction speed of the bromine explosion in the liquid phase while leading to slight reduction of α from 2 to approximately 1.97 (Herrmann, 2021). This reaction pathway is also sketched in Figure 2.2.

The uptake of halogen nitrates can also lead to further activation of bromide through the heterogeneous surface reaction,

$$\mathrm{BrONO_2} + \mathrm{H_2O} \xrightarrow{\mathrm{aq}} \mathrm{HOBr} + \mathrm{HNO_3} \tag{R22}$$

which was first proposed by Aguzzi and Rossi (2002) (see Figure 2.2). The produced HOBr can then subsequently release Br_2 via Reaction (R11). In a laboratory study by Pratt et al. (2013), it was found to contribute to the observed Br_2 release. A model study by Cao et al. (2014) demonstrated that this mechanism can increase halogen release, with the rate limiting step being the surface uptake of $BrONO_2$ and therefore increase ozone depletion if NO_x levels are not too high[1].

Besides anthropogenic emissions, the main source of NO_x, especially of NO_2, in the polar region is snow (Jones et al., 2000, 2001). NO_3 is produced mainly via the reaction:

$$NO_2 + O_3 \longrightarrow NO_3 + O_2 \tag{R23}$$

The formed NO_3 can then produce N_2O_5 from the reaction:

$$NO_2 + NO_3 + M \longrightarrow N_2O_5 + M \tag{R24}$$

The produced N_2O_5 can also release bromine from the surface via Reaction (R27) as discussed in section 2.1.1. However, outside of heavily polluted areas, the concentrations of NO_2 and especially NO_3 are very low in the Arctic, which is why the influence of this release pathway is usually negligible .

[1]High levels of NO_x increase the formation of the chemically less active bromine nitrite $BrNO_2$, which was shown to slow down the destruction of ozone (Zielcke, 2015). Likewise, a strong shift in partitioning of reactive bromine towards high mixing ratios of bromine nitrate $BrONO_2$ can also slow down ozone destruction (Custard et al., 2015).

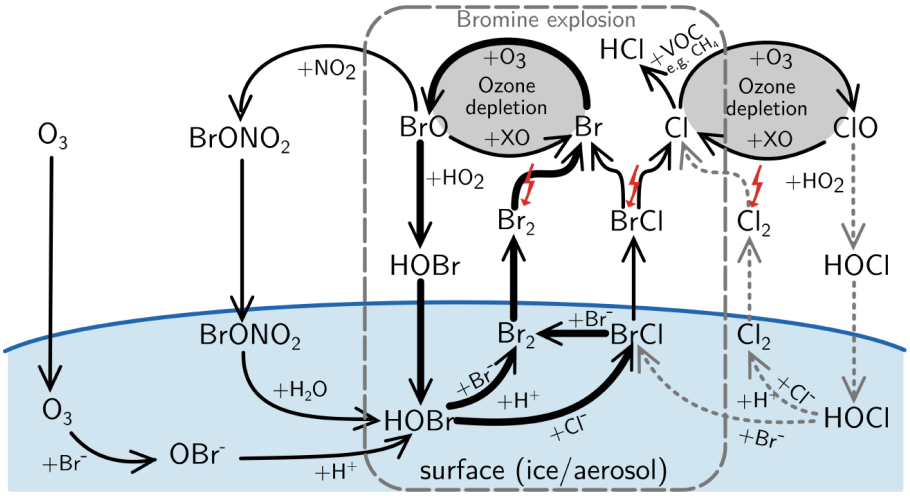

Figure 2.2: *Visualization of different reaction pathways of heterogeneous bromine release. The bromine explosion reaction cycle (R10 – R14) is contained inside the grey dashed-line box with bold arrows marking reactions that lead to an increase of atmospheric bromine. Photolytic reactions are marked with a red arrow. Ozone depleting reaction cycles (e.g. (R1 – R4)) are highlighted as grey areas. The grey dotted arrows indicate reactions of chlorine equivalent to that of bromine as proposed in Wren et al. (2013). These do not lead to an increase of active halogen in the gas phase and play only a minor role for ozone destruction due to the high reactivity of Cl with hydrocarbons. The left side shows a possible mechanism responsible for releasing the initial bromine seed mixing ratio "triggering" the bromine explosion, see Reaction (R25). Figure adapted from Nasse (2019).*

2.1.1 Initial release mechanism

The autocatalytic bromine explosion reaction requires an initial "seed" mixing ratio of activated bromine in the gas phase. A number of different mechanisms have been proposed to provide this initial bromine release, serving as "trigger" for the bromine explosion reaction sequence. An incomplete list includes the release of bromine from oxidation of surface bromide via ozone (Oum et al., 1998), from photolysis of $CHBr_3$ of biogenic origin (Tang and McConnell, 1996), the oxidation of bromide via aqueous-phase OH radicals (Mozurkewich, 1995; Sjostedt and Abbatt, 2008) or the release of reactive bromine via heterogeneous reactions from sea salt aerosol (SSA) sublimated from blowing snow (Yang et al., 2008; Huang and Jaeglé, 2017).

Often these mechanisms were proposed analogous to known stratospheric reaction pathways and many have been confirmed only in laboratory studies (if at all) or tested in 3D numerical models. The importance of all these mechanisms as potential triggers for the bromine explosion comes from the fact that they are independent of the activated bromine concentration already present in the atmosphere. As an example, the rate of the bromide oxidation by ozone ((R25)) depends only on the ozone concentration in the gas phase above the surface[2]. This dependence on the ozone concentration is of linear nature, in contrast to the exponential bromine emission rate of the bromine explosion. However, it is limited by the surface deposition rate of ozone, which in itself is dominated by the surface resistance (Wesely, 1989). This is visualized in Figure 2.3. The mechanisms considered to be most important for the initial release of reactive bromine are discussed in the following.

Oum et al. (1998) proposed a release of bromine from surface snow via the uptake of ozone (see also Figure 2.2). The mechanism can be summarized with the net reaction

$$O_3\,(g) + 2\,Br^- + 2\,H^+ \xrightarrow{\text{mp}} Br_2\,(g) + H_2O\,(l) + O_2\,(g) \qquad \text{(R25)}$$

Pratt et al. (2013) investigated this in a laboratory study and found that it likely requires light to efficiently occur. In contrast to this, Artiglia et al. (2017) were able to directly confirm this mechanism (adding some clarifications regarding the reaction dynamics) and demonstrated that the release of Br_2 is not accelerated noticeably by the influx of light. This could allow a build-up of dihalogens also at night which are then photolysed at sunrise, accelerating the bromine explosion. Direct vertical gradient measurements of Br_2 and BrCl near Utqiaġvik, Alaska reported significant emission fluxes of reactive bromine from the snow-pack approximating $1 \times 10^8\,\text{molec}\,\text{cm}^{-2}\,\text{s}^{-1}$ (Custard et al., 2017). It has also been shown that bromine release correlates with the occurrence of first- and multi-year (FY and MY) sea ice (Wagner et al., 2001; Simpson et al., 2007b; Wagner et al., 2007; Bougoudis et al., 2020; Peterson et al., 2019), as will be discussed in more detail in section 2.2.1. Both surfaces have in common that they are usually covered by snow. Additionally, this mecha-

[2]This also requires that the surface has a high enough bromide concentration and low enough pH value, which is a prerequisite for the bromine explosion too.

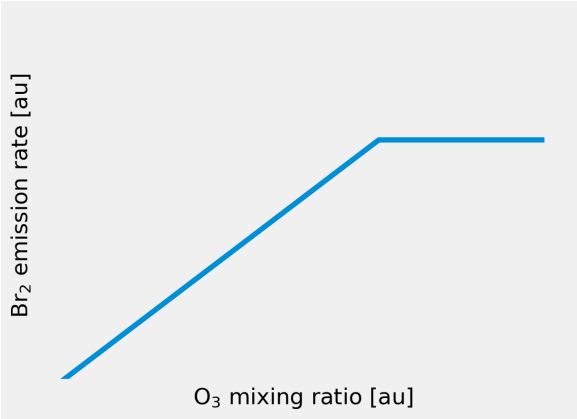

Figure 2.3: *Sketch of the emission rate of molecular bromine via surface uptake of ozone (Reaction (R25)) in arbitrary units (au). The rate of bromine emission depends linearly on the ozone mixing ratio up to a certain threshold when the surface resistance becomes the limiting factor for surface deposition.*

nism has been shown to reliably trigger bromine explosion events in several 3D models (e.g. Toyota et al., 2011, 2014; Falk and Sinnhuber, 2018; Herrmann et al., 2021; Marelle et al., 2021; Swanson et al., 2022).

In a very recent study, Yang et al. (2022, in review) performed daily salinity and bromide measurements on surface snow collected at Eureka, Canada. Based on the small vertical gradient of bromide deposition in comparison to nitrate emissions in the investigated snow samples, they concluded that bromine emissions from the snow-pack are unlikely to be a large source of reactive bromine and should not be able to cause bromine explosion reactions. However, the emission flux of reactive bromine of approximately $1 \times 10^7\,\mathrm{molec\,cm^{-2}\,s^{-1}}$ estimated from their measurements is only one order of magnitude smaller compared to the snow-pack parameterisation scheme applied in numerous models (e.g. Toyota et al., 2011; Herrmann et al., 2021), where this flux is enough to constantly trigger bromine explosions all over the arctic region.

Another mechanism releasing bromine from the surface layer of snow grains via reaction with the hydroxyl radical OH was suggested by George and Anastasio (2007) and Sjostedt and Abbatt (2008), leading to a series of reactions summarized in the following net reaction:

$$\mathrm{OH\,(aq)} + 2\,\mathrm{Br^-} + \mathrm{H^+} \longrightarrow \mathrm{Br_2\,(g)} + \mathrm{H_2O\,(l)} \qquad \text{(R26)}$$

Thus far, evidence for the existence of this mechanism was found only in laboratory studies (Abbatt et al., 2010; Pratt et al., 2013; Halfacre et al., 2019). To date only one model study estimated the impact of this mechanism on the occurrence of ODEs (Wang and Pratt, 2017) with inconclusive results.

Bromine can also be released via a heterogeneous reaction of N_2O_5 in the presence of sunlight as proposed by Sander and Crutzen (1996) and confirmed by Bertram and Thornton

(2009) as well as Lopez-Hilfiker et al. (2012):

$$N_2O_5\,(aq) + Br^- \longrightarrow BrNO_2\,(g) + NO_3{-}\,(aq) \tag{R27}$$

$$BrNO_2 + h\nu \longrightarrow Br + NO_2 \tag{R28}$$

In principle, this mechanism can be a potential trigger for the bromine explosion since it has no dependence on the amount of reactive bromine present in the atmosphere. However, N_2O_5 is formed from NO_3, which itself is formed via Reaction (R23). As alluded to earlier, the concentrations of both are low in the arctic region, therefore bromine emissions from Reactions (R27) and (R28) are unlikely outside of heavily polluted areas such as Prudoe Bay in Alaska.

Another mechanism for the activation of bromine was proposed by Yang et al. (2008) based on ideas from Sander et al. (2003). It involves the release of bromine from SSA, produced via sublimation of lofted snow from sea ice in conditions of high surface wind speed (see also section 2.2.3 and section 2.2.4). These aerosol particles contain trace amounts of bromide, which can be released as reactive bromine into the atmosphere via heterogeneous chemistry, which is proposed to be fastest in the presence of sunlight. A multitude of heterogeneous reactions capable of releasing bromine directly from these aerosol particles, without direct dependence on activated bromine in the atmosphere, have been proposed (e.g. Sander and Crutzen, 1996; Sander et al., 2003). These include all reactions discussed in this section, which could also release bromine from aerosol particles instead of the surface. However, no evidence for bromine release from aerosol particles was found yet.

A number of different model studies implemented bromine emissions from blowing snow as trigger for the bromine explosion reaction with varying agreements to (mostly satellite) observations (Yang et al., 2008, 2010; Theys et al., 2011; Huang and Jaeglé, 2017; Yang et al., 2019, 2020; Huang et al., 2020). In these models, the emissions from blowing snow are implemented without reference to any specific heterogeneous reaction as a function of the sea salt salinity flux and an aerosol-size dependent factor describing the fraction of bromide released as bromine from a single aerosol bin, see also section 2.2.3. Some of these model studies report good agreement especially to satellite observations of enhanced BrO events. However, as it is pointed out for example by Yang et al. (2020), this good agreement could also be indicative of a bias of the satellite observations towards vertically more extended events, discussed in more detail in section 2.2.4.

Recently a study by Marelle et al. (2021) implemented both blowing snow emissions as well as bromide oxidation from ozone as potential triggers for the bromine explosion. They found that emissions from blowing snow inluence less than 5 % of all observed ODEs if surface emissions of bromine are accounted for and there is little difference between purely ground-based emissions from the snow-pack and a combination of ground-based and blowing snow emissions. It was also demonstrated that previous model studies which attested larger significance to blowing snow sourced bromine emissions overestimated the amount of SSA produced from blowing snow by a factor of 10. However, they did not explicitly test blowing

snow emissions as replacement of the bromide oxidation by ozone, so it cannot be ruled out completely that blowing snow might be an efficient trigger for some ODEs.

It is beyond doubt that aerosol particles influence the tropospheric bromine chemistry and ODEs in general. They can provide a source of bromide for the bromine explosion and can sustain activated bromine even above the boundary layer via recycling (e.g Peterson et al., 2017), which is discussed in more detail in section 2.2.3. There are also indications that blowing snow can influence the availability of SSA in the polar atmosphere (e.g. Yang et al., 2019; Frey et al., 2020).

However, observational evidence for the influence of direct bromine emissions from blowing snow on the occurrence of ODEs is lacking. Lieb-Lappen and Obbard (2015) measured depleted Br^-/Cl^- ratios in blowing snow compared to a constant ratio in surface snow, which was almost equivalent to seawater. This can be interpreted as evidence of strong bromine emissions from blowing snow. However, the depleted ratio could also stem from bromine recycling on the aerosol particles or release of bromide via the bromine explosion reaction. This is also pointed out by the authors, who add that another possible explanation among others is that the replenishment of bromide in the snow-pack is faster then bromide activation under the mid-strength wind conditions their measurements were performed in. On the other hand, there are several studies reporting that no clear link between surface wind speeds and bromine activation could be established (e.g. Halfacre et al., 2014; Peterson et al., 2015), which is discussed in greater detail in section 2.2.4. Since increased surface wind speeds are a precondition for the formation of blowing snow (see section 2.2.3), this can be seen as evidence against blowing snow sourced bromine emissions.

It has to be mentioned that bromine release from these mechanisms is no prerequisite for the occurrence of an ODE. In principle, even a very small number of atmospheric bromine atoms or molecules[3] can produce a very large bromine enhancement from the bromine explosion cycle (R10 – R14), given a large enough time frame. As an example, Swanson et al. (2022) performed a simulation with the snow-pack emissions in their model turned off. Although no bromine enhancements could be discerned during February and March, in April there were some BrO enhancements predicted by their model that they also measured. Yet, even these were strongly underestimated.

However, one has to consider the fact that bromine chemistry is influenced by a range of environmental processes (see also the next section 2.2), including but not limited to availability of Br^- at the surface, surface temperature, surface acidity, atmospheric dynamics and light availability, whose delicate interplay determines if the bromine explosion even takes place and when it results in significant observable enhancement of atmospheric bromine. Although it is still not fully understood how theses processes are affecting the bromine chemistry, it is clear that conditions facilitating bromine release can change on a relatively short time scale as it is discussed in more detail in the next section. This is even more critical at the beginning of Arctic spring when day length and therefore the time frame in

[3]Which is emitted for example from sea water and open oceans (Gong et al., 1997).

which a bromine explosion can occur is still short.

Therefore, release mechanisms independent (or less dependent) of the atmospheric bromine concentration or mechanisms favored by other environmental conditions than the bromine explosion (for example independent of sunlight) make it far more likely to observe an ODE, by providing an initial seed mixing ratio of activated bromine from which the bromine explosion can produce significant amounts of bromine on a much shorter timescale. This is also supported by observations, which suggest that the bromine explosion mechanism alone is insufficient to explain bromine release in the field (e.g. Toyota et al., 2011; Pratt et al., 2013; Swanson et al., 2022).

Nonetheless, if enough activated bromine is still present in the atmosphere, for example from previous ODEs, which can be expected especially later in the season as discussed in section 8.3, then these reactions can lose importance due to their speed being limited by surface processes as alluded to previously. This will be further discussed in chapter 9.

While there is a general agreement upon the necessity for additional release mechanisms for reactive bromine, currently the major debate revolves around the relative importance of emissions from the snowpack, e.g. via Reaction (R25) or Reaction (R26), and emissions from blowing snow (e.g. Bognar et al., 2020; Swanson et al., 2022).

2.1.2 Evolution of a typical ozone depletion event

Based on the last two sections, this section summarises the typical progression of an ODE as it is currently understood.

(I) An initial seed mixing ratio of reactive bromine in the atmosphere is provided. This can occur for example through advection or by surface emission from bromine, e.g. from uptake of N_2O_5 in polluted areas via Reactions (R27 – R28) or from surface uptake of ozone via Reaction (R25). This is not yet well understood and likely subject to various environmental influences, see also section 2.2.

(II) This initial bromine mixing ratio increases rapidly during the day via the bromine explosion reaction cycle (R10 – R14), provided suitable environmental conditions are present (see section 2.2).

(III) The catalytic ozone depletion is increasing rapidly with an increasing concentration of atmospheric bromine due to the rate-limiting step being the BrO self reacion (R2). Typically at BrO mixing ratios of above $30\,\mathrm{pmol\,mol^{-1}}$ a strong decrease of ozone is measurable.

(IV) With a decreasing ozone mixing ratio conversion of Br to BrO slows down and consequently, the reaction of Br with aldehydes forming HBr becomes more likely, which is leading to a decrease of the bromine mixing ratio and eventually to an end of the ODE.

(V) If the abundance of reactive bromine is low enough, ozone can be replenished, for example from transportation, either vertically through (turbulent) diffusion from the free troposphere or horizontally via advection, or it can be replenished photochemically.

(VI) An increase in the ozone concentrations can again cause bromine release via the bromine explosion, provided the necessary conditions for the bromine explosion are still met. At the beginning bromine release is slower than the ozone replenishment due to it being dependent both on the bromine and the ozone concentration.

2.2 Influence of environmental and meteorological factors on ODEs

In recent decades, significant progress has been made in the understanding of the various ways that environmental factors such as the meteorology or the surface type can influence ODEs and the corresponding bromine chemistry. Yet despite this huge body of research, there are still no conclusive results regarding the exact relationship between ODEs and some of these factors. Many parameters potentially affecting the chemistry of ODEs and bromine release are highly intercorrelated and it is difficult to discriminate their delicate interplay. What is agreed upon is that the relationship between observations of enhanced BrO and the dominant physicochemical parameters is complex and non-linear (e.g. Sihler, 2012).

This section provides a compilation of existing hypotheses with respect to environmental parameters potentially correlating with ODEs as well as field measurements and model studies providing evidence for or against specific theories.

2.2.1 Surface type

As it has been discussed in the previous section, the bromine explosion is favored by a low pH value and high concentration of halides with an increased Br^-/Cl^- ratio compared to sea water. Sea ice provides all of these conditions in certain circumstances (cf. section 2.2.2). Although SSA can also exhibit these qualities (cf. section 2.2.3), the observed bromide content of typical aerosol concentrations (especially those sourced only from open sea water) is not enough to explain ODEs. It is generally agreed upon by now that the bromide reservoir for ODEs is sourced by sea ice (e.g. Wagner and Platt, 1998; Simpson et al., 2007a). However, the relative importance of the specific sources of bromine emission are still under debate, with numerous candidates having been proposed. This section will give an overview of the bromide sources currently considered most important.

The most attention has been given to younger and especially first-year (FY) sea ice. Satellite measurements by Wagner et al. (2001) reported no significant amounts of boundary layer BrO after melting of all FY sea ice and linked the development of BrO plumes to locations of mainly FY sea ice. Sihler (2012) concluded from the analysis of several years of GOME-2 data that bromine release is highly increased over sea ice compared to release over

(snow-covered) land or open water. Based on earlier studies by Wagner et al. (2007), it could be ruled out that the difference in BrO measured from satellite results from the differing surface albedo of these surfaces. It is assumed that the much higher salinity of FY sea ice compared to older ice (e.g. Nghiem et al., 2012) provides a larger concentration of bromide in the liquid layer, increasing the likelihood of both the bromine explosion (R10 – R14) as well as other mechanisms for reactive bromine release (cf. section 2.1.1). Additionally, the freezing process of sea ice leads to the formation of brine above the sea ice, which is highly concentrated in sea salts.

The snow-pack is another bromide source credited with major importance for ODEs (Custard et al., 2015; Peterson et al., 2019). Since large parts of the sea ice is snow-clad (e.g. Kwok et al., 2020), the sea ice surface cannot be the main source of bromine emissions in most cases and halides have to be brought to the surface of the snow-pack. This can occur via transportation of SSA from sea spray (Buat-Menard et al., 1974) or alternatively via upwards migration of brine from the sea ice surface to the snow-pack (Perovich and Richter-Menge, 1994; Domine et al., 2004). A model study by Yang et al. (2010) demonstrated that FY sea ice allows an easier sea salt accumulation in the snow-pack. Measurements by Pratt et al. (2013) reported that the snow over FY sea ice features a higher salinity. The mechanisms considered most important for release of bromine from the snow-pack are discussed in section 2.1.1.

Hollwedel et al. (2004) reported that a 5-year time series of tropospheric BrO columns measured from GOME showed a significant increase in the area covered by enhanced BrO. They proposed that anthropogenic influences on the climate system, i.e. global warming, could have led to an increase of FY sea ice which in turn led to the observed trend. An analysis of a 22-year time series of tropospheric BrO vertical column densities (VCDs) measured from the instruments GOME, GOME-2 and SCIAMACHY reported a moderate but significant correlation of the tropospheric BrO VCDs and FY sea ice extent both temporally and spatially (Bougoudis et al., 2020). Although the results are not completely conclusive probably due to transportation away from regions of FY ice, they conclude that an observed increase of the magnitude of enhancement and area where plumes appear is linked to retreat of MY ice and corresponding increase of FY ice, confirming the proposition made by Hollwedel et al. (2004).

Another possible reason for the distinction of FY sea ice as source of reactive bromine responsible for ozone depletion are the so-called frost flowers, ice crystals with a diameter of a few centimeters forming from re-sublimating water on freshly frozen sea ice. Due to their high salinity (about three times higher than in sea water) (Rankin et al., 2002) and their large surface area, Kaleschke et al. (2004) proposed them to be a primary source of reactive bromine. They assessed this claim by comparing satellite observations of tropospheric BrO and sea ice coverage with regions of potential frost flower coverage derived from a simple thermodynamic model, from which they concluded that FY sea ice regions potentially covered by frost flowers are the main source of bromine for the bromine explosion. Although laboratory experiments by Wren et al. (2013) demonstrated that a larger surface area of

artificial snow grains (i.e. smaller snow grains) increase the production of dihalogens, the importance of frost flowers was already questioned early on. Domine et al. (2005) questioned their proposed high surface area, as field measurements of them revealed that their total surface area on ice is only $1.4\,m^2\,m^{-2}$. An analysis of airmass trajectories by Simpson et al. (2007b) found no significant correlation of the bromine mixing ratio to air masses with contact to frost flowers and instead established a clear link to contact with FY sea ice surfaces. For these reasons they are no longer believed to be a distinct source of bromide (Abbatt et al., 2012; Simpson et al., 2015).

It was also suggested that frost flowers could play an important role in the release of aerosol particles and therefore contribute to the bromine explosion (see section 2.2.3), for example via salination of blowing snow (Obbard et al., 2009). However, recent investigations of frost flowers in the lab could not confirm their influence on aerosol release despite very high wind speeds (Roscoe et al., 2011; Yang et al., 2017). A model study by Huang and Jaeglé (2017) indicated that the influence of frost flowers on the production of SSA has to be very minor. They proposed this is due to the fact that they do not become airborne easily and their occurrence is not widespread enough, both in time and space, to produce larger quantities of aerosol particles relevant for bromine explosions.

Recent studies questioned the presumed irrelevance of MY sea ice for the formation of enhanced tropospheric BrO. Both Peterson et al. (2019) and Bognar et al. (2020) reported significant mixing ratios of activated bromine over MY sea ice, indicating that snow on MY ice might also contribute to bromine release.

2.2.2 Temperature

For a long time, the air temperature was thought to be the parameter with the strongest influence on ODEs. It is highly correlated with the meteorology of the boundary layer, which is also thought to exert a strong influence on bromine activation (see section 2.2.4). Likewise, the temperature can affect the release of bromine by altering surface conditions and changing the involved release and recycling mechanisms for halogens. For these reasons, the interpretation of results can be ambiguous.

Evaluations of ozonesonde profiles at all Arctic measurement stations led Tarasick and Bottenheim (2002) to the conclusion that surface temperatures below $-20\,°C$ are a prerequisite for the occurrence of ODEs. The authors attributed this to different factors. They argued that increased atmospheric stability may favor the processes leading to bromine activation at the surface. Such increased stability can be caused by lower surface temperatures. This is discussed in more detail in section 2.2.4. Furthermore, Tarasick and Bottenheim (2002) also noted that decreasing surface temperatures cause an increase in the concentration of halogen ions in the brine. This was first reported by Richardson (1976) who found that salinity in the brine is increased fourfold at $-10\,°C$ compared to freezing temperature and further supported by Morin et al. (2008) who confirmed an increase of bromide concentrations with increasing salinity of the brine.

All of these mechanisms may allow for an increase in the salinity of the brine and the bromide concentration at the surface. However, sea water and in particular the brine formed above sea ice is naturally alkaline and its alkaline pH is additionally buffered by HCO_3^- and CO_3^{2-}. Since the bromine explosion reaction requires H^+ ions, it requires an acidic pH value, likely smaller than 6 (Fickert et al., 1999). This was confirmed recently in a study by Halfacre et al. (2019), where they reported a strong pH dependence of the likelihood for an ODE to occur, yet a high surface halide concentration was found to be of similar importance. A model study by Sander et al. (2006) investigated mechanisms by which this buffer capacity can be reduced. If the surface cools below −8 °C, most of the carbonate reaches its solubility limit and precipitates which reduces the buffering capacity of sea water. Sander and Morin (2010) argued that at temperatures of about −20 °C, precipitation of calcium carbonate could further reduce the buffering capacity. Subsequently, the acidity can then be increased for example by uptake of sulphuric acid advected from mid-latitudes, leading to a pH value below 6 (e.g. Brimblecombe and Clegg, 1988).

As discussed in section 2.1, the bromine explosion reaction releases both Br_2 and BrCl. Sander et al. (2006) reported a temperature dependence of the fraction of Br_2 compared to BrCl released from the heterogeneous phase, with lower temperatures shifting this towards Br_2, resulting in a higher amplification ratio of the bromine explosion mechanism (cf. Reaction (R21)). There are also several studies reporting that an increased bromide to chloride ratio on the surface compared to ocean water increases this fraction of released Br_2 (e.g. Simpson et al., 2007a; Wren et al., 2013). Koop et al. (2000) described that the Br^-/Cl^- ratio could be further amplified by precipitation of $NaCl \cdot {}_2H_{20}$ below −21 °C. Sander et al. (2006) proposed that cold temperatures could therefore also lead to an increase of the bromide to chloride ratio in the aerosol, facilitating the recycling of reactive bromine on aerosol particles, see also section 2.2.3.

In conclusion, there is a variety of explanations regarding an influence of surface temperature on the occurrence of ODE and the activation of surface bromine. Yet in recent years, the assumption of a strong influence of low temperatures was questioned. Koo et al. (2012) analyzed a long-term dataset of ground-based measurements and reported that ODEs occur at a wide range of temperatures. Similar findings were reported e.g. by Bottenheim et al. (2009) and Jacobi et al. (2010). Burd et al. (2017) did not find any significant influence of the surface temperature on Br_2 emissions and recycling as long as sea ice is not melting, so up to −1 °C.

At the same time, an analysis of a long-term dataset of satellite observations found a weak negative correlation between the likelihood of enhanced BrO (total) columns and surface temperature (Seo et al., 2020). Swanson et al. (2020) reported two distinct sets of meteorological conditions favoring the occurrence of ODEs, one of which contained low surface temperatures. However, it is possible that the low surface temperatures are merely an indication of other, more important conditions such as a stable boundary layer, which will be discussed in section 2.2.4.

While the influence of surface temperature on ODEs remains a source of uncertainty,

recent studies could show that it is likely not as important as previously thought.

2.2.3 Aerosols

The term aerosol denotes a suspension of small particles or liquid droplets in gas. Ordinarily the aerosol particles themselves will also be loosely termed as aerosols. The size of aerosols ranges from 2 nm up to 10 µm (McNeill, 2017).

The influence of aerosols on ODEs has been suspected for a long time. Due to the long atmospheric lifetime of aerosol particles, it has been conjectured that they can provide a surface for recycling of reactive bromine as well as a source of new bromide in the air above the atmospheric boundary layer.

Ground-based measurements by Frieß et al. (2004) reported enhanced BrO events associated with high aerosol concentrations. Begoin et al. (2010) investigated a BrO explosion event spatially coincident with a polar cyclone using satellite observations and trajectory calculations. They proposed that recycling on aerosols sustains the bromine explosion reaction cycle and explains the long lifetime of the observed BrO plume. Similar conclusions were drawn by Blechschmidt et al. (2016) and Zhao et al. (2016) who both examined an ODE in the context of frontal activities near a low-pressure system. They argued that vertical lifting and high wind speeds driven by the cold front of a polar cyclone can transport cold brine-coated snow and salt aerosols above the boundary layer which would provide a source for the bromine explosion and extend the lifetime of observed BrO plumes by a continuous supply of reactive bromine.

A study by Peterson et al. (2017) used ground-based measurements to demonstrate that indeed aerosols can extend the atmospheric lifetime of atmospheric bromine significantly and sustain bromine activation above the boundary layer. Furthermore, satellite measurements of tropospheric BrO from OMI together with GEOS-5 simulations of SSA showed a significant association between the temporal and spatial extent of enhanced BrO concentrations and SSA (Choi et al., 2018).

A one-dimensional box model from Sander and Crutzen (1996) first demonstrated that bromide from SSA could provide the main source of reactive bromine for an ODE as discussed in section 2.1.1.

Based on ground-based Multi-AXis Differential Optical Absorption Spectroscopy (MAX-DOAS) measurements of enhanced BrO together with high aerosol extinction, Frieß et al. (2011) proposed that in addition to recycling, the transport of aerosols to the snow-pack over land provides a source, allowing bromine explosions away from direct bromide sources such as sea ice.

The aerosols relevant to bromine activation are presumably SSA rich in bromide (cf. section 2.2.1). Several mechanisms have been proposed explaining the formation of these SSA in polar regions, such as wave breaking in the open ocean (e.g. Lewis et al., 2004; Andreae et al., 2009). It has also been proposed that SSA can be sourced by erosion of frost flowers (Rankin et al., 2002) or by snow lofted from the surface by strong surface winds

(blowing snow, see also sections 2.1.1 and 2.2.4).

The latter has been thoroughly investigated in recent years. Model studies have shown that blowing snow plays a important but minor role for the formation of SSA, demonstrating improved agreements to measurements of sea salt aerosols when including aerosols sublimated from blowing snow (Huang and Jaeglé, 2017; Rhodes et al., 2017; Huang et al., 2018; Yang et al., 2019). The common assumption in these models is that blowing snow formation starts when the wind speed at 10 m height is above a critical threshold between $7\,\mathrm{m\,s^{-1}}$ to $10\,\mathrm{m\,s^{-1}}$ depending on the temperature, with lower temperatures enabling blowing snow events at lower wind speeds. The snow sublimation flux is then calculated from the the local wind speed, the temperature and the humidity (e.g. Yang et al., 2008; Marelle et al., 2021), which in turn determines the sea salt aerosol emission flux. Ship-based measurements by Frey et al. (2020) also indicate that blowing snow sourced SSA impact the availability of aerosols in the atmosphere. Swanson et al. (2022) compared ground observations of enhanced BrO at Utqiaġvik with results of the atmospheric chemical transport model GEOS-Chem. They reported improved agreement between model and observations when accounting for sea salt aerosol production from blowing snow, concluding that sea salt aerosol particles provide a necessary additional surface for reactive bromine recycling. Their model setup was very similar to Marelle et al. (2021) and Herrmann et al. (2022), using bromine emissions from the snow-pack as trigger mechanism (cf. section 2.1.1).

2.2.4 Wind speeds and boundary layer stability

The stability of the atmospheric boundary layer (BL) is associated with vertical potential temperature gradients, vertical wind shear and horizontal pressure gradients. Investigations regarding the relation between boundary layer stability and ODEs often focus on surface wind speed as well as pressure gradients as easily accessible proxies for the stability of the atmospheric boundary layer. Numerous studies indicate that it affects the bromine chemistry and the occurrence of ODEs in several ways. However, the causality between changes in boundary layer meteorology and bromine chemistry is still unclear and findings are contradictory in some cases and inconclusive in others. This section compiles a summary of field observations, simulations and hypotheses regarding the influence of boundary layer meteorology on ODEs.

Early studies showed that a large fraction of observed ODEs are associated with strong atmospheric stability in the atmospheric boundary layer (e.g. Frieß et al., 2004; Simpson et al., 2005; Jacobi et al., 2006). Low wind speeds, temperature inversions and slow vertical mixing correspond to a shallow and stratified boundary layer which is found often over ice and snow in the polar regions (e.g Anderson and Neff, 2008). Such a stable boundary layer can then serve as an enclosed "reaction chamber", increasing the contact time between air masses and the surface and allowing for an accumulation of high concentrations of reactive bromine at the surface (Lehrer et al., 2004; Peterson et al., 2015). For condensed phase reactions restricted to the Earth's surface such as the majority of those described in section 2.1,

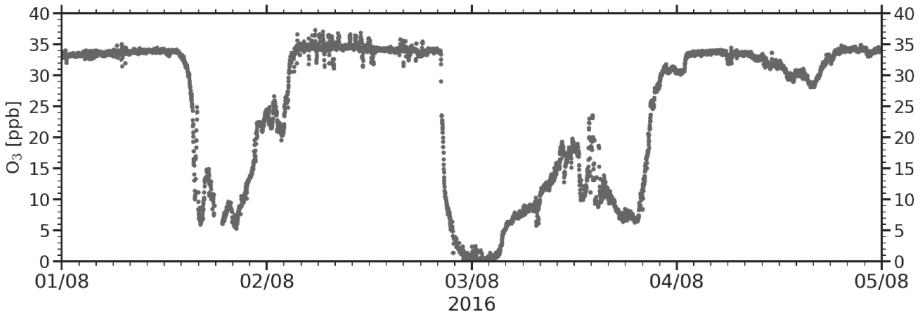

Figure 2.4: *Example of an ozone depletion event at Neumayer III. Figure adapted from Nasse (2019), data from Weller (2017).*

the reaction rate can be accelerated by increasing the concentration of reactants in the air just above the surface (Simpson et al., 2007a; Saiz-Lopez and von Glasow, 2012).

This was supported further by measurements from satellite instruments, which observed many ODEs under clear sky conditions associated with a stable troposphere (Wagner et al., 2001; Jones et al., 2006). It was also argued by Morin et al. (2005) that a stratified boundary layer leads to maximum tropospheric BrO VCDs, based on observation of boundary layer ozone chemistry.

Simpson et al. (2005) and Wagner et al. (2007) deduced from these observations that bromine release from the surface, particular from snow-covered sea ice (see section 2.2.1), is of special importance for both the initial bromine release triggering ODEs (see also section 2.1.1) as well as for significant BrO enhancement.

While most ODEs were measured during conditions of low wind speeds and strong atmospheric stability, a smaller number was also observed during high wind speeds, particularly at measurement stations at greater distances from sea ice. In the past, it has been assumed that this association arises from advection of air masses in which ozone has been depleted previously or which have been enriched in reactive bromine over corresponding surfaces (Hausmann and Platt, 1994; Hönninger and Platt, 2002; Hönninger et al., 2004; Simpson et al., 2007a). This is exemplified in Figure 2.4, where a rapid change of the ozone mixing ratio at Neumayer station on a time scale usually impossible for chemical processes (only few hours) was measured, indicating the importance of advection.

However, Jones et al. (2009) reported significantly elevated BrO VCDs and ozone depletion measured from satellite occurring in regions of high surface wind speeds. They developed a qualitative model demonstrating that very calm weather conditions as well as 10 m wind speeds larger than $10\,\mathrm{m\,s^{-1}}$ are very strong predictors of ODEs. Similar findings of enhanced BrO column linked to high surface wind speeds were reported later, particularly from satellite instruments (e.g. Begoin et al., 2010; Sihler, 2012; Blechschmidt et al., 2016; Zhao et al., 2016), but only few ground-based measurements reported associations of high BrO concentrations and higher surface wind speeds (Hönninger and Platt, 2002; Hönninger et al., 2004; Jones et al., 2010; Frieß et al., 2011). There are several explanations for these observations.

Morin et al. (2008) proposed that an increase in surface wind speed leads to an increased diffusion of the reactive bromine produced in the interstitial air above the snow-pack into the atmosphere, a phenomenon called wind pumping.

Higher surface wind speeds could increase the concentration of SSA in the atmosphere, for example from sublimation of blowing snow (e.g. Yang et al., 2008; Begoin et al., 2010; Yang et al., 2019). Indeed some of the observed ODEs associated with higher surface wind speeds have been linked to conditions of blowing snow. Such an increased concentration of bromide rich aerosols could then extend the lifetime of enhanced BrO events and sustain bromine activation even above the boundary layer as discussed in section 2.2.3. Since satellites measure BrO columns, even very high mixing ratios could be hard to detect if they are isolated in a very shallow boundary layer (e.g. Sihler et al., 2012). A larger aerosol concentration could therefore increase the likelihood of detection of such events from satellite by enabling (and sustaining) a vertically more extended BrO enhancement, explaining especially the aggregation of satellite measurements associated with conditions of high wind speeds and decreased boundary layer stability (cf. section 2.2.3 and e.g. Peterson et al. (2017)).

Toyota et al. (2011) suggested that high surface wind speeds could increase the availability of radical bromine precursors in the snow-pack by a return of the lofted aerosols to the surface.

It was also suggested that the correlation between high wind speeds and ODEs could be indicative of an additional release of reactive bromine from blowing snow, triggering rapid bromine enhancement via the bromine explosion (Jones et al., 2009; Abbatt et al., 2012). This followed the ideas proposed prior by Yang et al. (2008), who demonstrated that reactive bromine emissions from blowing snow sourced SSA could trigger bromine explosions (cf. section 2.1.1).

Despite several model studies reporting agreements to observational data using simulations utilizing bromine emitted from blowing snow during conditions of high wind speed as trigger for ODEs, there is only weak observational evidence for this release mechanism (cf. section 2.1.1).

Lieb-Lappen and Obbard (2015) measured depleted Br^-/Cl^- ratios in blowing snow compared to a constant ratio in surface snow, possibly indicating a release of bromine from the snow sourced aerosols. In a study by Peterson et al. (2015), the association between wind speed and atmospheric stability on one side and the vertical distribution of tropospheric BrO on the other side was investigated using several years of MAX-DOAS observations. They reported that some of the very high columns extending 1000 m or more above the surface were linked to wind speeds above $7\,m\,s^{-1}$ caused by low pressure systems, agreeing with previous measurements of Jones et al. (2010) and Roscoe et al. (2014). Yet the very low frequency of these events led them to the conclusion that high wind speeds and blowing snow can only play a minor role for bromine activation if at all. Measurements at Eureka, Canada by Bognar et al. (2020) reported that the presence of coarse-mode aerosols larger than 0.5 µm was a necessary condition for the observation of enhanced BrO, confirming

that a high aerosol optical depth is required to maintain lofted BrO, probably via recycling. Another study by Halfacre et al. (2014) analyzed ground-based observational data gathered over several years and found no clear influence of surface wind speed on BrO enhancement.

In the polar atmosphere, higher wind speeds are indicative of increased vertical mixing and a boundary layer which is less stable and stratified (Stull, 1988). Many satellite based measurements therefore linked the higher wind speeds to an uplift of the reactive bromine from the surface to higher air masses even above the boundary layer (Begoin et al., 2010; Choi et al., 2012; Sihler et al., 2012; Blechschmidt et al., 2016; Zhao et al., 2016; Choi et al., 2018). As discussed before, this was most often interpreted to stem from either new emissions of reactive bromine or recycling on aerosols, both sourced from blowing snow. However, Sihler (2012) and Moore et al. (2014) proposed that an increased vertical mixing could also prolong bromine explosions as well as increase their likelihood by providing a continuous supply of ozone by mixing air masses depleted in ozone but rich in reactive bromine and vice versa. As it was pointed out by Sihler (2012), this would be especially pronounced in frontal systems and likely become more frequent later in the season when surface ozone is depleted in vast areas over sea ice (e.g. Wagner et al., 2007).

There have been several studies trying to investigate this ostensible discrepancy in meteorological conditions associated with bromine explosions. A long-term analysis covering ten years of GOME-2 satellite measurements investigated the relation between enhancement of total BrO columns and different meteorological parameters (Seo et al., 2020). They only found significant correlations of BrO to the tropopause height, with inconclusive results regarding surface wind speed and boundary layer height. However, the use of total columns in their study restricts the explanatory power of the analysis as the authors also point out.

An investigation of the relationship between tropospheric BrO VCDs from GOME-2 and meteorological parameters from the ECMWF Re-Analysis (ERA-interim) based on case studies by Sihler et al. (2014) found that ODEs are clearly influenced by BL meteorology, however, the exact causality could not be discerned.

Bougoudis et al. (2022) used an artificial neural network to reproduce ODEs and determine the sensitivity on environmental parameters of BrO enhancements predicted by the model. They found that the 2 m air temperature and mean sea level pressure have the most predictive power of all parameters in their model. However, the authors point out that the model shows a very strong bias towards BrO events occurring in low-pressure systems during low air temperatures and in deeper boundary layers. This is most likely the result of using satellite observations as training data, which seem to be biased towards such events as discussed before. Therefore these results are inconclusive.

These apparent ambiguities were reconciled in parts in a study by Swanson et al. (2020). A principal component analysis (PCA) of over six years of ground-based BrO observations combined with meteorological data from the Modern Era Retrospective Analysis for Research and Applications 2 (MERRA-2) identified two distinct sets of meteorological conditions with high predictive power towards tropospheric BrO enhancements. The first set with the highest predictive power consists of cold and stable conditions with low wind

speeds, consistent with enhanced BrO measured under surface-based temperature inversion and a low atmospheric boundary layer. The second set consists of less-stable mixed layer atmosphere with low atmospheric pressure, consistent with observations of enhanced BrO in low-pressure systems such as frontal systems and cyclones. The authors showed that a simple regression model based on their PCA was able to accurately predict enhanced VCDs of BrO both in the lowest 200 m as well as extending in the lowest 2000 m of the troposphere. However, the study did not provide any insights why these sets of conditions favor BrO explosions. The limitations of the analysis method also did not allow to provide information on the frequency of the two sets of conditions, so it could still be possible that the less-stable atmospheric conditions are only associated with a small fraction of all ODEs, neither did it allow to discern any seasonal differences in the set of atmospheric conditions leading to ODEs.

The lingering debate on the relative importance of these two distinct sets of meteorological conditions on the occurrence of ODEs is closely associated with the debate about the initial release mechanisms discussed in section 2.1.1. The stable, shallow boundary layers with low wind speed provide favorable conditions for triggering bromine explosions from snow-pack release of reactive bromine while the less stable atmospheric boundary layer related to high wind speeds could enable bromine release from blowing snow sourced aerosols.

3 | Tropospheric bromine monoxide observations from satellite

Spectroscopic instruments aboard of satellite instruments can be used to measure the abundance of trace gases. Depending on the trace gas in question, light of different wavelength regions reflected at the surface and backscattered in the atmosphere is utilized for this and correspondingly, different measurement techniques are used to solve the inverse problem of measuring the trace gas concentration causing specific absorption patterns in the measured light. For spectroscopy in the UV and visible spectral range, in which bromine monoxide shows characteristic absorption features, the Differential Optical Absorption Spectroscopy (DOAS) technique is used most often (see chapter 4). DOAS measurements performed using satellite instruments yield the total column density, which includes contribution from BrO molecules in the stratosphere as well as the troposphere. Because the stratospheric column density of BrO is significantly larger than the tropospheric column density except for some strong bromine explosion events, an accurate method is needed to estimate the stratospheric column density to extract the tropospheric BrO amount from the total column.

This chapter presents a brief review of existing approaches to separate stratospheric and tropospheric partial columns.

3.1 Overview of stratospheric correction approaches

The light reaching the satellite instrument, from which the BrO column is determined, was scattered by molecules, aerosol particles and clouds or reflected on the surface. For this reason, it contains information on both stratospheric and tropospheric abundance of bromine monoxide. In contrast to measurements of other gas species made in different spectral ranges, BrO measurements in the UV and visible wavelength region do not contain intrinsic information on the vertical distribution (Richter and Wagner, 2011). An accurate determination of tropospheric BrO columns therefore also requires a method to estimate the stratospheric partial column. For many species, including BrO, the accuracy of this estimation has a large influence on the overall retrieval accuracy, because the light path in the spectral range in which the measurement is performed is usually significantly larger in the stratosphere compared to the troposphere. This also affects the total absorption

measured from spectroscopic instruments.[1]

For bromine monoxide retrievals this is complicated further by the fact that variability in the total column density introduced by the stratosphere is comparable in magnitude to variability induced by surface release of bromine (Salawitch et al., 2010; Theys et al., 2011). The stratospheric variability is dependent mainly on stratospheric dynamics, in particular on the tropopause height. Air parcels descending with a lowering tropopause are adiabatically compressed, which leads to an increase in the concentration of trace gases and hence an increase in the stratospheric column of BrO (Wagner, 2000; Theys et al., 2009; Salawitch et al., 2010). As a consequence spatial BrO structures mimicking tropospheric events may appear in maps of total BrO columns.

For this reason an accurate separation of possible tropospheric BrO enhancememts from stratospheric variability is required. Over the years, different approaches were developed, which are summarized in the following.

3.1.1 Ozone as tracer for stratospheric air

The first observation of tropospheric BrO from space was enabled by the insight that stratospheric and tropospheric air can be distinguished by an observation of the O_3 column made by Wagner and Platt (1998). They observed strongly increased columns of BrO while simultaneously the columns of ozone and NO_2 remained basically unchanged. While they did not explicitly separate tropospheric and stratospheric partial columns from this insight, it led them to the conclusion that such enhancements must be located in the troposphere (see also Figure 3.1).

Additionally, they observed that neither the oxygen nor the oxygen collision complex $(O_2)_2$ column densities changed considerably during some of the events presumably located in the troposphere. Since both species are indicators for the sensitivity towards the troposphere they could rule out the possibility that the variations in the BrO column were due to variations in the sensitivity of the observations.

3.1.2 Reference sector approach

Another method used in one of the first satellite observations of tropospheric BrO enhancements is based on the assumption that the stratospheric BrO colum is mainly dependent on latitudinal variations and much less on longitudinal variations (Richter and Wagner, 2011). For this approach, averaged columns at certain latitudinal bands were subtracted from measurements at different longitudes in the same band. This method was applied first by Richter et al. (1998) and subsequently also by Hollwedel et al. (2004).

[1] The intricacies surrounding these wavelength dependent light path differences are described by the theory of radiative transport (RT) and its influence on the sensitivity of spectroscopic measurement in different atmospheric layers are discussed in more detail in sections 4.5 and 7.4.1.

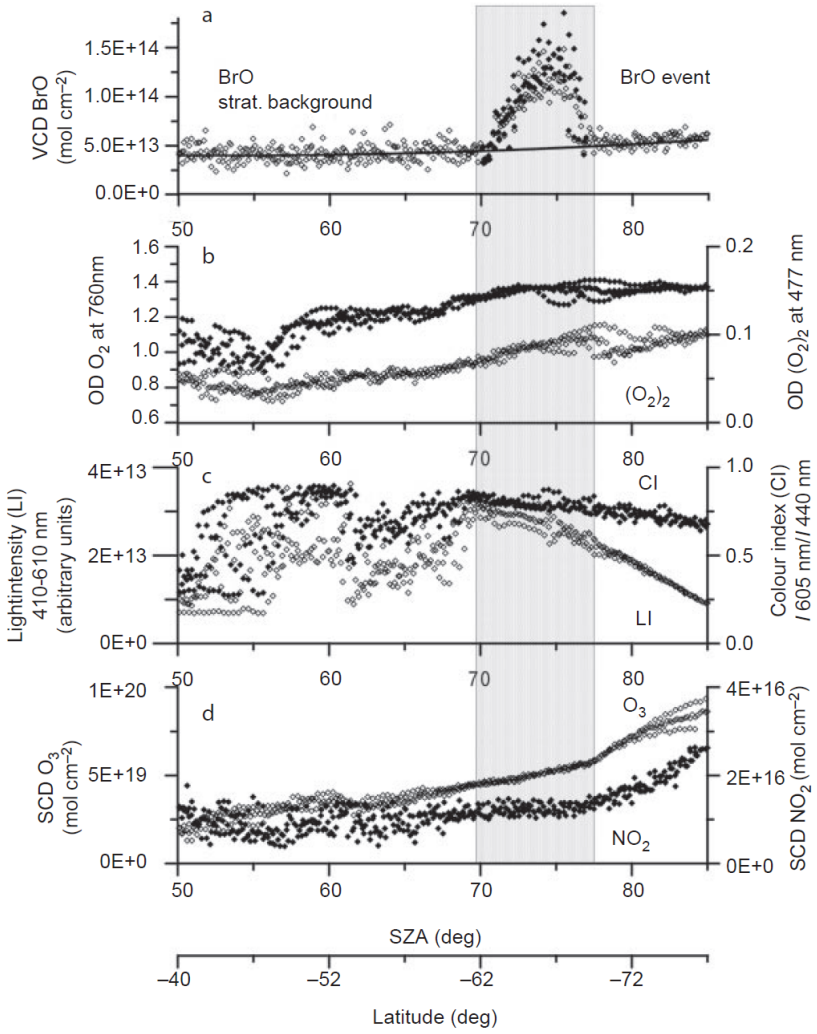

Figure 3.1: *Latitudinal variation of the column densities of atmospheric trace gases, the average light intensity and a colour index for part of an orbit on 15 September 1996 as a function of the solar zenith angle and corresponding (approximate) latitude. (a) Open diamonds, BrO VCD calculated using the stratospheric AMF; filled diamonds, the enhancement expressed as tropospheric BrO VCD calculated using tropospheric AMFs. (b) Open diamonds, absorption of $(O_2)_2$ (right axis); filled diamonds, absorption of O_2 (left axis). (c) Open diamonds, measured average intensity (*410 nm *to* 610 nm*, left axis); filled diamonds, colour index (intensity ratio at the wavelengths* 605 nm *and* 440 nm*, right axis). (d) Open diamonds, SCD of O_3 (left axis); filled diamonds, SCD of NO_2 (right axis). Figure and caption taken from Wagner and Platt (1998).*

3.1.3 Atmospheric chemistry model approach

A 3D atmospheric chemistry transport model with sufficient accuracy enables the removal of the stratospheric component of the signal from the total column. This method was first employed by Salawitch et al. (2010). They utilized a combination of the Goddard Earth Observing System Data Assimilation System Version 5 (GEOS-5) and the Whole Atmospheric Community Climate Model (WACCM) to calculate the stratospheric BrO column.

However, models potentially introduce new biases in addition to biases already present from the measurements. It is possible that the bromine budget or the chemical mechanisms governing it are incomplete. Furthermore, the spatial resolution of stratospheric models is usually too coarse to resolve small-scale effects such as tropopause folds. To compensate for this one can scale the model to measurements (in this case of stratospheric BrO) over the corresponding region. Toyota et al. (2011) applied this to stratospheric columns calculated from the Single Layer Isentropic Model of Chemistry And Transport (SLIMCAT).

3.1.4 Climatological approach

Theys et al. (2009) developed a more elaborate approach, in which simulated stratospheric BrO profiles derived from the BASCOE model (Errera and Fonteyn, 2001) were parametrized using O_3 columns as indicator for stratospheric dynamics (see section 3.1.1) and NO_2 columns as indicator for photochemical effects. These parametrizations are then stored in a climatology. The simulated stratospheric BrO profile for each measurement is then calculated from this climatology using time and latitude of the measurement as well as column measurements of O_3 and NO_2. From this, the stratospheric BrO vertical column is then derived by integrating the stratospheric BrO profile from the tropopause to the top of the atmosphere, with the tropopause height being determined from an assimilated meteorological model.

This climatological approach has been applied in numerous publications (e.g. Begoin et al., 2010; Theys et al., 2011; Blechschmidt et al., 2016; Choi et al., 2018; Bougoudis et al., 2020).

3.1.5 Statistical approach

As discussed in the previous sections, stratospheric corrections based on atmospheric chemistry models have potential biases and systematic errors from incomplete chemical mechanisms and a strong dependence of the model results on the choice of initial conditions. Furthermore, the spatial resolution of newer satellite instruments such as OMI or TROPOMI (see chapter 5) is oftentimes greater than the spatial resolution of these models. Their use therefore effectively limits the spatial resolution of the whole retrieval algorithm.

To overcome these limitations, Sihler et al. (2012) developed a column separation method similar to the climatological approach of Theys et al. (2009) but using only measurements of the satellite instruments themselves without any external model results. This method also relies on the use of proxies to capture variations in the stratospheric BrO column from

dynamical and chemical changes of the stratospheric air, with the O_3 column accounting for changes in the stratospheric BrO column from atmospheric dynamics and the NO_2 column together with viewing geometrical parameters including the solar zenith angle and the viewing zenith angle accounting for photochemical variations. In contrast to Theys et al. (2009), these parameters were then utilized in a statistical approach allowing for a differentiation between measurements of the stratospheric BrO background and measurements including a tropospheric BrO signal. From this analysis, the stratospheric BrO column is calculated for each satellite pixel. The retrieval algorithm used in this thesis is based on this approach and its further improvement and application to TROPOMI measurements is described in detail in chapter 7.

Part II

Methods and Instruments

4 | Differential Optical Absorption Spectroscopy

A cornerstone of remote sensing of the atmosphere is spectroscopy. It allows us to identify the constituents of the atmosphere. Without the knowledge of how to interpret and extract information from electromagnetic spectra our understanding of the atmosphere would be severely restricted.

One very important technique in the field of spectroscopy is the Differential Optical Absorption Spectroscopy (DOAS), a combination of measurement techniques and analytical methods allowing the detection and accurate retrieval of trace gases at mixing ratios of up to 0.1 ppt. This is enabled by the insight that different trace gas species can be distinguished via their unique absorption spectra, leaving a "fingerprint" in the observed light spectrum. Therefore DOAS enables the simultaneous retrieval of different trace gases in one measurement, letting one examine the composition of the atmosphere remotely (i.e. not in-situ), for example from space using satellites.

First published by Perner and Platt (1979) as well as Noxon (1975), the DOAS technique has seen many improvements and enhancements (see e.g. Platt et al. (2009)) over the years. It is of great significance to this thesis since the satellite measurements central to the work presented here all utilize DOAS as retrieval method. There are two basic operating principles for DOAS: (1) *active* DOAS instruments use an artificial light source either installed outside to shine directly at the instrument or being cast back to the instrument via a reflector and (2) *passive* DOAS instruments using natural light sources (usually sunlight), requiring no further light source but introducing more factors which have to be corrected for, such as the strong solar Fraunhofer lines and the *Ring effect*, as discussed in section 4.4.

The focus of this thesis lies on the application of DOAS to satellite measurements, meaning that for the following description will be focused on passive DOAS using solar light backscattered from the Earth (illustrated in Figure 4.4).

This chapter introduces the theoretical basis and the underlying concepts of the DOAS technique based on the far more detailed account of Platt and Stutz (2008); Platt (2006). In section 4.1, the concept of absorption spectroscopy and the Beer-Lambert law is introduced, with its application to atmospheric remote sensing specified in section 4.2. The fundamental DOAS technique is described in section 4.3. Additional effects that have to be accounted

for in DOAS retrievals are discussed in section 4.4. Lastly, the concept of air mass factors is presented in section 4.5. A more detailed description of the application of DOAS to satellite instruments can be found in Richter and Wagner (2011).

4.1 Absorption spectroscopy and the Beer-Lambert law

The starting point for every endeavor in spectroscopy is always the fundamental equation of the Beer-Lambert law, which relates the attenuation of electromagnetic radiation passing through any medium to the optical absorption properties of that medium. For a wavelength λ the radiation attenuation $\mathrm{d}I$ along a segment of a light path with sufficently small length $\mathrm{d}s$, such that particles in the slice will not obscure each other is given by

$$\mathrm{d}I(\lambda) = -I(\lambda)\,\sigma(\lambda)\,\rho(s)\,\mathrm{d}s\,, \tag{4.1}$$

with $\sigma(\lambda)$ as material dependent attenuation cross section[1] and $\rho(s)$ the number density of the attenuating substance.

This equation in its fundamental formulation is completely agnostic to the source of the attenuation, be it elastic scattering, for example in the form of Thompson or Rayleigh scattering, inelastic scattering in the form of Raman or Compton scattering or absorption of radiation by molecules or atoms. Such absorption occurs either by exciting inner degrees of freedom of a molecule, which are commonly described as vibrational or rotational modes, by inducing transitions of the outer electrons to higher energy states or by a combined excitation of roational, vibrotional and electronic states, known as rovibronic absorptions (see Figure 4.1). Following the laws of quantum mechanics, these changes of state only occur at quantized energy levels, i.e. they are induced by photons of distinct wavelengths.

Due to these distinct wavelength requirements of absorption processes they exhibit a narrow-band spectral structure, in contrast to the broad-band spectral nature of scattering processes. It is therefore customary to treat these forms of attenuation separately,

$$\sigma(\lambda)\,\rho(s) = \sigma_a(\lambda)\,\rho_a(s) + \frac{\mathrm{d}\sigma_s(\lambda)}{\mathrm{d}\Omega}\,\mathrm{d}\Omega\,\rho_s(s)\,, \tag{4.2}$$

with σ_a as absorption cross section of the respective absorber and σ_s the scattering cross section of a scattering center. This yields for Eq. (4.1)

$$\mathrm{d}I(\lambda) = -I(\lambda)\,\left[\sigma_a\,\rho_a(s) + \frac{\mathrm{d}\sigma_s}{\mathrm{d}\Omega}\,\mathrm{d}\Omega\,\rho_s(s)\right]\,. \tag{4.3}$$

[1] For simplicity, we drop a possible temperature dependence of the cross section.

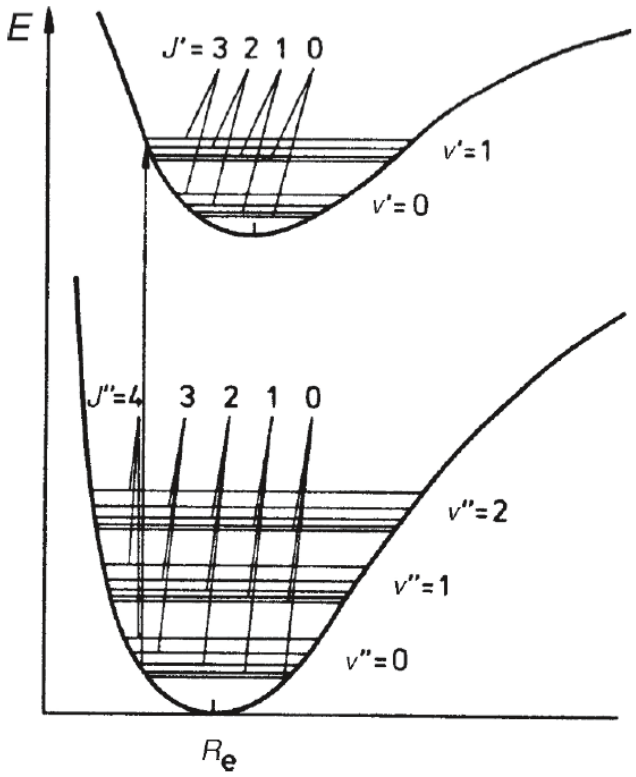

Figure 4.1: *Potential energy curves of a diatomic molecule. The two wells are distinct electronic states, the horizontal lines inside the wells denote possible rovibrational states for both electronic excitations. Figure taken from Platt and Stutz (2008).*

This differential equation[2] can be solved for a light path L as

$$I(\lambda, L) = I_0(\lambda)\, \exp\left(- \int_0^L \left[\rho_a(s)\, \sigma_a(\lambda) + \epsilon_s(\lambda, s)\right] \mathrm{d}s \right) , \tag{4.4}$$

with boundary condition $I(\lambda, 0) = I_0(\lambda)$. Here we also introduced the scattering coefficient

$$\epsilon_s(\lambda, s) = \rho_s(s) \int_{4\pi} \frac{\mathrm{d}\sigma_s}{\mathrm{d}\Omega}\, \mathrm{d}\Omega \tag{4.5}$$

as a slight simplification, summarizing all sorts of scattering.
Once the above quantities have been measured, it is possible to determine the density of the attenuating material. Assume for simplicity that the density ρ does not change along the light path and that we have only absorption as attenuation source, this yields as density of the absorber,

$$\rho = \frac{\tau(\lambda)}{L \cdot \sigma_a(\lambda)} , \tag{4.6}$$

[2]This equation is also called *radiative transfer equation*. Note that a complete treatment has to include the thermal radiation of the attenuating substances. Since our interest in this thesis is in UV and visible spectroscopy, the influence of thermal radiation can be neglected. For a complete treatment, we refer to Platt and Stutz (2008).

where the optical density along the light path τ was introduced,

$$\tau(\lambda) = \log\left(\frac{I_0(\lambda)}{I(\lambda)}\right) . \tag{4.7}$$

4.2 UV/Vis Absorption spectroscopy in the atmosphere

The primary interest in spectroscopy in this work is as remote sensing tool to investigate the constituents of the atmosphere. Of special importance is the UV and visible spectral range, in which BrO, O_3 and other trace gases absorb the strongest. In this energy regime, the dominating source of photon absorptions are electronic excitations of molecules, accompanied by changes in the rotational and vibrational energy states, collectively known as rovibronic absorptions (see Figure 4.1). The absorption part of expanded Beer-Lambert law Eq. (4.4) is therefore dominated by rovibrational absorptions. Of course the atmosphere is composed of many different species which means the single absorber with cross section $\sigma_a(\lambda)$ in Eq. (4.1) has to be replaced by a multitude of absorbers,

$$\sigma_a(\lambda)\,\rho_a(s) \rightarrow \sum_i \sigma_i(\lambda)\,c_i(s)\,, \tag{4.8}$$

with absorption cross sections σ_i and concentrations $c_i(s)$ of the involved species i.

Since the atmosphere is dominated by elastic scattering the general scattering coefficient of Eq. (4.5) can also be specified. General elastic scattering on particles is described by the *Mie solution* to Maxwell's equations (Hulst and van de Hulst, 1981). For particle sizes with spatial dimensions in the order of the observing wavelength, like scattering on cloud droplets and other aerosol particles, the corresponding scattering cross section as a weak wavelength dependence of approximately $\lambda^{-1.3}$ for the general atmosphere. This is also known as *Mie scattering*.

Due to the strong dependence on the particle size relative to the scattered radiation wavelength, there are several important approximations of the Mie solution. One such approximation for particle sizes at least one order of magnitude smaller than the corresponding wavelength (i.e. smaller than 100 nm for UV/Vis spectroscopy) is known as *Rayleigh scattering*. Most molecules in the atmosphere as well as small aerosol particles fall into this regime. Noteworthy is the eminent λ^{-4} dependence of the Rayleigh scattering cross section (Hulst and van de Hulst, 1981) discussed again later.

The general scattering coefficient introduced in Eq. (4.5) can therefore be expressed as combination of both sorts of scattering:

$$\epsilon_s(\lambda, s) = \epsilon_R(\lambda, s) + \epsilon_M(\lambda, s)\,, \tag{4.9}$$

with $\epsilon_R(\lambda, s)$ as Rayleigh scattering coefficient and $\epsilon_M(\lambda, s)$ as Mie scattering coefficient. Combining these changes to scattering as well as to absorbers yields for Eq. (4.4) the lengthy

expression

$$I(\lambda, L) = I_0(\lambda)\, \exp\left(\int_0^L \left[\sum_i \sigma_i(\lambda)\, c_i(s) \; + \epsilon_R(\lambda, s) + \epsilon_M(\lambda, s) \right] \mathrm{d}s \right) , \tag{4.10}$$

which describes the attenuation of light in the atmosphere. However, for passive DOAS an accurate determination of the initial intensity I_0 is necessary which is non-trivialFor a satellite instrument being able to record the sun spectrum from outside of the atmosphere, the initial intensity can be assumed to be known.. For measurements using scattered light this is complicated since the initial intensity does also depend on the scattering efficiency in the atmosphere as well as on the surface reflectivity for the case of satellite-based nadir measurements (Richter and Wagner, 2011). This is usually expressed with the introduction of a wavelength dependent scaling factor $c(\lambda)$ describing the fraction of light scattered back to the instrument,

$$I_0(\lambda) = c(\lambda)\, I_0^*(\lambda)\, , \tag{4.11}$$

with $I_0^*(\lambda)$ describing the background spectrum as measured by the instrument.

By taking the logarithm, one can write Eq. (4.10) in terms of optical density as introduced in Eq. (4.7) as

$$\tau(\lambda) = \int_0^L \left[\sum_i \sigma_i(\lambda)\, c_i(s) \; + \epsilon_R(\lambda, s) + \epsilon_M(\lambda, s) \right] \mathrm{d}s\, . \tag{4.12}$$

The optical density of the atmosphere along the light path can therefore be ascribed to the combination of elastic scattering and the sum of absorption processes.

This poses a challenge however: it is highly non-trivial to distinguish the contributions of each of these processes to the overall attenuation of radiation in the atmosphere. This is further complicated by the presence of an abundance of different absorbers each contributing to the absorption. If the goal is to determine the density of a specific trace gas via spectroscopy, one would need to single out the influence of this one specific absorber among all consitutents absorbing in the wavelength range of our analysis as well as the effects of scattering. A daunting task further compounded by the difficulty to accurately determine the true intensity $I_0(\lambda)$ without absorption or scattering as discussed above.

4.3 Differential Absorption spectroscopy

The technique known as Differential Optical Absorption spectroscopy (DOAS) removes all these obstacles in an elegant way. The crucial insight of the DOAS method is the distinction between the spectrally narrow-banded, vibronic absorption structures and broad-banded or even smooth features like extinction from scattering and many absorption structures too small to resolve with the limited spectral resolution of measurement instruments.

It is then possible to use the *differential* absorption, the differences of light attenuation

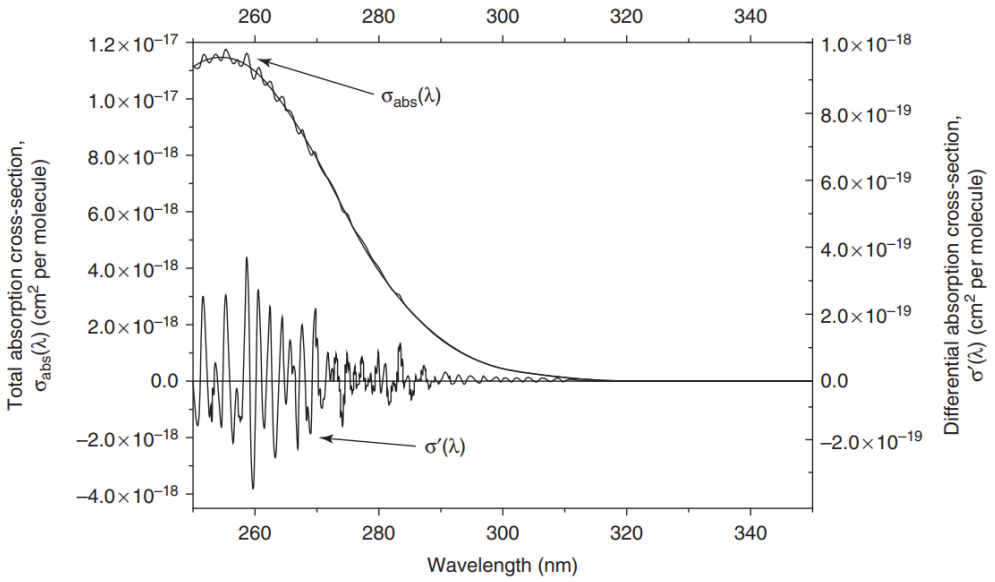

Figure 4.2: *Total absorption cross section* $\sigma_{\text{abs}}(\lambda)$ *and differential cross section* $\sigma'(\lambda)$ *of ozone. Figure taken from Platt (2006).*

between narrow-banded structures and broad-band structures at different wavelengths as illustrated in Figure 4.3. This is done by focusing on specific wavelength regions with distinct narrow-band structures in the absorption cross sections of the corresponding absorbers with a strong contrast between narrow- and broad-band structures (see Figure 4.2).

Historically this entailed a separation of trace gas cross sections in narrow- and broadband structures via

$$\sigma_i(\lambda) = \sigma_{i,b}(\lambda) + \sigma'_i(\lambda)\,, \tag{4.13}$$

with *differential* cross section $\sigma'_i(\lambda)$ and a broad-band cross section $\sigma_{i,b}(\lambda)$, visualized in Figure 4.2. This is achieved by a smoothing of the cross section corresponding to the spectral resolution of the instrument[3] and adequate filtering processes. Rewriting Eq. (4.12) in terms of a *differential* optical density τ' gives

$$\tau' = \log \frac{I'_0(\lambda)}{I(\lambda)} = \int_0^L \sum_i \sigma'_i(\lambda) \cdot c_i(s)\,\mathrm{d}s\,. \tag{4.14}$$

Here the "broad-band" intensity I'_0 was introduced,

$$I'_0(\lambda) = I_0(\lambda) \cdot \exp\left(\int_0^L \left[\sum_i \sigma_{i,b}(\lambda)c_i(s) + \epsilon_R(\lambda) + \epsilon_M(\lambda)\right] \mathrm{d}s\right)\,, \tag{4.15}$$

describing the observed intensity if it was only affected by scattering and broad band absorption as sketched in Figure 4.3.

The broad-band contributions are usually accounted for by fitting an appropriate polyno-

[3]This step is no longer necessary for modern DOAS applications, where the cross sections will be used directly without separation into broad- and narrow-band structures. We include it here for consistency.

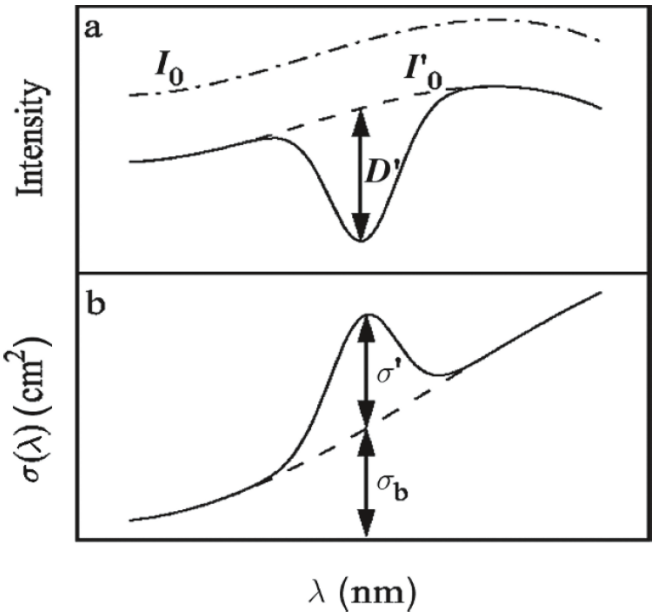

Figure 4.3: *DOAS Principle: The initial intensity I_0 is reduced to the broad-band intensity I'_0, mainly via Rayleigh and Mie scattering and other broad-band structures. Differential changes between different wavelengths can then be ascribed to narrow-band structures in the cross sections of the examined trace gases. Figure taken from Platt and Stutz (2008).*

mial to the observed spectrum, allowing the determination of the differential optical density τ'. Then the species concentrations integrated along the light path can be deduced by fitting[4] the so-called Slant Column Density (SCD)

$$S_i = \int_0^L c_i(s)\,\mathrm{d}s\,, \tag{4.16}$$

to Eq. (4.14), giving for the differential optical density

$$\tau' = \sum_i \sigma_i(\lambda) \cdot S_i\,. \tag{4.17}$$

This defines the differential optical density simply as the sum of the differential absorptions of all trace gases in the light path.

4.3.1 Measurements of trace gas SCDs from DOAS

As discussed, the fundamental idea of DOAS is the separation of broad- and narrow-band structures. This can involve measurements for more than 500 wavelength channels to achieve an accurate distinction between narrow- and broad-band absorptions, in turn allowing the

[4] As a matter of fact, the common phrase of "fitting" slant column densities represents an oversimplification of the process. Technically, an inverse problem has to be solved by constructing and inverting a model function describing the observed attenuation, which is optimized by minimizing the residuals of the constructed function (Rodgers, 2000).

detection of optical densities on an order of 10^{-4} (Platt and Stutz, 2008). For BrO, this means BrO concentrations as low as 5 pptv can be detected (Fleischmann et al., 2004).

To determine trace gas SCDs from Eq. (4.17), the differential optical density τ' has to be calculated, which means not only measuring the attenuated intensity $I(\lambda)$ but also the *reference* broad-band intensity $I'_0(\lambda)$. Since this reference spectrum has to be void of differential absorptions from the absorbers, it needs to be measured for a different light path than the measured spectrum $I(\lambda)$ in most cases. Also changes for the scaling factor c introduced in Eq. (4.10) has to be taken into account here due to different intensities of light scattered into the field of view of the instrument. As a consequence the scattering contributions to the light attenuation between both recorded spectra are differing. The latter can be corrected for by using different wavelengths simultaneously and assuming the change of scattering is only weakly dependent on the wavelength (Richter and Wagner, 2011)

Usually a DOAS retrieval combines a standard least-squares fit and a Levenberg-Marquard algorithm (Platt and Stutz, 2008) to fit the polynomial and the SCDs S_i simultaneously to the logarithm of the measured spectra.

For application to a satellite instrument this is changed to only using a standard least-squares fit (Beirle et al., 2013). The reasons for this are two-fold: (1) the processing speed is increased drastically, a necessity for instruments like the TROPOspheric Monitoring Instrument (TROPOMI) discussed in section 5.1 measuring 10^7 pixel daily and (2) wavelength shifts and stretches with respect to the reference spectrum are usually small, allowing the linearization of both effects, which makes a separate, non-linear fit for their estimation obsolete (Beirle et al., 2013).

4.4 Additional DOAS effects

A few key assumptions were made in the derivation of the DOAS principle in section 4.3, including (1) omitting the effects of inelastic scattering in the broad-band extinction processes and (2) assuming small trace gas optical densities with no effect on the light path. Both of these assumptions should be seen as simplifcations and although these do not effect the DOAS principle in a fundamental way, a precise retrieval needs to correct for deviations stemming from these simplifications.

4.4.1 Ring effect

In the discussion of the Beer-Lambert in section 4.1, inelastic scattering as potential source of radiation extinction was mentioned. Although it was neglected in the review of the DOAS method in section 4.3, the effects of inelastic *Raman scattering* in the atmosphere can not be brushed aside especially in the UV spectral range[5], where it can affect the retrieval of weakly absorbing trace gases such as BrO (Wagner et al., 1999).

[5]Note that for UV/Vis spectroscopy, only the effects of rotational Raman scattering are important. The wavelength shifts of vibrational Raman scattering are too large.

Raman scattering will manifest itself in the form of a stronger radiance intensity for the Fraunhofer lines in the spectrum of scattered light compared to direct sunlight (Grainger and Ring, 1962) which has been named *Ring effect*. Initially it was conjectured this is due to "daylight airglow" and only later rotational Raman scattering was concluded to be the most likely explanation of this observation (Kattawar et al., 1981). There are different methods to account for this, e.g. the inclusion of a pseudo-absorber with a Ring effect cross section (Solomon et al., 1987) or via direct calculation of a Ring effect spectrum from the solar spectrum $I_0(\lambda)$ (Joiner et al., 1995; Wagner et al., 2009a). In this thesis the second approach is used.

4.4.2 Puķīte terms

Another assumption made in the discussion of the DOAS method was the wavelength-independence of the light path, based on the expectation of weakly absorbing trace gases. Although this is reasonable to assume for most absorbers and wavelength regimes in the atmosphere, it can lead to deviations for ozone absorption in the UV (Puķīte et al., 2010), where strong absorption actually reduces the effective light path at wavelengths with a higher absorption cross section compared to other wavelengths. Therefore it is necessary to modify Eq. (4.17) to

$$\tau' = \sum_i \sigma_i(\lambda) \cdot S_i(\lambda)\,, \tag{4.18}$$

which leads to the retrieved SCDs being wavelength dependent quantities. Following the proposition of Puķīte et al. (2010), one can correct for this effect by expanding Eq. (4.18) for ozone as Taylor series:

$$\tau' = \sigma_{O_3}(\lambda) \cdot S_{O_3}(\lambda) = \left[\sigma_{O_3}(\lambda) \cdot S_{O_3} + \lambda\,\sigma_{O_3}(\lambda) \cdot S_{P1} + \sigma_{O_3}(\lambda)^2 \cdot S_{P2}\right]\,. \tag{4.19}$$

Here $\lambda\,\sigma_{O_3}(\lambda)$ and $\sigma^2_{O_3}$ are the so-called *Puķīte-terms* which are added to the DOAS fit as pseudo absorbers with their own SCDs.

4.5 Conversion of SCD to VCD

The DOAS fit provides the SCD S (Eq. (4.16)), describing the trace gase absorption along a light path. As discussed in the previous section 4.4.2, the implicit assumption for the light path was that it is influenced only by the concentration profile $c_i(s)$ of the corresponding species i and different amounts of atmospheric scatterers. In reality, it is also influenced by the viewing geometry, surface properties, wavelength and the concentration profile of strongly absorbing species like ozone. Consequently, two retrieved SCDs are hardly comparable if they are not measured under similar conditions (see Figure 4.4). This holds especially true for satellite based instruments which measure SCDs over a vast spatial extent with differing viewing geometries as discussed in chapter 5. This section briefly describes how SCDs obtained via DOAS can be converted to Vertical Column Densities (VCDs).

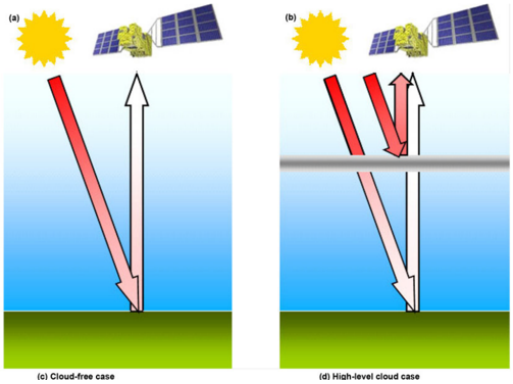

Figure 4.4: *Sketch of satellite measurement under different optical conditions. Even with identical viewing geometry, the resulting light path can vary strongly. Figure taken from Eguchi and Yoshida (2019).*

The Vertical Column Density is defined as the vertically integrated density of a trace gas from surface to a specific height, usually the top of the atmosphere (TOA) Θ,

$$V_i = \int_0^\Theta c_i(s)\,\mathrm{d}s\,. \tag{4.20}$$

Note that this definition is completely independent of any path of light used to observe this trace gas. The VCD V is related to the SCD S via the so-called *Air Mass Factor* (AMF) A,

$$A = \frac{S}{V}\,, \tag{4.21}$$

from which follows the simple interpretation that the AMF A describes the ratio between the "actual" light path and the vertical light path, i.e. it measures the *relative air mass* along the line of sight. Indeed, the AMF encapsulates all information about the optical properties of the atmosphere and gives an effective description of the radiative transfer (RT) along the light path.

Data about optical characteristics of the atmosphere and the radiative transfer is often sparse but for many cases a geometric approximation can be made by assuming the light path is lengthened in a purely geometric fashion. This is called the *geometric AMF* A_{geom} and is defined as

$$A_{\mathrm{geom}} = \frac{1}{\cos\theta} + \frac{1}{\cos\varphi}\,. \tag{4.22}$$

The angles are the *solar zenith angle* (SZA) θ and the *viewing zenith angle* (VZA) ϕ, discussed in more detail in section 5.3. The geometric approximation for the AMF gives a good approximation for the stratosphere where the influence of scattering and clouds can be neglected due to the low air density (Solomon et al., 1987). However, for high SZAs the curvature of the earth becomes relevant and the approximation can break down even in the stratosphere as demonstrated by Figure 4.5. More complex scenarios, such as measurements of trace gases located primarily near the ground, also require a different treatment.

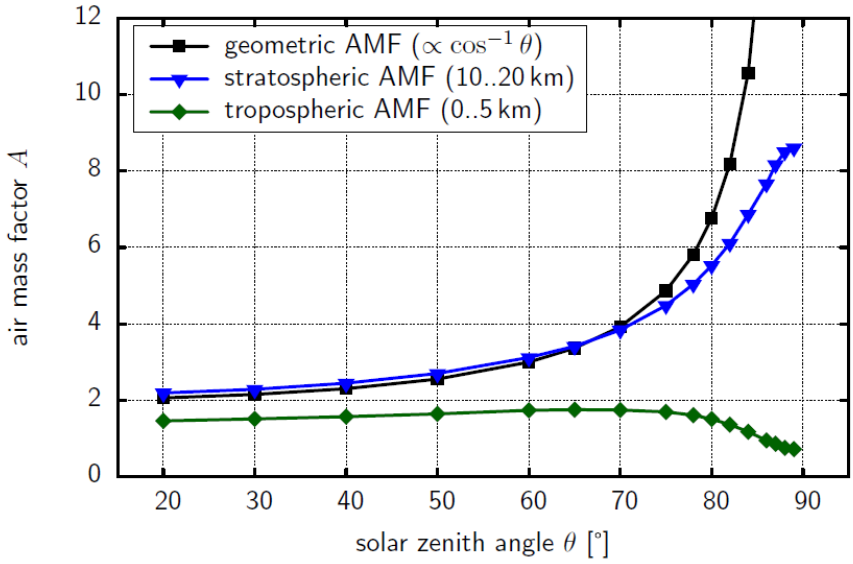

Figure 4.5: *Dependence of different Box AMFs on solar zenith angle (SZA) in the UV (λ = 360 nm) calculated for a surface albedo of* 0.1 *and nadir viewing geometry. The tropospheric AMF assumes a box profile for the lowest 5 km, the stratospheric AMF one between 10 and 20 km. Both were calculated using McArtim. Figure adapted from Sihler (2012).*

For example, measuring trace gas concentrations primarily located in the (lower) troposphere from satellite, the SCD measured by the satellite instrument can be very low due to effective shielding of the trace gas through scattering by air molecules, aerosols and clouds as depicted in Figure 4.4. This means that only a fraction of the detected photons actually had contact with the absorber, rendering the satellite effectively blind to the trace gas for very thick clouds. However, this does not mean that the actual trace gas concentration below the cloud is low. The shielding effect is expressed by an AMF smaller than 1 for the tropospheric trace gas as shown in Figure 4.5, resulting in VCD larger than the corresponding SCD. For that reason, the AMF is sometimes also understood as a measure of the sensitivity of a specific measurement. In the example discussed above, the lower the AMF the less photons have actually penetrated the near-surface layer and had contact with the trace gas. Therefore, a lower AMF means the measurements is less *sensitive* to that trace gas.

To resolve this vertical dependence of the measurement sensitivity, it is useful to define an AMF for specific atmospheric layers i individually, the so-called Box-AMF (BAMF),

$$\mathrm{BAMF}_i = \frac{\partial S}{\partial V_i} \,. \tag{4.23}$$

Here V_i denotes the partial vertical column density for the layer i (Richter and Wagner, 2011). For weak absorbers (corresponding optical density $\tau << 1$) the Box-AMFs become independent of the general profile shape of the absorber and this can be approximated (Palmer

et al., 2001) to

$$\mathrm{BAMF}_i = \frac{S_i}{V_i}\,, \tag{4.24}$$

with S_i describing the partial SCD observed in the atmospheric layer i. The *stratospheric* and *tropospheric* AMFs shown in Figure 4.5 should be understood as corresponding Box-AMFs of the respective atmospheric layer. From this follows that for weak absorbers, the total AMF A can be understood as the sum of relative "box" concentrations $c_i = V_i/V$ weighted by the corresponding Box AMF,

$$A = \frac{S}{V} = \frac{\sum_i S_i}{V} = \sum_i \mathrm{BAMF}_i \cdot c_i\,. \tag{4.25}$$

An accurate estimation of the AMF can be gained with the help of RT simulations such as the Monte Carlo atmospheric radiative transfer model (McArtim) (Wagner et al., 2009a; Deutschmann et al., 2011) or the Vectorized Linearized Discrete Ordinate Radiative Transfer (VLIDORT) (Spurr, 2006). Commonly this is done via the simulation of observed radiances with and without the trace gas in question (Solomon et al., 1987; Richter and Wagner, 2011). With the help of an *a priori* trace gas profile ρ, a VCD V can be determined serving as input for the RT simulation, which allows the calculation of the corresponding AMF using Eq. (4.17) and Eq. (4.21):

$$A = \frac{\tau}{\sigma(\lambda)\,V} = \frac{\log I - \log I_0}{\sigma(\lambda)\,V}\,, \tag{4.26}$$

with I and I_0 as simulated radiances with and without trace gas respectively. The information on the a priori profile can be obtained in various ways, for example through independent simulations or measurements. Also, standardised profiles or proxy-informations can be used (Richter and Wagner, 2011), such as the assumption of a constant "box profile" ρ_i for a specific layer i (Sihler et al., 2012), as it is also used for the calculation of the tropospheric AMF for BrO in this work. Depending on the trace gas of interest, additional input data describing other phenomena affecting the AMF, such as clouds and aerosols, are required. These are listed in Table 4.1.

In this thesis, McArtim is used for the calculation of tropospheric air mass factors. The model simulates radiances via explicit ray tracing of model photons through grid boxes k, based on the backward Monte Carlo method: a photon emerges from a detector and is followed in a backwards trajectory until it leaves the top of the atmosphere. It yields the Jacobian of the radiance with respect to the absorption coefficient $\mu = \sigma(\lambda)\,\rho$ of the absorber,

$$\mathbf{J}_k = \frac{\mathrm{d}}{\mathrm{d}\mu_k} I_*\,, \tag{4.27}$$

with simulated radiance I_* (normalized by the solar spectrum I_0) for each grid box k (Deutschmann et al., 2011). From Eq. (4.7) it can be seen that the logarithm of the normalized simulated radiance yields an inverse optical density τ^{-1}. Of interest is the Jacobian of this quantity

with respect to the absorption coefficient,

$$\frac{\mathrm{d}}{\mathrm{d}\mu_k}\tau = -\frac{\mathrm{d}}{\mathrm{d}\mu_k}\log I_* \,. \tag{4.28}$$

An inspection of the definition of the optical density from a simple version of the Beer-Lambert-law (Eq. (4.7)),

$$\tau = \int_0^h \mu \,\mathrm{d}z \,, \tag{4.29}$$

allows the speculation that this quantity describes the length of the light path. Indeed, the Jacobian of the logarithm can be described as the averaged photon path length L_k weighted by the intensity through the grid box k (Deutschmann et al., 2011),

$$L_k = -\frac{\mathrm{d}}{\mathrm{d}\mu_k}\log I_* \,. \tag{4.30}$$

Following Marchuk et al. (1981), the Box AMF for the grid box k with height h_k is then given by

$$\mathrm{BAMF}_k = \frac{L_k}{h_k} \,. \tag{4.31}$$

In turn, this encourages the aforementioned interpretation of the AMF as a measure of the lengthening of the light path compared to the vertical path. However, in contrast to the geometric approximation of the AMF, in this interpretation the light path is changed by scattering and absorption processes and not simply by a geometrical extension.

Table 4.1: *Assessment of importance of different input informations used by radiative transfer simulations for tropospheric trace gases. Table adapted from Richter and Wagner (2011).*

Input data	Importance	Typically used	Source of information
Trace gas profile	High	Yes	Independent information, e.g., from atmospheric models or general assumptions
Surface albedo	High	Yes	Climatology, e.g., created from the same satellite instrument, sometimes also retrieved from the measurements
Cloud properties	High	Yes	Simultaneous measurements, e.g., cloud fraction and cloud top height
Aerosol properties	High	No	General assumptions, atmospheric models, potentially also simultaneous measurements
Surface elevation	Medium	No	Databases
Solar zenith angle	Medium	Yes	Observation description
Viewing zenith angle	Medium	No	Observation description
Relative azimuth angle	Medium	No	Observation description
Pressure and temperature profile	Low	Yes	Standard profiles

5 | Satellite instruments

The work presented in this thesis relies heavily on measurements carried out by the TROPOspheric Monitoring Instrument (TROPOMI) onboard ESA's Sentinel-5 Precursor (S5-P) satellite. In section 5.1, the main characteristics of the instrument and the corresponding satellite mission will be described.

The original retrieval methods to obtain tropospheric BrO on which this thesis improves upon (Sihler et al., 2012) were developed for the Global Ozone Monitoring Experiment-2 (GOME-2). Therefore section 5.2 provides a short description of the GOME-2 instrument, highlighting differences between the instrument important for the tropospheric BrO retrieval. In section 5.3, a description of the satellite viewing geometry is provided. Finally, section 5.4 provides a brief description of the methods utilized to visualize satellite data as well as map projections used in this thesis.

5.1 TROPOMI instrument aboard the Sentinel-5 Precursor satellite

The Sentinel-5 Precursor satellite is a low Earth-orbit satellite dedicated to monitor air quality, pollutants like NO_2 and ozone as well as forecasting and climate monitoring (ESA, a, ESA). By providing long-term measurements of tropospheric trace gases it will be helpful in understanding the life cycle and anthropogenic influences on these pollutants as well as greenhouse gases like methane. It was launched in October 2017.

In this section key characteristics of the S-5P satellite and the TROPOMI instrument aboard the satellite are presented.

5.1.1 Orbit description

The satellite is on a sun-synchronous orbit, which is achieved by choosing the inclination of the satellite with respect to the equator in a precise relation to the altitude of the orbit (Rosengren, 1988; Burrows et al., 2011; Capderou, 2005). For S-5P orbiting earth at approximately 824 km this implies an inclination of 98.7° (see Figure 5.1), leading it to nearly cross the poles on each orbit which is called a near-polar orbit. The satellite then takes approximately 103 minutes for one complete orbit around earth, resulting in 14 orbits

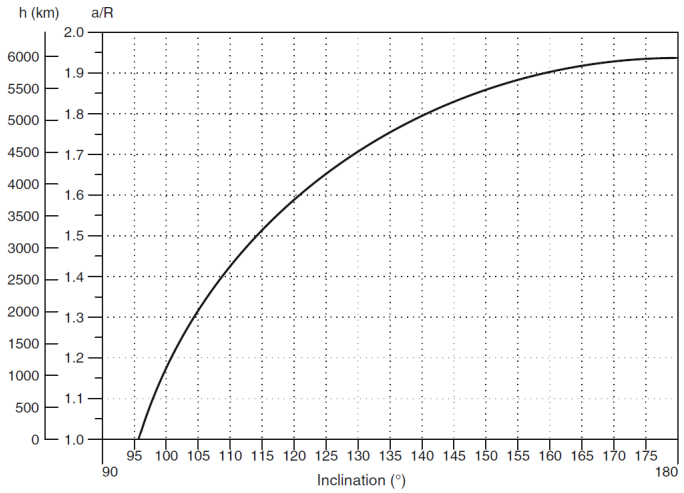

Figure 5.1: *Possible satellite altitude as function of inclination angle under assumption of sun-synchronicity of the orbit. Figure taken from Capderou (2014).*

each day.[1] One great advantage of such a sun-synchronous orbit for remote sensing is the fact that the satellite passes over any given point of the planets surface at the same local mean solar time (Capderou, 2014). This means that the sun will be in a similar position and the solar angle will be comparable for each measurement at any given time of the year. Of course the local time of each overpass will also be the same up to possible time shifts from time zones and daylight saving times. For S-5P the local mean solar time of the ascending node at equatorial crossing is 13:30 h (ESA, b).

5.1.2 TROPOMI instrument

The S-5P satellite carries only one instrument, the hyperspectral imaging spectrometer TROPOMI. This instrument consists of four detectors measuring in different spectral bands: the Ultraviolet (UV) detector (270 nm to 320 nm), the UV-visible (UVIS) detector (310 nm to 500 nm), the Near-InfraRed (NIR) detector (675 nm to 775 nm) and the Short-Wave-IR (SWIR) detector (2305 nm to 2385 nm). This broad spectral coverage allows the observation of various atmospheric compounds including O_3, NO_2, SO_2, BrO, CO and CH_4 as well as clouds and aerosols. While the measurement principle of the detectors is identical, each detector is adapted to its specific spectral region as shown in Table 5.1.

Scanning method

The TROPOMI instrument is a so-called *push-broom* imaging spectrometer, in reference to the operating principle of such brooms, which are pushed in a straight line over the surface. For TROPOMI, this "broom" is the imaging swath in which the instrument scans the surface as visualized in Figure 5.3 while the satellite moves perpendicular to this swath along the

[1] The orbital repeat cycle for S-5P is 16 days, with a total of 227 orbits, which means that 3 days out of 16 will include one additional orbit.

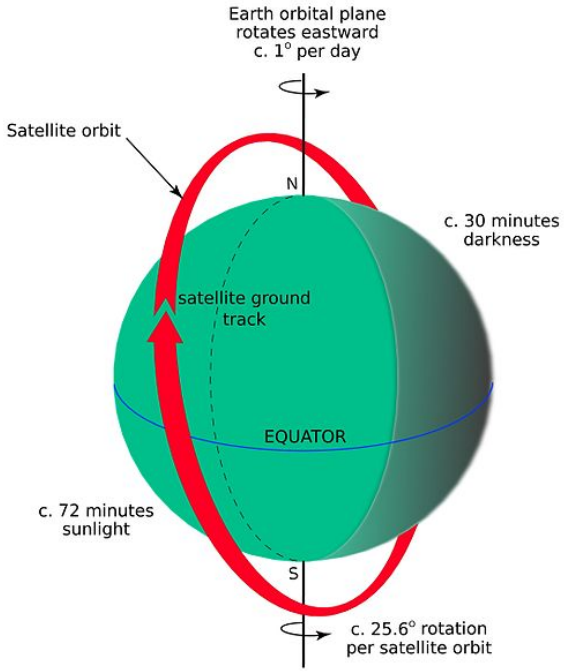

Figure 5.2: *Example of sun-synchronous orbit of MetOp with approximately 820km height. Figure taken from Wikipedia (2022).*

so-called along track. With an opening angle of 108° TROPOMI's swath is approximately 2600km wide. This means that the 14 daily orbits of S-5P lead to global coverage each day with the exception of a small area in the equator region while high latitude regions and especially the poles will be covered multiple times per day.

The backscattered light reaching the instrument from inside this angle is separated in different wavelengths using grating spectrometers before it is mapped onto a 2D Charged Coupled Device (CCD) sensor of the respective detectors. The two dimensions of this CCD sensor are used to resolve different ground pixels along the dimension called the *across track* (see Figure 5.3) as well as different wavelengths along the other dimension.

Table 5.1: *Key characteristics of the TROPOMI detectors for the different spectral bands. Table adapted from Veefkind et al. (2012).*

TROPOMI spectral bands.

Detector	UV		UVIS		NIR		SWIR
Band	1	2	3	4	5	6	7
Spectral range [nm]	270–300	300–320	310–405	405–500	675–725	725–775	2305–2385
Spectral resolution [nm]	1.0	0.5	0.55	0.55	0.5	0.5	0.25
Spectral sampling [nm]	0.065	0.065	0.2	0.2	0.1	0.1	<0.1
Spatial sampling [km^2]	21×28	7×7	7×7	7×7	7×7	7 (1.8)[c]	7×7
Detector binning factor	16	4	4	4	4	4 (1)	1
Minimum signal-to-noise	100–800[a]	90–700[a]	800–1000[a]	800–1000[a]	100–500[a]	100–500[a]	100–120[b]

[a] The minimum signal to noise is specified for a scene with an albedo of 2% and the Sun in zenith.
[b] The minimum signal to noise is specified for a scene with an albedo of 5% and solar zenith angle of 70°.
[c] The spatial sampling of Band 6 can be reduced to improve the spatial co-registration with the other bands.

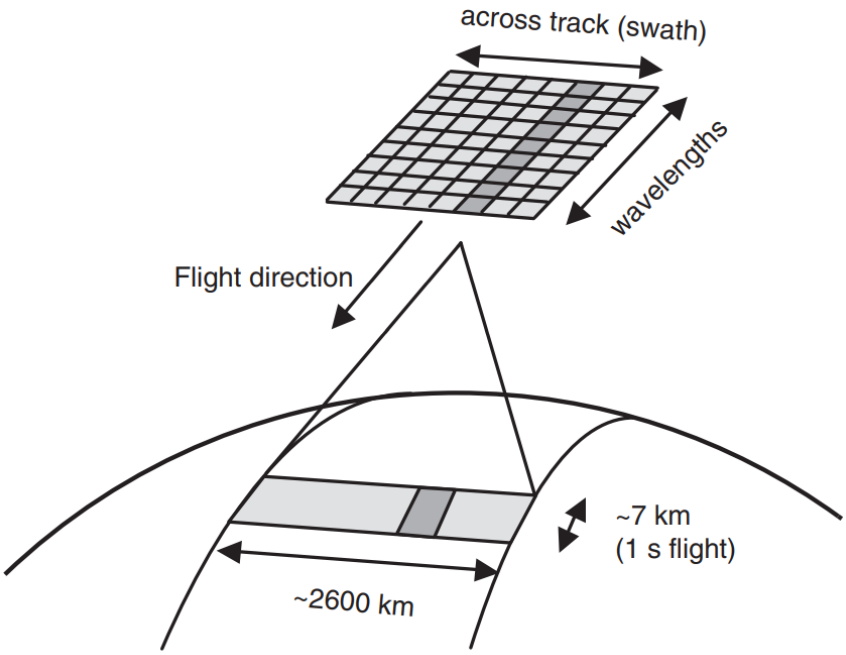

Figure 5.3: *Push-broom measurement principle. The ground swath, depicted in grey, is mapped on the 2D-CCD detector. Figure taken from Veefkind et al. (2012).*

TROPOMIs improved resolution

The across row consists of 450 pixels with a nadir pixel size of of 3.5 km, increasing up to 14.4 km towards the ends of the swath. As discussed in detail in the pre-launch calibrations (Kleipool et al., 2018), the last 30 rows have to be sampled with a smaller resolution, resulting in the overall swath with of 2600 km. In-depth characterization for current in-flight details can be found in Ludewig et al. (2020).

Depending on the spectral band in which a measurement is performed a single scan can take up to 3 seconds to achieve the signal-to-noise requirements. For the UVIS detector, the scan time is approximately 1 second. During this period, the satellite moves 7 km in along track direction, which gives a spatial resolution of 7 $\times$ 3.5 km^2 sub-satellite. On August 6 2019 the scan time has been reduced further, improving the resolution to a maximum of 5.5 $\times$ 3.5 km^2.

This constitutes a seminal improvement in spatial resolution compared to previous satellite instruments and facilitates TROPOMIs mission statement by allowing for example the precise pinpointing of pollutant sources (Beirle et al., 2019) and to estimate their emissions (Finch et al., 2022).

The improved spatial resolution is visualized in Figure 5.4 over the Rhein-Main region. There it can be seen that in contrast to previous instruments, the TROPOMI pixel size is small enough to resolve the closely neighboured cities Mainz and Wiesbaden.

Compared to the GOME-2 instrument's (see section 5.2) spatial resolution of 80 $\times$ 40 km^2, TROPOMI's resolution signifies an improvement in spatial resolution by a factor

of 130 while still retaining a high signal-to-noise ratio (SNR)[2]. This necessitates substantial changes to the retrieval algorithm previously applied on GOME-2 data as discussed in chapter 7.

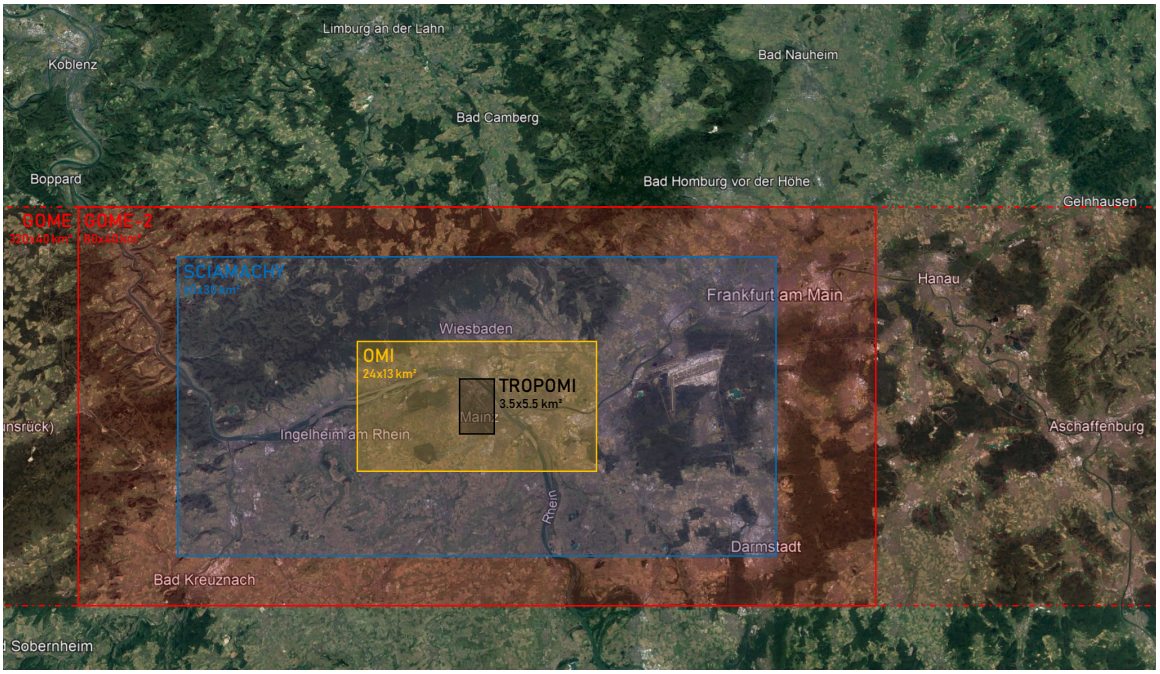

Figure 5.4: *Comparison of resolutions of satellite instruments over Mainz and the Rhein-Main region. Figure taken from Warnach (2022).*

5.2 GOME-2 instrument aboard the MetOp satellite

The European Meteorological Operational satellite (MetOp) mission consists of a series of three satellites launched between 2006 and 2018 with the primary objective to provide data for numerical weather predictions. The satellites carry a range of different instruments. This section focuses solely on the GOME-2 instrument (Munro et al., 2006, 2016) onboard the MetOp-A satellite (also called GOME-2A).

The MetOp-A satellite is on a near-polar sun synchronous orbit as described for S-5P (see Figure 5.2). In contrast to S-5P the equator crossing time of MetOp-A is at 09:30 h local time.

GOME-2 is a so-called *whisk-broom* optical spectrometer measuring backscattered solar radiation (see Figure 5.5). It covers one large spectral band, measuring between 240 nm and 790 nm with a spectral resolution between 0.26 and 0.51 nm in four different channels. The whisk-broom scanner uses a mirror to scann across the ground track, reflecting light

[2]The SNR describes the ratio between signal strength and background noise. For an ideal instrument the signal strength is determined by the number of photons collected by the detector in a single measurement while the noise is given by the photon shot noise (see also section 7.5). A higher spatial resolution requires a shorter integration time, which causes a significant contribution of instrument noise (for non-ideal instruments), which results in a lowering of the SNR.

back into a single detector. Because of this, a whisk-broom instrument is not prone to the across-track variability affecting push-broom sensors as discussed in section 7.2.2.

While the scan width of the instrument with only 1920 km is smaller than that of TROPOMI, it still provides good coverage on an almost daily basis. The spatial resolution of the instrument was 80 × 40 km^2, which was reduced to 40 × 40 km^2 at the cost of the reduction of the scan width to 960 km in July 2013.

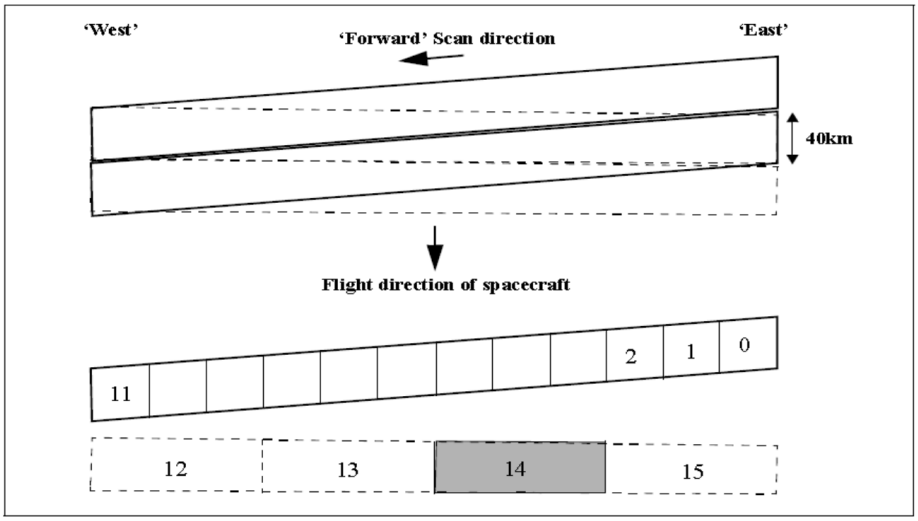

Figure 5.5: *Whisk-broom measurement principle. Visualization of default scan mode of GOME-2. One scan is defined as the time interval it takes the scan mirror to do one complete sweep. Figure taken from EUMETSAT (2011).*

5.3 Satellite viewing geometry

As described in the previous section, the spatial resolution of pixels measured by the instrument varies depending on their relative position in the swath. Of course the light path from the point of measurement to the instrument also increases for pixels at the edges of the swath. For remote sensing purposes, it is crucial to have at least an estimate on the path length of the light in atmosphere, so we need to capture the information on the relative position of the ground pixel in the swath. Additionally, the solar influx onto the ground pixel changes depending on the relative position of the sun and the satellite, further altering the path of light reaching the instrument. The aggregate of this information is known as Sun-target-satellite constellation. The target means here the point of measurement on the ground. Remarkably, the geometry of the Sun-target-satellite constellation can be described fully by three angles (Capderou, 2014). These are (see Figure 5.6)

- The solar zenith angle (SZA) θ describing the angle between the ideal direct path of the sun to the target (Solar Irradiance Line) and the zenith.
- The viewing zenith angle (VZA) ϕ describing the angle between the direct light path of backscattered light from target to satellite (Line of Sight) and the zenith.

- The relative azimuth angle (RAA) β, sometimes also abbreviated as RAZI, describing the angle between the projected solar irradiance line and the line of sight.

Note that this holds for nadir looking instrument, i.e. instruments looking directly down towards the ground. Both TROPOMI as well as GOME-2 are nadir looking instruments.

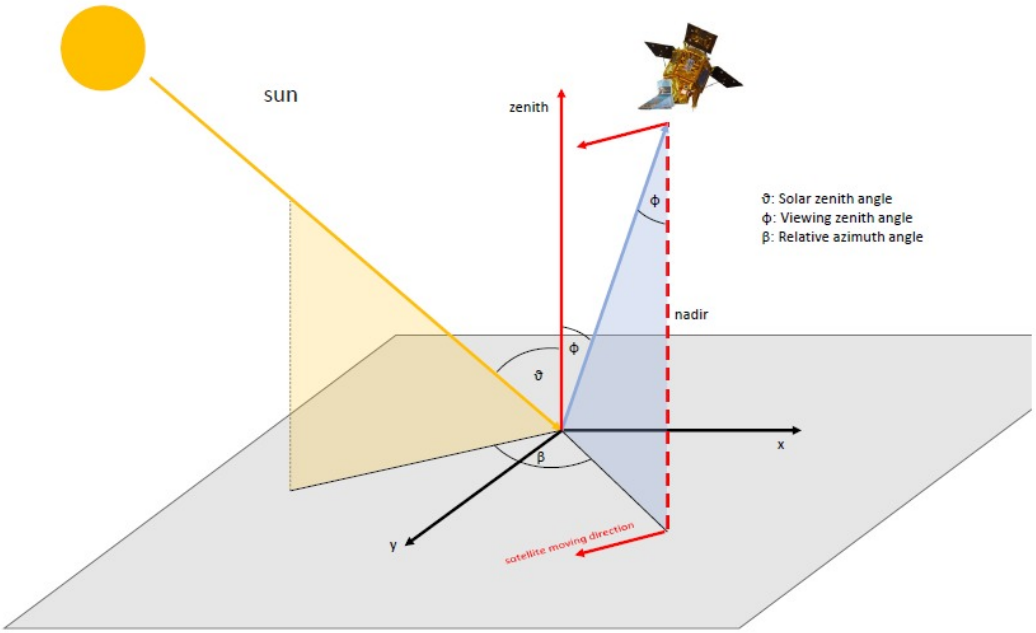

Figure 5.6: *Illustration of satellite viewing geometry. The viewing zenith angle ϕ describes the angles between the satellite's viewing plane (blue shaded area, orthogonal to the satellite moving direction) and the zenith. The relative azimuth angle β describes the angle between the satellite's viewing plane and the solar plane (yellow shaded area). The solar zenith angle θ describes the angle between the solar viewing plane and the zenith. Figure taken from Warnach (2022).*

5.4 Visualization of S-5P data

Satellite measurements are commonly visualized using maps. This process usually entails a few steps to accurately represent measured data on the two-dimensional curved surface of the globe on a plane surface. First, the measurement locations expressed as latitude and longitude in the L1 data of TROPOMI need to be transformed to the correct projected coordinate system.

In a second step, the data need to be *rastered* in order to visualize it as a 2D image. This means the data has to be transformed on a regular grid suitable for plotting and involves taking care of the different sized pixel in the middle and the edges of the swath as well as overlapping measurements. The rastering applied in this thesis achieves this by first

determining the satellite pixels at least partially overlapping with each raster cell. Then the weighted average of pixels in each cell is calculated using their spatial overlap with the cell as weighting. A detailed explanation of this technique can be found for example in Chan et al. (2022).

Both of these steps are especially important for measurements in polar regions: the canonical projections implied by the use of latitude and longitude coordinates distort the image heavily in polar regions. The near-polar orbit of S-5P means that many pixel will overlap due to the high spatial coverage.

5.4.1 Projections

One of the most remarkable corollaries from Carl Friedrich Gauss famous **Theorema Egregium** is that no conformal projection of a sphere on a planar map can be equal area and, vice versa, no equal area projection can be conformal (O'Neill, 1966). Therefore all efforts to accurately visualize satellite data on planar maps necessitate a choice between the degree of area and angle preservation.

Here the projections used in this thesis will be briefly discussed. Note that latitude and longitude variables will always be defined in terms of radians in the following.

Equirectangular projection

The equirectangular projection is a simple and well-known map projection. The most common variant of this projection is also called *plate carrée projection* or *geographic projection*. In this variant, used exclusively in this work, the geographical latitude ϕ and the geographical longitude λ coincide with the orthogonal coordinates x and y of the projection:

$$x \equiv \lambda \qquad \text{and} \qquad y \equiv \phi\,. \tag{5.1}$$

This is visualized in Fig. 5.7 For a more general version of this projection, these relations can be shifted to a different standard parallel φ_1 and central meridian λ_0,

$$x = (\lambda - \lambda_0)\cos\varphi_1 \qquad \text{and} \qquad y = \varphi - \varphi_0\,, \tag{5.2}$$

with φ_0 describing the central parallel of the map. This projection however is neither an equal area nor a conformal projection, which results in strong distortions, especially near the poles where the shown area is distorted strongest. It is therefore not suited for purposes other than a global overview of S-5Ps measurements in the context of the work presented here.

Stereographic projection

The stereographic projection, also known as *azimuthal conformal projection* is a conformal projection as the name already suggests. In this work only the special variant of the *north*

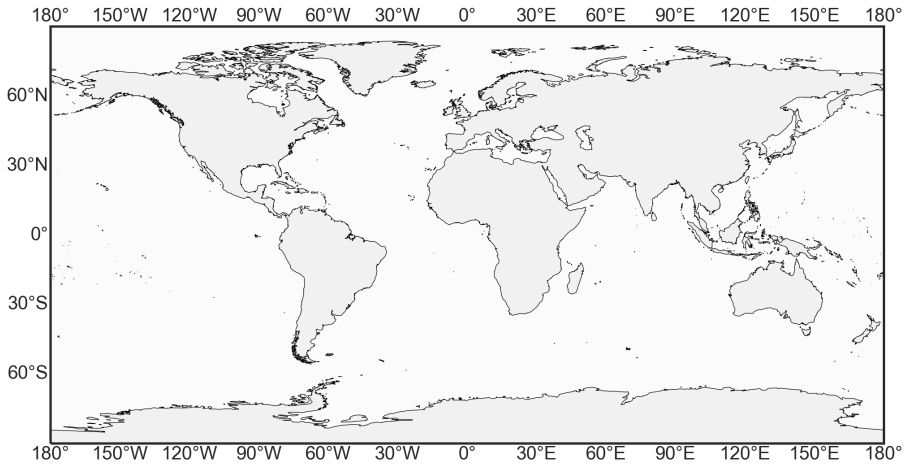

Figure 5.7: *Map of the whole globe in plate carreé projection.*

polar stereographic projection is used, where the central latitude is set to $\varphi_0 = 90°$ as shown in Fig. 5.8. It can be described easiest in polar coordinates (Snyder, 1987),

$$r = 2\,\mathbf{R}\tan(\frac{\pi}{4} - \frac{\varphi}{2}) \tag{5.3}$$

$$\theta = \lambda - \lambda_0\,, \tag{5.4}$$

with $\mathbf{R}$ describing the earths radius and λ_0 the central longitude. For the projections shown in this thesis $\lambda_0 = 0$ is used. Plotting these coordinates on a rectangular plane using a computer requires the conversion to rectangular coordinates via

$$x = 2\,\mathbf{R}\tan(\frac{\pi}{4} - \frac{\varphi}{2})\sin(\lambda - \lambda_0) \tag{5.5}$$

$$y = -2\,\mathbf{R}\tan(\frac{\pi}{4} - \frac{\varphi}{2})\cos(\lambda - \lambda_0)\,. \tag{5.6}$$

This projection preserves all angles but distorts areas. However, the area distortion in close proximity to the pole is very limited and the area of interest for BrO explosions is in most cases close enough to the pole to prevent larger distortions. Therefore this map is used most often in this thesis when it is important to have a broader overview of the area and assess trends over the whole area.

Lambert azimuthal equal-area projection

The transformation equations to planar coordinates x and y in this projection are

$$x = \mathbf{R}\,k\cos\varphi\sin(\lambda - \lambda_0) \tag{5.7}$$

$$y = \mathbf{R}\,k\,[\cos\varphi_1\sin\varphi - \sin\varphi_1\cos\varphi\cos(\lambda - \lambda_0)] \tag{5.8}$$

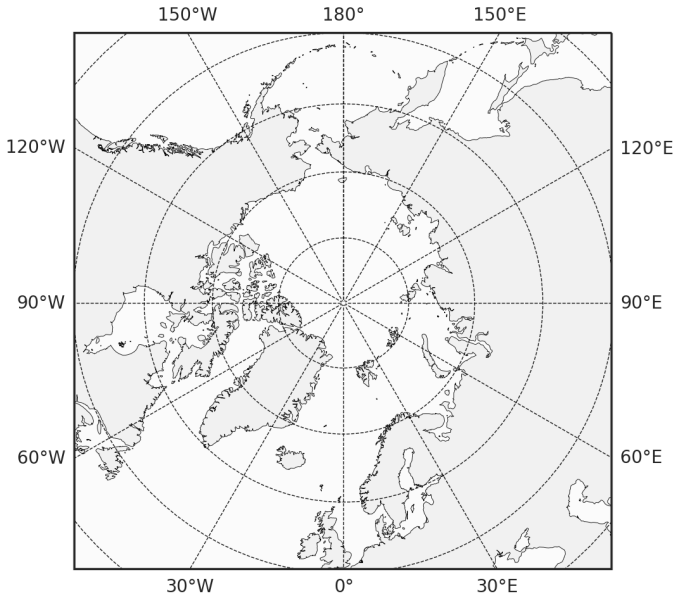

Figure 5.8: *Map of the latitude band of* 40° *to* 90° *N in stereographic projection.*

with the scale factor k as

$$k = \sqrt{\frac{2}{1 + \sin\varphi_1 \sin\varphi + \cos\varphi_1 \cos\varphi \cos(\lambda - \lambda_0)}}\,, \tag{5.9}$$

where φ_1 and λ_0 are once again denoting the standard parallel and the central longitude, respectively (Snyder, 1987).

This projection is used in this thesis mainly to look at single events contained to smaller regions. In these cases the angle distortions introduced by the projections are very small and are outweighted by the advantages of no area distortion, especially compared to the equirectangular projection as shown in Fig. 5.9.

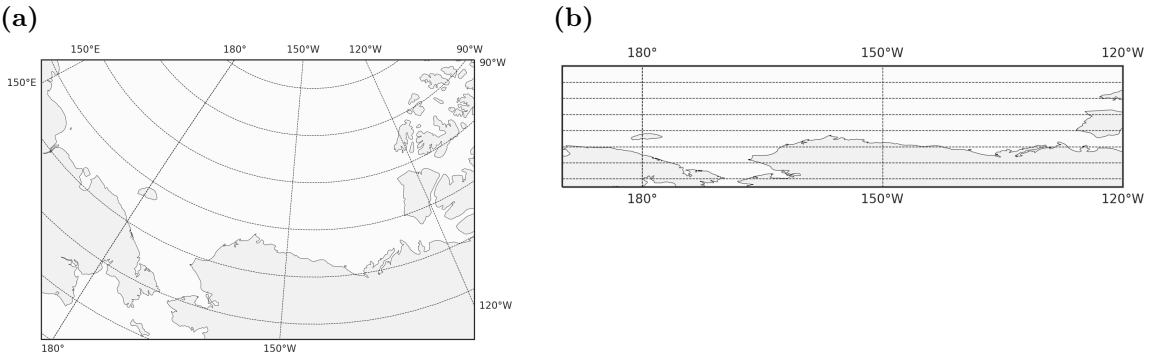

Figure 5.9: *Maps of the small region between* 170° *and* 240° *E longitude and* 65° *to* 80° *N latitude. (a) Lambert equal area projection with small angle distortions. (b) Plate carreé projection with visible distortions.*

6 | Additional data sources

This chapter gives a description of the data sources used in addition to the satellite measurement (see section 5.1 and chapter 7). First, a brief description of a meso-scale weather model used for the extraction of information on stratospheric potential vorticity is given in section 6.1. Then in section 6.2 a detailed description of the meteorological and atmospheric chemistry model used for intercomparison with satellite measurements is provided. TROPOMI's high spatial resolution exceeds the spatial resolution of both models used in this work. It is therefore necessary to interpolate the data from the model onto satellite coordinates as described in section 6.3

6.1 Potential Vorticity from ECMWF

The ERA-5 dataset (Hersbach and Dee, 2016) is used to obtain potential vorticity at two different isentropic levels (475 K and 550 K). This data is used to identify satellite measurements located within the polar vortex in the context of the tropospheric BrO retrieval as discussed in chapter 7. The data is provided with a 1 h time resolution at a spatial resolution of $0.25° \times 0.25°$.

The performance of the ERA reanalysis in the arctic has been improving, especially with the release of ERA5, which has been shown to outperform several other global atmospheric reanalyses (Graham et al., 2019). However, the performance for surface level meteorological parameters in polar regions is still under debate (Wang et al., 2019; Deb et al., 2016). For this reason, a regional WRF model is used for comparisons to meteorological parameters in the troposphere, which will be discussed in the following.

6.2 Atmospheric Chemistry and Meteorological data from WRF-CHEM

The Weather Research and Forecasting (WRF) model is a 3D numerical weather prediction system developed collaboratively by the scientific community (Skamarock et al., 2008). While WRF is used only for meteorological predictions there exists the possibility to couple this with atmospheric chemisty predictions. This is called the Weather Research and Forecasting model coupled with CHEMistry (WRF-CHEM).

Meteorological as well as atmospheric chemistry data obtained from WRF-CHEM simulations are used in this work in manifold applications. In chapter 8 results of the model and in-situ measurements as well as satellite observations are compared, while in chapter 9 conclusions about the underlying atmospheric chemistry are drawn in case studies.

The work in this thesis uses the implementation provided by Herrmann et al. (2022) (see also Herrmann et al. (2020, 2021) and Herrmann (2021)). The simulations use a nested model with two domains (see Figure 6.1). The coarser domain, referred to as domain 1, covers an area of 12 600 km × 12 600 km with a spatial resolution of 60 km × 60 km. The inner domain, referred to as domain 2, covers a 6000 km × 6000 km area with a spatial resolution of 20 km × 20 km. The simulation covers a period between February 1 and May 15 in time steps of one minute. The velocity, temperature and humidity at the ground and above the boundary layer are nudged towards ERA5 data (cf. section 6.1).

For the chemistry, the Model for OZone and Related chemical Tracers (MOZART) mechanism (Emmons et al., 2010) is extended with bromine-chemistry (Herrmann et al., 2019) for a total of 103 gas-phase species and 359 reactions. Aerosols are accounted for via the Model for Simulating Aerosol Interactions and Chemistry (MOSAIC) framework. A detailed description of the model is found in Herrmann et al. (2022, 2021). In the following, aspects of the model important for the discussion in part III are presented.

There are four different reactions emitting bromine from snow surfaces implemented in the model Herrmann et al. (2022):

$$\mathrm{HOBr} \xrightarrow{\mathrm{aBr^- + bCl^- + H^+}} \mathrm{aBr_2 + bBrCl + H_2O} \tag{R29}$$

$$\mathrm{BrONO_2} \xrightarrow{\mathrm{H_2O}} \mathrm{HOBr + HNO_3} \tag{R30}$$

$$\mathrm{N_2O_5} \xrightarrow{\mathrm{aBr^- + H^+}} \mathrm{aBrNO_2 + (1\ + b)HNO_3} \tag{R31}$$

$$\mathrm{O_3} \xrightarrow{\mathrm{\gamma(2\,Br^- + 2\,H^+)}} \mathrm{a\gamma\,(Br_2 + H_2O + O_2)} \tag{R32}$$

The parameters a and b give the emission probabilites of Br_2 and BrCl in the model while the SZA dependent rate constant $\gamma = \gamma(\theta)$ (see below) couples the emission flux of Br_2 to the dry deposition flux of O_3.

In this thesis we are analyzing the results of three different model runs, differing mainly in their choice for the parameters a and b. While chloride content of snow surfaces is always assumed to be infinite, there are two sets of assumptions for the bromide supply of snow-covered surfaces differing between first-year (FY) sea-ice, multi-year (MY) sea-ice and snow-covered land (see also section 2.2.1):

- The bromide supply on FY ice is assumed to be infinite and zero on all other surfaces. This leads to $b = 1 - a$ on all snow-covered surfaces and $a = 1$ on FY ice covered by snow. On MY ice and snow-covered land, a depends on the depositions of HBr and the bromine emitting species given in Reactions (R29 – R32). Expressed differently,

on surfaces other than FY ice, bromine is only emitted from the recycling of HBr but not from fresh bromine in the surface. This set of assumptions will be referred to as *infinite first-year ice bromide* from now on and underlies on one of the three model runs.

- The bromide content is assumed to be finite on all surfaces and is tracked by a surface variable $\mathrm{Br}_{\mathrm{surf}}$ describing the column density of bromide in the snow. The amount of releasable bromide is set to be dependent on the surface with parameters c_1, c_2, c_3 with

$$[\mathrm{Br}_{\mathrm{surf}}] = \begin{cases} c_1 & \text{on FY ice and } h < 1 \text{ km} \\ c_2 & \text{on MY ice and } h < 1 \text{ km} \\ c_3 & \text{on snow covered land and } h < 1 \text{ km} \\ 0 & \text{otherwise} \end{cases} \tag{6.1}$$

  These values are also nudged towards the initial values on a timescale of one week. This is necessary as otherwise the releasable bromide would be depleted at the beginning of march. It is also not unreasonable, since bromide can diffuse upwards from sea ice.

  There are two different simulation runs corresponding to low and medium initial bromide concentrations as described in Table 6.1. The amount of initial releasable bromide for the two runs is visualized in Figure 6.1. In the following, these will be referred to as *low* and *medium* bromide simulations. A detailed discussion of the choice of the parameter values can be found in Herrmann et al. (2022).

Of crucial importance is the bromine release from dry deposition of ozone, as implemented in Reaction (R32), since it acts as an initial "trigger" for the BrO explosion. This means it supplies a large fraction of the initial amount of bromine before the BrO explosion reaction cycle and recycling of other bromine species begin to dominate. The reaction should be seen as a substitute for the collection of all possible trigger reactions[1] mentioned in section 2.1.1 following the ideas presented in Toyota et al. (2011). The trigger strength is enhanced under sunlight, giving an emission probability γ of 7.5 % of the dry deposition rate of O_3 for an SZA of less than 85° and 0.1 % otherwise (Toyota et al., 2011). The implementation of this

[1] Note that additional possible trigger reactions such as the photolysis of $CHBr_3$ are also implemented in the model, however they produce far too less bromine to be of importance for the occurence of ODEs.

Table 6.1: *Overview of the amount of initial releasable bromide for all three simulations, see Eq. (6.1). Table adapted from Herrmann et al. (2022).*

Simulation name	Initial releasable bromide, c_1, c_2, c_3 [10^{14} molec cm^{-2}]	Definition of snow-covered land
infinite first-year ice bromide	∞, 0, 0	USGS 30s landuse
Low bromide	3, 1, 0.5	USGS 30s landuse
Medium bromide	3, 1.5, 1.5	300 km distance to sea ice

reaction is identical for all model runs.

No new bromine emissions from blowing snow (see section 2.1.1) are implemented in the model. To date, only Marelle et al. (2021) and Swanson et al. (2022) implemented both blowing snow emissions as well as emissions from bromide oxidation via ozone in a model. However, they reported that blowing snow emissions had no considerable impact on the occurrence of ODEs if used together with a bromide oxidation trigger reaction (Reactions (R25) and (R32), see also section 2.1.1). Nevertheless, bromine recycling on aerosols (see section 2.2) is implemented via the MOSAIC mechanism. However, there are also no aerosols produced from blowing snow. As discussed in section 2.2.3, only Swanson et al. (2022) included this in a model using snow-pack emissions of bromine thus far. The aerosols in the model presented here can emit Br_2 via the following reactions:

$$HOBr\,(g) \longrightarrow HOBr_m\,(aq) \tag{R33}$$

$$HBr\,(g) \longrightarrow HBr_m\,(aq) \tag{R34}$$

$$BrONO_2\,(g) \longrightarrow HOBr_m\,(aq) + HNO_3\,(g) \tag{R35}$$

$$HOBr_m\,(aq) + HBr_m\,(aq) \longrightarrow Br_2\,(g) \tag{R36}$$

This bromine aerosol mechanism is based on Sander et al. (2011), a more detailed description is found in the supplement to Herrmann et al. (2021). The first three reactions describe the transfer reactions of gas-phase bromine species to the liquid phase in the aerosol-size bin m. If the liquid state aerosol has a pH of 6 or less, then Reaction (R36) can occur (see section 2.2 and (McConnell et al., 1992; Peterson et al., 2017)), producing again gas phase Br_2. Detailed reaction rates and parameter requirements for these reactions can be found in Herrmann et al. (2021).

Lastly, it should be noted that the definition of snow-covered land as used for the determination of Br_{surf} via the value of c_3 is differing between the simulations. For the medium bromide simulation, the amount of bromide is further increased by assuming that land within a distance of at most 300 km to sea ice is considered to be snow-covered. For the other two simulations the USGS 30s landuse category *Snow and Ice* is utilized, which results in only few land surfaces considered to be snow-covered (see Figure 6.1).

6.3 Interpolation of model data to TROPOMI resolution

The additional data used in this thesis is provided neither at the same resolution as measurements from TROPOMI nor at the same measurement time. Therefore, both for comparison with the WRF-CHEM model as well as to use ECMWF data for our retrieval algorithm, spatial and temporal interpolation is required. Since both datasets have a high temporal resolution for any given location compared to TROPOMI, it is easiest to use trilinear interpolation. This is also sufficient since TROPOMIs high spatial resolution exceeds the spatial

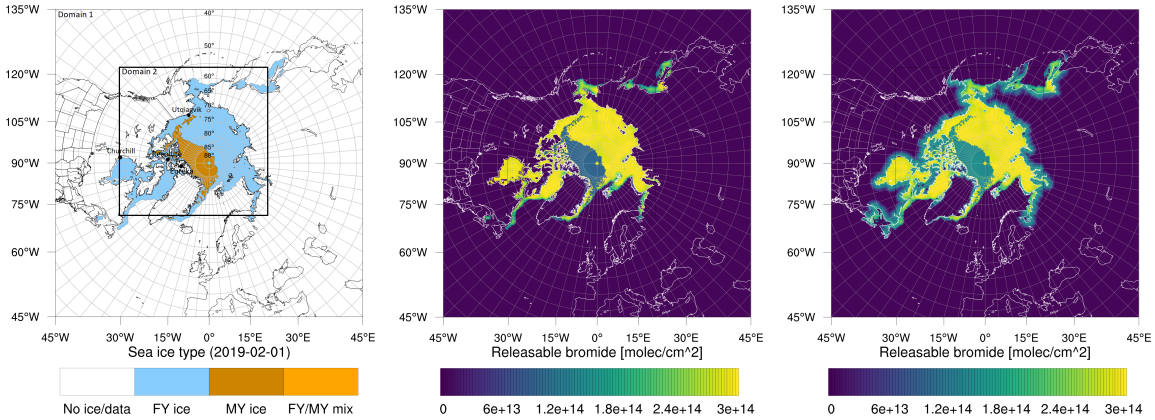

Figure 6.1: *From left to right: Sea ice type data (Aaboe et al., 2017) and initial releasable bromide for the low bromide (center) and medium bromide (right) simulations. Figure and caption adapted from Herrmann et al. (2022).*

resolution of both datasets. Any given quantity $X(\varphi, \lambda, t)$ will then be interpolated as

$$X_k = (\varphi_k, \lambda_k, t_k)\,, \tag{6.2}$$

where φ_k and λ_k describe the center location of the measurement pixel k and t_k is the time at which the measurement took place.

Since BrO explosion occur on a time scale of days with a typical spatial extent larger than the 20 km resolution of the WRF-CHEM model (cf. chapter 10 and Jones et al. (2013)), a linear interpolation of WRF (which is saved in one hour timesteps) should be of sufficient accuracy.

7 | Retrieval of tropospheric BrO

One of the main achievements of this thesis was the improvement of the tropospheric BrO retrieval algorithm from Sihler et al. (2012) and its application to the new TROPOMI measurements. Since this algorithm is not using any external information from models or climatologies (cf. section 3.1.5), it is particularly suited for validation of simulation results (see chapter 8). The independence of (usually spatially coarser) stratospheric models of the retrieval also allow the full utilization of TROPOMIs high spatial resolution (see section 5.1.2) which can be particularly helpful for statistical analyses as prestend in chapter 10.

This chapter explains the full processing chain beginning at the DOAS evaluation of the spectra recorded by TROPOMI to the final tropospheric BrO VCD. It begins with an overview of the complete retrieval process in section 7.1 after which the determination of the SCDs of various trace-gases using the DOAS technique is discussed in section 7.2. The method to separate stratospheric and tropospheric BrO partial columns is then presented in section 7.3. The calculation of AMFs used to convert the retrieved tropospheric BrO SCD to VCDs is discussed in section 7.4 followed by an in-depth discussion of sources of uncertainties in the final retrieved tropospheric BrO VCDs in section 7.5.

7.1 Overview of Retrieval

For trace gases with appreciable stratospheric column densities such as BrO an accurate observation of the tropospheric partial column density first requires the determination of the SCD contained in the stratosphere. The variability in the stratospheric BrO column can get comparable to or even larger than the variability induced by the surface release of bromine (e.g. Salawitch et al., 2010; Theys et al., 2011; Toyota et al., 2011). Stratospheric disturbances may alter the stratospheric column which can mimic tropospheric BrO events in the resulting total column. Furthermore, the sensitivity towards stratospheric BrO can be substantially higher compared to the sensitivity towards tropospheric BrO, in particular at high SZAs as demonstrated by the large difference in the corresponding AMFs in Figure 4.5. This means that the measured differential stratospheric BrO absorption contributes to a large degree to the observed total BrO column. For this reason one of the largest uncertainties in the determination of column densities of tropospheric BrO enhancements comes from the assessment of the stratospheric background column density (Richter and Wagner, 2011).

This is the main objective of the column separation algorithm presented in this chapter. As discussed in chapter 3, several retrievals of tropospheric BrO columns use results of (stratospheric) chemistry models. This can introduce unknown biases from incorrect chemical mechanisms in the model. Furthermore, it imposes a limit on the effective spatial resolution of the retrieval to a certain extent based on the spatial resolution of the utilized model.

In contrast, the retrieval used in this thesis overcomes all of these drawbacks by deriving an estimation of the stratospheric partial column based on only measurements of the instrument themselves. As a first step, several DOAS retrievals are performed to obtain the slant column densities for O_3, BrO and O_4. The NO_2 vertical column density is obtained from the TROPOMI operational NO_2 product. The retrieved O_3 SCDs and NO_2 VCDs are then used as proxies of dynamical and chemical effects in the stratospheric affecting the stratospheric BrO distribution as shown in Figure 7.1. This allows an estimation of the stratospheric background BrO SCD from which the tropospheric SCD is determined as discussed in section 7.3.

It has become common in remote sensing to use measured absorption of the oxygen collision complex (denoted as O_4 in this thesis) to retrieve information on cloud parameters as well as aerosols, both for ground based measurements (Wagner et al., 2002, 2004; Frieß et al., 2006; Irie et al., 2008) as well as for nadir satellite observations (Deschamps et al., 1994; Wagner and Platt, 1998; Acarreta et al., 2004; Sneep et al., 2008; Veefkind et al., 2016). While the underlying nature of the molecular interactions are still not decided upon (Sneep et al., 2006) with the equilibrium constant k unknown,

$$O_2 + O_2 \overset{k}{\rightleftharpoons} O_4 \tag{R37}$$

a pseudo O_4 column can be measured using DOAS, assuming the availability of an accurate pseudo cross section for the oxygen dimer. This stems from the fact that the O_4 spectrum shows several absorption bands in the UV/Vis (for example at 360 nm and 380 nm (Wagner et al., 2002)).

This is utilized in the second step of the tropospheric BrO retrieval. In that step, results of a radiative transfer model are used to generate Look Up Tables (LUTs) populated with different AMFs for BrO located close to the ground as well as corresponding reflectances and AMFs of the differential absorption of O_4. These are representing a range of different viewing geometries and sensitivity conditions (e.g. different aerosol extinction and cloud coverage). Then individual reflectances measured from the satellite are combined with measurements of the differential absorption of O_4 to classify each measurement as either sensitive to near-surface BrO or possibly obscured to it. For sensitive measurements an AMF is determined from the LUTs, allowing the conversion of the previously calculated tropospheric BrO SCDs to tropospheric BrO VCDs (see Figure 7.1).

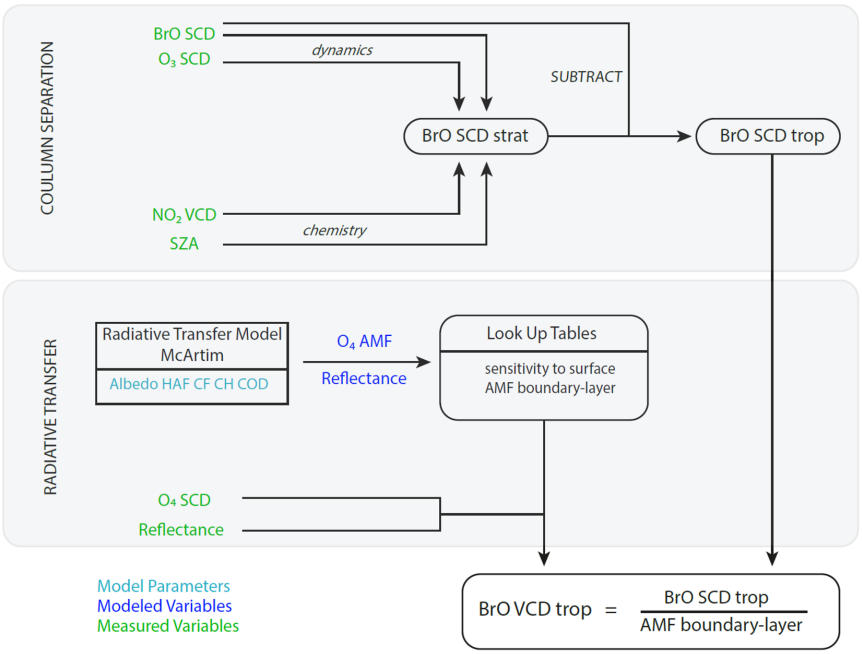

Figure 7.1: *Flowchart visualizing the algorithm for the retrieval of vertical column densities of tropospheric BrO. The retrieval can be separated into two disjoint algorithms. First, the total BrO column is separated into a stratospheric and tropospheric BrO partial column using several proxy parameters to capture the influence of dynamical and chemical processes in the stratosphere on the stratospheric BrO column. This is titled Column Separation (section 7.3). Next, LUTs populated from RT simulations covering a range of different viewing conditions are used to quantify the sensitivity towards BrO in a near-surface layer. This is used to convert the tropospheric BrO SCDs from the previous step to tropospheric BrO VCDs and titled Radiative Transfer in the illustration (section 7.4). The abbreviations stand for High Albedo Fraction (HAF), Cloud Fraction (CF), Cloud Height (CH) and Cloud Optical Density (COD). Figure adapted from Sihler (2012).*

7.2 Evaluation of TROPOMI spectra

The first step towards the determination of tropospheric BrO vertical column densities is the evaluation of the spectra recorded by TROPOMI using the DOAS technique (see chapter 4).

The optimal fit parameters of a DOAS retrieval depend on the application and the region of interest. For example, the abundance of other trace gases interfering with a measurement (e.g. HCHO or O_3 for BrO retrievals) can vary strongly over the globe, therefore a choice of fit settings has to take the specifics of the application into account.

As discussed in the previous section, the algorithm presented in this chapter requires the retrieval of four different trace gas SCDs. BrO, O_3 and NO_2 SCDs are all deployed to retrieve the tropospheric BrO slant column. The SCD of the oxygen collision complex O_4 is then utilized for an estimation of the tropospheric AMF used to convert the tropospheric BrO slant column density to a vertical column density. To this end, the DOAS method is deployed in three different wavelength ranges. In this section, the details of these retrievals

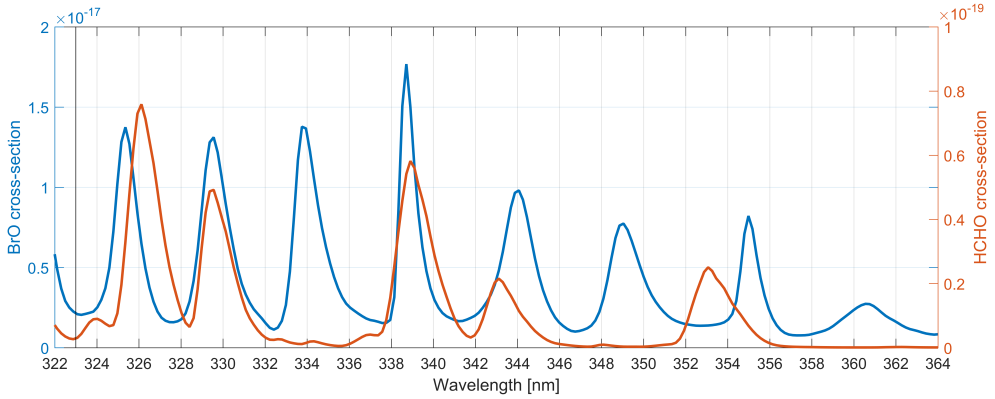

Figure 7.2: *Comparison of cross-sections of BrO (blue) and HCHO (red) convolved with a TROPOMI instrument spectral response function (ISRF). Figure taken from Warnach (2022).*

are presented.

7.2.1 Parameters of DOAS retrievals

For the retrieval of NO_2 VCDs the official TROPOMI Level 2 NO_2 product (Van Geffen et al., 2020, 2022; Eskes et al., 2022) is used. For this a DOAS fit in the wavelength range of 405 nm to 465 nm is performed, resulting in a total SCD for NO_2. This is converted to vertical column density using a total AMF taking into account clouds and the averaging kernel of TROPOMI among others. It is described in detail in Van Geffen et al.. The level 2 algorithm is designed to determine the tropospheric NO_2 VCD. Although this retrieval algorithm uses a climatology for the estimation of the stratospheric NO_2 partial column, the separation algorithm presented in the following uses only the total vertical column density of NO_2, which is solely the result of a DOAS retrieval and not biased through the use of a model or other retrieval scheme.

The other three different trace gas SCDs are retrieved using two different fit scenarios. For both, the universal DOAS fit routine for satellite DOAS retrievals from Borger et al. (2020) with a linearized shift and stretch (see section 4.3.1) is employed. The fit settings for both are summarized in Table 7.1.

As discussed in section 4.3, the wavelength range of a DOAS retrieval has to be chosen such that it is possible to distinguish the differential absorption structure of the target trace gas. For BrO, this highlights the wavelength range between 320 nm to 364 nm, covering nine absorption peaks in the cross-section of the molecule.

However there are several other trace gases with absorption structures in this wavelength range interfering with a BrO retrieval. An example of such a spectral interferences is exemplified in Figure 7.2, showing the similarity of the absorption cross-sections of BrO and HCHO in parts of the spectral range. In additon to formaldehyde, ozone is another absorber in that wavelength region, with strong absorptions especially for shorter wavelengths falling in the Huggins absorption band. Further interferences can in principal be expected from

NO_2, SO_2 as well as O_4 and OClO, but their influence on the BrO results is usually rather small. To minimize these potential spectral interferences, the cross-sections of these trace gases are included in a DOAS fit for BrO. Additionally, various pseudo absorbers are fitted to account for different effects such as rotational raman scattering as discussed in section 4.4.

However, the optimal choice of fit parameters is also dependent on the application as mentioned earlier, which is reflected in the huge variation of BrO fit settings over time and different applications. Early studies limited the influence of interference by choosing a smaller wavelength range of approximately 345 nm to 359.5 nm (Wagner and Platt, 1998; Richter et al., 1998; Chance, 1998; Richter et al., 2002) at the cost of a higher signal-to-noise ratio. Later, this range was expanded for the GOME-2 and SCIAMACHY instruments, with a lower limit of 336 nm and the upper limit varying between 347 nm and 360 nm depending on the application (Kaleschke et al., 2004; Begoin et al., 2010; Theys et al., 2009; Heue et al., 2011; Sihler et al., 2012; Hörmann et al., 2013). With the advent of TROPOMI, the lower boundary was further reduced to 332 nm (Seo et al., 2019) and reaching as low as 323 nm for the detection of volcanic plumes (Warnach, 2022).

The retrieval of tropospheric BrO presented in this thesis is based on the method developed by Sihler et al. (2012) and consequently, the DOAS fit settings of the DOAS BrO retrieval are based on the arctic BrO fit of Sihler et al. (2012). Therefore a fit range of 336 nm to 360 nm was chosen in difference to Theys et al. (2011) and Seo et al. (2019) and the formaldehyde cross-section was not taken into account for the fit. Although it can be beneficial for the SNR to include a larger wavelength region in the retrieval, in difference to Warnach (2022) the lower wavelengths were omitted deliberately to limit interference with ozone absorption at high latitudes where ozone columns and atmospheric light paths through the ozone layer can both get very large. The fit also differs in its inclusion of the so-called Puķīte terms (see section 4.4.2 and Puķīte et al. (2010)) with respect to Sihler et al. (2012) and Seo et al. (2019), which further limits the dependence on ozone. Additionally, albeit spectral interferences with HCHO can be important at lower latitudes, the relatively small amounts present in arctic regions justify the exclusion from the fit (e.g. Wagner and Platt, 1998; Richter et al., 1998). Sensitivity studies by Warnach (2022) confirmed that the inclusion of HCHO is in general also not necessary for TROPOMI. However, in contrast to the retrieval of Sihler et al. (2012), the BrO retrieval presented here uses an equatorial *earthshine* spectrum as reference spectrum which is discussed further in section 7.2.2. One might expect the exclusion of HCHO to pose a problem when using an equatorial reference, where biomass burning can lead to very large HCHO colums. Nevertheless, extensive sensitivity studies by Warnach (2022) have shown that an inclusion of HCHO and possibly an accompanying lowering of the fit boundary (as used by Seo et al. (2019); Theys et al. (2011)) resulted in a worse SNR of the fit for Arctic as well as equatorial regions. Further fit settings are shown in Table 7.1. Compared to Sihler et al. (2012), most cross sections were updated with more recent data. The resulting BrO VCDs computed from BrO SCDs and a geometric AMF A_{geom} (see Eq. (4.22)) are shown in Figure 7.3.

Due to the strong differential absorption structure of ozone, the SCD of O_3 can be

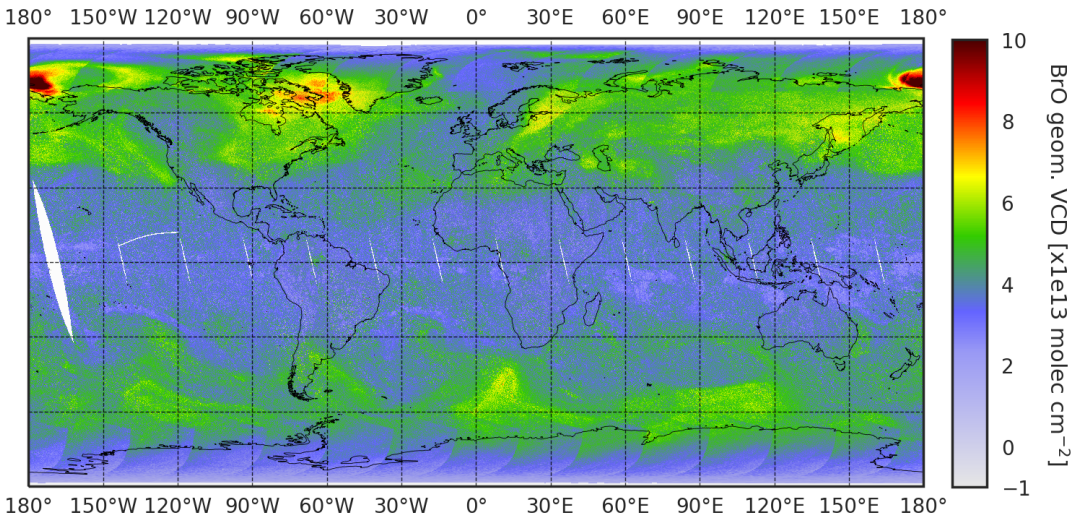

Figure 7.3: *Global map of BrO VCDs calculated with geometric AMFs (see Eq. (4.22)) illustrating the results of the BrO fit on 19 March 2019.*

retrieved simultaneously using the same DOAS evaluation as the weak absorber BrO at a much higher SNR. It is calculated as the sum of the fit results of both O_3 reference spectra for different temperatures. As discussed in Sihler et al. (2012), although this simultaneous retrieval might lead to a systematic error for the ozone SCD, this will cancel out in the parameterization of the stratospheric BrO column (see section 7.3.1).

The SCD of O_4 is retrieved in the wavelength range between 355 and 390 nm. This includes two absorption bands of the oxygen collision complex at 360 nm and 380 nm. Further fit settings are summarized in Table 7.1. The retrieved O_4 column is used for the calculation of the tropospheric AMF as discussed in section 7.4. In contrast to the BrO fit, the O_4 fit uses an irradiance reference spectrum because for the assessment of the measurement sensitivity the absolute atmospheric O_4 absorption is needed, see also section 7.4.

7.2.2 Selection of Fraunhofer reference spectra

As discussed in section 4.2, one advantage of satellite instruments for DOAS applications is their ability to measure the solar spectrum directly on a daily basis. Using these solar spectra as background spectra I_0 (cf. Eq. (4.10)) allows for a retrieval of absolute SCDs of corresponding trace gases from the DOAS method. Yet these daily solar spectra have to be recorded using a different optical channel then the ones recording nadir observations.

While this also slightly affects the retrieval for *whisk-broom* instruments such as GOME-2 which use only one sensor, instruments such as TROPOMI with its 450 different across-track sensors can be heavily impacted by this. Differences in the sensitivity of individual CCD pixel will result in a across-track variability of the measured SCDs visible as stripes in the final product (Boersma et al., 2007, 2018) which are not completely compensated for by the level 1 calibration. The impact of these stripes on the final product varies depending on absorber in question. While the effect on a weak absorber such as BrO is especially apparent

and has to be corrected for, it might be ignored for a trace gas with stronger absorption such as O_4.

For BrO retrieved from TROPOMI L1B spectra using a solar irradiance reference, there is distinct striping visible which has to be corrected. This can be achieved in two ways: (1) explicit *destriping* by determination of the across-track variability on a daily or orbitwise basis over a reference region with "known" trace gas VCDs (e.g. Hörmann et al. (2016); Boersma et al. (2011)) or (2) replacement of the solar irradiance background spectra by a so-called earthshine spectrum, recorded also over a reference region with known trace gas abundance (e.g. Seo et al. (2019)).

In this thesis, the second approach is used. In past studies, a reference region over the equatorial pacific was used, where BrO columns should usually neither be affected by anthropogenic pollution nor by emissions of volcanoes (Richter et al., 2002; Sihler et al., 2012; Seo et al., 2019). For the work presented here this equatorial reference region is extended over the whole equator latitude band to a region between 20° N and 20° S. Since BrO has a significant stratospheric background signal over this equatorial reference region with VCDs of approximately $V_{\mathrm{norm}} = 3.5 \times 10^{13}\,\mathrm{molec\,cm^{-2}}$ (Richter et al., 2002), the use of an earthshine reference in the DOAS retrieval will yield differential SCDs instead of absolute SCDs.

To account for this, a correction is calculated for each row in the across-track (cf. section 5.1.2). This correction is calculated as the median difference between the measured SCDs in the reference sector and the normalized SCDs calculated using a geometric AMF (see Eq. (4.22)),

$$S_{\mathrm{norm}} = V_{\mathrm{norm}} \cdot A_{\mathrm{geom}}\,. \tag{7.1}$$

In a second step, the corrected SCD is calculated pixelwise as the difference between the measured SCD and the determined offset value for the respective across row. This method also accounts for any viewing angle dependencies in the determined earthshine reference spectrum.

Table 7.1: *DOAS fit settings used for the BrO and O_4 slant column retrievals. The asteriks (*) indicates that the corresponding cross section of the BrO fit is included, while a hypen (-) indicates it is omitted in the O_4 fit. The O_3 SCD is retrieved simultaneously with the BrO SCD.*

Parameter	BrO Fit	O_4 Fit	Reference
Fit window	336-360 nm	355-390 nm	
Absorption cross-sections	BrO, 223 K	-	Fleischmann et al. (2004)
	O_4, 203 K	O_4, 293 K	Thalman and Volkamer (2013)
	O_3, 223 K, 243 K	O_3, 243 K	Serdyuchenko et al. (2014)
	NO_2, 220 K	*	Vandaele et al. (1998)
	SO_2, 203 K	-	Bogumil et al. (2003)
	OClO, 293 K	-	Bogumil et al. (2003)
Ring effect	Ring (norm), 230 K Ring (λ), 230 K	*	Wagner et al. (2009a)
Polynomial	5^{th} order	4^{th} order	
Pseudo absorbers	inverse spectrum	inverse spectrum	Beirle et al. (2017)
	shift and stretch	shift and stretch	Beirle et al. (2013)
	2 x Puķīte O_3 terms, 223 K	-	Puķīte et al. (2010)
Reference spectra	daily equitorial earthshine spectrum	solar irradiance spectrum	

7.3 Column separation

This section presents the stratospheric correction algorithm utilized in this thesis in order to obtain tropospheric BrO SCDs from the total SCDs obtained by the DOAS evaluation of the measured spectra (section 7.2). The method is based on previous ideas by Sihler et al. (2012). It represents an update of the methods to the improved spatial resolution and the associated daily high data volume of TROPOMI compared to GOME-2.

As discussed in section 3.1, the approach presented in the following is made unique by its independence from external data. It is capable of an estimate of the stratospheric BrO column with the use of proxy parameters to capture stratospheric dynamics and chemistry, which are measured by the instrument directly. In section 7.3.1, the fundamental concept of the separation method is described. This is followed by a detailed description of the concrete implementation, which also highlights the differences to the previous implementation by Sihler et al. (2012) and explains the reason for changes made. The section is then concluded with a validation of the algorithm using simulated data in section 7.3.3. For the sake of brevity, for the rest of the section the total BrO SCD and VCD will be denoted as S or V respectively while the stratospheric and tropospheric equivalents are denoted as S_{strat}, V_{strat}, S_{trop} and V_{trop}.

7.3.1 Concept

The aim of the column separation algorithm is to estimate the stratospheric BrO column density based on measured parameters. Although the main focus of this work lies on tropospheric BrO, first the stratospheric SCD has to be determined to separate the tropospheric SCD from the total SCD:

$$S_{\text{trop}} = S - S_{\text{strat}} \,. \tag{7.2}$$

To this end, several parameters are used as proxies for the stratospheric dynamics and chemistry affecting BrO as described in section 7.1. This section will discuss the fundamental idea of the column separation approach.

A lowering tropopause will cause a descending air parcel to be adiabatically compressed, which leads to a corresponding increase in the concentration of trace gases if mixing ratios do not substantially change. Hence, this will lead to an increase in the stratospheric column of BrO as first explained by Wagner (2000). Therefore stratospheric dynamics can lead to spatial structures that mimic tropospheric BrO events, which may lead to an overestimation of the tropospheric column as discussed by Salawitch et al. (2010).

One solution to distinguish between an enhancement of the total BrO column due to stratospheric influences and an increase of tropospheric BrO (probably during an ODE) was proposed by Wagner and Platt (1998). They proposed that the variability of stratospheric BrO column introduced by stratospheric dynamics is mirrored by a similar variability in the ozone column. The authors then used measurements of the total ozone column to differentiate between stratospheric and tropospheric BrO enhancements (see also section 3.1.5).

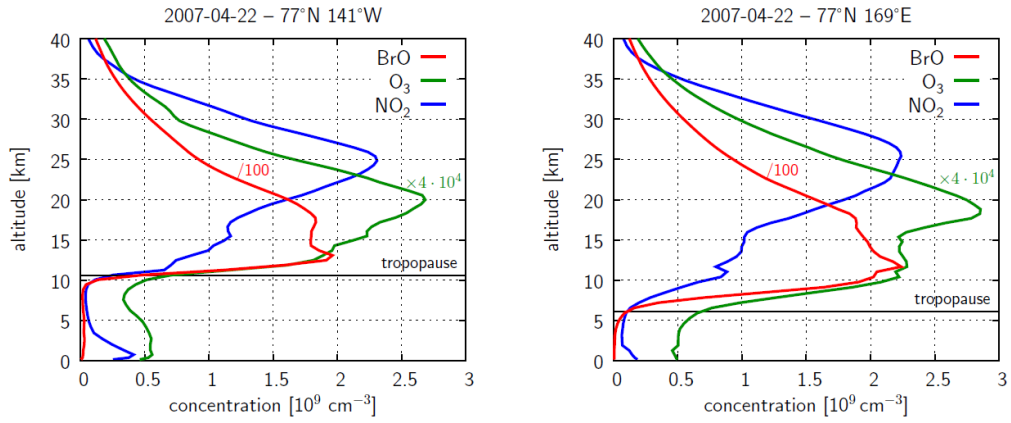

Figure 7.4: *Simulated vertical profiles of BrO, O_3 and NO_2 from the EMAC model for different tropopause heights. On the left, a tropopause height of* 12 km*, while the right shows a relatively low (for the polar region) tropopause height of* 7 km*. All profiles are simulated for the same day, solar zenith angle and latitude. Figure taken from Sihler (2012).*

This insight was utilized by Sihler (2012) in his development of the tropospheric BrO retrieval. He proposed that for sufficient resemblance in the response of the stratospheric BrO SCD and the stratospheric O_3 SCD to dynamical changes in the tropopause height, the ratio

$$z_{\text{strat}} = \frac{S_{\text{strat}}}{S_{\text{O}_3}}\,, \tag{7.3}$$

should be unaffected by dynamical changes of the stratospheric air column. For this reason, the O_3 SCD is used as proxy for the stratospheric dynamics as shown in Figure 7.1. Since almost the entire ozone column is located in the stratosphere, it is not necessary to distinguish between the stratospheric O_3 SCD $S_{\text{O}_3,\text{strat}}$ and the total O_3 SCD S_{O_3} (Sihler, 2012).

This assumption is illustrated in Figure 7.4, which shows simulated profiles of NO_2, O_3 and BrO from the EMAC model for different tropopause heights. It can be seen that the BrO profile responds very similar to the O_3 profile under changes of the tropopause height. However, the use of O_3 as proxy also requires a similar sensitivity of the satellite measurements towards both stratospheric BrO and O_3. The uncertainty introduced by this assumption in the retrieval is discussed in more detail in section 7.5.1.

The total BrO colum S as measured from the satellite can also contain a tropospheric BrO signal. For high mixing ratios of BrO in deeper boundary layers, the tropospheric fraction of the BrO column can become comparable or even larger than the stratospheric fraction. This introduces an unknown positive contribution $\xi_{\text{trop}} = \frac{S_{\text{trop}}}{S_{\text{O}_3}}$ to the ratio z_{strat}, which means the measured ratio from TROPOMI can be written as

$$z = z_{\text{strat}} + \xi_{\text{trop}}\,, \tag{7.4}$$

with $\xi_{\text{trop}} \geq 0$. Significant (positive) deviations in the ratio z are then likely to be of

tropospheric origin.

The determination of z_{strat} in Eq. (7.4) would allow an estimation of the stratospheric BrO SCD. However, it is also necessary to account for any variations in the ratio z due to stratospheric chemistry. The partitioning of bromine between BrO and other inorganic bromine species such as $BrONO_2$ or HOBr in the stratosphere depends primarily on the stratospheric NO_2 concentration (e.g. Sinnhuber et al., 2002; Atkinson et al., 2007; Theys et al., 2009; Salawitch et al., 2010). The formation of bromine nitrate from BrO,

$$BrO + NO_2 + M \longrightarrow BrONO_2 + M \tag{R38}$$

is usually limited by the abundance of NO_2. On the other hand, $BrONO_2$ produces mostly BrO when photolysed which leads to a quasi equilibrium between stratospheric BrO and $BrONO_2$ depending on the NO_2 concentration and the actinic flux.

As a result, the ratio z_{strat} should decrease with increasing NO_2 concentration, which is also depending on the SZA θ influencing the actinic flux. For this reason, Sihler et al. (2012) proposed the use of both of these parameters as proxy parameters to capture the influence of stratospheric chemistry on the BrO SCD and hence z_{strat}. Because NO_2 concentrations are not accessible from satellite measurements, measured total NO_2 SCDs V_{NO_2} are used instead.

The concept of the algorithm then is as follows: first, a set of reference measurements of the ratio z is partitioned in a suitable way in the SZA-V_{NO_2}-plane into a large number of clusters. This allows to further differentiate influences from changes in the stratospheric chemistry governing z from variations in the tropospheric BrO mixing ratio. If the clusters are chosen reasonably small, then variations of z induced by the stratospheric chemistry should be small compared to variations sourced by the measurement uncertainty in the BrO SCD S. Inside each cluster, the ratio z should be approximately Gaussian distributed while measurements with a strong tropospheric BrO signal will skew this distribution towards higher ratios z (see Eq. (7.4)). An accurate determination of the underlying Gaussian distribution should then allow an estimate of the ratio z_{strat}, from which the stratospheric BrO SCD can be calculated. This however requires a sufficiently large number of measurements inside each cluster, in particular to guarantee that only a small fraction of measurements contains a significant tropospheric BrO enhancement. In some sense it is therefore diametrically opposed to the requirements of small clusters for the minimization of variance introduced by stratospheric chemistry, which is why the algorithm settings have to be optimized empirically. While the variability of z induced by stratospheric dynamics and the uncertainty of the BrO measurements are dominating compared to the variance introduced from stratospheric chemistry in most instances, the partitioning into small clusters in the SZA-V_{NO_2}-plane may allow the differentiation of weaker tropospheric BrO enhancements from the stratospheric background. Hence, this can increase the accuracy of the retrieval and allows the detection of smaller tropospheric columns.

Finally, the stratospheric BrO SCD determined in each cluster can then be interpolated

over the whole domain to calculate the stratospheric BrO SCD for all measurements.

For this thesis, the assumptions underlying the concept of the column separation algorithm were reviewed. Several principal component analyses involving a huge range of parameters confirmed the same parameter combination as utilized by Sihler (2012) to be of crucial importance for the total BrO column (and hence also the stratospheric column). This also lead to the exclusion of one further parameter utilized by Sihler et al. (2012). In their implementation, they also sorted measurements into six VZA bins. This was done to avoid strong gradients in the actinic flux over the whole swadth due to the early GOME-2 orbit at 09:30 local time (see section 5.2). Investigations performed for this work showed no further influence of the VZA on BrO columns in the Arctic.

Unfortunately, the assumptions made for the algorithm are not applicable inside the polar vortex and during conditions of stratospheric ozone depletion. The chemical loss of BrO (R38) is altered in the very cold temperatures inside the polar vortex and NO_2 is no longer capable to capture the stratospheric chemistry with acceptable accuracy. Similarly, massive ozone loss, as it is occurring within the polar vortex, destroys the correlation between the stratospheric BrO and O_3 column. For this reason, regions inside the polar vortex have to be excluded from analysis as discussed in section 7.3.2. Furthermore, this also renders the algorithm inapplicable in its current state for an estimation of stratospheric BrO over the Antarctic region for large parts of polar spring, where the polar vortex occurring in springtime is spatially very extended.

The result of the column separation algorithm is illustrated in Figure 7.5.

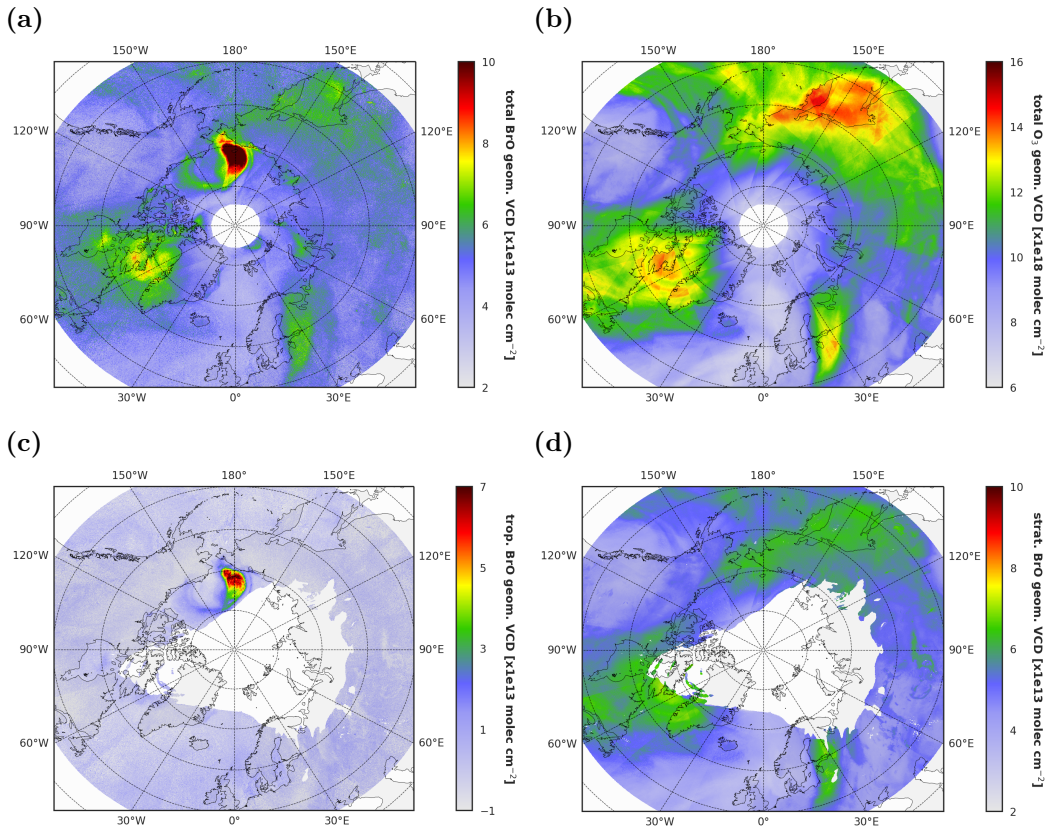

Figure 7.5: *Illustration of the algorithm separating stratospheric and tropospheric partial BrO columns on 19 March 2019. The figure shows different VCDs calculated using a geometric AMF (see Eq. (4.22)): (a) total BrO VCD, (b) O_3 VCD, (c) tropospheric BrO VCD $S_{\mathrm{trop}}$and (d) stratospheric BrO VCD S_{strat}. The coinciding spatial structures in the O_3 VCD and the BrO VCD are noteworthy, which the algorithm identifies as stratospheric dynamics and variations of the tropopause height. Consequently, the enhancements of the total BrO column are attributed to stratospheric BrO at these locations. The large grey area in (c) and (d) corresponds to the location the polar vortex. The decomposition into stratospheric and tropospheric column can fail there, because no clear correlation between the O_3 VCD and the tropopause height is ensured anymore. Note that a geometric AMF is applied here for illustrative purposes. Later a more appropriate tropospheric AMF is applied (Figure 7.14).*

7.3.2 Implementation

This section presents the concrete implementation of the separation algorithm and highlights differences to the method shown in Sihler et al. (2012). The algorithm can be divided into four consecutive steps:

(I) A set of reference measurements for the further processing steps is selected

(II) These measurements are partitioned into appropriate clusters in the SZA-V_{NO_2}-plane

(III) A stratospheric background BrO/O_3 ratio z_{strat} is determined in each cluster

(IV) The stratospheric background is interpolated over the whole domain, allowing the estimation of the stratospheric BrO SCD for all measurements.

This analysis is performed on a daily basis, combining all measurements of one day in order to guarantee for a sufficient amount of measurements without significant tropospheric signal (see also section 7.3.2). Since the stratospheric chemistry usually does not change significantly over the course of one day[1], this "averaging" of stratospheric measurements is justified. This is in contrast to the implementation of Sihler et al. (2012), which had to use data of a seven day period in order to guarantee a similar amount of measurements in each cluster.

Parts of this section are published in Herrmann et al. (2022).

Selection of reference measurements

As a first step a subset of measurements Ω_0 is selected for further processing steps in order to increase the accuracy of stratospheric signals and to avoid interference from anthropogenic NO_2 emissions.

To this end, measurements with a ground elevation above 1000 m and measurements over land masses at latitudes below 73° N are excluded from Ω_0 to account for areas with strong anthropogenic NO_2 emissions such as Norilsk or the oil fields near Prudhoe Bay. Additional selection criteria are listed in the following and only measurement fulfilling all these conditions are taken into account for the further processing:

- a SZA below 87°,
- a fit error of the total BrO column below 5×10^{13} molec cm^{-2},
- an O_4 SCD larger than 6.5×10^{42} molec^2 cm^{-5} (see also section 7.4),
- a non-negative NO_2 VCD smaller than 8×10^{15} molec cm^{-2}.

[1] Keep in mind that TROPOMI is on a sun-synchronous orbit, so it does not see strong variations in daylight over the course of a day.

Furthermore, areas inside the polar vortex are excluded since ozone is depleted in the vortex and consequently the O_3 SCD does not represent a good proxy for stratospheric air anymore. The stratospheric location of the vortex is identified from information on the potential vorticity at two different isentropes at 475 K and 550 K derived from data of the meteorological model ERA5 (see section 6.1). All observations exceeding a potential vorticity of 35 PVU at the 475 K isentrope or 75 PVU at the 550 K isentrope are excluded from further analysis.

These selection criteria are based on Sihler et al. (2012). They are only updated with regards to the SZA: Sihler et al. (2012) implemented an SZA cutoff at 80°, however for the implementation presented here studies showed no significant decrease in the retrieval quality up to 87°. Application of this selection criteria results in approximately 2×10^6 observations for each day of measurements, from which the stratospheric BrO column is estimated. This is approximately a one order of magnitude increase compared to the analysis of GOME-2 data from Sihler et al. (2012).

Clustering of measurements

In this section the segmentation of the reference subset of measurements Ω_0 into clusters is described, which will be used to determine the stratospheric BrO background.

The measurements are partitioned into k subsets of similar size in the plane spanned by the solar zenith angle (SZA) θ and the NO_2 vertical column density V_{NO_2}. If the extent of these cluster is chosen small enough, one can utilize that the stratospheric BrO/O_3 ratio z only weakly depends on θ and V_{NO_2} (Theys et al., 2011; Sihler, 2012) to then distinguish between measurements of z containing a significant troposheric BrO signal and measurements which are primarily stratospheric (see section 7.3.2).

The method used for the segmentation of measurements into clusters is based on the k-means ++ algorithm (Vassilvitskii and Arthur, 2006).

The basic goal of a k-means clustering (e.g. Bock, 2007, and references therein) is to find k cluster centers among a set of n observations, such that the summed euclidean distances from the cluster centers m_j are minimized. The k-means ++ algorithm represents a significant optimization of this fundamental clustering algorithm. Since the specific improvements of this optimization are hard to graph without an understanding of the fundamental algorithm, this section starts with a short description of the so-called naive k-means implementation. This algorithm is initialized by picking k observations at random from the set of n measurements and assigning them as cluster centers m_j. Then, it proceeds in a two-step way:

(i) Assign each observation to the cluster with the nearest center. This means the observation vector x_p is assigned to the cluster S_j which minimizes the cost function

$$L_p = \|x_p - m_i\| \text{ for } i = 1, \ldots, k\,. \tag{7.5}$$

(ii) Update the cluster centers by calculating the centroids for each cluster via the arithmetic mean,

$$m_i = \frac{1}{N_i} \sum_{x_j \in S_i} x_j \,, \tag{7.6}$$

where N_i is the number of observations in the cluster S_i.

These steps are repeated until the cluster center assignments no longer change, i.e. at least a local minimum in the cluster variance is found. Note that *variance* here denotes the within-cluster variance in the SZA-$V_{\mathrm{NO_2}}$-plane, which is unrelated to variance in the $\mathrm{BrO/O_3}$ SCD ratio z, which becomes important later (see section 7.3.2). The algorithm is visualized on a synthetic set of 10^4 randomly generated points in Figure 7.6.

However, this version of the clustering algorithm has one major drawback in the form of the initial random cluster assignment. As pointed out by Vassilvitskii and Arthur (2006), this can lead the algorithm to fall into local minima far away from the global mimimum of the optimal solution. To address this issue, they proposed an alternative initialization procedure denoted as k-means ++, where only one cluster center is chosen at random from the observations. The other centroids are sampled from an empirical distribution of the points contribution to the summed cluster variance.

This clustering algorithm is controlled by the single hyperparameter k determining the number of clusters to which observations are assigned to. In general, the specific choice of hyperparameters for machine learning processes is a complex empirical process and requires iterative tuning of these parameters to optimize model performance. For the purpose of this retrieval algorithm for tropospheric BrO, the parameter range for k is restricted to a certain extent. The size of clusters should not get too large as otherwise variations in z due to changing conditions in the stratospheric chemistry become too large. Likewise, clusters can not get too small as the determination of the stratospheric background ratio z_{strat} requires that only a fraction of measurements contains a significant tropospheric BrO signal (see also section 7.3.2). An empirical hyperparameter tuning revealed that around 100 clusters yielded sufficiently accurate results with approximately 10^4 measurements in each cluster.

Figure 7.7 illustrates the results of the clustering for TROPOMI measurements inside the reference region Ω_0 on 19 March 2019. Note that the algorithm strongly favors a similar numbers of measurements in each cluster, which is why the extent of clusters increases towards the edge of the domain where the density of measurements decreases. In contrast to the implementation of Sihler et al. (2012), no weighting of measurements towards the edge was added as numerical investigations showed that it worsened the overall accuracy of the algorithm.

A major drawback of the k-means ++ clustering is the non-deterministic nature of the algorithm. Even with the improved k-means ++ initialization, the first cluster assignment is still random and not guaranteed to find the optimal clustering. This means that individual cluster assignments can be different for the same data set when comparing two runs of the algorithm. In principle, this could pose a severe problem, especially for smaller data

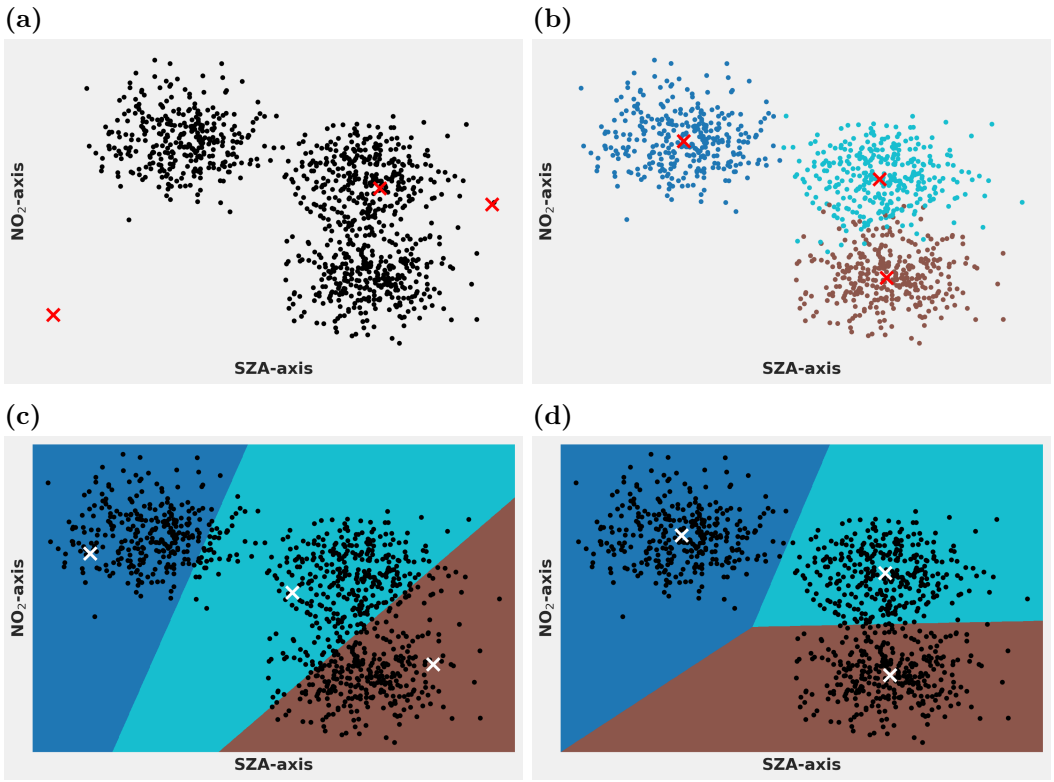

Figure 7.6: *Illustration of the k-means algorithm using a combination of three simulated clustered data sets. Shown are (a) simulated measurements in the SZA-NO_2-plane (black dots) and the initial, random centroids for the k-means algorithm (red crosses), (b) the simulated measurements annotated with their affiliation to the respective simulated cluster (color) with the respective centroids chosen for the data simulation (red crosses), (c) the simulated measurements (black dots) with decision boundaries from the k-means algorithm after the first iteration (color) and the centroids determined by the algorithm (white crosses) and (d) the final prediction of clusters from the k-means algorithm in form of decision boundaries (color) and centroids (white crosses). Note the close resemblance between the "true" clusters and the predicted clusters from the k-means algorithm. Some points in the overlapping clusters on the right are classified wrongly since the k-means algorithm only takes spatial distance and cluster sizes into account.*

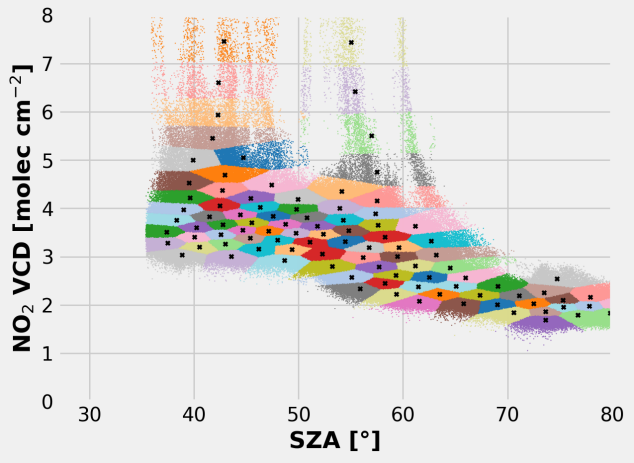

Figure 7.7: *Visualization of the clustering algorithm in the SZA-V_{NO_2}-plane for one day of TROPOMI measurements. The different colors are only for illustration purposes to distinguish the different clusters to which measurements are allocated. The black crosses denote the cluster centers, which are used as nodes of a bilinear interpolation (cf. Figure 7.10).*

sets. Yet the final clusters consist of approximately 10^4 measurements and the cluster assignments themselves will only be used to calculate the nodes for the interpolation of the stratospheric background (see section 7.3.2). Therefore changing the assignments of individual measurements will hardly have any effect on the statistics used for the determination of the interpolation nodes provided that the number of cluster assignment changes are small enough. A numerical analysis for 500 different runs with the final cluster number $k = 100$ showed a maximum relative difference of around 0.5 % between the resulting means of the final clusters.

This resulted in an overall variance of less than 0.1 % on the resulting individual tropospheric BrO observations, which is less than the variance resulting from the arbitrary choice of the cluster number k. It should be noted though that this error is likely to increase as the number of clusters k increases since the number of measurements in each cluster decreases, resulting in less stable statistics (and super Gaussian fit, see section 7.3.2) in each cluster.

Compared to Sihler et al. (2012), the implementation of the clustering of measurements is has undergone drastic changes to be applicable to TROPOMI measurements. Previously, the partitioning of measurements was achieved by an iterative shift of the decision boundaries as described in the appendix in Sihler et al. (2012). The replacement of this approach by a k-means ++ algorithm has the following advantages:

- The new implementation of the clustering automatically minimizes within-cluster variance, which effectively increases the accuracy of the estimation of the stratospheric mode in each cluster as described in the next section.

- Related to that, the number of hyperparameters was reduced to only one, namely k as the number of clusters. In contrast, the old algorithm had to make additional empirical inferences, e.g. the incremental changes per iteration to partiton the data,

whereas the new version of the clustering does not need any additional input besides the amount of clusters.

- The new clustering is less susceptible to hyperparameter changes, i.e. changes in the number of clusters. Whereas changes to the number of clusters could induce a variance in the retrieved tropospheric BrO of up to 10 % for the old algorithm, the new version only introduces a variance of about 1 % to 2 % for a sensible parameter range (25-500 clusters). This means that the number of clusters does not need to be tuned as precisely, although this is resulting in part from the increased number of measurements from TROPOMI and therefore the better statistics per cluster.
- The runtime complexity was reduced by $\mathcal{O}(n^2)$ to $\mathcal{O}(n \log n)$. Considering the large increase in measurements each day, this reduction in computational complexity represents a large improvement in performance of the algorithm. After applying the aforementioned selection criteria (see section 7.3.2), the number of measurements to process each day is approximately 50 times larger than for GOME-2.

Lastly, the implementation of Sihler et al. (2012) required a division of the measurements into viewing zenith angle (VZA) bins to accurately retrieve the stratospheric BrO SCD. This is no longer necessary for this implementation of the algorithm, however this is not due to inherent improvements in the algorithm itself but rather due to specifics of TROPOMI. While for GOME-2 a weak dependence on the VZA was detected, this was no longer the case for TROPOMI (see section 7.3.1). This can probably be ascribed to the different equator crossing times of the two satellite instruments. MetOp-A has an equator crossing time of 9:30 h local solar time (see section 5.2) and at that time the edges of the swath may exhibit greater variance in the actinic flux (Sihler et al., 2021).

Determination of stratospheric BrO/O_3 ratio in each cluster

As a next step, for each cluster of measurements in the SZA-V_{NO_2}-plane the stratospheric mode of the BrO/O_3 SCD ratio is determined. Variations of this ratio over the observations of one day should mostly be sourced by changes in the stratospheric chemistry for different measurements as described in section 7.3.1. The fundamental idea is then that conditions affecting the ratio of SCDs (or simply put, the mixing ratio of stratospheric BrO) are comparable for all measurements partitioned together in one cluster (if the clusters are chosen small enough) and consequently, variations from changes in the stratospheric chemistry are minimized. This implies that a purely stratospheric signal of the ratio z will be dominated by the uncertainty in the retrieved ratio. Because the uncertainty in BrO is far larger than for O_3, this means that z containing only stratospheric signals will be dominated by the error in the measurement of the total BrO column (see section 7.5).

For this reason, the BrO/O_3 SCD ratio should exhibit an approximate Gaussian distribution,

$$\phi(x) = \frac{1}{\sqrt{2\pi}} e^{-\frac{1}{2}\left(\frac{x-\mu}{\sigma}\right)^2} . \tag{7.7}$$

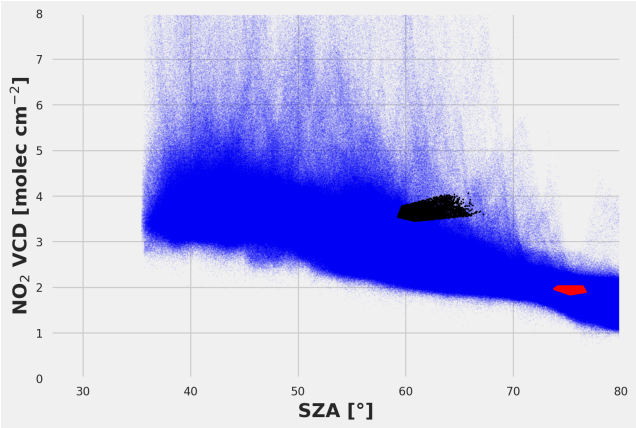

Figure 7.8: *Illustration of two specific clusters in the SZA-V_{NO_2}-plane for the same set of measurements as in Figure 7.7 on 19 March 2019. The dots marked in black correspond to the histogram Figure 7.9a, the BrO/chO3 ratios of the observations marked in red are shown in Figure 7.9b.*

Tropospheric enhancements of BrO will skew this distribution towards the right, which can be written in the form of $f(x) = \phi(x)\gamma(\alpha x)$, with γ describing the asymmetry and α as skewness parameter. Determining the mean μ of the underlying Gaussian distribution $\phi(x)$ therefore allows an approximation of the stratospheric BrO signal in each cluster, provided that a significant fraction of measurements in a cluster is still dominated by the stratospheric signal. This also explains why a large number of measurements in each cluster is required for the algorithm.

The determination of the peak of the distribution used to calculate the stratospheric mode was previously performed via an iterative cropping of distribution until a certain skewness threshold was achieved (Sihler et al., 2012). The problem with this approach was the calculation of the distribution mean σ via the arithmetic mean, which only holds if the distribution is indeed Gaussian. To reduce the systematic error from deviations from this assumption, also measurements on the left tail of the distribution were cropped. However, TROPOMIs higher SNR lead to a reduction in the variance of the distribution compared to GOME-2 and this approach lead to a systematic overestimation of the mean μ, especially for clusters with only weak tropospheric enhancements.

For this reason, this algorithm was also updated. To this end, an asymmetric super-Gaussian (Beirle et al., 2017),

$$S(x) = A(w,\, k) \times e^{-\left\| \frac{x}{w} \right\|^k}, \tag{7.8}$$

is fitted to the distribution using a standard least squares fit. Some parameters of this Gaussian were empirically tuned. The left half of the super-Gaussian is chosen to correspond to a regular Gaussian while the right half is allowed to vary to represent the introduced by enhanced tropospheric BrO SCDs. This results in an improved fit of the underlying Gaussian $\phi(x)$ (see Figure 7.9) compared to the implementation of Sihler et al. (2012). The peak of

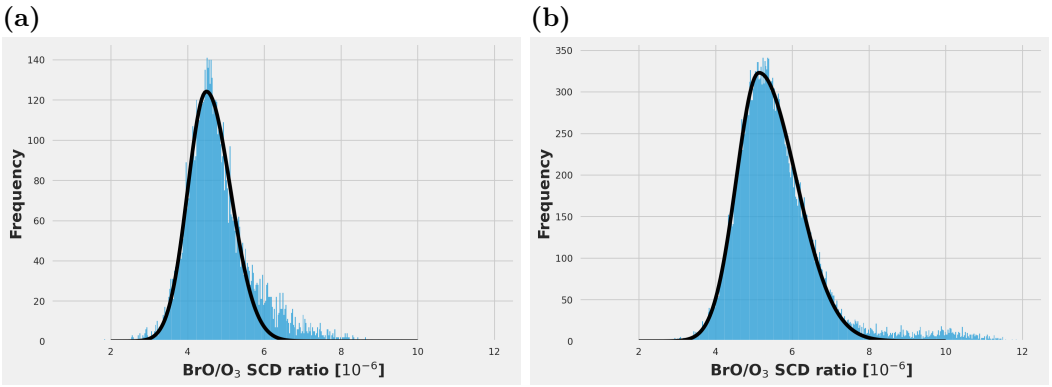

Figure 7.9: *Distribution of measured BrO SCD to O_3 SCD ratios in the example clusters visualized in Figure 7.8. The algorithm fits an asymmetric super Gaussian (black) to the distributions in each cluster. The mean of this super Gaussian is assumed to represent the stratospheric mode for this particular combination of parameters representing the stratospheric chemistry while the standard deviation furnishes an error estimation for the stratospheric correction. The distribution shown in (a) corresponds to the black cluster in Figure 7.8 and shows a larger number of measurements slightly enhanced in z while the distribution in (b) corresponds to the red cluster in Figure 7.8. It shows a larger skewness towards the right with a small number of measurements exhibiting significantly enhanced ratios z.*

the fitted super-Gaussian (described by w) in a cluster n is then assumed to approximate the ratio of the SCDs of stratospheric BrO and ozone $\mu_{z,n}$, while its standard deviation $\sigma_{z,n}$ is utilized as estimate for the uncertainty of the determined stratospheric mode (see also section 7.5).

As an example, Figure 7.8 shows the same data set of $\mathrm{BrO}/\mathrm{O_3}$ SCD ratio z as Figure 7.7 with two clusters highlighted. The application of the stratospheric mode algorithm in these two clusters is exemplified in Figure 7.9.

Interpolation of stratospheric ratio to whole domain

In a last step, the stratospheric backgrounds $\mu_{z,n}$ as well as the uncertainty estimations $\sigma_{z\,n}$ calculated for each cluster are mapped to the respective cluster centers. The resulting triplets (θ_n, $V_{\mathrm{NO_2},n}$, $\mu_{z,n}$) respectively (θ_n, $V_{\mathrm{NO_2},n}$, $\sigma_{z,n}$) are then used as support for a bilinear interpolation over the whole domain, yielding two surfaces $z_{\mathrm{strat}}\left(\theta, V_{\mathrm{NO_2}}\right)$ and $sigma_{\mathrm{z}}\left(\theta, V_{\mathrm{NO_2}}\right)$. From these the SCD of stratospheric BrO and the corresponding uncertainty can be calculated from

$$S_{\mathrm{strat}} = z_{\mathrm{strat}}(\theta, V_{\mathrm{NO_2}}) \cdot S_{\mathrm{O_3}} \tag{7.9}$$

$$\sigma_{\mathrm{strat}} = sigma_{\mathrm{z}}(\theta, V_{\mathrm{NO_2}}) \cdot S_{\mathrm{O_3}}\,. \tag{7.10}$$

An exemplary interpolation for 19 March 2019 is illustrated in Figure 7.10 with the resulting stratospheric and tropospheric BrO VCD for the same day being shown in Fig-

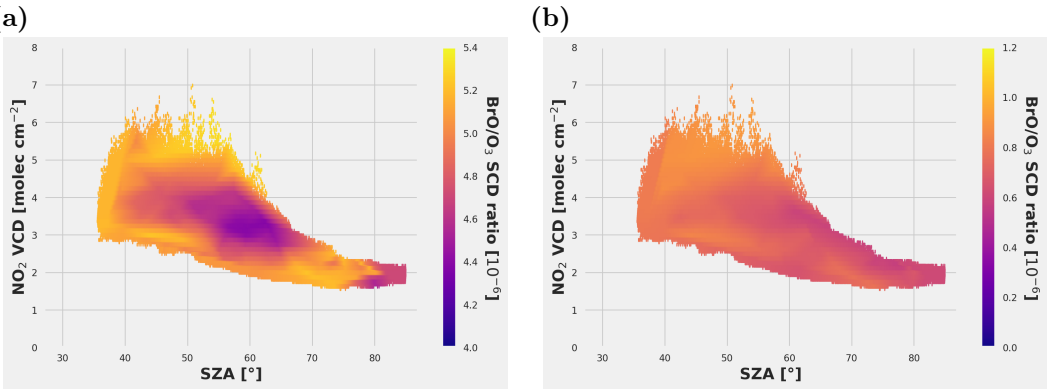

Figure 7.10: *Interpolation of the (a) BrO/O_3 stratospheric SCD ratio z_{strat} and (b) the corresponding error σ_{strat} over all measurements in the SZA-V_{NO_2}-plane for 19 March 2019. The nodes of the interpolations are the cluster centers determined in the clustering process as shown in Figure 7.7. Note that measurements in this figure are binned for the purpose of visualization. Measurements near the edge of the domain are outside of the convex hull for the linear interpolation and are interpolated by a nearest neighbor interpolation.*

ures 7.5c and 7.5d. Note that approximately 1 % of all measurements are outside the convex hull of the triangulation for the bilinear interpolation. These measurements are interpolated using a nearest neighbor interpolation instead.

Lastly, it should be noted that the implementation of this step of the algorithm is unchanged to the implementation of Sihler et al. (2012).

7.3.3 Validation of the algorithm using simulated data

The accuracy of the algorithm presented in the previous section has already been validated in a previous study (Sihler et al., 2012). Although the fundamental idea of the stratospheric correction approach did not change, major parts of the algorithmic implementation have been changed. Both the clustering of measurements 2D bins as well as the identification of the stratospheric measurements have undergone significant changes compared to Sihler et al. (2012). This section presents an application of the full algorithm to a synthetic data set in order to benchmark the numerical performance of the changed implementation, to compare its performance to the previous implementation by Sihler et al. (2012) and to estimate potential systematic errors introduced in the stratospheric correction.

Because the true stratospheric column S_{strat} is not known, a set of simulated measurements based on mathematical distributions is used. This data set is based on an artificial data set used by Sihler et al. (2012) to ensure optimal comparability of the results. It is chosen empirically to resemble the distribution seen in real measurement data without any a priori knowledge of the chemistry or radiative transfer. The surface

$$z_m = a\, x\, \cos y\, \pi + b\,, \tag{7.11}$$

is assumed to describe the ratio between the stratospheric BrO SCD and the O_3 SCD z

in the SZA-V_{NO_2}-plane (see Figure 7.11a). It is dependent on the normalized coordinates $x = (\theta - 30°)/50°$ and $y = V_{NO_2}/8 \times 10^{15}\,\mathrm{molec\,cm^{-2}}$. The parameters in Eq. (7.11) are chosen as $a = 5 \times 10^{-7}$ and $b = 4.9 \times 10^{-6}$. From this triplets (z, x, y) used for the benchmark are then generated using three overlapping multivariate normal distributions to capture correlation between the SZA and NO_2 parameters. As mentioned, the parameters of the normal distribution are chosen such that the resulting distribution (see Figure 7.11b) resembles the distribution seen in real measurements (e.g. Figure 7.7).

As a next step, deviations from the "true" stratospheric ratios z are then added to each triplet (z, x, y) in the form of statistical uncertainties and tropospheric BrO enhancements of the total column. The statistical uncertainties are described by a normal distribution centered around 0 with standard deviation $\sigma_{stat} = 4 \times 10^{-7}$ which is added to every value of z. In contrast, the tropospheric contribution are added to only 15 % of measurements and are normally distributed around $\mu = 1.5 \times 10^{-6}$ with standard deviation $\sigma_{trop} = 1.5 \times 10^{-6}$. Figure 7.11d shows the resulting distribution of z (after application of the clustering) in a single cluster centered at $\theta = 80.2°$ and $V_{NO_2} = 2.1\,\mathrm{molec\,cm^{-2}}$.

The results of the application of the separation algorithm are compiled in Figure 7.11. The difference between the simulated surface z_m (see Eq. (7.11) and Figure 7.11a) and the retrieved surface z' (see Figure 7.11c) is illustrated further in Figure 7.12. There are residual linear structures seen in the difference of the surfaces (Figures 7.12a and 7.12b) caused by the inability of the bilinear interpolation (see section 7.3.2) to capture the non-linear structures of Eq. (7.11). Yet the deviations between retrieved and modeled stratospheric ratios are very small as demonstrated also in Figure 7.12c, which shows the relative error below 2 % for all triplets and lower than 1 % for more than 95 % of triplets. A comparison of Figures 7.12b and 7.12d also demonstrates that the error estimated by the algorithm (which is mainly dominated by the uncertainty in the retrieved trace gas SCDs, see section 7.5) greatly exceeds systematic errors of the stratospheric corrections.

In conclusion, the new implementation of the column separation algorithm is capable to reproduce a modeled surface used as proxy for the stratospheric BrO/O_3 SCD ratio within a typical SZA-NO_2 sampled area. Furthermore, this also demonstrates a strong improvement in the accuracy of the retrieval compared to Sihler et al. (2012), since errors are approximately three times lower on the same synthetic dataset using the new implementation.

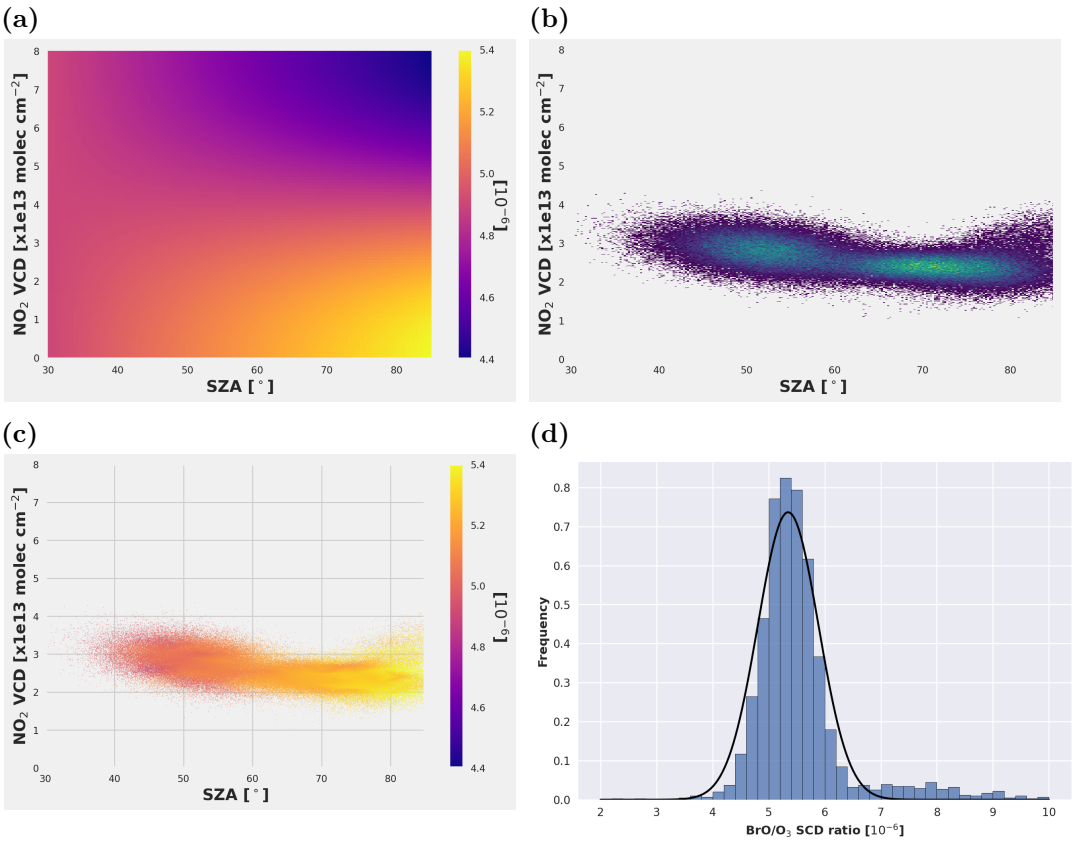

Figure 7.11: *Results of a validation study of the column separation algorithm from simulated measurements. The figure shows (a) the simulated stratospheric BrO/O_3 SCD ratio as function of the SZA and NO_2 VCD as described by Eq. (7.11), (b) the distribution of simulated measurements in the SZA-V_{NO_2}-plane generated from three normal distributions (the color is an indication for the number of measurements), (c) the resulting interpolated stratospheric ratio z' computed by the separation algorithm and (d) the exemplary application of the stratospheric filter in a single cluster.*

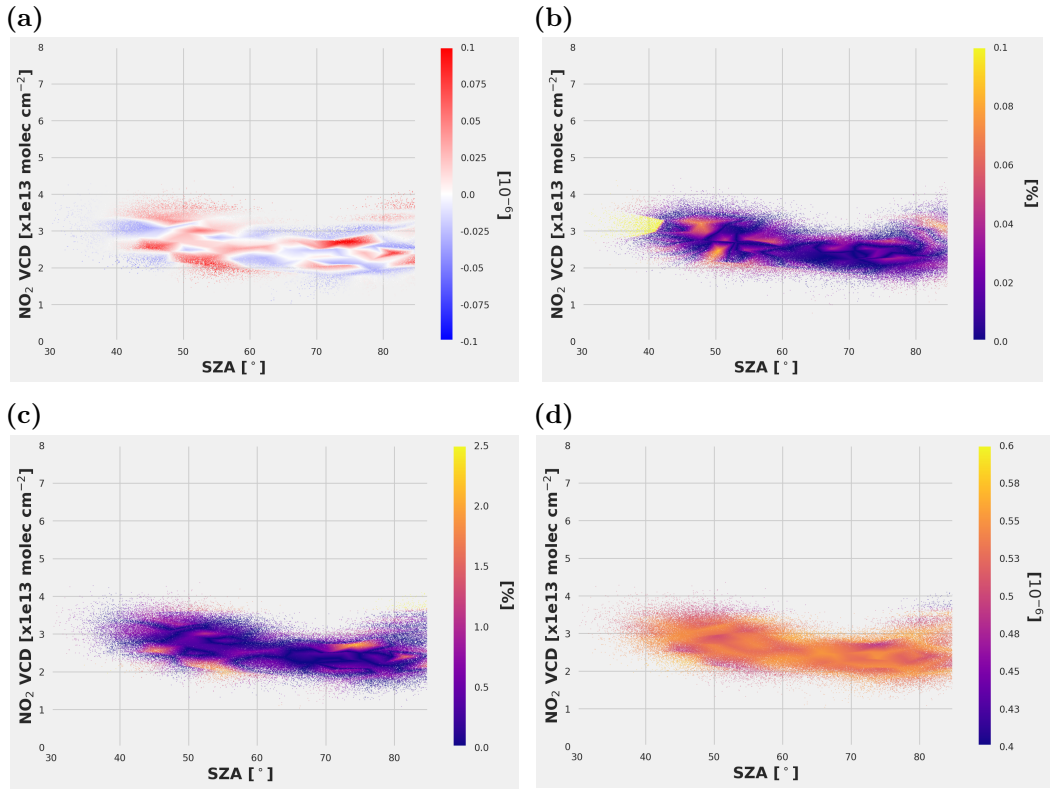

Figure 7.12: *Resulting differences between the "true" stratospheric ratio z and the stratospheric ratio computed by the column separation algorithm z'. Shown are (a) the difference between the true and retrieved ratio, (b) the absolute difference between true and retrieved ratio, (c) the relative error between true and retrieved ratio and (d) the error of the stratospheric ratio estimated by the separation algorithm.*

7.4 Tropospheric air mass factors

This section presents the method to deduce the AMF for the conversion of the tropospheric slant column to a vertical column. As a byproduct, the method also allows the classification of observations as either *sensitive* to near-surface BrO or *possibly obscured*.

As it was already discussed in section 7.4.1, the precise determination of (Box-)AMFs is a non-trivial problem. Especially for tropospheric trace gases (or the partial tropospheric column of a trace gas), this can become very complex. The sensitivity towards such absorbers can be strongly influenced by a range of different properties, such as surface albedo, cloud coverage, tropospheric aersols and the vertical trace gas profile (see Table 4.1). The UV measurements in arctic regions presented in this work are affected by this in particular for two reasons.

On the one hand, measurements in the UV/vis are more heavily influenced by scattering than measurements at larger wavelengths, i.e. near-infrared (NIR) or shortwave infrared (SWIR). The λ^{-4} dependence of Rayleigh scattering (see section 4.2) implies a higher influence of scattering on UV measurements.

On the other hand, the polar regions exhibit a specific radiative transfer originating in the snow/ice coverage of the region, which entails a high surface albedo. While this alone already renders it more likely that a photon measured by the satellite instrument has indeed reached the ground, the sensitivity towards trace gases near the surface is further increased over bright surfaces by the larger Rayleigh scattering cross section in the UV, which leads to multiple scattering in the troposphere (Rozanov and Rozanov, 2010). The increase in sensitivity from high surface albedo generally even outweighs the comparatively large optical thickness due to Rayleigh scattering at large SZAs in the arctic (Wagner, 2000). To a large extent, this holds true even for cloudy scenes, however, optically thick clouds reduce the sensitivity substantially even over bright surfaces.

For these reasons, accurate input information (see Table 4.1) for the RT simulations is crucial. However, data on several of these parameters are difficult to obtain, especially at TROPOMI's high spatial resolution.

Several cloud products have been developed for TROPOMI yielding information on the Cloud Top Height (CTH), the Cloud Fraction (CF), Cloud Optical Density (COD) and combinations thereof (e.g. Wang et al. (2008); Veefkind et al. (2016); Loyola et al. (2018, 2021); Sihler et al. (2021); Compernolle et al. (2021)). Yet most of the cloud algorithms to date are based on the identification of either white (color) or bright (reflectivity) surfaces. Snow-covered land and ice are particularly challenging for these algorithms, as it becomes difficult to distinguish between brightness from snow, thick aerosol layers, water clouds and ice clouds (Vasilkov et al., 2010). Most algorithms, such as the Fast Retrieval Scheme for Clouds (FRESCO) (Wang et al., 2008), which is used for the TROPOMI L2 NO_2 product (Van Geffen et al., 2022), utilize snow and ice masks from ECMWF to distinguish between snow- and snow-free scenes and their performance above bright surfaces is usually poor (e.g. Latsch et al., 2022).

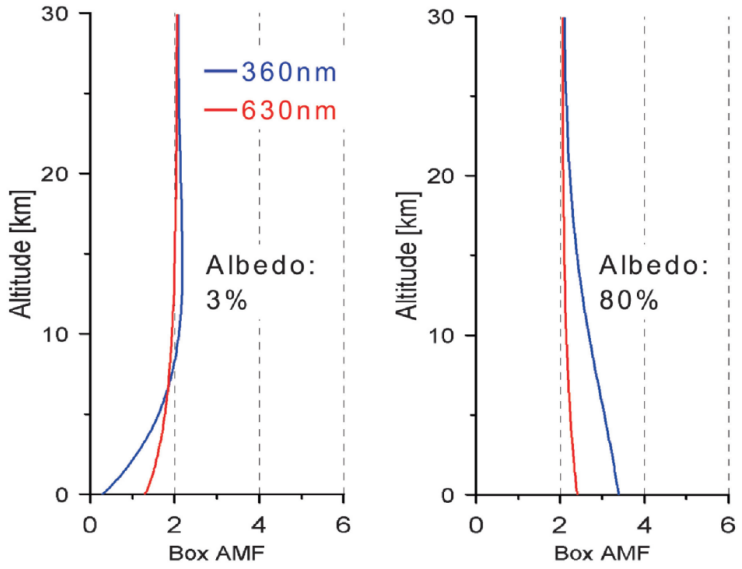

Figure 7.13: *Influence of the surface albedo on the Box AMF at different heights for different wavelengths. For shorter wavelengths, the larger extinction from Rayleigh scattering reduces sensitivity towards the surface for a low albedo and increases it for a high albedo. Figure adapted from Richter and Wagner (2011).*

In contrast, the method presented here relies on proxies to capture the influence of these parameters on the RT and hence on the AMF of tropospheric BrO based on Sihler et al. (2012). The concept of this method will be introduced in section 7.4.1. In section 7.4.2, the concrete implementation will be described and differences to the method of Sihler et al. (2012) will be discussed.

7.4.1 Concept

Information on the observational viewing geometry are readily available from the satellite measurements and surface elevation levels are known with high accuracy and spatial resolution. However, information atmospheric properties critical to RT are sparse as discussed. This work utilizes a method introduced in Sihler et al. (2012), estimating the influence of clouds, aerosols and surface albedo from measured O_4 SCDs and reflectances.

As discussed, existing cloud retrieval algorithms are ruled out for the work presented here. Nevertheless, the use of O_4 as tracer for the retrieval of cloud information has been widely used. This can be attributed to the fact that its absorption scales with the squared oxygen density (e.g. Greenblatt et al., 1990; Pfeilsticker et al., 1999). On the one hand, the vertical profile of O_2 is well known, meaning that the detected amount of O_4 allows inference on the pressure of the cloud (or more generally, reflecting surface). On the other hand the proportionality to the squared O_2 density increases its sensitivity towards the lower altitudes in the atmosphere, helping for example in detection of lower clouds and providing a better sensitivity to near-surface absorbers in comparison to O_2.

For this work, the O_4 AMF is used to approximate cloud information as well as sensitivity

near the surface. It is calculated from the measured O_4 SCD S_{O_4} and a profile, from which the VCD $V_{O_4}$is calculated on a per-pixel basis.

Additionally, measurements of the O_4 SCD require a scaling factor of about 0.75-0.89 to reproduce the SCD predicted by RT models (Wagner et al., 2009b; Clémer et al., 2010). This will also be applied here using a factor of 0.8 following Wagner et al. (2009b), giving for the O_4 AMF A_{O_4},

$$A_{O_4} = 0.8 \cdot \frac{S_{O_4}}{V_{O_4}} \,. \tag{7.12}$$

The reflectance R is used as proxy for the surface albedo. It is defined as

$$R = \frac{I}{I_0} \cdot \frac{\pi}{\cos\theta} \,, \tag{7.13}$$

with I the Top Of the Atmosphere (TOA) radiance, I_0 the solar irradiance and θ describing the SZA.[2] The reflectance is simulated (and calculated from measured radiances) at a wavelength of 372 nm. This minimizes interferences with trace gases like O_4 absorbing in the same range.

In particular the combined use of both parameters allows a good approximation of the atmospheric information important for the radiative transfer. For example, high reflectance could not only result from a high surface albedo but also be the result of an optically thick cloud. In such a scenario, the satellite would be effectively blind to the surface layer, nevertheless the assumption of high albedo could lead to the conclusion that sensitivity to ground is high. In this case however, the O_4 absorption would also be low, resulting in a low retrieved O_4 SCD. The discrepancy allows the distinction between clear-sky, high albedo and cloudy-sky scenarios.[3]

At the same time, the approximation of the surface layer BrO AMF from the O_4 AMF worsens for a low albedo scenario as discussed in section 7.5. Such a scenario should then be captured by a low reflectivity.

Previous measurements detected a major fraction of the enhanced tropospheric BrO located in the BL, most often very close to the surface (e.g. Hönninger et al. (2004); Wagner et al. (2007); Pöhler et al. (2010); Prados-Román (2010); Frieß et al. (2011)). These findings are also supported by results of the WRF-CHEM model used in this work.

Therefore, following the suggestions of Sihler et al. (2012), a box profile for the lowest 500m is used as BrO profile in the RT simulations. This choice of layer height represents an average of the layer height found in previous studies, see Table 7.2. However, sensitivity studies have shown that the influence of the specific choice of the layer height is very small, which will be discussed in more detail in section 7.5. The corresponding AMF for the tropospheric BrO will therefore be denoted as the AMF of the chemically disturbed boundary layer A_{BL}.

[2] Note that this is the quantitiy McArtim yields as result of its RT simulations as discussed in section 4.5, normalized by its SZA dependence.

[3] This assumption does not hold if the cloud is very low, which would still allow a signifcant O_4 absorption to be detected. This scenario will be discussed later.

With these assumptions, the idea is to model triplets of $\left(R, A_{O_4}, A_{BL}\right)$ for a comprehensive set of cloud/aerosol scenarios and surface albedos using McArtim (see section 7.4.1). This is done for a range of different observational geometries, each of which using the modeled values for a study of the interrelation between the different parameters. The aim is to understand the conditions under which the sensitivity towards the surface drops below a certain threshold A_{BL}^{min}. This condition is approximated geometrically with the corresponding parameters getting stored in Look-Up Tables (LUTs) for each discrete observation geometry, allowing a classification of measurements based on their sensitivity towards near surface BrO.

Additionally, the functional relationship between the the BrO AMF and the proxies are approximated by a multilinear function derived via a least-square fit, using only values corresponding to RT scenarios deemed to be sensitive to the surface layer in the previous step,

$$A_{BL}(R, A_{O_4}) = a + b \cdot R + c \cdot A_{O_4}\,. \tag{7.14}$$

The fitted parameters are also stored in LUTs in analogy to the geometrical sensitivity parameters and will be used to calculate tropospheric AMFs. The algorithm is illustrated in Figure 7.14.

The concrete implementation of the concept presented here will be discussed in the next section. However, the performance of this algorithm relies on the validity of the underlying assumptions regarding the proxy parameters. The choice of the layer height respectively BrO profile could vary, possibly inducing errors on the retrieved AMF. It is also necessary to study the influence of the different profile shapes of BrO and O_4 as well as the influence of clouds on the assumed cloud proxy O_4. This will be discussed in section 7.5.

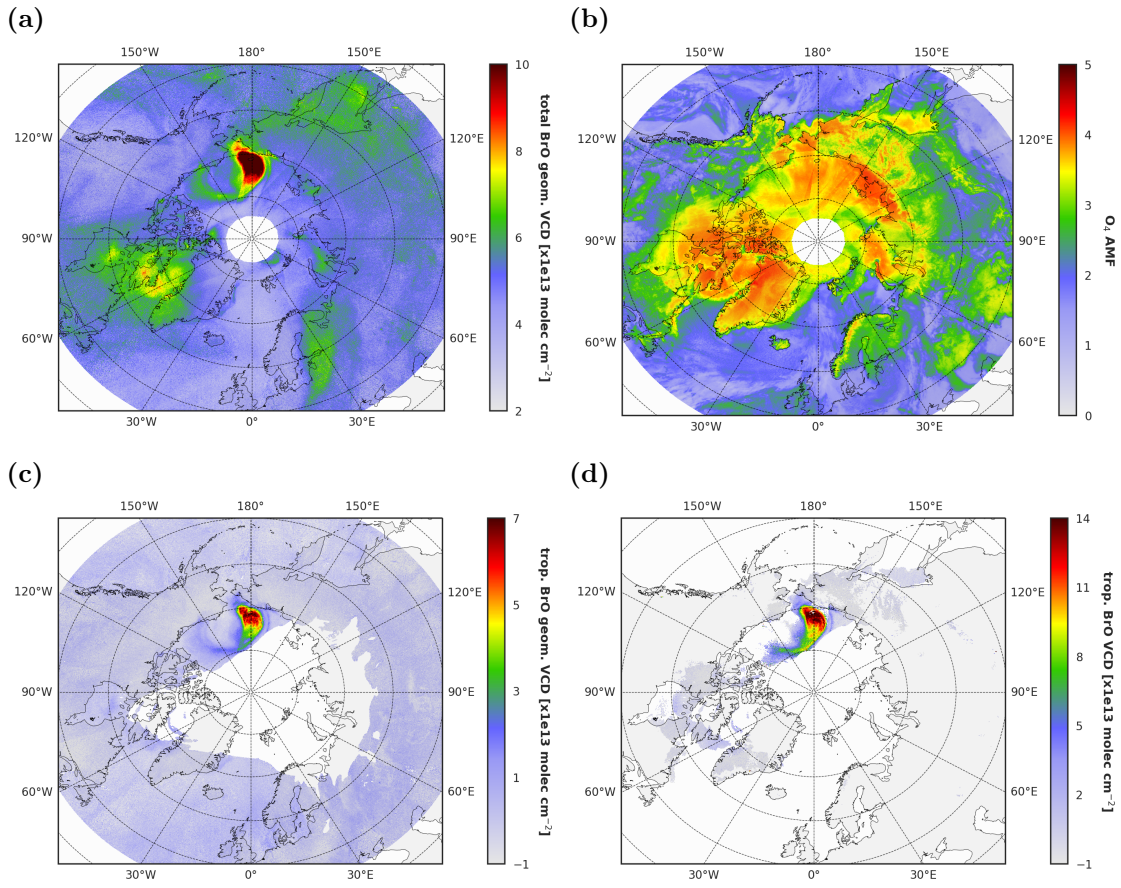

Figure 7.14: *Illustration of the surface sensitivity classifier and the calculation of tropospheric AMFs on 19 March 2019 (same as in Figure 7.5). The figure shows (a) total BrO VCDs calculated from a geometrical AMF, (b) O_4 AMFs calculated from measured SCDs and a standard O_4 profile, (c) tropospheric BrO VCDs calculated from a geometrical AMF and (d) tropospheric BrO VCDs calculated using the AMF determined in the algorithm. Areas where measurements are probably not sensitive are left in gray. Note that the locations of the sensitive measurements coincide with regions of enhanced O_4 AMFs. However, the inclusion of reflectance measurements causes some measurements with high O_4 AMF to be classified as possibly obscured too.*

Table 7.2: *Height of the chemically perturbed surface layer in polar spring from selected publications. Table and caption adapted from Sihler (2012).*

reference	height of surface layer	species	method
Anlauf et al. (1994)	50 - 400 m	O_3	ozonesonde
Solberg et al. (1996)	3000 - 4000 m	O_3	ozonesonde
Wessel et al. (1998)	500 - 1000 m	O_3	ozonesonde
Bottenheim et al. (2002)	100 - 1400 m	O_3	ozonesonde
Tarasick and Bottenheim (2002)	50 - 2000 m	O_3	ozonesonde
Hönninger and Platt (2002)	500 - 1500 m	BrO	MAX-DOAS
Hönninger et al. (2004)	1000 m	BrO	LP-/MAX-DOAS
Frieß et al. (2004)	1500 m	O_3	ozonesonde
Wagner et al. (2007)	$<$ 1000 m	BrO	MAX-DOAS
Prados-Roman et al. (2011)	1000 m	BrO	AMAX-DOAS
Frieß et al. (2011)	500 m	BrO	MAX-DOAS
Seabrook et al. (2011)	200 - 600 m	O_3	O3-DIAL

7.4.2 Implementation

In this section, the concrete algorithmic implementation of previously described concept will be described. The algorithm consists of four steps for each set of viewing geometries:

(I) modeling the AMF for tropospheric BrO A_{BL} and the accompanying proxies R and $A_{\mathrm{O_4}}$ for a set of different RT scenarios,

(II) interpolating additional RT scenarios accounting for gradients in the surface albedo and cloud coverage assuming the independent pixel approximation,

(III) establishing a classifier to flag possibly obscured RT scenarios via geometric approximation of the (R, $A_{\mathrm{O_4}}$) exceeding the boundary layer AMF threshold $A_{\mathrm{BL}}^{\mathrm{min}}$,

(IV) bilinearly fit Eq. (7.14) using only RT scenarios deemed to be unobstructed by the classification established before and store all parameters, the fit parameters as well as the geometric approximation parameters, in a LUT. This LUT is then used to interpolate the parameters for specific observational viewing geometries to decide if a measurement is sensitive to the surface and calculate the corresponding AMF.

In the following, these steps will be discussed in detail.

Table 7.3: *Simulated layers of scattering media (aerosol/clouds) defined by their vertical extent and optical density.*

Parameter	Node	
	Aerosol/cloud layer extent [km]	Optical depth
Aerosol/cloud scenario	0-1	1,3, 10, 20, 50
	1-2	1,3, 10, 50
	3-4	10, 50
	7-8	1, 3, 10, 50
Surface albedo	0.03, 0.09, 0.24, 0.39, 0.54, 0.66, 0.78, 0.90, 0.96	

Table 7.4: *Summary of all simulated viewing geometries (see section 5.3) in the RT simulations.*

Parameter	Node
SZA [°]	10, 28, 44, 56, 64, 66, 68, 72, 76, 80, 82, 84, 86, 88
VZA [°]	0, 16, 32, 48, 56, 64, 68, 70, 76
RAA [°]	0, 20, 32, 36, 40, 44, 48, 52, 56, 60, 64, 68, 72, 108, 112, 116, 120, 124, 128, 132, 136, 140, 144, 148, 160, 180
Elevation [km]	0, 1, 2, 3, 4, 5, 6

(I) Using McArtim (see section 4.5 and Deutschmann et al. (2011)), the reflectance R, the O_4 AMF $A_{\mathrm{O_4}}$ and the boundary layer BrO AMF A_{BL} are simulated for different

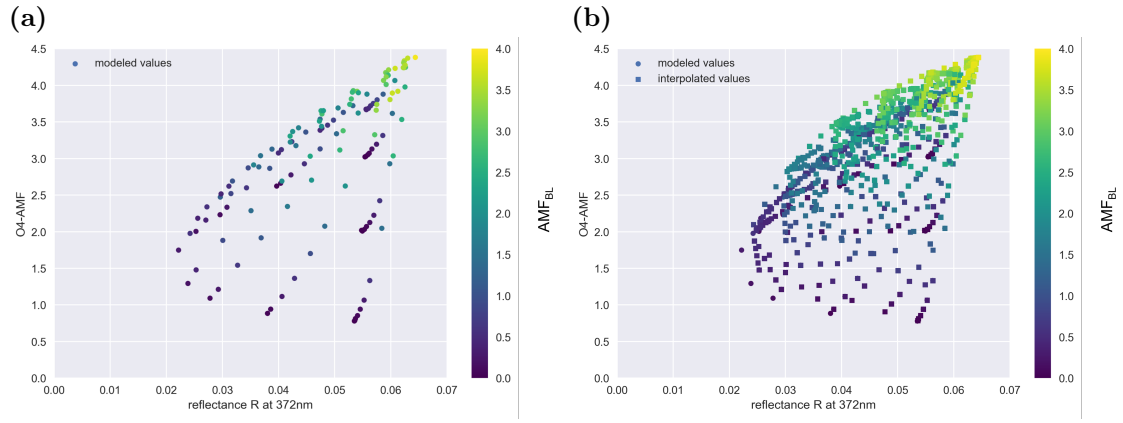

Figure 7.15: *(a) Results of the radiative transfer simulation for a nadir viewing geometry at SZA= 66°. (b) Interpolated triplets* $(R, A_{O_4}, A_{\mathrm{BL}})$ *accounting for gradients in surface albedo and cloud coverage in one pixel for the same viewing geometry. Figures based on Sihler et al. (2012).*

aerosol/cloud scenarios and surface albedos, depicted in Table 7.3. The two different AMFs are simulated at a wavelength of 360 nm, while the reflectance is simulated at 372 nm to minimize interferences with atmospheric absorptions. The scattering media (aerosol/clouds) in the model atmosphere is parametrized by the cloud top height (CTH) and the cloud optical density (COD). It is always modeled as a single layer with a geometrical thickness of 1 km containing particles with a scattering albedo of 1.0 and Henyey-Greenstein asymmetry parameter of $g = 0.85$ (King, 1987). The scenarios for the two lower layers were designed to approximate typical arctic aerosol/cloud scenarios, such as blowing snow. The layer between 3 km to 4 km is designed to capture the influence of a low, optically dense cloud, potentially not detected by the use of the O_4 AMF, discussed in more detail in section 7.5. The upper layer simulates typical aerosol/cloud scenarios.

There are also 9 different settings for the surface albedo, ranging from very dark surface to very bright surfaces, and 15 different aerosol/cloud scenarios, resulting in a total of 135 different simulations.

These simulations are done for a total of 22932 viewing geometries defined by the angles describing the sun-target-satellite constellation (see section 5.3) and the surface elevation, shown in Table 7.4. The 135 different RT scenarios are then stored in a LUT spanned by the viewing geometries, resulting in a distinct RT "profile" for each viewing geometry. As an example, the results for one specific nadir looking viewing geometry at an SZA of 60° is depicted in Figure 7.15a.

Additional viewing geometries (especially more VZA and RAA nodes) have been added compared to Sihler et al. (2012) to account for TROPOMI's higher pixel density and larger swath.

(II) A single satellite observation measures over a spatial extent which might exhibit a gradient in either surface albedo, which is typical i.e. for ice-edges over oceans, cloud cov-

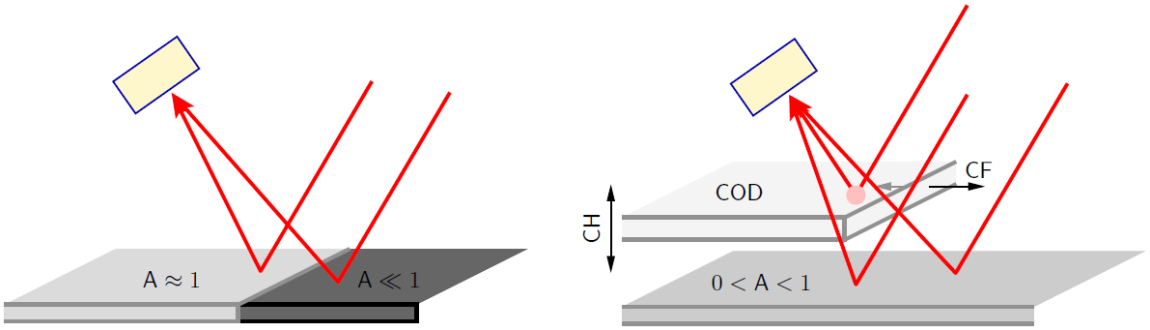

Figure 7.16: *Illustration of the gradient interpolation under the independent pixel approximation. Assuming the influence of light from neighboring pixels is negligible, gradients in the surface albedo (left) and cloud coverage (right) can be approximated from Eq. (7.15). The surface albedo is characterized by its albedo* A*, which is varied by high albedo fraction* ξ_s*. Meanwhile, a cloud layer is characterized by the layer height and the optical density of the cloud. For cloudy scenarios, the effective cloud fraction* ξ_c *is varied to account for partial cloud coverage. Figures adapted from Sihler et al. (2012).*

erage, also denoted as cloud fraction, or a combination thereof. For this reason, further RT scenarios are interpolated from the simulated values. This also has the benefit of improving the accuracy of the parametrization in the next steps with an increase in the number of scenarios.

It is assumed that the radiative properties of one pixel may be considered in isolation from its neighboring pixels. This is called the independent pixel approximation (e.g. Zuidema and Evans (1998); Martin et al. (2002)) and allows the effective application of 1D RT also for scenarios with horizontal gradients. Under this assumption, the effective reflectance is the weighted average of a cloudy and clear-sky part or respectively a low and high albedo part of the pixel,

$$R(\xi_s) = (1 - \xi_s)\, R_{\text{low}} + \xi_s\, R_{\text{high}} \tag{7.15}$$

$$R(\xi_c) = (1 - \xi_c)\, R_{\text{clear}} + \xi_c\, R_{\text{cloud}}\,, \tag{7.16}$$

with ξ_s describing the effective fraction of high surface albedo and ξ_c as effective cloud fraction. The wavelength dependence of the reflectance R is dropped here, since this algorithm always uses reflectances determined at 372 nm as discussed.

The resulting gradient affected AMFs can then be calculated as follows:

$$A(\xi_s) = \frac{(1 - \xi_s)\, R_{\text{low}}\, A_{\text{low}} + \xi_s\, R_{\text{high}}\, A_{\text{high}}}{(1 - \xi_s)\, R_{\text{low}} + \xi_s\, R_{\text{high}}} \tag{7.17}$$

$$A(\xi_c) = \frac{(1 - \xi_c)\, R_{\text{clear}}\, A_{\text{clear}} + \xi_c\, R_{\text{cloud}}\, A_{\text{cloud}}}{(1 - \xi_c)\, R_{\text{clear}} + \xi_c\, R_{\text{cloud}}} \tag{7.18}$$

Using Eq. (7.15) and Eq. (7.17), additional RT scenarios are then interpolated for each viewing geometry (see Table 7.4) by varying the effective cloud fraction ξ_c and the effective

albedo fraction ξ_s. For these interpolations, R_{high} denotes the corresponding scenario with a surface albedo of 0.96, while R_{low} is varied over all albedos (see Table 7.3).

There are three different sets of interpolations:

(i) Variation of effective cloud fraction ξ_c for all constant albedos and all cloud scenarios (see Table 7.3) with $\xi_c \in \{0.2, 0.3, \ldots, 1\}$.

(ii) Variation of effective fraction of high surface albedo ξ_s for the clear-sky scenarios $\xi_s \in \{0.05, 0.1, \ldots, 1\}$.

(iii) Simultaneous variation of albedo and cloud fraction for all cloud and albedo scenarios, with $\xi_s \in \{0, 0.2, \ldots, 1\}$ and $\xi_c \in \{0.2, 0.4, \ldots, 1\}$.

This results in 1216 different RT scenarios for each viewing geometry. As an example, the results for one specific nadir looking viewing geometry at an SZA of 60° is depicted in Figure 7.15b. It should be noted that these scenarios cover more than 97 % of all measured RT scenarios as described by the reflectance R and the O_4 AMF A_{O_4}.

(III) The modeled and interpolated RT scenarios contain many triplets $(R, A_{O_4}, A_{\text{BL}})$ exhibiting a very low boundary layer AMF A_{BL}. Some of these triplets correspond to scenarios where the assumption about the proxies breaks down and the reflectance or O_4 AMF are not be able to approximate A_{BL} very well (more on this in section 7.5), such as very low, optically dense cloud.

Since these values should not be taken into account for the least-squares fit of Eq. (7.14), the convex hull[4] H of all points below the sensitivity threshold $A_{\text{BL}}^{\min}$ is used to approximate a range containing only RT scenarios sensitive to the surface.

This is visualized in Figure 7.17a for the same nadir viewing geometry as before. The upper edge of the convex hull (depicted in grey) can be approximated by a parabola g,

$$g(R) = g_0 + g_1\, R + g_2\, R^2\,. \tag{7.19}$$

For small surface albedos, the approximation of A_{BL} by the O_4 AMF gets worse (see section 7.5). To ensure that errors introduced from this are minimized, an intensity threshold h is introduced as the center of mass of the upper right edge A and the lower left edge B of H, given by the mean

$$h = \frac{R_{\text{A}} + R_{\text{B}}}{2}\,. \tag{7.20}$$

The parabola g is then fitted to the upper edge of H using a least-squares fit considering only points for which $R \geq h$.

This geometric approximation also furnishes a classifier able to differentiate between measurements which are sensitive to the boundary layer and measurements which are possibly obscured. The decision boundaries for the nadir viewing geometry looked at before are visualized in Figure 7.17b.

[4] That is, the smallest convex surface containing all points satisfying $A_{\text{BL}} \leq A_{\text{BL}}^{\min}$.

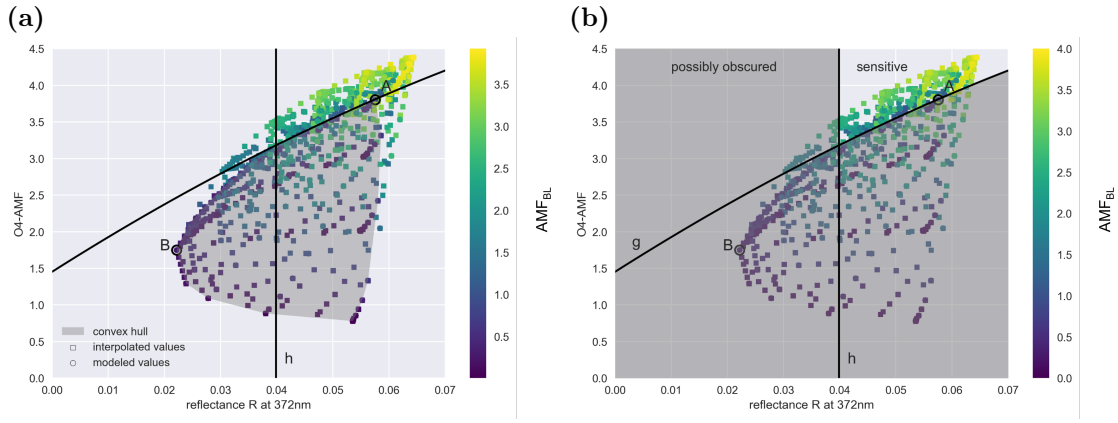

Figure 7.17: *(a) Geometric approximation of the convex hull H (depicted as shaded area in grey) of all measurements below the sensitivity threshold of* $A_{\mathrm{BL}}^{\mathrm{min}} = 1$ *for a nadir viewing geometry at SZA= 66°. The parabola g is fitted to the upper edge of H for all* $R \geq h$*. (b) Visualization of decision boundary for the surface sensitivity classifier for the same viewing geometry. Measurements which would fall in the shaded area would be classified as possibly obscured and masked. Figures based on Sihler et al. (2012).*

The parameters h, g_0, g_1, g_2 are then stored in a LUT, which is used to interpolate them for a given observational viewing geometry. A measurement is then flagged as *possibly obscured* and subsequently masked if either R or A_{O_4} is smaller than h or g, respectively.

(IV) Using the geometric sensitivity classification established before, all RT simulations deemed to be sensitive to the boundary layer are used in a least-squares fit of the bilinear model function Eq. (7.14). The parameters a, b, c are then also stored in a LUT used to interpolate them for specific viewing geometries.

The final results of the tropospheric AMF algorithm are illustrated in Figure 7.14. There are only minor modifications to the algorithm established in Sihler et al. (2012) as discussed in this section. Therefore no additional validation study was done and instead the interested reader is referred to the extensive validation studies in Sihler et al. (2012).

7.5 Uncertainties and biases of the retrieval algorithm

The retrieved tropospheric BrO VCDs are influenced by several sources of errors, which need to be taken into account when interpreting the results and for comparisons with other data sets such as model predictions.

These uncertainties can be roughly categorized into three different sources: (i) uncertainties in determining the (total) SCD, (ii) uncertainties in the methods of stratospheric correction and (iii) uncertainties in the determined AMFs used for converting the tropospheric SCD to the tropospheric VCD.

The uncertainty in the determination of the SCD has several causes. On the one hand,

the accuracy of a measurement of the radiance signal is limited by the photon shot noise (poisson noise) which represents a fundamental uncertainty. This is compounded by noise from the instrument (especially over dark surfaces) and potentially stray light (Richter and Wagner, 2011). On the other hand, the spectral analysis is also afflicted by several sources of uncertainty, such as limited spectral resolution of the instrument, uncertainties in the absorption cross-sections used for the retrieval (Stutz and Platt, 1996) or spectral interference (for example between BrO and HCHO, see section 7.2).

A main source of uncertainty for the tropospheric BrO SCD are the determined stratospheric BrO slant column densities. These can be caused from systematic errors in the assumptions made for the stratospheric correction as well as from the methods used to estimate the stratospheric column.

The calculation of tropospheric VCDs from the retrieved SCDs introduces an additional error through the imperfect knowledge of the light path through the atmosphere. It requires the estimation of the AMF for each measurement, which is often difficult due to limited knowledge of important parameters influencing the radiative transport (see section 4.5). The method applied in this thesis for the estimation of tropospheric AMFs will be affected by a statistical uncertainty in the measured proxies as well as a potentially systematic biases introduced by the assumptions made for the algorithm.

All of these potential error sources are discussed and assessed in this section, concluding in an estimation for the overall uncertainty of the retrieved tropospheric BrO VCDs.

It should be noted that the spatial averaging (rasterization, cf. section 5.4) of pixels can also introduce errors in the resulting plots, since the value depicted in a pixel might not correspond to the maximum BrO VCD measured over that day. This however will mostly affect visualization of daily averages as shown in chapter 8 and is negligible compared to other sources of uncertainty.

7.5.1 Uncertainty in the tropospheric slant column density

As discussed above, the measurement error of the tropospheric BrO SCDs consists of uncertainties in the retrieved total slant column as well as errors introduced by an incomplete separation of stratospheric and tropospheric signals. The measurement error of the total SCD retrieval is often based on the fit error of the DOAS retrieval. However, this fit error may underestimate the true error, for example in the presence of systematically structured residual spectra (Stutz and Platt, 1996), which can be difficult to quantify. This also holds true for errors in the stratospheric correction scheme. Due to the high sensitivity towards stratospheric BrO (in particular at high SZAs, see Figure 7.20), the contribution of uncertainties in the stratospheric correction to the overall SCD error can be significant.

The column separation approach presented in this work features an empirically derived measurement error that not only furnishes an estimation of the uncertainty of the stratospheric correction scheme (see section 7.3.3) but also provides a realistic error estimation for the retrieval error as shown in Sihler et al. (2012). The estimate for the uncertainty in

the stratospheric SCD S_{strat} calculated by the algorithm will therefore be used equivalently as an estimate for the uncertainty in the tropospheric SCD $S_{\text{trop}} = S_{\text{total}} - S_{\text{strat}}$ in the following.

As discussed in section 7.3.2, the uncertainty estimation is performed in each cluster and then interpolated over all measurements, resulting in a per-pixel estimate of the uncertainty. This means an assessment of the SCD error can only be performed in a statistical way. The uncertainty for the stratospheric slant column densities in the Arctic region ranges between 0.76×10^{13} molec cm^{-2} and 3.93×10^{13} molec cm^{-2} (5th and 95th percentile) with a median error σ_{median} of approximately 2.35×10^{13} molec cm^{-2}. These statistics included only measurements deemed to be sensitive towards the boundary layer according to the surface sensitivity classification. Note that the median error determined by the column separation algorithm is more than twice as high as the median fit error of the total BrO SCD calculated by the least-squares fit of DOAS analysis (approximately 1.09×10^{13} molec cm^{-2}). Note that the retrieval error of O_3 is negligible compared to the error in the total BrO column due to the higher SNR in the O_3 retrieval as discussed in section 7.2.1).

This implies a relative error of the determined stratospheric SCD between 10 % to 20 % with a median relative error of 14 % (the median stratospheric SCD in the Arctic region in the time period from middle of January to the beginning of March is 1.57×10^{14} molec cm^{-2}).

There are further sources of possible systematic errors not discussed yet. The column separation algorithm uses the O_3 SCD as tracer for the tropopause height and its influence on the stratospheric BrO column (see section 7.3.1). This requires that both absorbers have a similar stratospheric profile and the sensitivity towards both is comparable. Sihler et al. (2012) performed sensitivity studies for stratospheric BrO and ozone showing that the difference between the AMF of stratospheric BrO and O_3 are below 5 % in most scenarios. For a high tropopause over dark surfaces however, these can reach as high as 10 %, which represents an upper limit for the systematic error introduced by the assumption of similar sensitivity towards both BrO and O_3. However, the separation algorithm may cluster measurements of different tropopause heights and surface albedos together (see section 7.3.2). Hence, the averaging performed in each cluster reduces the influence of the tropopause height and the surface albedo as pointed out by Sihler et al. (2012). Note that the error is also reduced for a low tropopause, for which the stratospheric column is largest. In conclusion, the systematic uncertainty introduced by this assumption of the algorithm can be estimated to be around 5 %.

The empirical choice of parameters for the column separation algorithm (e.g. the number of clusters) also presents a source of uncertainty in the column separation. Yet in section 7.3.3 it was shown that this error is mostly below 1 % and it is therefore negligible.

If one assumes that the error estimated by the algorithm as well as the systematic uncertainties from the sensitivity assumptions and empirical parameter choices are uncorrelated, the error for the stratospheric BrO SCD can be determined via

$$\sigma_{\text{SCD, total}} = \sqrt{(\sigma_{\text{retrieval}})^2 + \sum (\sigma_{\text{systematic}})^2}\,. \tag{7.21}$$

From this a median relative error of approximately 16 % can be calculated. Using the median stratospheric BrO SCD determined from the retrieval it can be concluded that the median total error is approximately 2.5×10^{13} molec cm^{-2}. As discussed above, this also represents the median uncertainty for the tropospheric BrO SCD. Considering that typical bromine explosion events observed from satellite show enhanced tropospheric BrO SCDs from 10×10^{13} molec cm^{-2} to 25×10^{13} molec cm^{-2}, this implies a relative error ranging from 10 % to 25 % for the tropospheric BrO slant column.

7.5.2 Uncertainty in the AMF

In general, there are four sources of uncertainty in the conversion of tropospheric SCDs to VCDs, namely the trace gas profile, the surface albedo, the cloud height and fraction as well as the aerosol loading (Richter and Wagner, 2011).

For the algorithm presented in section 7.4, these sources of potential errors are expressed by uncertainties regarding the proxy parameters and assumptions thereof. These uncertainties have both a random and systematic nature. Statistical variations in the measured proxy parameters, mainly in the O_4 SCD, introduce a random error for the calculated AMFs. Meanwhile, potentially flawed assumptions regarding the a priori BrO profile or the grade of approximation of aerosol/cloud scenarios and surface albedo via the chosen proxy parameters could introduce systematic deviations in the conversion to a VCD.

In this section, both sources of uncertainty are discussed and the relative AMF error is estimated. First the influence of systematic uncertainties regarding the assumptions about the proxies is discussed, followed by a discussion of statistical uncertainties.

BrO box profile

For the McArtim RT simulations, a box profile of BrO for the lowest 500 m is used. This was chosen based on the average observed chemically disturbed layer height of previous studies (see Table 7.2). However, although most layer heights were measured or assumed closely to this mean value, one campaign determined a layer height as high as 2 km.

To investigate the influence of errors in the assumed layer height, RT simulations using BrO box profiles between 100 m and 5 km are shown in Figure 7.18 for nadir viewing geometries and clear-sky conditions.

Over dark regions, the potential relative error from deviations from the assumed 500 m box profile can reach as much as 100 % for a typical SZA of 70°. Confied to a reasonable choice for the scale height (2 km or below), the relative error still reaches 30 % with the AMF always below 1.

In contrast, over bright surfaces the relative systematic error introduced by the choice of a 500 m box profile stays below 10 %, with a relative error of only 3 % if limited to scale heights of 2 km or below.

First it can be noted that differences over bright surfaces are far smaller than over dark surfaces, again emphasizing the influence of a high surface albedo on the RT in the

considered wavelength region. Furthermore, it is clear that measurements over regions with a low surface albedo are afflicted with large uncertainties. For this reason, the reflectance threshold is introduced in section 7.4.2, which should ensure that only measurements with a reasonable high albedo (approximately 0.6 or higher) are classified as sensitive and taken into account for further derivations of the AMF. Furthermore, the SZA dependence over bright surfaces affirms the cutoff criterion for measurements above an SZA of 87° discussed in section 7.3.2.

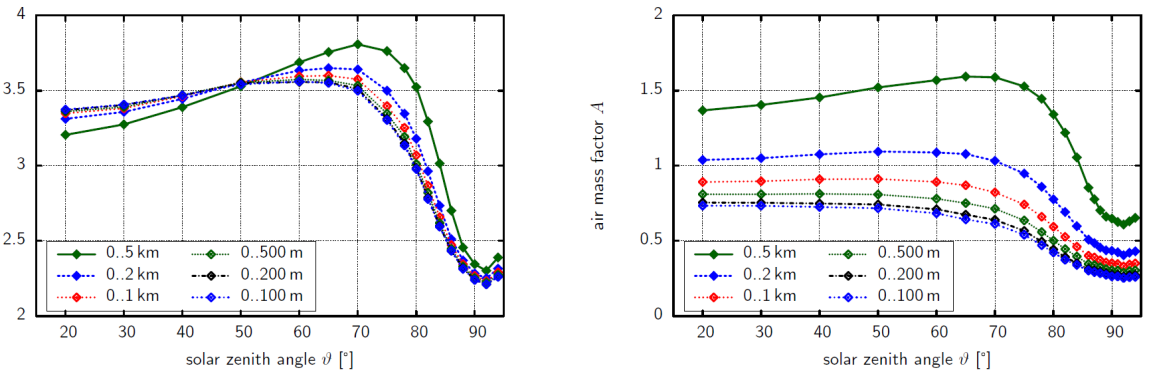

Figure 7.18: *The near surface AMF A_{BL} for bright surfaces (left, albedo of 0.8) and dark surfaces (right, albedo of 0.1) is shown as function off the SZA θ for different layer heights (denoted in the legend). Figures adapted from Sihler (2012).*

In Figure 7.19, A_{BL} and A_{O_4} are depicted for a clear-sky nadir viewing scenario at an SZA of 70°. There, a small spread between the A_{BL} can be seen between the different box profiles, staying below 5 % if the extreme case of a 5 km layer height is ignored. However, this spread also decreases with increasing surface albedo, highlighting again that a potential bias introduced by the choice of scale height gets small for higher surface albedos. This agrees with the conclusions from Sihler et al. (2012) as well as Seo (2020), where the exact value of the BrO box profile height was found to be non-critical for the RT in the Arctic region due to the generally high surface albedo.

Reflectance and O_4 AMF

The Box AMF for the surface layer is derived using measured O_4 columns and reflectances as proxies. The uncertainties introduced by the use of these proxies will be discussed here, first for the clear-sky case and then with clouds present.

The sensitivity towards O_4 is higher than the sensitivity towards BrO at the surface, even for a layer height of 5 km, as depicted in Figure 7.19, with a decreasing difference for both increasing box profile height as well as surface albedo. Since the scale height of O_4 is approximately 4 km, the difference in the AMFs is to be expected. However, it is negligible as potential error source for the following reason: both the O_4 AMF and the surface BrO AMF show approximately a linear relation with the surface albedo. In this instance, a constant offset between both AMFs should be captured by a linear relation. While there is

a slight difference in the dependence on the surface albedo for both AMFs, the bilinearity of Eq. (7.14) should approximate this also very closely, especially if one takes into account that only RT scenarios above a certain reflectance threshold are considered to avoid errors introduced from the assumed box profile as discussed before.

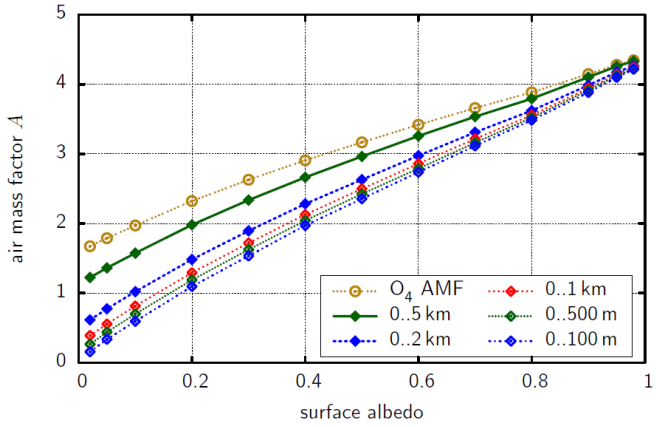

Figure 7.19: *Comparison of surface AMF A_{BL} and O_4 AMF A_{O_4} for different layer heights as function of the surface albedo. The considered viewing RT scenario is again a nadir viewing geometry at an SZA of $\theta = 70°$ with no clouds or aerosols present. Figure adapted from Sihler (2012).*

In stark contrast, the relationship between the surface BrO AMF and the proxies gets more complex if clouds or aerosols are accounted for. In the presence of clouds, the reflectance no longer represents a good approximation of the surface albedo as discussed before. In order for the O_4 AMF to approximate the "cloudiness" of a pixel well, the surface layer AMF and the O_4 AMF both need to behave similarly in the presence of clouds. A detailed study presented in Sihler et al. (2012) showed that this assumption holds for most scenarios featuring higher clouds. However, it was shown that for clouds with a layer top altitude of 2 km or below this approximation gets worse.

This can also be seen in Figure 7.20, where two scenarios of an optically thin respectively thick cloud/aerosol layer between 1 and 2 km altitude are depicted. The variance between different BrO box profiles increases very strongly, potentially introducing a strong systematic bias through the choice of the box profile. In the UV, the sensitivity decreases inside clouds and below it, while it increases slightly above it. This is reproduced by the RT simulations which show a sensitivity close to 0 for profiles completely below the cloud, especially for low surface albedos. For a cloud optical density of 50, the BrO AMF for a layer height of 500 m is only larger than the chosen threshold of $A_{\mathrm{BL}}^{\mathrm{min}} = 1$ for very bright surfaces with an albedo above 0.85, for an optical density of 10 the threshold requires at least 0.6 as surface albedo. This is contrasted by the high sensitivity for profiles reaching above the cloud as well as O_4 even for very dark surfaces.

The reason for this inferior performance of the proxy parameters is that surface layer BrO is completely shielded from the satellite[5], but a large fraction of the O_4 column still

[5]For a BrO box profile of 500 m and cloud layer top altitude of 2 km.

resides above the cloud. This scenario is especially difficult to approximate via the proxy parameters.

Nevertheless, the error in the calculated AMF resulting from this will be very small. The algorithm presented in the previous section not only derives an AMF for a given measurement but also gives a classification of it either as sensitive or obscured based on the measured O_4 AMF and reflectance. For the two scenarios with low clouds presented in Figure 7.20 most RT scenarios will be classified as *possibly obscured*. This is illustrated best for the optically thick cloud (right figure in Figure 7.20). There, the BrO AMF is lower than the sensitivity threshold $A_{\mathrm{BL}}^{\mathrm{min}}$ for all but the brightest surfaces, for which the good sensitivity to the surface can be assumed even for thick clouds as discussed previously. For this RT scenario the variance between different box profile AMFs also reduces. It should be noted that the reflectance as proxy for the surface albedo also tends to underestimate the surface albedo for most scenarios slightly. Although fine-grained snow possesses a surface albedo of 0.97 to 0.99 (Light et al., 2003; Warren et al., 2006), the TOA reflectance even over snowy surfaces does not reach values nearly as high due to extinction in the atmosphere, introducing a bias towards falsely flagging a measurement as obscured.

A detailed analysis presented in Sihler et al. (2012) showed that the surface sensitivity classification has a very low false negative rate, meaning that almost all pixels flagged as sensitive are indeed sensitive to near-surface BrO. Only very low, thick clouds might not get captured by this classifier in all cases, leading to a potential overestimation of the surface layer BrO AMF in rare instances. Conversely, the classifier is potentially biased towards a higher false positive rate[6], meaning that it flags measurements with a possibly high sensitivity as obscured. Examples of this could be a relatively high BrO layer over a dark surface (see Figure 7.18) or rather near surface BrO over a high albedo surface residing under a low, thick cloud as discussed (Sihler et al., 2012). However, this will not introduce any uncertainties for the measurements deemed as sensitive.

Bilinear fit

The strong contrast in the relation of A_{BL} and $A_{\mathrm{O_4}}$ between clear-sky and cloudy scenarios could introduce a large systematic error via the assumption of their linear relationship. For example, for a surface albedo of 0.6 and an O_4 AMF of 3.3, the clear-sky scenario predicts an AMF of 2.8 for a layer height of 500 m. For the optically thick cloud, an O_4 AMF of 3.1 predicts an AMF of 0.3 for the same layer height and surface albedo. Similarly, a comparison of the AMFs as a function of the surface albedo reveals a strong difference between the clear-sky and cloudy-sky scenarios.

A large fraction of the RT scenarios for the cloudy scenarios will be classified as possibly obscured anyway and therefore not be taken into account for the fit of Eq. (7.14). Nevertheless even for very high reflectance scenarios with A_{BL} well above the threshold of $A_{\mathrm{BL}}^{\mathrm{min}} = 1$,

[6]The high false negative rate is ensured by using the *convex hull* of all A_{BL} below the sensitivity threshold $A_{\mathrm{BL}}^{\mathrm{min}}$ as domain of obscured scenarios. In turn, this encloses many RT scenarios for which high sensitivity towards the ground is ensured.

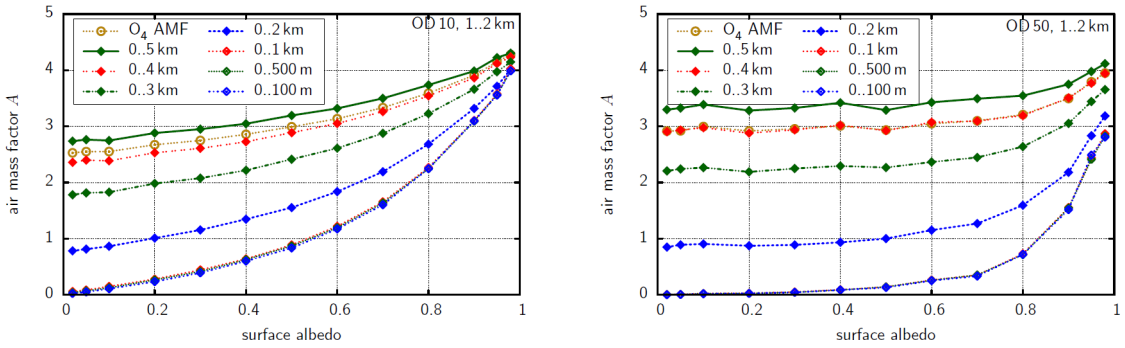

Figure 7.20: *Surface AMF and O_4 AMF depending on the surface albedo in the presence of a cloud with either an optical density (OD) of 10 (left) or 50 (right). The cloud is simulated as a layer between 1 and 2 km, the viewing geometry is identical to Figure 7.19. Figures and caption adapted from Sihler (2012).*

the relative difference between A_{BL} and $A_{\mathrm{O_4}}$ can reach 25 %, almost three times as high as for the the clear-sky case. Additionally, although the relationship between AMFs and surface albedo becomes approximately linear for high surface albedos, its slope increases for the cloudy-sky scenario, caused by strong light path enhancements for photons "trapped" between the cloud and the reflective surface once penetrated. The assumption of a bilinear relationship (see Eq. (7.14)) therefore introduces an additional systematic error. This can be seen in Figure 7.21, where the fitted AMF A_{BL} for a layer height of 500 m is plotted against the respective RT results. The relative difference reaches as high as 150 %, on average the relative error can be estimated to be approximately 30 %.

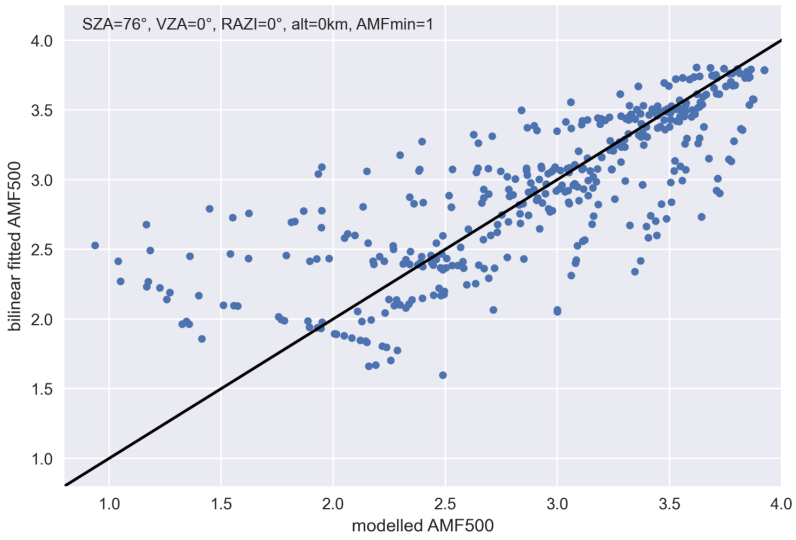

Figure 7.21: *Comparison between modeled AMF and AMF derived from Eq. (7.14) for a nadir viewing geometry at an SZA of $\theta = 76\,°$. The black line demonstrates perfect agreement. Figure based on Sihler et al. (2012).*

Statistical uncertainties

The main source of statistical uncertainties for air mass factors in a parameter range deemed to be sensitive to near surface concentrations is the uncertainty in the measured O_4 SCDs which are used to calculate the AMFs from LUTs. The resulting error in the AMF is discussed here. This discussion features excerpts from the authors work published in Herrmann et al. (2022).

The relative statistical error of the calculated O_4 AMF is below 7.5 %, which allows an estimation of the influence on the tropospheric AMF for different viewing geometries, reflectances and cloud scenarios. This yields an estimate for the relative uncertainty in the AMF of around 10 % to 15 % for the clear-sky scenario and 15 % to 25 % for a mostly cloudy scenario as depicted in Figure 7.22. Note the missing values for a reflectance of 0.8 for the cloudy scenario. This scenario describes a high reflectance together with low visibility of O_4, i.e. a thick aerosol/cloud layer located at an higher altitude. The surface sensitivity classifier flags *all* possible viewing geometries in this parameter range as possibly obscured, which is why no boxplot is given for it. Other scenarios can have much higher relative errors but the corresponding measurements are discarded anyway as they are deemed to be possibly obscured.

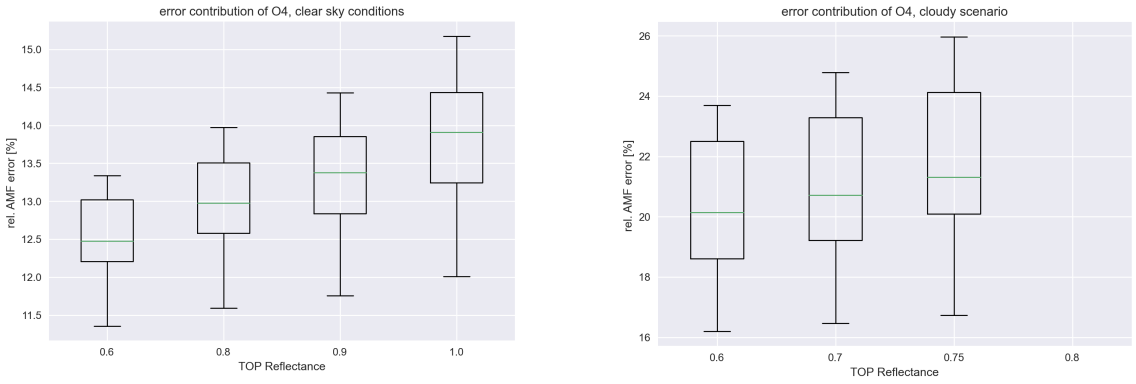

Figure 7.22: *Contribution of the statistical O_4 uncertainty to the overall AMF error for different reflectances, assuming either a typical clear-sky O_4 SCD (left) or an O_4 mean SCD over different simulated cloud scenarios (right). Figure taken from Herrmann et al. (2022).*

Overall AMF uncertainty

Combining the results of the previous two sections yields as relative error for the AMF,

$$\frac{\sigma_{\mathrm{AMF,\,total}}}{A_{\mathrm{BL}}} = \sqrt{\left(\frac{\sigma_{\mathrm{stat}}}{A_{\mathrm{BL}}}\right)^2 + \left(\frac{\sigma_{\mathrm{systematical}}}{A_{\mathrm{BL}}}\right)^2}. \tag{7.22}$$

From the previous findings, this yields a relative error of approximately 35 % for clear-sky scenarios and approximately 45 % for cloudy scenarios. Note that an ODE often extends over many satellite pixels (see chapter 10), so the statistical error can be reduced due to

averaging over a larger spatial extent for the purpose of detecting an ODE, reaching as low as 30 %.

Compared to other AMF calculations for polar tropospheric BrO (e.g. Seo et al., 2019, 2020), the method presented here is more sophisticated. For example, the AMF derivation utilized in Seo et al. (2019) does not take cloud effects into account in the RT simulations. It also obtains surface albedo data directly from the satellite (Tilstra et al., 2017), which itself is affected by a larger uncertainty without taking the effects of clouds into account as discussed previously. In conclusion, although the uncertainty of the AMF calculations is quite large, the presented algorithm allows an estimation of potential errors. Additionally, the surface sensitivity classification ensures that in large parts only pixels with a definitive visibility towards surface BrO are considered.

7.5.3 Overview of statistical and systematic uncertainties

In this section, the error estimates from previous sections are summarized and a combined error for the tropospheric BrO VCD is determined. The relative AMF error is significantly larger than the relative error on the tropospheric SCD if one observes typical enhanced columns in an ODE. On the other hand, the total error of approximately $2.5 \times 10^{13}\,\mathrm{molec\,cm^{-2}}$ impedes upon the detection of smaller column densities, e.g. large mixing ratios contained in a shallow boundary layer.

Assuming uncorrelated errors, the total relative error can be calculated as the quadratic sum of the individual relative errors:

$$\frac{\sigma_{\mathrm{VCD,\,total}}}{V_{\mathrm{trop}}} = \sqrt{\left(\frac{\sigma_{\mathrm{AMF,\,total}}}{A_{\mathrm{BL}}}\right)^2 + \left(\frac{\sigma_{\mathrm{SCD,\,total}}}{S_{\mathrm{trop}}}\right)^2}. \tag{7.23}$$

Some errors may be weakly correlated, e.g. the AMF error is influenced by the surface albedo which is also true for the systematic error in the column separation from the assumption of similar AMFs for stratospheric BrO and O_3. However, this specific cross correlation would in fact reduce the overall error and the overall correlation should be negligible.

Combining both sources of error yields a relative uncertainty for each pixel ranging from 35 % for large BrO enhancements in clear-sky enhancements to 50 % for small BrO column densities in cloudy scenarios.

Detection limit

The smallest column density or mixing ratio of a sought-after trace gas that can be clearly discerned in a spectral analysis is commonly denoted as detection limit (McNaught et al., 1997). In this section a detection limit is estimated as the VCD threshold above which observed tropospheric BrO VCDs can be safely assumed to stem from a tropospheric signal and not be the result of an erroneous stratospheric correction or measurement errors.

An error in the estimation of the stratospheric partial slant column density can pass as tropospherically enhanced pixel without the actual presence of enhanced tropospheric BrO.

A conversion of the median error in the SCD to a VCD using the median AMF of 2.2[7] yields a VCD of $1.02 \times 10^{13}\,\mathrm{molec\,cm^{-2}}$. This can be amplified by an underestimation of the AMF. An upper limit for this VCD can be calculated using the 95th percentile of the SCD error ($3.93 \times 10^{13}\,\mathrm{molec\,cm^{-2}}$) and the 5th percentile of AMF (approx. 1.26), which yields $\sigma_{\mathrm{detection}} = 3.1 \times 10^{13}\,\mathrm{molec\,cm^{-2}}$.

This represents a limit for the tropospheric BrO VCD for an individual observation below which it is not possible to differentiate between errors in the determination of the (stratospheric) SCD and actual tropospheric BrO enhancements, which is denoted as the detection limit of the algorithm from now on.

It also allows an estimate of the minimal column height, and in extension a minimal boundary layer height, at which the instrument is capable to reliable detect enhanced BrO mixing ratios. As discussed in chapter 2, ODEs are often confined to a very shallow boundary layer, which can result in even significantly enhanced BrO mixing ratios not being detected by satellite instruments, since they are only able to measure column densities (see section 2.2.4 and chapter 3). Since an increasing BrO mixing ratio causes a quadratic increase in the ozone depletion rate (see Reactions (R1 – R4)) and the continued release of bromine via the bromine explosion requires ozone, the BrO mixing ratio is somewhat self-limiting. Typical bromine explosions peak at around $80\,\mathrm{pmol\,mol^{-1}}$ mixing ratio while more extreme events reach mixing ratios up to $100\,\mathrm{pmol\,mol^{-1}}$ (e.g. Simpson et al., 2015). Using the detection limit estimated before, the lowest column height h necessary to detect a BrO enhancement at this maximum mixing ratio can then be determined via

$$h = \frac{V_{\mathrm{limit}}}{c_{\mathrm{max}}}\,, \tag{7.24}$$

with V_{limit} as minimum VCD possible to detect from TROPOMI and c_{max} describing the concentration of BrO at typical maximum mixing ratios. The concentration can be calculated from the mixing ratio $r_{\mathrm{BrO,\,max}}$ using the ideal gas law,

$$c_{\mathrm{max}} = \frac{n_{\mathrm{BrO,\,max}}}{V_{\mathrm{air}}} = \frac{n_{\mathrm{BrO,\,max}}\,p}{n_{\mathrm{air}}\,R\,T} = \frac{r_{\mathrm{BrO,\,max}}\,p}{R\,T}\,, \tag{7.25}$$

which yields in Eq. (7.24):

$$h = \frac{V_{\mathrm{limit}}\,R\,T}{r_{\mathrm{BrO,\,max}}\,p}\,. \tag{7.26}$$

It is reasonable to assume that the minimal column does not extend far above the ground, so one can assume a constant pressure and temperature for the estimation. At $T = 253\,\mathrm{K}$ and standard atmospheric pressure (1013 hPa), this yields a minimum column height of approximately 105 m below which the retrieval cannot detect even strongly enhanced BrO mixing ratios reliably.

The detection limit established here can of course be improved by a (spatial or temporal)

[7] This represents the median AMF over the time period between mid of January and beginning of May. Note that the statistics only inlcudes measurements deemed to be sensitive towards the boundary layer, which explains the relatively high median sensitivity.

averaging of measurements. Rastering the measurements on a coarser grid (cf. section 5.4) will decrease the spatial resolution, yet it improves the accuracy in the detection of small BrO enhancements extending over a sufficiently large area since it reduces the statistical error of the mean by a factor of $n^{-1/2}$ with n the number of measurements that are averaged. Such a rasterization on a coarser grid can be useful for long-term time-series using also data of older satellite missions (e.g. Bougoudis et al., 2020) or for comparison with model results which usually have a lower spatial resolution than TROPOMI. Likewise, a temporal averaging, for example in the form of weekly or monthly means of the determined VCDs will also improve the detection limit. This can be useful to investigate long-term trends, such as the areas of frequent occurrence of ODEs over different months as in Seo et al. (2019).

Part III

Results and Discussion

8 | Comparison of Model and observation results

Intercomparison of observations and model results allows deeper insights in the physics and chemistry of the underlying processes in nature. While agreements between simulation and measurements can indicate a good understanding of the chemical and meterological processes forming the basis of ODEs, this is only one possible (albeit likely) interpretation. However, since the trace gas VCD observed by the satellite yields no information on the trace gas profile, also a wrong trace gas profile can lead to optimal agreement between simulated and observed VCD. In contrast, differences of the simulation to the observed reality only allow only one conclusion, namely that the datasets do not agree. Nevertheless, this can point us towards aspects of the phenomena of ODEs potentially not yet understood.

Note that here and in the following chapters, tropospheric BrO observed from satellite is used as an indicator for activated bromine species in general (or rather of ODEs), although reactive bromine species can be abundant even when BrO concentrations are low (for example in the absence of sunlight, as discussed in section 2.1).

There are three noteworthy implementations of the WRF-CHEM model as discussed in section 6.2, differing mainly by their assumptions for the bromide reservoir of the BrO explosion reaction. The model results were provided by Maximilian Herrmann, they are published in parts in Herrmann et al. (2022). The first two sections compares the results of the different model runs to satellite and in-situ observations. The focus lies on high-level comparisons of the data using statistical analysis. This is done not only to assess performance and limitations of the simulations but also to evaluate which model implementation has the best overall agreements with observations in order to use it in the next chapter for case studies of specific ODE events. The subsequent chapter inspects seasonal trends in the concentrations of reactive bromine and ozone predicted by the model. Finally, the results drawn from these comparisons are summarized at the end of the chapter.

Parts of the first two sections are adapted from the authors work published in Herrmann et al. (2022).

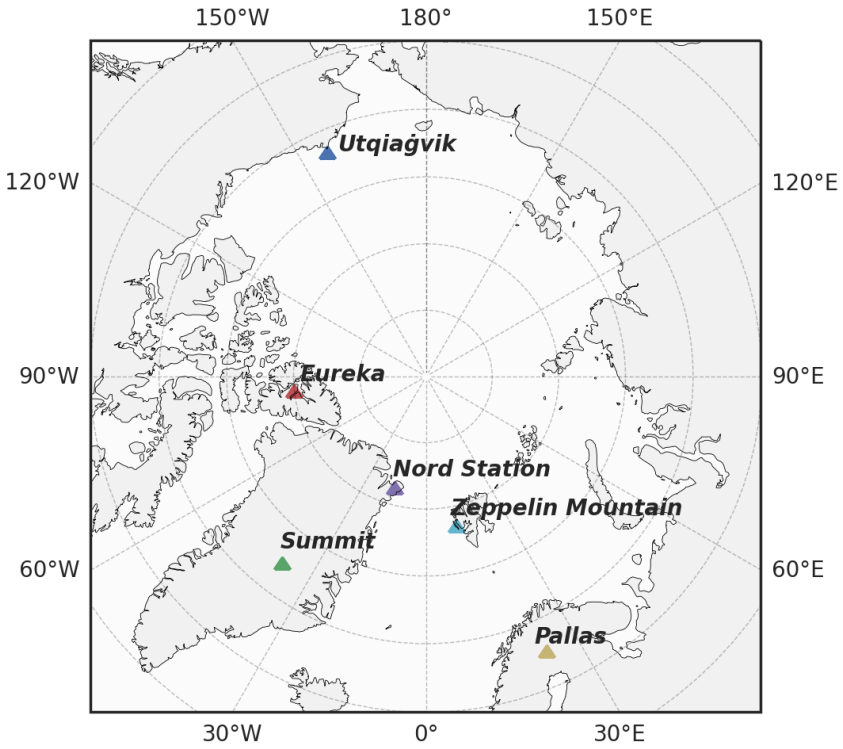

Figure 8.1: *Locations of the measuring stations.*

8.1 In-situ measurements

The modeled ozone mixing ratio is compared to in-situ measurements at Utqiaġvik (Alaska), Summit (Greenland), Eureka (Canada) (McClure-Begley et al., 2014), Nord Station (Greenland), Pallas (Finland) and Zeppelin Mountain (Svalbard) (Tørseth et al., 2012) (see Figures 8.1 and 8.2). Statistics for the modeled ozone mixing ratio in comparison to in-situ measurements at the various locations are shown in Table 8.1. Listed are the correlation R, simulated average ozone mixing ration, mean bias, MB and root mean square error, RMSE. For a positive value of the mean bias, the average of the modeled ozone mixing ratio is larger than the average of the observed ozone mixing ratio.

For Utqiaġvik, the infinite FY ice bromide simulation agrees quite well with the observations during February and March, except for an overestimated ozone depletion around March 16 (see Figure 8.2). In April, however, the infinite FY ice bromide assumption leads to a full ozone depletion for nearly the whole month. The observations find only partial ozone depletion events for the same timeframe. Comparison with different studies using the same emission scheme reveals that overestimation of ozone depletion also occurs frequently during March and April: Toyota et al. (2011), Falk and Sinnhuber (2018), Herrmann et al. (2021) and Marelle et al. (2021) found several instances of overestimation of ozone depletion at locations such as Alert (Canada), Utqiaġvik, Nord Station and Zeppelin Mountain. This may be due to readily available bromide depleting over time, so that the infinite FY ice

bromide assumption becomes invalid (Herrmann et al., 2022).

The finite bromide assumption improves the agreement with the observations significantly, including the weak ozone depletion around March 16. The correlation increases from 0.66 to 0.81 for the low bromide simulation as seen in Table 8.1. The medium bromide simulation allows for emissions from land near Utqiaġvik which causes a slight overestimation of ozone depletion with the mean bias decreasing from 1.1 to -1.8 nmol/mol and a decrease in correlation coefficient from 0.81 to 0.79. This could be indicating that the initially releasable bromide on land-covered snow may be chosen too high.

Zeppelin Mountain is located in an area close to FY ice (see Figure 6.1), which again causes an overestimation of ODEs in April for the infinite FY ice bromide simulation. The finite bromide simulations show an improved agreement with the observations, but ozone is still underestimated during April. Ozone levels around March 19 are similar for all simulations, which suggests that the bromide emission mechanism is not the cause of the underestimation. Even though the correlation of the low bromide simulation and the observations are slightly worse compared to the medium bromide simulation, the low bromide simulations performs best which is demonstrated by the lowest mean bias and RMSE.

Eureka differentiates itself from the other measurement stations looked at so far as it is surrounded by MY ice and snow covered islands. For the infinite FY ice bromide assumption, there is no emission of new bromide from MY ice implemented. Probably due to the lack of nearby bromide sources, bromine emissions are strongly underestimated for this simulation, which results in a consistent overestimation of ozone levels. The finite bromide assumption allows a differentiation of MY and FY ice in the emission mechanism. With the finite bromide assumption, weak bromine emissions are allowed on MY ice and snow covered ice. However, the prediction of ozone has not changed much between the infinite and low bromide simulation and actually becomes a little worse during April for the low bromide assumption. This suggests that the real releasable bromide levels for MY ice and/or snow covered land are probably significantly higher than those assumed for the low bromide simulation. The medium finite bromide simulation improves the results at Eureka even over the infinite FY ice bromide simulation, but still not removes the underestimation of ODEs.

Around April 25, all simulation results differ only little, so that it is unlikely that increas-

Table 8.1: *Statistics for the modeled ozone mixing ratio in comparison to in-situ measurements at different locations from February 1 to May 1, 2019. The three values in each entry are for the three simulations in this order: Infinite FY ice bromide, low bromide, medium bromide. The best value is marked in* ***bold****. Table adapted from Herrmann et al. (2022).*

location	R [-]	simulated average [nmol/mol]	MB [nmol/mol]	RMSE [nmol/mol]
Utqiaġvik	0.66, **0.81**, 0.79	21.4, 29.1, 26.2	-6.5, **1.1**, -1.8	13.3, **7.2**, 8.4
Zeppelin Mountain	0.48, 0.62, **0.67**	29.4, 33.1, 31.4	-10.3, **-6.6**, -8.4	14.0, **9.7**, 10.9
Eureka	0.51, 0.47, **0.58**	29.8, 32.1, 28.8	6.4, 8.7, **5.4**	14.0, 15.3, **12.9**
Nord Station	0.64, 0.55, **0.65**	36.4, 38.2, 36.2	2.1, 2.0, **0.6**	8.5, 9.2, **8.2**
Summit	0.30, 0.32, **0.34**	49.5, 49.3, 49.3	6.3, 6.2, **6.1**	11.2, 10.7, **10.7**
Pallas	0.71, **0.88**, 0.83	33.1, 38.5, 35.0	-10.1, **-4.7**, -8.1	11.9, **6.3**, 9.6

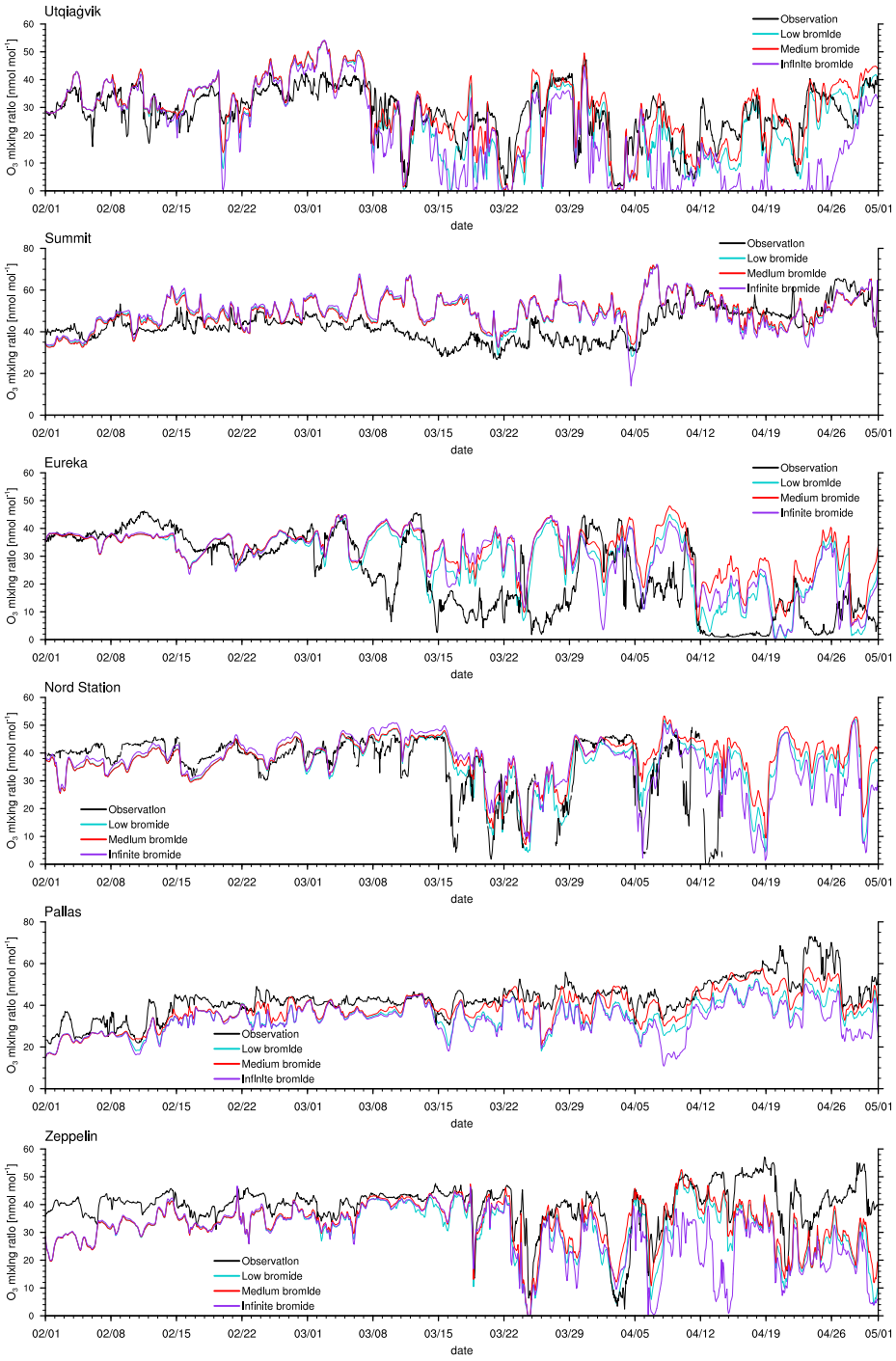

Figure 8.2: *Modeled and observed ozone mixing ratios at Utqiaġvik, Summit, Eureka, Nord Station, Pallas, and Zeppelin Mountain from top to bottom. Figure adapted from Herrmann et al. (2022).*

ing emissions even further will cause significant changes. Some bromine source or another ozone depletion mechanism might be missing to explain the ODEs in Eureka, such as blowing snow, which was discussed by Marelle et al. (2021), who showed rare ODEs that are not explainable with emissions from the snow surface alone. It is, however, more likely that the

model resolution is not sufficient to correctly simulate ODEs at Eureka since the topography around Eureka is very complex. The weather station at Eureka is located at a height of 10 m, whereas the closest grid cell is at an altitude of 155 m (Herrmann et al., 2022). This assumption is further supported by a comparison of the results of domain 2 with 20 km resolution to those of domain 1 with a 60 km resolution. It shows that the simulation of ODEs at Eureka is affected by the resolution: The correlation of model results with observations at Eureka for the refined domain 2 is, in comparison to domain 1, increased by 0.02, 0.09 and 0.08 for the infinite, low and medium bromide simulations, respectively. It is still remaining at overall relatively low values of the correlation coefficient below about 0.6. Differently to Eureka, the correlations of the simulations with the two different domains with observations at Utqiaġvik agree within 0.01 for all simulations, which is likely due to the simpler local topography at Utqiaġvik. Additionally, it is possible that a significant amount of bromine affecting the chemistry at Eureka is emitted from snow-covered sea ice at the strait and fjords near Eureka, which are less than 20 km wide and can thus not be resolved by the model.

At Nord Station, the observations are not available at the end of April. The comparison to the simulations between February 1 and April 15 shows some similarities to Eureka, in that ODEs are generally underestimated, however, the agreement between simulations and observations at North Station is better compared to Eureka. Nord Station is surrounded by mostly MY ice and snow covered land, so the discussion regarding the underestimation for Eureka also holds for North Station. In the same vein the slightly better performance of the medium finite bromide simulation compared to the FY ice bromide simulation can be understood. Note that the simulation results improve with larger emissions, with a correlation of 0.56 and 0.62 for the low and medium simulations, respectively. The weather station is located at an altitude of 20 m, whereas the closest grid cell is at 85 m. Differently to Eureka, however, there is no improvement for the increased grid resolution of domain 2. Correlations of results of domain 2 with observations increase by 0.04, -0.02 and -0.03 in comparison to domain 1 for the infinite, low and medium bromide simulations, respectively.

At Summit, the model finds very little influence of the halogen chemistry on ODEs, while the measurements show no obvious ODEs. The correlation of 0.3 is relatively low. Ozone is generally larger in the model, especially during March, when a very long, weak partial ODE has occurred. However, it is more likely that dynamical errors cause the discrepancy in March. During a measurement campaign in 2007 and 2008 (Stutz et al., 2011; Liao et al., 2011), small BrO mixing ratios of around 2 and 5 ppt were measured, which is consistent with the modeled BrO. On a few days, such as March 22 and April 5, modeled BrO mixing ratios exceed 5 ppt and reach up to 30 ppt.

Greenland is effectively excluded from emitting new bromine in the model.[1] The reason for this is that past satellite missions showed no evidence of enhanced BrO over Greenland. Since the model overestimates Ozone, significant bromine emissions over Greenland might

[1] BrO emissions are turned off in all simulations for surfaces elevated 1 km or higher.

improve correlations. However, the in-situ measurements at Summit suggest small bromine emissions if any at all. Additionally, assuming that the sea salt originates from sea water, sea salt may not easily be transported to higher elevations. On the contrary, there might be an overestimation of the orographic lift towards the interior of Greenland since the southern part of Greenland is part of domain 1 with a 60 km resolution only, so that the topography is smoothed and might allow air masses in the model to be blown over Greenland, which in reality would have stayed near the sea ice. This could explain the discrepancy between model and satellite observations over Greenland discussed in section 8.2.

Finally, at Pallas little ozone depletion is observed except for potential ODEs on April 22 and from April 27 to May 1, whereas the model finds a few additional partial ODEs at the end of March and in April. The source of bromine is most likely the nearby White Sea located at a distance of about 500 km. Due to the reduced bromine sources, the low bromide simulation shows the best agreement with the observations and a high correlation of 0.88. The changed definition of snow-covered land, which allows for recycling of bromine near ice-covered coast water, is likely to cause the differences.

Overall, the low bromide simulation performs best for the measurement sites near FY ice and the medium bromide simulation is best at Eureka and Nord Station, which is located near MY ice. This suggests that MY ice might indeed be effective, albeit not necessarily as effective in emitting bromine as FY ice, whereas larger emissions for snow-covered land generally reduce the agreement with the observations.

It is worth emphasizing that significant ODEs are only observed at Utqiaġvik, Nord station, Zeppelin Mountain and Eureka. Since the satellite observation measure tropospheric BrO, especially BrO enhanced in an ODE, the model performance for these stations is of special importance to us.

8.2 Satellite measurements

The independence of the retrieval algorithm presented in chapter 7 avoids systematic biases from other sources, for example other models (cf. chapter 3). This makes the resulting satellite observations especially useful for comparison of other data considered independent such as the WRF-CHEM model discussed here, providing another source usable for model verification.

For a comparison of the model with satellite observations, the vertical column densities of modeled BrO are derived by vertically integrating BrO concentrations from the ground to 4 km height in order to calculate tropospheric BrO VCDs. The data is then interpolated to the satellite coordinate system by trilinear interpolation as described in section 6.3. Then both datasets are rastered onto the same grid for each day and the results are visualized using a northpolar stereographic projection (see section 5.4.1). Figure 8.3 shows exemplaric days of very good agreement between simulation and measurements, whereas days with strong discrepancies between simulation and satellite observations are shown in Figure 8.5. Note that the satellite measurements represent daily means as some orbits overlap due to

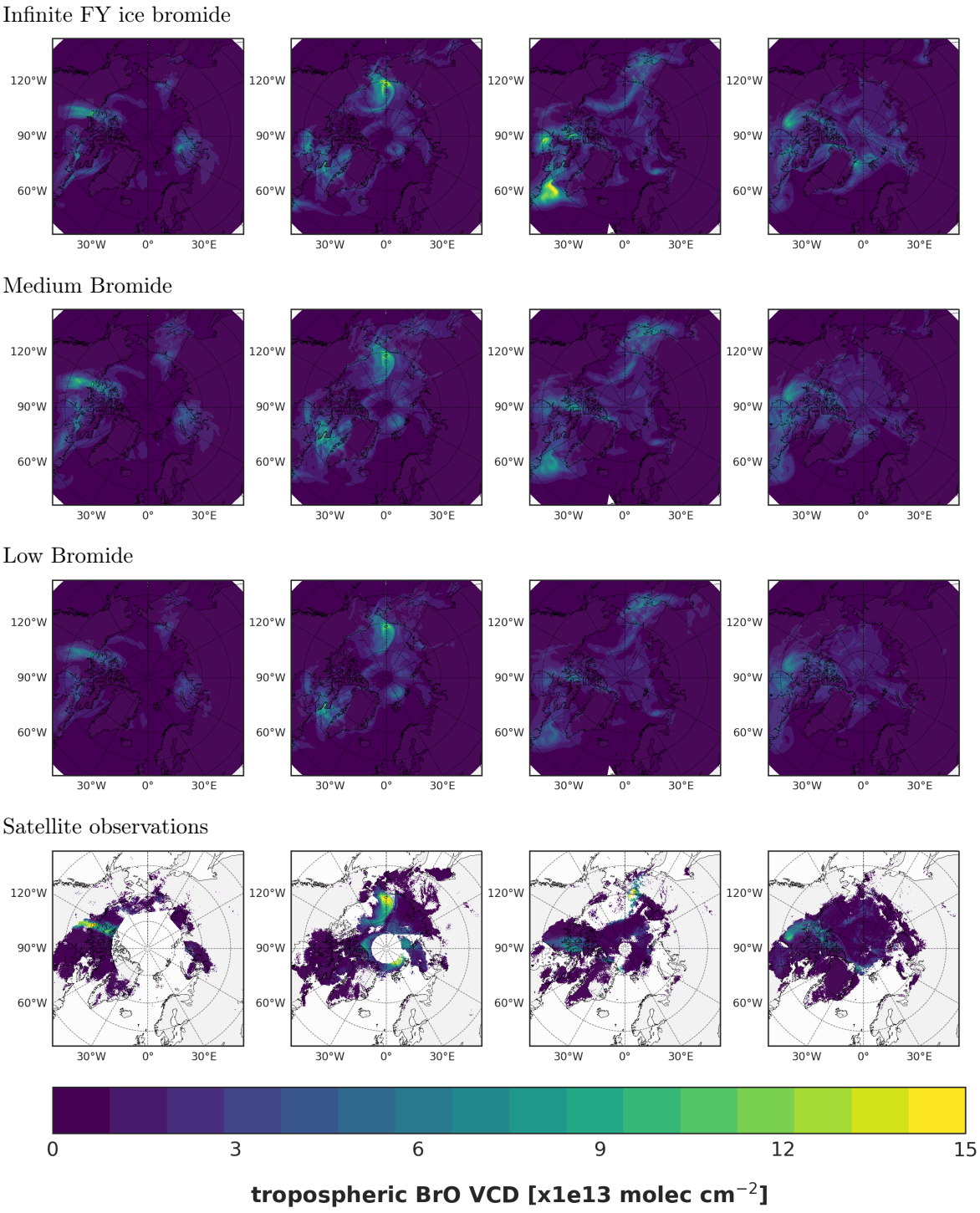

Figure 8.3: *Observed (bottom row) and simulated (rows 1-3) tropospheric BrO VCDs in 2019. Examples of good agreements between satellite measurements and simulations. From left to right: February 27; March 19; March 27; April 5. The uncolored pixels in the satellite observation maps are pixels which are classified as not sensitive towards the surface.*

the increased coverage of TROPOMI over the poles (see section 5.4) and consequently also the model data is spatially averaged during the rasterization process.

The model simulates almost all of the enhanced BrO VCDs found by the satellite. On February 27 displayed in the first column of Figure 8.3, the North-South stripe-like region with the elevated BrO VCD extending over the Canadian mainland is captured by all three simulations. Here the low bromide simulation underestimates the BrO VCD compared to the satellite measurements. The infinite and medium bromide simulations find VCD-values comparable to the satellite data. The simulated peak of the BrO VCD is located over the mainland for the medium bromide simulation, whereas the satellite and the infinite FY ice bromide simulation find the peak further north near the coast.

On March 19 shown in the second column of Figure 8.3, the large BrO VCD over Chukchi Sea and the two small stripes near the north pole are predicted by all simulations. The BrO VCD over Chukchi Sea is located over FY ice, where the releasable bromide values are the same for both finite bromide simulations. For that reason, the BrO VCDs simulated by the low and medium bromide simulations are very similar. The infinite FY ice bromide simulation calculates a ring-like BrO VCD over Chukchi Sea, which is caused by a full ozone depletion event over a large area covering the center of the ring and the stripe with small BrO VCDs. The finite bromide simulations simulate a full ozone depletion over a smaller area there, so that ozone from outside the ring can sustain the BrO. The structure near the north pole is also caused by a full ozone depletion, which is actually stronger for the finite bromide simulations, since the structure is located over MY ice, which is a bromide source in the finite bromide simulations.

On March 27, the models match well with the observed BrO VCD over East Siberian Sea and the main land as depicted in the third column in Figure 8.3. Interestingly, both finite bromide simulations calculate less BrO at the observed BrO VCD peak. The BrO VCD over the Canadian Arctic Archipelago is predicted by the simulations, but the low bromide simulation agrees best with respect to the magnitude. The satellite and the models find BrO VCDs at the northern coast of Greenland, however, the simulated location of the BrO resides west of the observed location.

On April 5 the models simulate both the BrO VCDs over the Arctic Archipelago and east of the coast of Greenland as seen in the last column of Figure 8.3. All simulations overestimate both the extent and the magnitude of the BrO VCD, where low bromide simulation is somewhat better than the medium bromide simulation which again agrees better with the observations than the infinite FY ice bromide simulation.

The correlation between model and satellite pixels was also calculated, allowing for a comparison of the results to the in-situ intercomparison. The temporal correlation were calculated by using the interpolated data, which is rastered onto the same grid orbitwise instead of using a daily gridding as was done for the maps. Finally, the correlation in time for every grid point is calculated. To the authors knowledge, this is the first time such an analysis is performed with this high temporal resolution (approximately hourly). A similar analysis was done before in Toyota et al. (2011), however the authors used VCDs averaged over 10 days and the study had additional limitations (for example they had to use adapted VCDs to correct for several systematic errors).

The correlations are then visualized for the whole region (see Figure 8.4) and summarized in Table 8.2 for the measurements stations discussed in section 8.1. For the latter, the nearest neighbour to the measurement sites in space was taken as correlation value.

It is important to note that this approach results in a bias towards measurements later in the year for some stations. This is due to the surface sensitivity classification discarding mostly early measurements. Affected are primarily stations farther north like Eureka, Nord station and Zeppelin Mountain, where the locations are corresponding to a high SZA early in the year. This also explains some isolated outliers with very high or low correlation visible in the correlation map for which only very few measurements were taken into account.

Beginning with Utqiaġvik, model and satellite observations agree well with correlations between a low of 0.41 for the infinite FY ice bromide simulation and a highest value of 0.51 for the low bromide simulation. Since the station is located mainly near FY ice, the difference between correlations of the finite bromide simulations is small. However, as discussed in the previous section, the bromine emission from snow-covered land might be chosen too high for the medium bromide simulation, especially in combination with a larger extent of snow-covered land due to the different definition. This leads to an overestimation of BrO VCDs compared to the low bromide simulation, explaining the lower correlation.

At Zeppelin Mountain, the satellite observations again agree very well with the simulations for the finite bromide assumption. The low bromide simulation performs slightly better than the medium bromide simulation with a correlation of 0.62. This also matches with the results of the comparison to in-situ measurements, for which the medium bromide underestimated ozone concentrations more severely (see Table 8.1).

However, the correlation to the infinite FY ice bromide simulation of only 0.2 is considerably lower. This can be explained by the aforementioned bias of the correlation towards measurements in late March and April. As discussed in the previous section 8.1, the infinite FY ice simulation overestimates ODEs in April due to FY ice located close to the station. Since the measurements in April constitute a larger fraction of the overall number of measurements compared to e.g. Utqiaġvik, the correlation is worsened for the FY ice

Table 8.2: *Correlation coefficients of modeled and measured BrO VCDs at different locations from February 1 to May 1, 2019 for the three different simulations in order. The best value is marked in* ***bold****. The correlation coefficients for Pallas station are discarded due to poor statistics. Table adapted from Herrmann et al. (2022).*

location	infinite FY ice bromide R [-]	low bromide R [-]	medium bromide R [-]
Utqiaġvik	0.41	**0.51**	0.46
Zeppelin Mt.	0.20	**0.62**	0.59,
Eureka	0.03	0.14	**0.22**,
Nord Station	0.51	**0.78**	0.78
Summit	0.02	0.03	**0.04**
Pallas	-	-	-

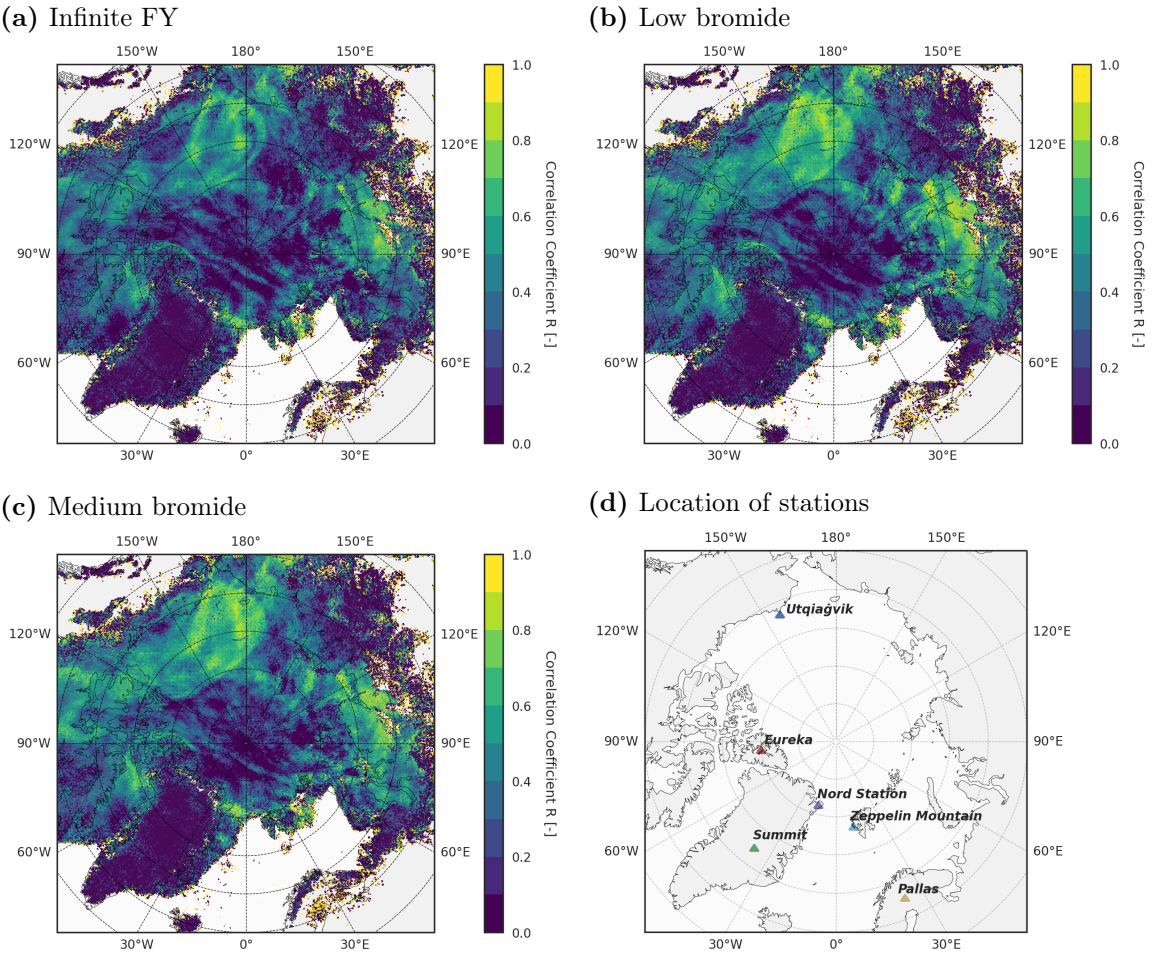

Figure 8.4: *Map of pixel-wise temporal correlations for the three different simulations. Some pixel exhibit a very high correlation coefficient due to a low number of underlying measurements, especially at the edges of the area of valid values. Correlation coefficients calculated from less than 10 samples are masked (pixels depicted in white).*

simulation.

For Eureka station it was already discussed in section section 8.1 that the model resolution is probably not sufficiently due to the complex topography. Therefore correlations to in-situ measurements there are low, which is mirrored by the correlations to BrO VCDs from the satellite. Note here too the bias towards measurements later in the year, where agreements between model and in-situ measurements were also worse. This could explain the lower correlations compared to the in-situ correlation coefficients. Furthermore, the reduced temporal sampling in the satellite observations compared to the in-situ measurements also has to be taken into account, where at most two measurements each day are available at a given location.

For Nord station, the correlations of the simulations with the satellite measurements are even better than for the in-situ measurements. It should be considered again that the correlations for these high latitudes are biased towards April, for which in-situ measurements

were not available after April 15. Following the discussion regarding the station in the previous section 8.1, the better agreement of the finite bromide simulations can be explained by its close proximity to mostly MY ice. However, the difference of the correlation to the infinite FY ice simulation is very small, indicating that the additional emissions from MY sea ice and snow-covered land in the model have very little influence. Another explanation could consist of the simple fact that an overestimation of the emissions in the medium bromide model could be compensated for by an underestimation of BrO emissions for the low bromide simulation. Finally, it would also be possible that the orographic lift is overestimated here the same way it is on the south side of Greeland, although the north side with its higher spatial resolution of $20 \times 20\,\mathrm{km}^2$ should be less prone for that. In this case, more BrO would get transported to higher atmospheric layers, leading to less BrO available for ODEs at the ground near the station. This would also explain why the medium bromide simulation performs better than the other simulations for ozone comparisons in section 8.1, since an overestimation of BrO would lead to a higher ozone destruction, compensating the BrO which is transported away.

For Summit the correlations are extremely low for all three simulations. Enhanced BrO VCDs are observed by the satellite only at the edges of Greenland (see Figure 8.3), however, the simulations calculate enhanced BrO VCDs over Greenland on several days. As discussed in section 8.1, Greenland is excluded as a surface for both bromide emission and recycling due to the height dependence of Eq. (6.1) and thus, the BrO over Greenland is produced elsewhere and then advected to Greenland. The model might overestimate air transport to Greenland, possibly due to smoothening the topography too much. This could be associated to an overestimation of enhanced BrO VCDs over the regions around Hudson Bay and Baffin Bay, including the Labrador Sea as seen in the comparison to satellite maps in Figure 8.3. From there, air potentially enriched in BrO is occasionally transported to Greenland.

Lastly, at Pallas the correlation varies between 0.96 and 0.99 for the different simulations. However, the surface sensitivity filter of the satellite retrieval discards almost all measurements near the station. Consequently only very few measurements are taken into account for the calculation of the correlation coefficient, all of which show no BrO enhancement. Due to the underlying poor statistics, this correlation is discarded.

In summary the trend discussed in the last section is also present for a comparison with satellite observations. The low bromide simulations tends to perform better over FY ice while the medium bromide simulation performs slighty better over MY ice.

In Figure 8.4, maps of the correlation coefficients for the different simulations over the whole Arctic region are shown. In general, correlations are high in regions associated with a high frequency of ODEs and enhanced BrO levels (see for example Sihler (2012) or Seo et al. (2019)). In contrast, in regions where BrO is rarely increased and consequently the observed VCD hardly vary, correlations are low. The finite bromide simulations show a higher correlation overall and outperform the infinite bromide assumption. This is especially striking over FY ice, e.g. near Utqiaġvik, where the infinite FY ice bromide simulation tends to overestimate the BrO VCDs compared to satellite measurements. The differences between

the low and medium bromide simulations are less pronounced. However, the general trend as discussed for the in-situ observations can be found here again. The low bromide simulation performs marginally better over FY ice while the medium bromide simulation is slightly better over MY ice. Additionally, there is a small region to the east of Victoria Island where mostly FY ice is found and where the medium bromide simulations shows a significantly higher correlation than the low bromide simulation. The situation over land varies. While the medium bromide simulation has a higher correlation over Canada to the south of Victoria Island, it tends to overestimate BrO VCDs compared to the satellite over Russia near the coast of Laptev Sea.

There is one region of systematically lower correlations. For latitudes above 80° N, the correlation begins to drop with increasing latitude. For high latitude regions there will be no measurements available early in the year as we are excluding measurements with an SZA above 85° as discussed in section 7.3.2. Additionally, most measurements with very high SZAs will be filtered out by the surface sensitivity filter for being potentially obscured. Therefore, these correlation values are affected by an even stronger bias than discussed before towards measurements later in the year. However, especially later in the year, all simulations tend to overestimate ambient BrO concentrations as will be discussed below, explaining the low correlations for high latitudes, for which measurements early in the year are not available.

Slightly enhanced BrO observations not observed by the satellite are predicted by the simulations frequently. Their occurence is slightly reduced for the low bromide simulation compared to the other simulations, but they still appear frequently. Especially striking are BrO enhancements near or on land, commonly predicted by the medium bromide model. Comparison to daily satellite observations (see Figure 8.3) sheds further light on the issue: the differences between simulations and satellite observations are most pronounced after long-term ODEs accompanied by high BrO VCDs. While the model will show slightly enhanced BrO VCDs immediately after, usually the satellite does not observe enhanced VCDs in the area for some time. This larger recurrence time might result from a depletion of the surface bromide reservoir and could indicate that the timescale for replenishment of the surface bromide reservoir is chosen too small.

The finite bromine emissions are modeled using a constant replenishment (see Eq. (6.1)) originating from a bromide reservoir such as sea ice, water or deeper layers of snow. Especially after long-term bromine emissions, this reservoir might actually be depleted, leading to a decrease of the constant replenishment rate c_i. However, there is currently no mechanism for a depletion of the bromine reservoir implemented in the model.

Another possible explanation might be the bromide oxidation due to ozone (see Reaction (R32)), which is used as trigger mechanism and might release bromine too frequently. As long as there is both sunlight and ozone, small amounts of bromine are always released, which may explain the slightly enhanced BrO VCDs over the whole Arctic region. A recent study by Swanson et al. (2022) using the same snow-pack emission mechanism reported reduced overestimations and overall better agreements to observations if the Br_2 yield was

constant day and night (with an adjusted emission flux).

It is also possible that another trigger mechanism would provide better agreement with lower overestimation, yet as discussed in section 2.1.1, currently there are no good alternatives known. Recent model studies by Marelle et al. (2021) showed little difference between purely ground-based emissions and the combination of ground-based emissions with blowing snow emission as discussed in section 2.1.1. Another possible candidate could be photolytic bromine emission (see Reaction (R26), (Pratt et al., 2013; Wang and Pratt, 2017)), possibly due to reactions with OH in the liquid phase. However, this reaction requires only sunlight and should thus emit even more background bromine.

Alternatively, the general overestimation of the BrO VCDs could also indicate the existence of a weak bromine sink. One such candidate would be a fast reaction with a low-concentration species such as mercury, which is currently not considered. Another mechanism which could act as sink for bromine would be wet deposition of halogen species, which is also not implemented in the model. However, this is unlikely to account for all of the differences between model and observations, as these are consistently present throughout the model domain, whereas precipitation affects only approximately 20 % of the area at a time. Aside from that, boundary layer bromine removal is dominated by dry deposition and during ODEs, enhanced bromine levels are primarily concentrated in the boundary layer.

It is unlikely that the aforementioned mismatch is due to issues in the observed data. As discussed in section 7.5, it might be possible that a very low and thick cloud might effectively shield a near-surface layer of BrO. But as already discussed, the discrepancies between model and measurements for these slighty enhanced BrO VCDs are consistently present, ruling such a scenario highly unlikely. As it was discussed in section 7.5, the lower limit of certainty for the measured BrO VCDs lies around $3 \times 10^{13}\,\mathrm{molec\,cm^{-2}}$, whereas most of these slight BrO enhancements are a factor of two or more larger than this limit.

In Figure 8.5 examples of tropospheric BrO enhancements detected by the satellite which are not predicted by the simulations are shown. While the model does simulate non-zero BrO VCDs, the magnitude of the enhancements are underestimated. For the event in April the underestimation can be attributed to the wrongly resolved topography around Eureka discussed previously. The mismatch in early February can probably be attributed to an underestimation of the bromide oxidation due to ozone which will be discussed in detail in section 9.1.

Summarizing, the agreement between satellite observations and simulations is very good except for few caveats discussed above. This not only gives higher confidence in the model ressults as well as the satellite retrieval algorithm, it also acts as basis of decision-making for the simulation to choose for the case studies in the following chapter.

The low bromide simulation seems to be placed best for this. Although it underestimates BrO enhancements in some cases, the general structures are always visible and mirror the observations of the satellite very closely. On the other hand, the overestimation of BrO over the whole region is much more pronounced for the medium bromide simulation, especially later in the year. This might make it harder to decide if the vast areas of slightly enhanced

BrO seen ubiquitously in the simulation but not in the satellite observations, such as on March 27 to the West of Greenland and over Hudson bay as seen in Figure 8.3, result from problems with the retrieval or overestimation by the simulation.

8.3 Seasonal trend in model results

This section analyzes a time series of model results over the Arctic region. It investigates a possible seasonal trend in the occurrence of ODEs in relation to the initial bromine release. In that context a possible seasonality in the meteorological conditions favoring bromine explosions are discussed.

In Figure 8.6 a seasonal overview of the surface Br_x and O_3 mixing ratio predicted by the model is shown. Additionally, Figure 8.7 shows the surface Br_y mixing ratio and the BrO VCD from the model for the same time frame. Here Br_x denotes the combination of all reactive bromine species in the model, that is BrO, Br, Br_2, HOBr, $BrONO_2$, $BrNO_2$ and BrCl while Br_y includes in addition the inactived bromine species HBr. The figures show each parameter on the 5th and 20th of February, March and Aprils respectively. The time of the simulation was chosen as 22:00 UTC always. Only results of the inner nest of the model are used (see chapter 6). Depicted here is only the low bromide simulation. The results for the medium bromide simulation are shown in the appendix chapter D, but the general remarks made in the following are equally valid for both simulations.

The model clearly shows a strong increase of reactive bromine species at the surface over the time of Arctic spring, accompanied by a similar strong decrease of ozone. Surface ozone mixing ratios are generally between 35 and 45 $\mathrm{nmol\,mol^{-1}}$ over the Arctic region in February and middle of march. Localized decreases of surface ozone can be discerned on 20 February and 5 March coinciding spatially with an increase of reactive bromine surface mixing ratios. There are even smaller stretches of completely depleted surface ozone extending over a few hundred kilometers. Yet already on 20 March, vast areas over the Arctic sea are completely void of surface ozone which is accompanied by an increase in surface Br_x and Br_y mixing ratios. This increases further with time and 20 April the surface ozone mixing ratio looks opposite to that early in the season: there are only small "pockets" of undepleted surface ozone extending at most over a few hundred kilometers while a large fraction of the sea ice covered ocean and even the coastal regions are void of ozone. This also agrees with the proposition from Wagner et al. (2007) that the air above sea ice is largely void of ozone later in the season based on ship-based measurements of bromine.

In large parts, the areas of depleted surface ozone coincide with areas of strongly elevated (reactive) bromine mixing ratios. However, later in the season there are a few areas where ozone is completely depleted but Br_x mixing ratios are also very low, such as over the Kara Sea at 20 April. It is possible that in these regions, temperature inversions cause a very stratified and stable boundary layer which hinder the mixing in of fresh ozone. Since NO_x can also be depleted during an ODE (which is the main driver for chemical reformation of ozone, see section 2.1), O_3 recovery could be further decelerated, leading to a total lack of

ozone at the surface. If this condition persists long enough (i.e. a few hours or longer with enough aerosols present, otherwise even shorter), this would also lead to the depletion of bromine levels, in particular when taking into account that the surrounding areas are also depleted in ozone which prevents horizontal diffusion of fresh ozone to sustain the activated bromine. Alternatively, a sustained bromine explosion extending above the boundary layer could also lead to a substantial depletion of ozone in the free troposphere (e.g. Blechschmidt et al., 2016). After the ODE comes to an end, this could also hinder the entrainment of fresh ozone to the surface. Later in the season it would also be conceivable that the sea ice in this region is beginning to melt, which forbids new bromine release from that surface in the model. If this happens during an ODE it might also lead to fast decrease of the bromine concentration at the surface.

A comparison with the BrO VCDs calculated from the model shows a similar trend of increasing prevalence of enhanced BrO columns over the Arctic region over the season. As expected they also coincide in large parts with regions of increased bromine surface mixing ratios and to a lesser extent to decreased surface ozone concentrations. What is striking though is that especially in February, BrO VCDs are very small and regions depicting an enhanced column are far smaller than the area of enhanced surface bromine concentrations. This also indicates that bromine increases seen over the region are confined to a small vertical extent, for example by a shallow boundary layer. It is also possible that bromine emissions are underestimated early in the season, but the good agreement between model and observations also early in the season, both from satellite and at measurement stations, makes this seem less likely. The low detection limit made possible by the tropospheric BrO retrieval (see chapter 7) in combination with TROPOMIs high SNR also allows an improved detection of small BrO columns possibly confined to a shallow boundary layer. Considering all possible uncertainties from stratospheric corrections and sensitivity towards the boundary layer, the lowest tropospheric BrO VCDs which can be reliably detected are approximately $2 \times 10^{13}\,\mathrm{molec\,cm^{-2}}$ as discussed in section 7.5. Assuming a maximum BrO mixing ratio of $100\,\mathrm{pmol\,mol^{-1}}$ allows the estimation of the minimum column height which can be detected from the satellite as approximately 105 m (see Eq. (7.26)). This represents a significant improvement over previous retrievals (e.g. using the GOME-2 instrument) where this limit was estimated to be around 200 m (see chapter 3 and (e.g. Choi et al., 2012)).

As mentioned there are a few specific events observed by the satellite but not predicted by the model which are probably related to an underestimation of snow-pack emissions for very high SZAs which could explain the lack of BrO for the very high latitudes during February. These will be discussed in detail in section 9.1.

Even later in the season on 20 March and during April, most areas with strongly elevated bromine mixing ratios do not exhibit highly elevated BrO VCDs. Only some events produce strongly enhanced BrO columns, such as on 20 March near Utqiaġvik. They seem to be associated with synoptic scale weather events (e.g. Sihler et al., 2012; Blechschmidt et al., 2016) and will be discussed in the context of a case study in section 9.2.

In summary, the model shows a seasonal trend of the reactants partaking in ODEs. Early

in the season, reactive bromine concentrations are low and their spatial distribution is also small compared to the distribution in March and April. The presence of reactive bromine seems to be the limiting factor for the occurrence of ODEs. The efficient destruction of ozone requires sunlight and due to the short day length early in the season an accordingly higher bromine mixing ratio is necessary to cause a strong or complete ozone depletion compared to later in the season. As discussed the model shows a slight overestimation of ambient BrO compared to satellite observations, so these established trends should be considered cautiously. However, the agreements of model and observations are very good nevertheless, both to satellite measurements as well and ground based observations (see sections 8.1 and 8.2). Since the trends seen in ambient ozone levels later in the season also agree with measurements (e.g. Wagner et al., 2007; Jones et al., 2013), it seems likely that the observed trend is indeed real.

In the model, the main pathway for the formation of reactive bromine in the absence of prior elevated reactive bromine mixing ratios is the ozone oxidation and this emission mechanism is rather slow (see Reaction (R32)) compared to the exponential bromine release from the bromine explosion (if enough reactive bromine is present). Therefore a limitation of reactive bromine as predicted by the model early in the season implies that stable meteorological conditions with a very shallow boundary layer will make the bromine explosion more likely. This follows from the fact that a stratified, shallow boundary layer facilitates the accumulation of the snow-pack emissions to a higher bromine mixing ratio, in turn allowing a faster release of fresh bromine from the bromine explosion as discussed in section 2.2.4.

This also coincides with one of the two sets of meteorological conditions favoring the bromine explosion, namely low wind speeds and a stable boundary layer (see section 2.2.4). Since the model does not consider emissions from blowing snow, higher wind speeds can not lead to additional emissions, hence these calm meteorological conditions are distinct for initial bromine release in the model. Nevertheless, the good agreement of model and observations already early in the season leads to the conclusion that blowing snow emissions only have a very minor influence on initial bromine release if at all (the select few cases where there is mismatch are discussed section 9.1). Additionally, it would also explain why most BrO columns predicted by the model as well as observed early in the season by satellite (see also section 9.3 as an example) only show small BrO enhancements. Even very large BrO mixing ratios could result in very small BrO columns if confined to a shallow enough boundary layer and as discussed in section 2.2.4, satellites might only be able to detect them reliably if they are transported to a region with a higher boundary layer height. This is discussed in the context of a case study in the next chapter, see section 9.3.

In contrast, later in the season the availability of reactive bromine in the Arctic region is strongly increased yet surface ozone is fully depleted in large parts, especially over sea ice. With an increased day length[2] far more bromine can be released via the bromine explosion. As discussed in section 2.2.3, aerosols can sustain reactive bromine concentrations for some

[2]For higher latitudes sunlight is available for the full day in late Arctic spring.

time (in the presence of ozone) and stable boundary layer conditions are far less important for the efficient release of reactive bromine. Instead the availability of ozone seems to be the limiting factor for bromine release[3]. This would imply that a stratified, shallow boundary layer could even be an obstacle to the formation of larger BrO columns as it would impede upon the entrainment of fresh ozone from the troposphere. On the other hand, the formation of significantly increased bromine mixing ratios in regions of an enlarged boundary layer becomes more probable with more reactive bromine being present and an increased day length, which would result in larger BrO VCDs. This is also predicted by the model as seen especially during April (see Figure 8.7f).

The formation of significantly enhanced BrO VCDs in the model therefore requires an increased (vertical) mixing of air masses enriched in reactive bromine and air masses not yet depleted in ozone as proposed first by Sihler (2012). As discussed in detail in section 2.2.4, higher surface wind speeds are indicative of a less stable boundary layer associated with increased vertical mixing from the troposphere, which could increase the amount of bromine released from both the surface as well as from aerosols. Together with an extended boundary layer this would also increase the likelihood for the formation of large BrO column as well as their detection from satellite. This is because a deeper boundary layer (oftentimes several 100 m deep) contains a larger ozone column, which can sustain a larger amount of reactive bromine, which itself can expand into a larger vertical column. As discussed in chapter 2, the rate of ozone depletion is quadratic in the BrO concentration and it begins to significantly increase at approximately 30 pmol mol^{-1}. This means that a deeper boundary layer can contain a significantly larger column even below the threshold when ozone depletion significantly increases. Likewise, synoptic scale weather events like polar cyclones and cold fronts associated with large BrO plumes observed from space (Sihler et al., 2012; Blechschmidt et al., 2016, e.g.) could also allow the uplift of air masses enriched in reactive bromine from the ground into the free troposphere, allowing the formation of strongly enhanced BrO columns. This assumption will be discussed further in section 9.2.

These meteorological conditions coincide with the other set of meteorological conditions assumed to favor bromine release and ODEs (see section 2.2.4 and Swanson et al. (2020)). In contrast to the conclusions drawn by Swanson et al. (2020) and others, the results discussed here indicate that, instead of new bromine emissions from blowing snow (which are not implemented in the model presented here), the increased mixing of air masses explain the influence of higher wind speeds on ODEs. This will be discussed more in the next chapter.

First of all it becomes apparent that the number of events detected by the algorithm increases significantly over the season. It stays almost constant for the first 45 days, from the beginning of February until mid of March, where the algorithm detects approximately 100 events each 15 days. Then it strongly increases reaching a peak of almost 1000 events in the time between mid of April and the beginning of May, from where on it starts to decrease

[3]It should be remembered that the bromine explosion reaction requires ozone for the formation of HOBr which releases new bromine from the halide ladden surface (see Reactions (R11 – R9)) or from bromide rich aerosol particles (see Reactions (R33 – R36)).

again. This also fits the trends predicted by the model, where the areas of enhanced BrO columns strongly increase from mid of March to the beginning of May (see section 8.3). As discussed this can probably be attributed to a combination of generally increased mixing ratios of activated bromine as well as to more bromine explosions taking place in a less shallow boundary layer, resulting in increased column densities.

From the seasonal trend in the bromine and ozone mixing ratios it is then possible to speculate that there should also be a seasonal character of the meteorological conditions favoring the occurrence of ODEs. Early in the season, the bromine emissions from the snow-pack seem of critical importance to provide a seed mixing ratio for the bromine explosion, which is supported by a stable boundary layer associated with low wind speeds. Later in the season, the release of fresh reactive bromine is limited more by the abundance of ozone and an increased mixing of air masses associated with a less stable boundary layer and higher wind speeds increases the likelihood of the formation of enhanced BrO columns.

This would also explain why all ODEs associated with cyclones and other synoptic scale weather events reported thus far (Begoin et al., 2010; Sihler et al., 2012; Blechschmidt et al., 2016; Choi et al., 2018, e.g.) have been observed in late March or April.

Moreover these findings agree well with results from Swanson et al. (2022). In their study they performed a number of different model runs using different sets of bromine emission mechanism. They reported that even with both snow-pack bromine release and SSA formation from blowing snow turned off, there are some ODEs predicted by the model agreeing with their observations (see also section 2.1.1). However, the BrO columns predicted by the model are strongly underestimated with both mechanisms turned off. Early in the season no significant bromine enhancements at all are predicted by their model with both mechanisms turned off. Adding only the SSA formation from blowing snow increases the BrO columns predicted later in the season marginally but does not lead to any increase in the bromine formation early in the season. Only by adding the bromine release from the snow-pack they could reproduce enhanced BrO columns measured earlier in the season.

Thus far there are almost no studies looking at an explicit seasonal trend of the correlation between ODE occurrences and meteorological conditions. Swanson et al. (2022) did only look at a six year aggregate of data and did not analyze specific monthly bins. Thus far, only Seo et al. (2019) analyzed a long-term data set of satellite data and calculated correlations to meteorological conditions separately for February, March and April. They did not find any significant correlations or trends besides a strong correlation to the tropopause height which did not change over the season. Unfortunately the use of total BrO VCDs calculated with a geometrical AMF (see eq. (4.22)) renders their results far less significant which is for example demonstrated by the strong tropopause height correlation.

In the next chapter, the assumed seasonality of meteorological conditions and the influence on the initial bromine release will be investigated in more detail using case studies.

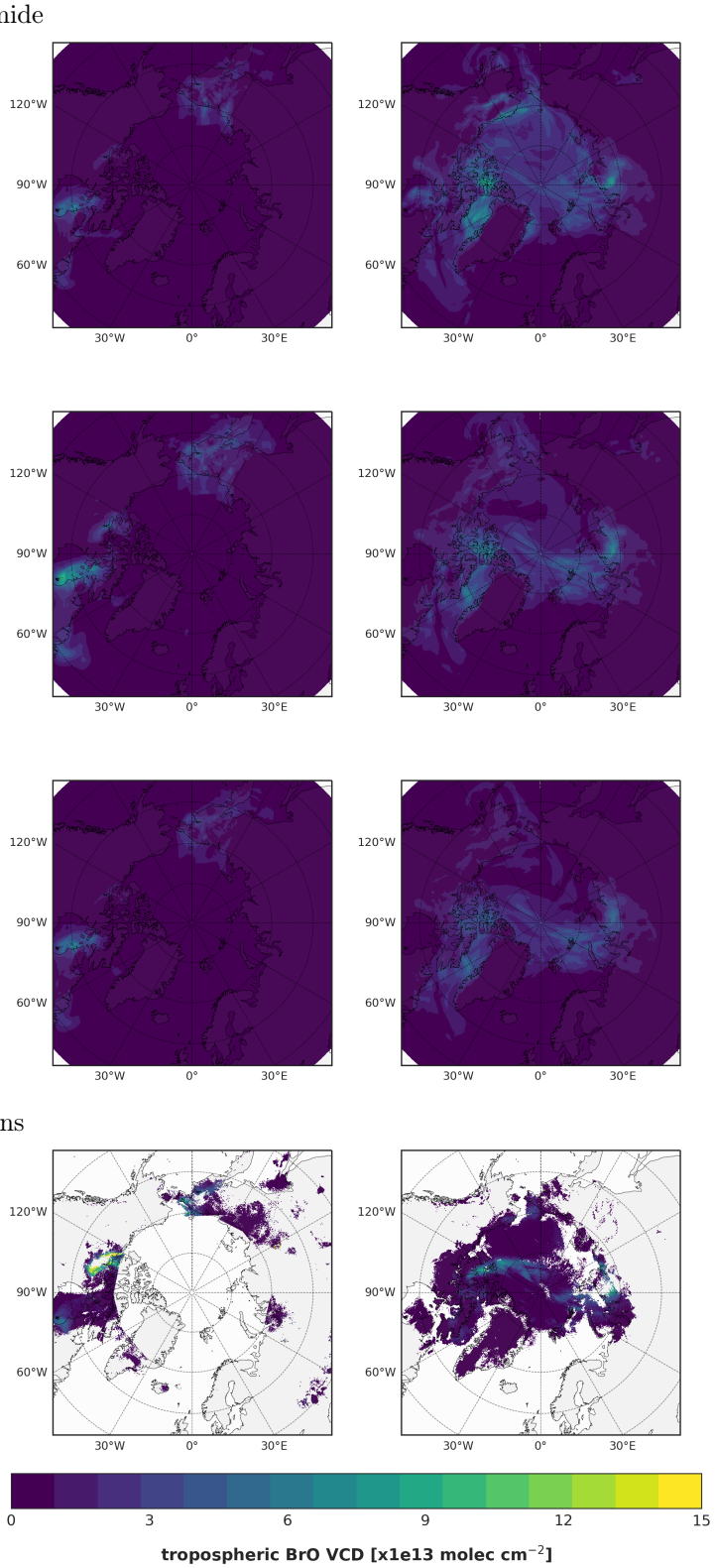

Figure 8.5: *Observed (bottom row) and simulated (rows 1-3) tropospheric BrO VCDs in 2019. Examples of tropospheric BrO enhancements measured by the satellite but not predicted by the simulations. From left to right: February 10, February 13, and April 24.*

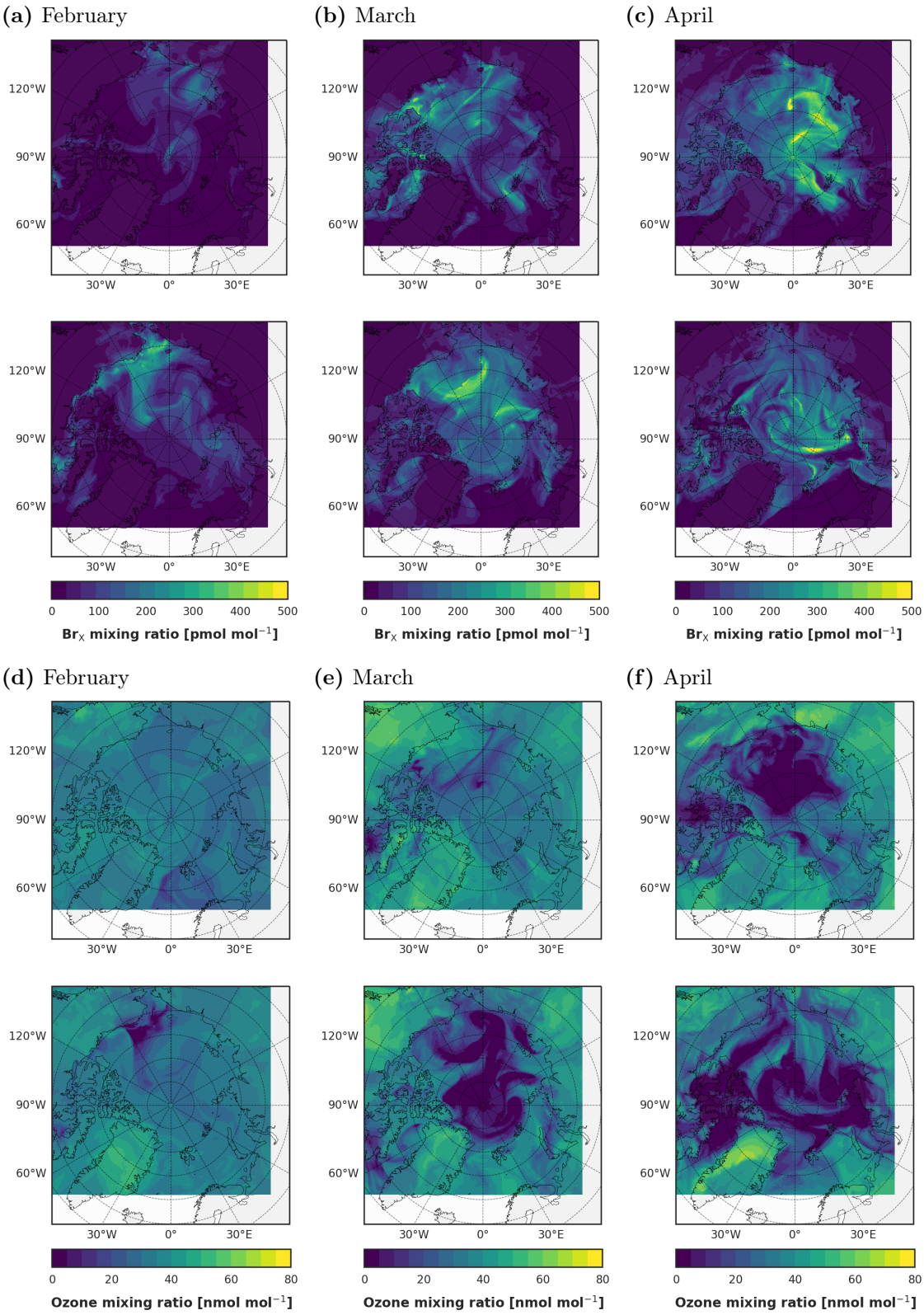

Figure 8.6: *Seasonal overview of simulated surface Br_X concentrations from February to April (a) - (c) and surface O_3 concentrations from February to April (d) - (f). In the top, the 5th of the corresponding month is shown. In the bottom, the 20th of the corresponding month is shown. The simulation time is always 22:00 UTC.*

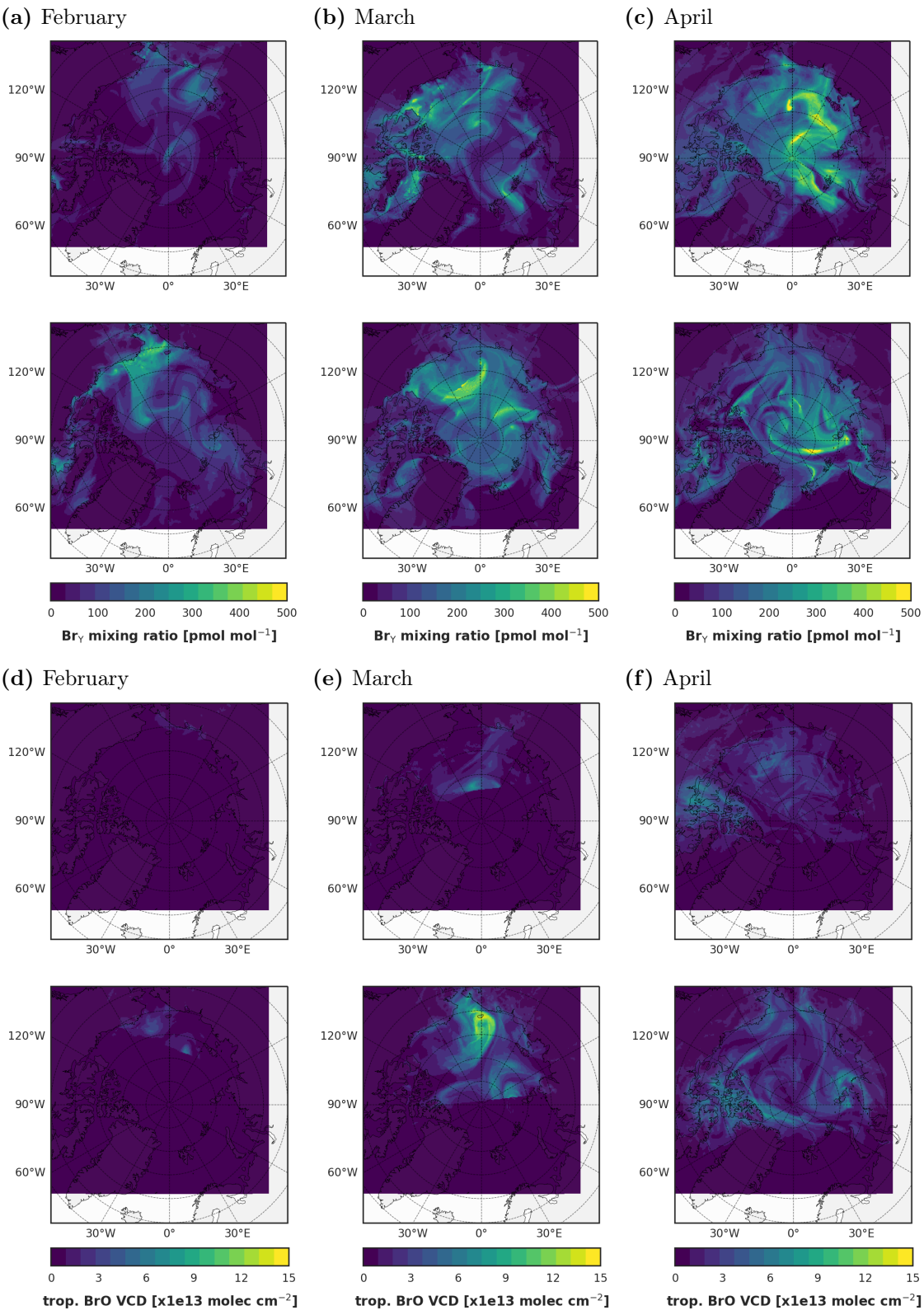

Figure 8.7: *Seasonal overview of simulated surface Br_Y concentrations from February to April (a) - (c) and tropospheric BrO VCDs from February to April (d) - (f). In the top, the 5th of the corresponding month is shown. In the bottom, the 20th of the corresponding month is shown. The simulation time is always 22:00 UTC.*

8.4 Summary

This chapter presented results of different WRF-CHEM simulations and compared them to available in-situ data and satellite observations of tropospheric BrO VCDs.

An alternative emissions scheme which is tracking the releasable bromide in surface snow based on Herrmann et al. (2022) was compared to previous schemes assuming an infinite bromide content in the snow covering FY sea ice. Two different bromide assumptions corresponding to low and medium amounts of initially releasable bromide were compared to the output of the infinite bromide assumption. Results were similar in February with increasing deviations in March and April. Both finite bromide emission schemes improve agreements to observations greatly, reducing overestimation of observed BrO VCDs as well as underestimations of ozone levels at the measurement stations. For stations near MY sea ice, best agreements were found using the medium bromide simulation. In contrast to the other two emission schemes, MY sea ice can emit larger quantities of bromine in the medium bromide scheme. This supports the findings of Peterson et al. (2019) that MY sea ice might also provide an important source of bromine for the bromine explosion. The finite bromide emission schemes also have improved agreements to satellite observations. Almost all instances of elevated BrO VCDs measured by TROPOMI were predicted by the model with a very good agreement in shape. The best quantitative agreement is found most often for the medium bromide simulation, whereas the low bromide simulation tends to underestimate BrO for some events. However, the medium bromide simulation overestimates general BrO levels more strongly later in the season and it performs worse at coastal sites such as Utqiaġvik and Pallas. For this reason the low bromide simulation is used for the case studies in the next chapter, which are all investigating events near the coast.

The model also shows a seasonal trend in the chemical constituents most relevant for ODEs with an increase of surface bromine mixing ratios towards April accompanied by a strong decrease of surface ozone mixing ratios. In February and beginning of March, an accumulation of a large enough bromine concentration seems to be a necessary prerequisite for the formation of large Br_x mixing ratios and a strong ozone depletion. The formation of large BrO columns observable from satellite then requires that these activated air masses also extend vertically over a greater height. This likely requires a very specific set of meteorological conditions, which first enables the accumulation of a sufficiently large Br_x mixing ratio followed or accompanied by appropriate vertical mixing. This would also explain why there are only few enhanced BrO events observed from satellites in early polar spring. In contrast later in the season an increased mixing with air masses not depleted in ozone seems to be a necessary condition for the development of large BrO VCDs. This also implies a seasonal trend in the meteorological conditions increasing the likelihood for an ODE, with calm conditions and a stable boundary layer favorable early in the season and high wind speeds and less stable boundary layers later in the season. This is discussed in more detail in the next chapter.

9 | Environmental influences on tropospheric BrO

In section 2.2.4 it was discussed that although a strong influence of meteorology on the occurrence of ODEs is undeniable, results regarding the exact nature of this influence have been inconclusive. Two sets of meteorological conditions have been identified to be closely associated with enhanced BrO in polar spring and the major debate currently revolves around the relative importance of both and corresponding initial bromine release mechanisms. Low surface wind speeds and a stable boundary layer are conjectured to provide an "enclosed reaction chamber" (Simpson et al., 2007a) for bromine emissions from the surface to accumulate. In contrast, high wind speeds associated to pressure gradients and increased turbulence in the boundary layer are thought to allow the emission of bromine from sea salt aerosols (SSA) produced via blowing snow.

The retrieval algorithm used to derive tropospheric BrO columns in this thesis is particularly suited to a comparison with other data sets, for example to study the relation of bromine activation and meteorological conditions. Since the retrieval does not rely on external data, it is also free of potential systematic biases from other sources. The sensitivity classification employed in the AMF calculation renders an underestimation of boundary layer BrO caused for example by clouds less likely. Thanks to TROPOMIs high SNR and unprecedented spatial resolution, the detection limit of the algorithm is considerably lower than previous versions using GOME-2 (cf. section 7.5) and the retrieval enables the detection of very small BrO vertical column densities down to $3 \times 10^{13}\,\mathrm{molec\,cm^{-2}}$. This also improves the detection of enhanced BrO mixing ratios confined to a relatively shallow boundary layer (approximately 105 m for the retrieval applied in this work) which is usually hard for satellite instruments (see the discussions in chapter 3 and sections 7.5 and 8.3 as well as Eq. (7.26)).

In the last chapter, results of a WRF-CHEM model were compared to satellite observations, demonstrating a high level of agreement. Although the possibility that the model does not approximate reality well still exists, as for example a wrong vertical profile of trace gases in the model could result in VCD comparable to that observed by the satellite, comparison with the model allows additional insights into potential release mechanisms and transport processes not accessible from the satellite measurements alone. This is leveraged

in this chapter to investigate three different ODEs associated with increased tropospheric BrO VCDs observed from satellite. The retrieved BrO columns are compared to different meteorological parameters suspected to influence the release and lifetime of reactive bromine on a regional scale.

The first section inspects an event in early February which is one of the few events not predicted by the model as mentioned already in section 8.2. Comparison of model and satellite observations together with data on the solar zenith angle allow insights into potential causes of the mismatch between simulation and measurement. Subsequently an extended BrO plume closely linked to the occurrence of a polar cyclone which is lasting over several days is investigated. Following that, an ODE observed very early in the middle of January is discussed. All case studies illustrate different aspects of the interconnection of meteorology and bromine activation events as well as a potential seasonal trend in that relationship as discussed in section 8.3. The results are then summarized at the end of the chapter.

Throughout this chapter, data from single satellite overpasses are used. This means that measurements shown are all (respectively) recorded during a single overpass of the satellite in a relatively short time frame (approximately 5 to 20 minutes). The model data is interpolated onto the time of the respective overpass as described in section 6.3.

9.1 Case study I - flawed snow-pack release mechanism in the model

In this section, a tropospheric BrO plume observed by the satellite over the coast of the Canadian mainland at February 10, near Victoria Island, located around 120° W and 120° N is investigated. The event in question was already briefly mentioned in section 8.2 as an example of a BrO enhancement observed by the satellite which is not mirrored by the simulation. The tropospheric BrO VCDs measured by the satellite are compared to results from the WRF-CHEM model. Furthermore, the observations are related to meteorological surface parameters, discussing potential explanations for the mismatch of simulation and measurements.

The plume can be seen first on satellite observations on 10 February at approximately 19:10 UTC. In Figure 9.1, satellite observations are shown together with results of the WRF-CHEM model for three days between 9 February and 11 February 2019. There, an extended plume stretching from the Amundsen Gulf over 1000 km inland into the Canadian mainland with VCDs up to $1.5 \times 10^{14}\,\mathrm{molec\,cm^{-2}}$ is observed.

Unfortunately, the sensitivity of the satellite observations is limited this early in the season at the location of the plume, mainly due to low light conditions. This results in a larger fraction of the measurements being classified as possibly obscured by the sensitivity classification (see section 7.4). As seen in Figure 9.1c, the SZA is 80° or larger at the location of the BrO plume on 10 February, thus reducing the sensitivity towards the lower layers of the

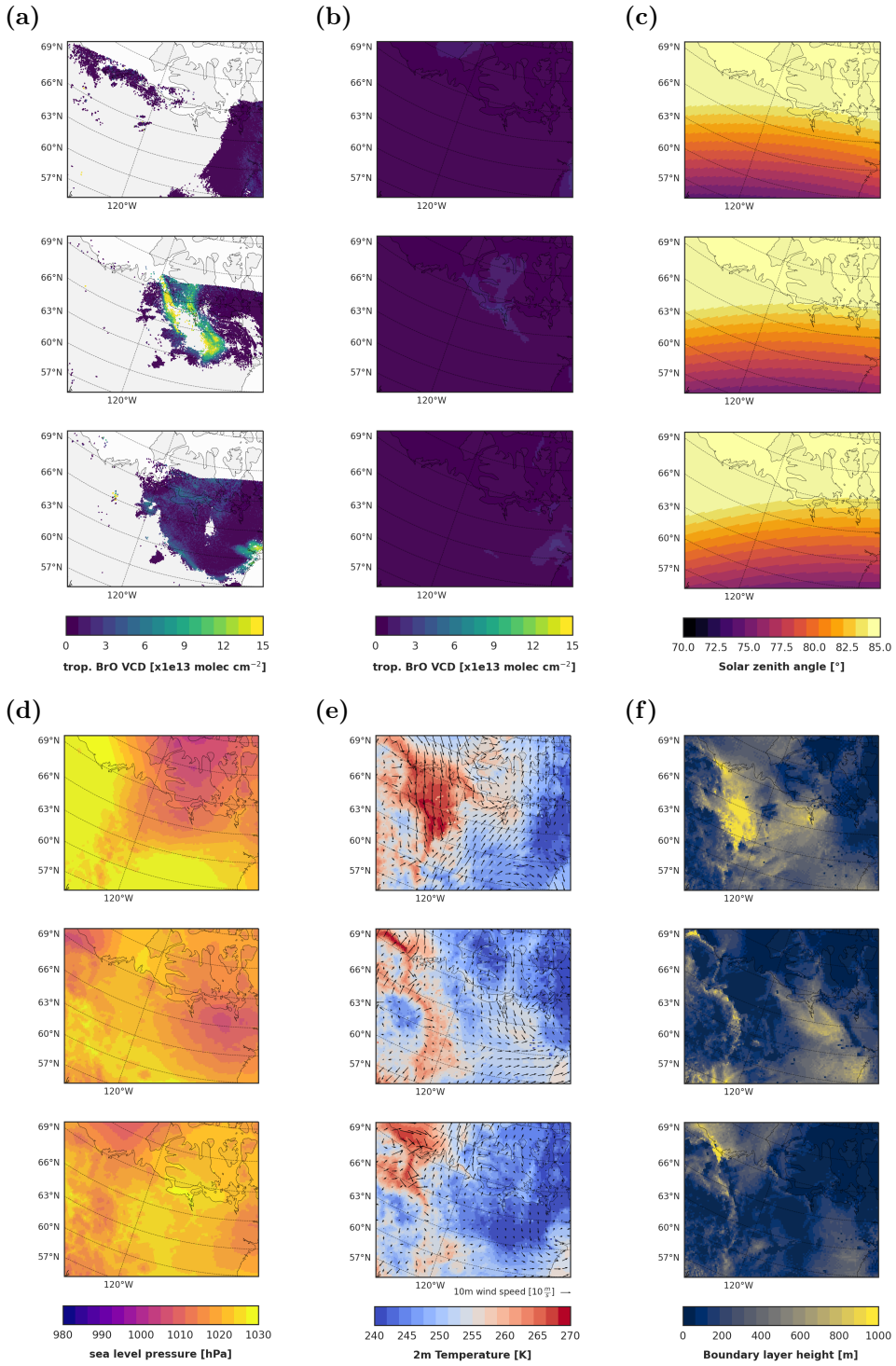

Figure 9.1: *Satellite observations and WRF-CHEM simulations of an ODE not reproduced by the model showing (a) TROPOMI tropospheric BrO VCDs, (b) modelled tropospheric BrO VCDs, (c) solar zenith angle, (d) sea level pressure, (e) air temperature at* 2 m *together with wind speeds at* 10 m *elevation and (f) boundary layer height. From top to bottom respectively are observations and simulations covering three different days: 9 February 2019 at 19:30 UTC, 10 February at 19:10 UTC, 11 February at 18:50 UTC.*

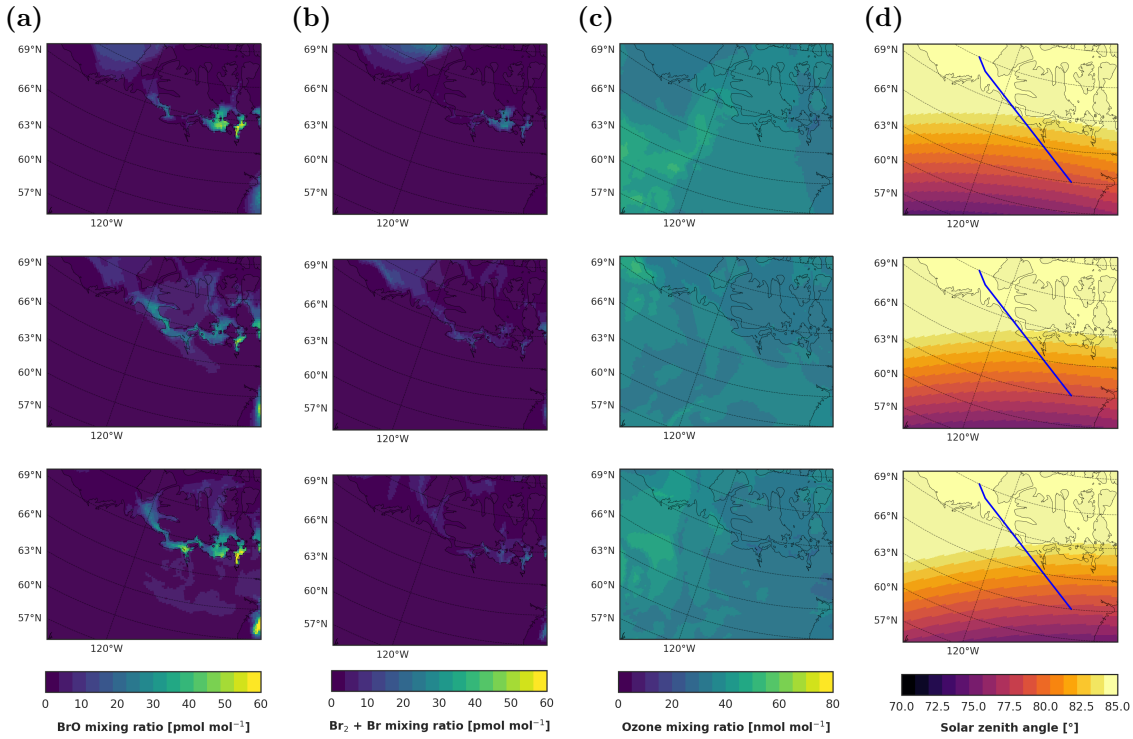

Figure 9.2: *WRF-CHEM simulations of an ODE not reproduced by the model showing (a) surface BrO mixing ratio, (b) combined surface Br_2 and Br mixing ratio, (c) surface O_3 mixing ratio and (d) solar zenith angle. The blue line indicates the cross section in Figure 9.3. From top to bottom respectively are simulations covering three different days: 9 February 2019 at 19:30 UTC, 10 February at 19:10 UTC, 11 February at 18:50 UTC.*

troposphere and rendering it more likely that satellite measurements are classified as possibly obscured. Additionally, as discussed in section 7.3.2, measurements with an SZA above 87° are all discarded , explaining the cutoff in the satellite observations at approximately 71° latitude.

For this reason, it is not possible to determine if an enhancement in tropospheric BrO was already present one day earlier on 9 February at 19:30 UTC or likewise if the plume originated even further north and is just advected. On February 11 at 18:50 UTC, the plume already dissolved in large parts, yet there is an enhancement visible in the east at the coast of Hudson Bay at 63° N. However, it is not possible from satellite observations alone to decide if this is simply an offshoot of the large plume on 10 February or a new BrO event. Nevertheless, it is expected that the BrO explosion terminates over land since there is very likely no bromide source available (see section 2.2.1).

An inspection of the meteorology (see Figure 9.1) allows a speculation about the origin of the BrO enhancement. The area close to the shore (approximately 71° N, 120° W, see Figure 9.1a) exhibits a very shallow boundary layer together with very low wind speeds. As discussed in section 2.2.4, these conditions are favorable for BrO enhancements, especially at the beginning of the season, allowing a faster accumulation of a high BrO mixing ratio

which could accelerate the BrO explosion. The area is also covered by FY ice as seen in Figure 6.1, a likely source of bromide (see section 2.2.1). In addition, surface temperatures in the area are very low, between $-15\,^\circ\,^\circ$C to $-20\,^\circ\,^\circ$C, which is also thought to support the release of reactive bromine from the surface, both by acidification of the surface as well as by influencing the equilibrium reactions between Br_2 and BrCl (see section 2.2.2). Therefore, this area seems a likely emission source of the BrO observed by the satellite. This is further supported by backward trajectories presented in Figure 9.4, which locate the likely origin of the BrO rich air mass over the Amundsen Gulf close to the shore.

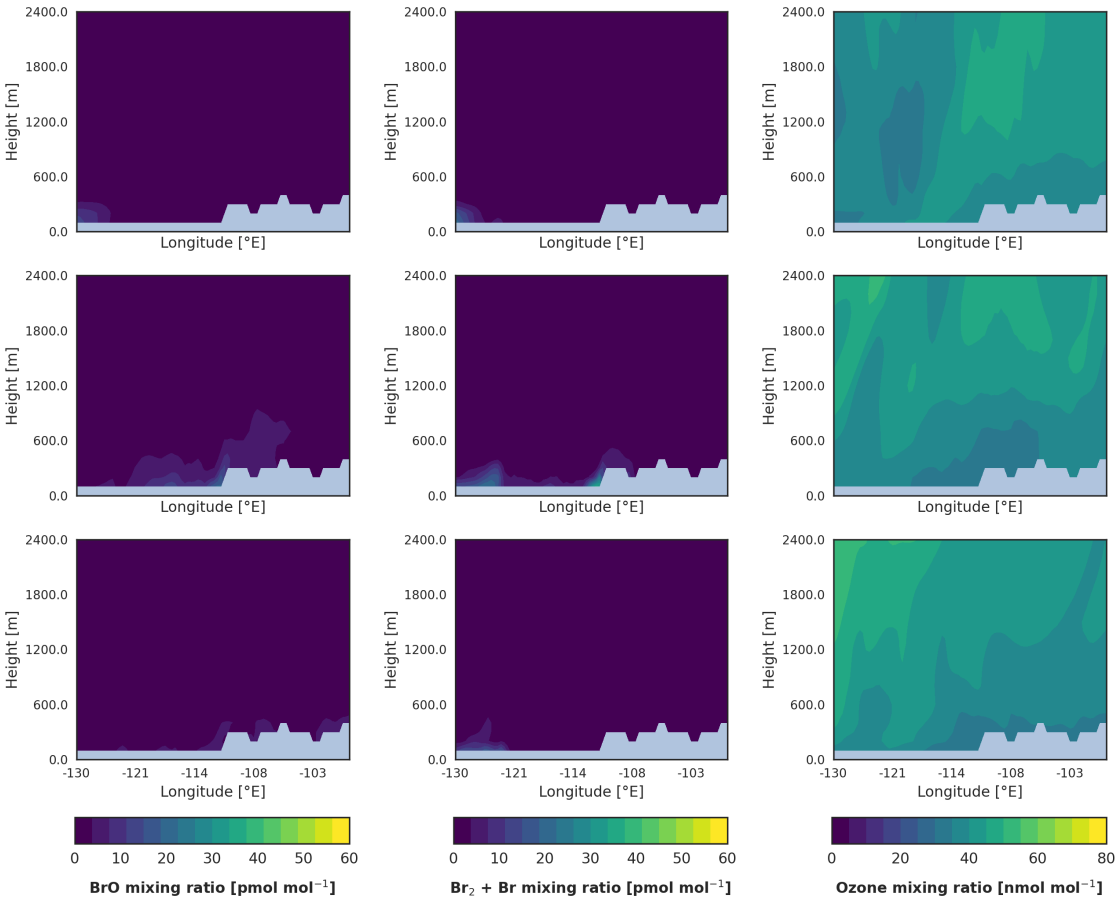

Figure 9.3: *Modeled vertical cross section of different trace gases. The area shaded in light blue is the landmass as assumed by the model. Note that the resolution of the topography in the simulation is limited as discussed in chapter 8. From left to right: BrO, the sum of* $2\,Br_2$ *and Br and* O_3 *for the Event on 10 February 2019. The cross sections are taken along the blue line in Figure 9.2d. From top to bottom respectively are simulations covering three different days: 9 February 2019 at 19:30 UTC, 10 February at 19:10 UTC, 11 February at 18:50 UTC.*

It should also be added that the winds, while rather slow over the sea ice area, increase in speed towards the coast, flowing towards the low pressure gradient. Additionally, the boundary layer height increases over land. These observations indicate a less strong separation between boundary layer and free troposphere and vice versa increased turbulent vertical

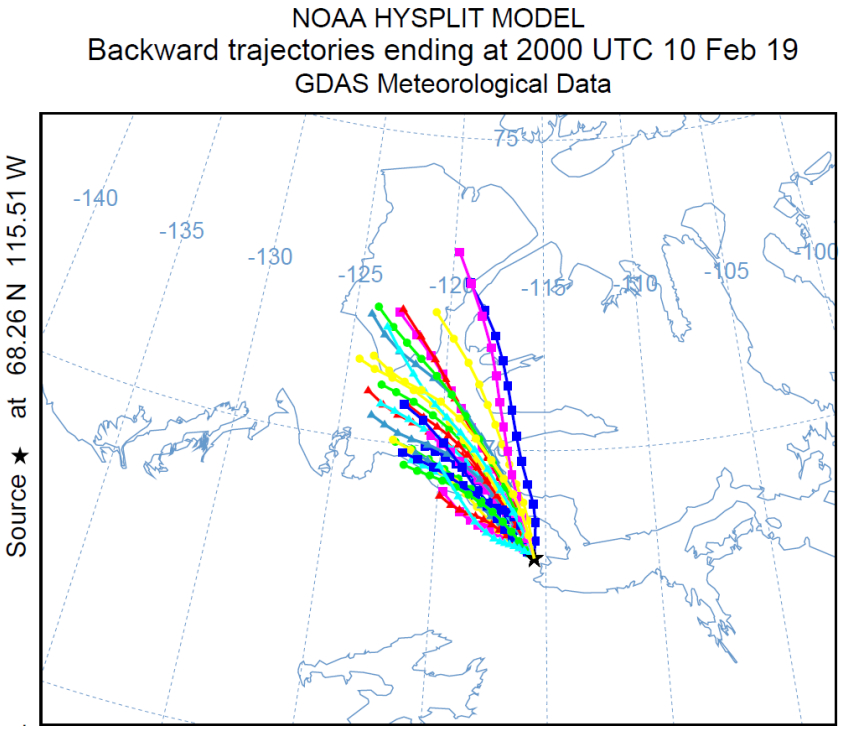

Figure 9.4: *Backward trajectories of air masses demonstrating the likely origin of the BrO enriched air mass seen in Figure 9.1a calculated using the HYSPLIT model (Stein et al., 2015). The different lines represent the different endpoint layer heights of the air mass, ranging from* 600 m *to* 10 m *layer height. The trajectories are calculated backwards in hourly time steps beginning at 20 UTC on 11 February 2019.*

diffusion. The wind direction also coincides strongly with the extent of the plume on 10 February. This could indicate that the air mass enriched in bromine over the sea undergoes an orographic lift and propagates aloft, where it is mixed with ozone-rich air as discussed in the last section. Following Peterson et al. (2017), this vertical uplift could also prolong the lifetime of the event, allowing the transport over a long distance, by allowing a recycling on aerosol particles over the land, independent of snowpack-driven halogen activation. This further supports the conjecture that the BrO originates over the FY ice in the Amundsen Gulf.

Yet, an inspection of the BrO VCD calculated from the WRF-CHEM model (see Figure 9.1b) shows almost no BrO enhancement at all in the VCD over all three days from 9 February to 11 February. This also excludes a potential time lag between model and observation. A very faint plume can be discerned, yet with a smaller extent than the observed BrO plume and VCDs below 4×10^{13} molec cm^{-2}. Figure 9.2 shows an enhanced concentration of up to 40 ppt BrO at the surface over the Amundsen Gulf. Yet, in Figure 9.3, a vertical cross section of O_3, BrO and its precursors Br_2 and Br is shown, where it can be seen that the concentrations decrease rapidly only a few meters above the surface. It is therefore apparent that bromine is emitted from the surface and a BrO explosion reaction is probably taking place close to the surface, meaning the conditions for an BrO explosion

reaction seem to be given also in the model. However, the amount of BrO produced in the model seems to be vastly underestimated. At the same time, ozone concentrations do not fall below 35 ppb even very close to the ground, so ozone can not be the limiting factor for the BrO production. Considering the shallow boundary layer and the generally very low wind speeds over the ice on 10 February, removal of bromine through transportation can also be ruled out.

Since the bromine explosion reaction cycle requires daylight, the BrO plume most likely developed between sunrise (approximately 16:50 UTC) and time of observation (19:10 UTC). Considering the short timeframe of only 2 hours since sunrise to observation, it becomes evident that there is simply not enough bromine present in the model to develop a large enough BrO concentration. Given the autocatalytic nature of the BrO explosion reaction cycle (it increases exponentially with the available BrO concentration, see section 2.1), a larger quantity of activated BrO species (discussed previously as "seed mixing ratio", see section 2.1.1), already has to be present for a large BrO VCD as observed by TROPOMI to develop. The model guarantees the presence of such a seed mixing ratio from which the BrO explosion can start under the right environmental conditions with different "trigger" reactions (see chapter 6), the most important being Reaction (R32), which emits Br_2 through the oxidation of bromide from ozone. This reaction depends only on the concentration of ozone in the atmosphere and bromide in the surface, not on the atmospheric bromine concentration (it has a somewhat linear relationship with the ozone concentration, cf. Figure 2.3).

There are five conceivable explanations for the lack of bromine in the model:

(i) An additional trigger reaction might be necessary to elevate initial bromine concentrations accordingly for the BrO explosion reaction cycle to take off. According to current knowledge the only serious candidate for such a trigger could be emissions from blowing snow as discussed in section 2.1.1. However, it seems unlikely that emissions from blowing snow could be responsible for that particular event, since wind speeds over the sea ice close to the coast, the most likely area of emission, are below the critical wind speed of $7\,\mathrm{m\,s^{-1}}$ and far below the wind speed of $10\,\mathrm{m\,s^{-1}}$ necessary for relevant blowing snow emissions (Yang et al., 2008; Marelle et al., 2021). Nevertheless, it cannot be ruled out that the stronger winds during the previous days transported SSA from sublimated snow land inwards and blowing snow over the land is the source of the BrO plume measured by the satellite.

(ii) As discussed previously, the bromide oxidation via ozone Reaction (R32) is the most important reaction for "triggering" bromine explosion reactions. It is possible that the assumptions regarding the dependence of this reaction on the solar influx are wrong. For an SZA above 85°, the emission of Br_2 is reduced to only 1.3 % compared to SZAs below 85° with an identical ozone dry deposition rate. An inspection of Figure 9.1c shows that regions previously identified as most likely emission source of the enhanced BrO have SZAs above 85°. Since this reaction is limited by the dry deposition rate of ozone, it is far too slow to produce a large BrO enhancement. However, it could

provide the necessary mixing ratio of Br_2 to accelerate the bromine explosion. Because this reaction is responsible for triggering most bromine explosions, especially early in the season, this seems to be the most probable explanation for the low initial bromine concentration.

(iii) An underestimation of actinic fluxes for high SZAs would lead to an artificially shortened day length. This could lead to a comparable effect as discussed for the SZA dependence of the trigger: the shortened day length would limit the time frame in which a bromine explosion can take place, which in turn would lead to an underestimation of the BrO column. Yet this seems unlikely, as such a systematic underestimation should also be visible in the comparison to in-situ data early in spring (see section 8.1), in particular with the increased temporal sampling compared to the satellite data.

(iv) In principle, there is another reaction capable of releasing bromine from the surface independent on the atmospheric bromine concentration via uptake of N_2O_5 (Reaction (R31)). An underestimation of the N_2O_5 concentration could therefore also reduce the amount of atmospheric bromine in the model. As discussed in section 2.1, the concentrations of the N_2O_5 precursors NO_2 and NO_3 are generally very low in the Arctic region and might be only increased by anthropogenic pollution. Therefore, an underestimation of air pollution could lead to an underestimation of the released amounts of bromine. This seems very unlikely though, since the nearest source of major pollution, the oil fields in Prudoe Bay, is several 1000 km away and even these are accounted for in the model.

(v) The necessary initial bromine concentration can of course be brought in from different parts of the arctic region via transport. Either a general underestimation of the bromine production throughout the whole region or an erroneous modeling of the meteorological processes underlying the transportation processes could therefore both be responsible for the lack of bromine in the investigated area. Considering the low amount of bromine present this early in the season and the fact that the model rather tends to overestimate the produced bromine compared (see chapter 8), the former seems unlikely. Since WRF is an established, well-tested meso-scale model shown to also produce very good results in arctic regions (e.g. Zaveri et al., 2008), the latter is also improbable.

As discussed, the most likely explanation for the observed discrepancy between model and observation seems to be the SZA dependence of Reaction (R32). This SZA dependence was chosen to account for the findings of Pratt et al. (2013), which measured no Br_2 emission from ozone without light as discussed in section 2.1.1.

However, our findings here seem to directly contradict this assumption or at least the hard cutoff implemented to represent it. Instead, it supports the proposal of Artiglia et al. (2017) that bromide oxidation from ozone at low light conditions could play a larger role for the bromine explosion. This is further supported by the results of ship-based measurement

campaign, which found enhanced BrO dSCDs even for SZAs close to 90° over Antarctic sea ice (Wagner et al., 2007).

This would also have implications regarding the initial release of bromine early in the season by implying a larger build-up of dihalogens under low light conditions or even during the night. This built-up Br_2 could then be photolysed at sunrise. Especially in a stable, shallow boundary layer, this would result in large BrO concentrations (assuming enough ozone is present), leading to a fast bromine explosion and a large BrO enhancement even at the beginning of the season when daylength is still short.

In the model, this could be remedied by relaxing the SZA dependence of Reaction (R32) or by an increase of emission rate of bromine under conditions of no light together with a decrease of the emissions below an SZA of 85°. This might also improve the general overestimation of BrO by the model all over the Arctic region discussed in chapter 6, which becomes more severe over time. As it was discussed in section 8.2, this could be the result of a missing sink term, but it could also be that too much bromine is emitted via Reaction (R32) in the model when daylength increases later in the season. Swanson et al. (2022) demonstrated that snow-pack bromine emission independent from sunlight can provide very similar results compared to the SZA dependent trigger if emission fluxes are adjusted accordingly and even reduce bromine overestimation in late March and April.

Because the Reaction (R32) together with the SZA cutoff from Toyota et al. (2011) is used by many different model descriptions of bromine emissions in polar chemistry (e.g. Toyota et al., 2011; Cao et al., 2016; Falk and Sinnhuber, 2018; Fernandez et al., 2019; Herrmann et al., 2020; Marelle et al., 2021; Herrmann et al., 2021; Swanson et al., 2022), these findings could potentially constitute a substantial improvement over current model implementations. It should be investigated if an SZA cutoff up to 93° is yielding better agreements, considering that the diffuse light present at such high SZAs should still be sufficient for the photolysis of Br_2 (peak absorption is approximately at 415 nm). Another possibility would be to test no SZA dependence at all, which could potentially lead to large build-ups of Br_2 reservoirs in the dark, which are then quickly photolysed at day. The emission probability has to be decreased accordingly, considering this leads to an overall increase of bromine emission.

9.2 Case study II - sustained BrO enhancement in a cold front

This section investigates a tropospheric BrO plume which developed over the Chuckchi Sea near Wrangel Island and was observed by TROPOMI for several days. The WRF-CHEM model also predicts the plume with very good agreement to the satellite observation. Use of the model allows to establish a link of the distribution of the BrO plume to a polar cyclone. Results of the chemistry model are then used to demonstrate an association of the enhanced BrO VCD to increased vertical lifting of bromine rich air along the cold front of the weather event.

The investigated ODE is very similar to an ODE associated with a polar cyclone previously investigated by Blechschmidt et al. (2016), both in shape, lifetime and origin. How-

ever, the case study presented here improves upon the investigations of Blechschmidt et al. (2016) by utilizing not only meteorological simulation results but also predictions by a halogen chemistry model. It is important to emphasize again that the WRF-CHEM model used here neither has added aerosol production from blowing snow nor does it allow emission of bromine from blowing snow or aerosols. Previous studies (Blechschmidt et al., 2016; Zhao et al., 2016; Choi et al., 2018) attributed the influence of weather events like polar cyclones and cold fronts to blowing snow.

Tropospheric BrO VCDs measured from the satellite are shown together with BrO VCDs and surface ozone mixing ratios from the model in Figure 9.5 over several days from 17 March 2019 to 21 March 2019. The WRF meteorological fields covering the same observational period are shown in Figure 9.6. In addition, a vertical cross section of BrO, O_3, the BrO precursors Br and Br_2, Br_x (excluding BrO) as well as aerosol density and several meteorological parameters are shown in Figures 9.7 and 9.8. The cross section includes pixels between 160° E and 130° W.

Sensitivity to the boundary layer is unfortunately limited in the first two days and the satellite first observes enhanced BrO VCDs on 18 March 2019 at 23:15 UTC while the model already predicts elevated BrO columns in form of a thin, extended line on 17 March 2019 at 23:30 UTC, with a maximum VCD of approximately 12×10^{13} molec cm^{-2} close to the shoreline. Additionally, there is also an area of slightly enhanced BrO columns between Alaska and Russia at approximately 165° W and 66° N, which can also be discerned on the few satellite pixels being classified as sensitive in the area.

The BrO plume observed on 18 March most likely developed between sunrise (approximately at 18:05 UTC) and the time of the observation at 23:15 UTC, since the bromine explosion reaction cycle requires sunlight (see section 2.1). Its shape looks very circular from the satellite, although the model predicts a more comma-like shape. However, the region where the plume expands towards Victory island is masked in the observations by the boundary layer sensitivity classification, so it is possible that the resemblance between model and reality could be even better. Comparison to the meteorological fields in Figure 9.6 shows that the small area of enhanced BrO VCDs seen in the model on 17 March was located to the northwest of a low pressure system (see Figure 9.6a) at an occluded front (identified by the temperature pattern in Figure 9.6d and Figure 9.6b).

Wind speeds at 10 m above the surface reach approximately 10 m s^{-1} at the front as seen in Figure 9.6d. Note that fronts and higher wind speeds indicate increased mixing of air masses and vertical lifting, which is in agreement with the increased atmospheric boundary layer height of approximately 600 m relative to the surrounding area (see Figure 9.6c). The low pressure area then moves northwards on 18 March, reaching minimum sea level pressure values of approximately 980 hPa. It coincides spatially with the large BrO plume measured from the satellite. The satellite measures vertical column densities of up to 1.5×10^{14} molec cm^{-2} at the center of the plume. In contrast, the model predicts a BrO VCD of about 9×10^{13} molec cm^{-2} over the whole plume region, therefore slightly underestimating the BrO column. The plume also strongly coincides with a potential temperature minimum

at the 850 hPa isobar with temperatures below 260 K as seen in Figure 9.6b. Surface temperature stays below 250 K in the plume area and wind speeds also remain generally high and follow the geostrophic flow along the low pressure system. The same holds true for the atmospheric boundary layer height, which generally remains above 600 m.

On 19 March at 22:55 UTC, the BrO plume is fully developed and strongly resembles a comma-shape as often associated with BrO plumes in cold fronts (e.g. Sihler et al., 2012; Blechschmidt et al., 2016). The BrO VCDs predicted by the model also increase and agreement between model and simulation is very good. The satellite now also observes an offshoot from the BrO plume which matches the shape of the cold air mass seen in Figure 9.6b. Wind speeds remain high towards the south end of the plume where maximum BrO VCDs are observed too, yet they decrease below $5\,\mathrm{m\,s^{-1}}$ above 75° latitude. This corresponds spatially to a decrease of the sea level pressure gradient, from which of course also a decrease of surface wind speeds can be expected. Accordingly the boundary layer height is also decreasing northwards of the BrO plume maximum. Surface ozone is largely depleted in the region of enhanced BrO VCDs.

On 20 March, the plume was transported further north-eastwards which is also predicted by the simulation. Observations and model predictions again agree very well, both showing a dilution of the plume with VCDs reaching approximately $10^{14}\,\mathrm{molec\,cm^{-2}}$. Yet the model shows a BrO VCD maximum in the plume which is slighty more pronounced, with an increase of about $2 \times 10^{13}\,\mathrm{molec\,cm^{-2}}$ above the satellite measurements. The surface ozone mixing ratio is largely depleted in the area where the plume resided the day before, however a large fraction of the plume is now located just south of the area where the surface ozone is completely destroyed. The low pressure system has weakened and the plume seems to have followed the wind directions north-eastwards as indicated in Figure 9.6d. Wind speeds stay above $7\,\mathrm{m\,s^{-1}}$ to $8\,\mathrm{m\,s^{-1}}$ in the area of the BrO plume while potential temperature at the 850 hPa isobar still shows a minimum below 260 K coinciding with the BrO plume. The boundary layer height is decreasing compared to the previous day but it is still elevated compared to its surroundings with an approximate height of 400 m in the regions of enhanced BrO VCDs.

Finally, on 21 March the plume moved farther north-eastwards. Column densities inside the plume decreased further, both for the satellite measurements as well as for the model predictions. Westwards of the plume, in the region of enhanced bromine activity in the days prior, lies an extended area which is completely void of surface ozone according to the WRF-CHEM simulation. The surface ozone mixing ratio in the location of the BrO plume is also severely depleted and lies below $10\,\mathrm{nmol\,mol^{-1}}$. The BrO plume seems to have been transported along with the cold air mass seen in the potential temperature at 850 hPa in Figure 9.6b towards the horizontal pressure gradient. This gradient has decreased further and subsequently wind speeds and the boundary layer height also decreased. Particularly the latter has become very shallow with heights below 100 m almost over the complete area shown in Figure 9.6c.

On 22 March (not shown), the plume has dissolved completely and is neither observed by

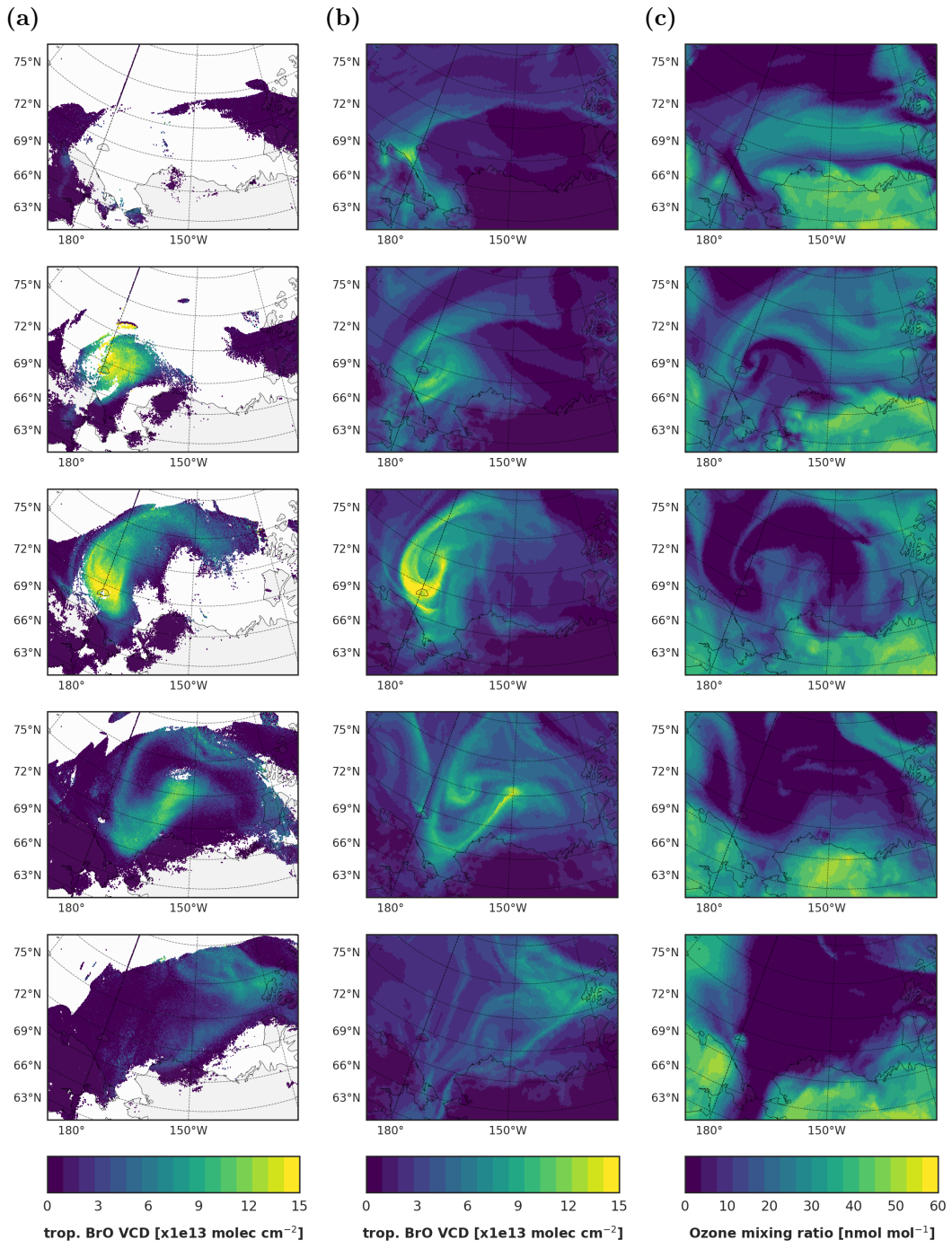

Figure 9.5: *Satellite observations together with WRF-CHEM simulation results for the ODE showing (a) TROPOMI tropospheric BrO VCDs, (b) modelled tropospheric BrO VCDs and (c) surface O_3 mixing ratio. From top to bottom respectively are observations and simulations covering five consecutive days: 17 March 2019 at 23:30 UTC, 18 March 2019 at 23:15 UTC, 19 March 2019 at 22:55 UTC, 20 March 2019 at 22:35 UTC and 21 March 2019 at 22:15 UTC.*

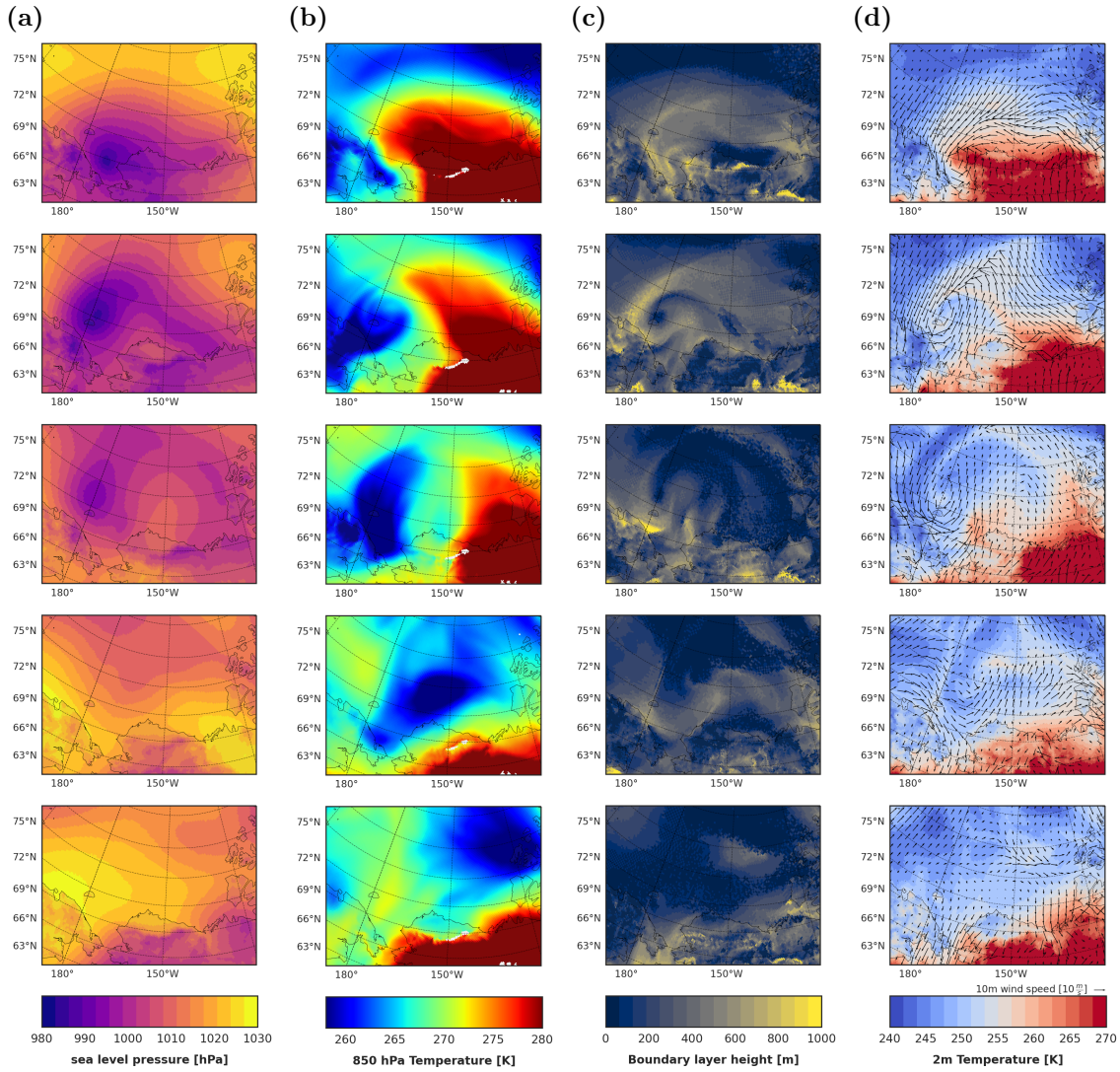

Figure 9.6: *WRF meteorological simulations for the ODE showing (a) sea level pressure, (b) equivalent potential temperature at* 850 hPa*, (c) atmospheric boundary layer height and (d)* 2 m *temperature combined with* 10 m *wind speed. From top to bottom respectively are simulations covering five consecutive days: 17 March 2019 at 23:30 UTC, 18 March 2019 at 23:15 UTC, 19 March 2019 at 22:55 UTC, 20 March 2019 at 22:35 UTC and 21 March 2019 at 22:15 UTC.*

the satellite nor predicted by the model. An inspection of meteorological fields shows that horizontal pressure gradients and correspondingly wind speeds decreased even more and the area showing an enhanced BrO VCD on 21 March is completely void of surface ozone in the WRF-CHEM simulation.

The very good agreement between the two independent data sources is impressive. The retrieval algorithm utilized in this thesis also gives a high confidence that the BrO signal observed by the satellite has indeed a tropospheric origin and the precise AMF calculation allows a good estimate of the sensitivity towards the boundary layer. Concurrently, the BrO plume predicted by the model does not only agree well in the lifetime, shape and location to the plume observed by the satellite, it also has good quantitative agreement with an exception on 19 March, when the VCDs in the center of the plume are underestimated by the model.

In addition, a comparison to meteorological parameters of the WRF weather simulation allows the conclusion that this ODE is closely associated to a polar cyclone. It is therefore very similar to previous observations of enhanced BrO VCDs in the context of meso- or synoptic scale weather events (e.g. Sihler, 2012; Blechschmidt et al., 2016). However, in contrast to previously published case studies, the additional simulation of the tropospheric halogen chemistry enables additional insights in the underlying chemical mechanisms for the bromine release. Previous ODEs observed in relation with cold fronts and Arctic cyclones were proposed to be heavily affected by aerosols from blowing snow, yet the WRF-CHEM simulation used here does not include aerosol production from blowing snow. An additional first-time investigation of the vertical structure of such an ODE associated with a polar cyclone allows an even deeper insight into the formation of enhanced BrO VCD in these extreme weather events.

Figure 9.7 shows vertical cross sections of the potential temperature, the sea level pressure and the atmospheric boundary layer height along the white line between 160° E and 130° W shown in Figure 9.7a from 17 March 2019 up until 21 March 2019. Additionally, Figure 9.8 shows a vertical cross section of the mixing ratios of BrO, Br_x (except BrO)[1] and O_3 as well as the sum of the mixing ratios of the BrO precursors Br and Br_2 along the same path. Furthermore, the aerosol surface density is shown in Figure 9.8e. It is given by the sum over the surface density of all relevant aerosol species for the bromine chemistry,

$$\rho_A = \sum_b \sum_i 4\,\pi\, r_b^2 \cdot n_{i,b}\,. \tag{9.1}$$

Here ρ_A describes the resulting surface density, $n_{i,b}$ is the number density per volume of the aerosol species i in the aerosol size bin b and $r_{i,b}$ is the respective radius of an aerosol particle of species i in size bin b. The aerosol surface density gives a good approximation for the probability of reactive bromine recycling on aerosols. It should be noted again that no additional aerosols are produced from blowing snow in the model.

[1] Br_x denotes the combination of all reactive bromine components, here with the exception of BrO. See section 8.3 for a detailed list.

On March 17, the sea level pressure shows a weak gradient in the cross section (see Figure 9.7c) as it proceeds in part through the low pressure system seen in Figure 9.6a. The boundary layer is generally deepened with heights (see Figure 9.7d) ranging from 200 m to 400 m in regions of enhanced BrO mixing ratios (see Figure 9.7d). The enhanced BrO concentrations are located inside the boundary layer and largely close to the ground. Enhanced BrO mixing ratios are vertically most extended near the minimum of the pressure gradient, showing strongly increased concentrations elevated more than 300 m. This peak in the vertical extent is also corresponding to the thin "line" of enhanced BrO VCD of around 7 molec cm^{-2} seen in Figure 9.7a at 72° N and 180° E. Since ozone levels inside the boundary layer are still around 25 ppb in that region, it is likely that even more BrO is emitted until the next day. This is likely the seed mixing ratio enabling the large BrO plumes observed in the following days. Since the model does not allow additional bromine release from blowing snow, BrO formation occurring in the frontal mixing has to be fast in order to explain the large BrO columns formed in the following days as well as the high spatial correlation between meteorology and chemical plume formation. The high mixing ratio of reactive bromine present in the boundary layer on 17 March could provide high enough mixing ratios for a fast bromine release from the surface during conditions of high lifting and an increased influx of fresh ozone to the surface.

In stark contrast to the vertically depressed BrO concentrations on the day prior, the enhanced BrO mixing ratio extends vertically for more than 1000 m on 18 March. The vertical expanse of the BrO enriched air mass seems to coincide with a decrease in the potential temperature gradient seen in Figure 9.7b which is probably indicating a cold front. This would also explain the sudden, strong vertical elevation of the bromine rich air, which is seen both in the BrO as well as in the Br_x mixing ratio, as fronts indicate vertical lifting. It also coincides with the moved low pressure (see Figure 9.6a) system through which the cross section is proceeding. In Figure 9.7c a strong pressure gradient can be seen, reaching as low as 990 hPa, which is reflected in a gradient in the boundary layer height (see Figure 9.7d). The atmospheric boundary layer is very deep over the low pressure system except for a small region in the center of the polar cyclone above Iultinsky District, decreasing below 200 m consistent with the low wind speeds in the center of the low pressure system (see Figure 9.6d). Outside of this region it increases sharply to 400 m or above along the pressure gradient. In general, reactive bromine shows an increased mixing ratio even far above the boundary layer (see Figure 9.8a and Figure 9.8c indicating strong vertical mixing, yet the decrease in the boundary layer height is mirrored by a decrease of the BrO VCD in the model (see Figure 9.7a). In the vertical cross section this is reflected in a decrease of the vertical extent of enhanced BrO mixing ratios, while it simultaneously allows a strong increase of the BrO mixing ratio inside the boundary layer as seen in Figure 9.8a. However, this is decrease of VCDs is not seen in the satellite observations (see Figure 9.5a) and neither is a similar "hole" in the model BrO VCD on 19 March. It could be possible that the boundary layer AMF is underestimating sensitivity, as it assumes that BrO is concentrated in the lowest 500 m and it is therefore overestimating the actual BrO VCD. This seems unlikely however, as the

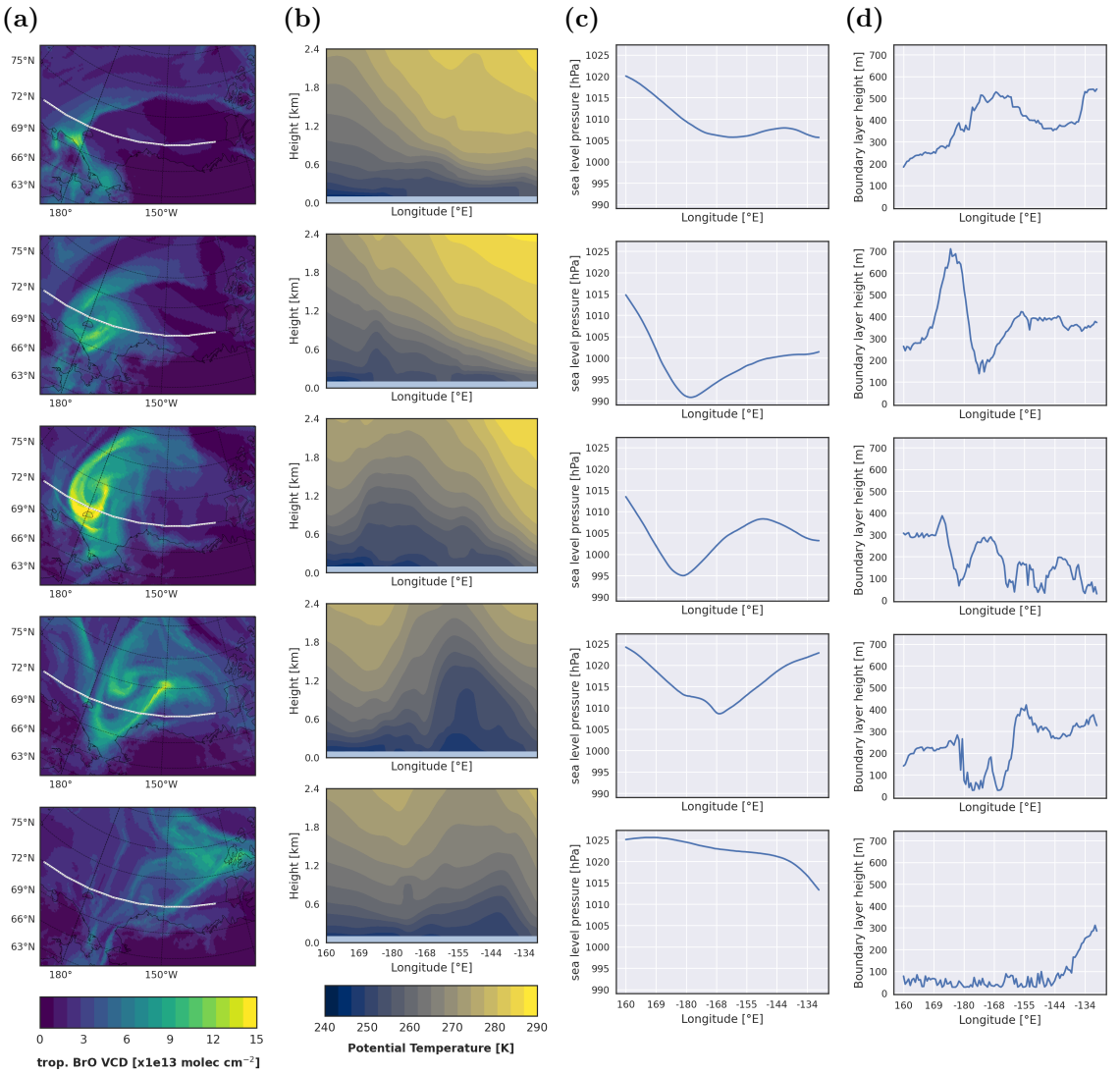

Figure 9.7: *Cross section of different meteorological parameter taken along the white line in Figure 9.7a. From left to right: (a) BrO VCD visualizing the cross section, (b) potential temperature, (c) sea level pressure and (d) atmospheric boundary layer height. From top to bottom respectively are simulations covering five consecutive days: 17 March 2019 at 23:30 UTC, 18 March 2019 at 23:15 UTC, 19 March 2019 at 22:55 UTC, 20 March 2019 at 22:35 UTC and 21 March 2019 at 22:15 UTC.*

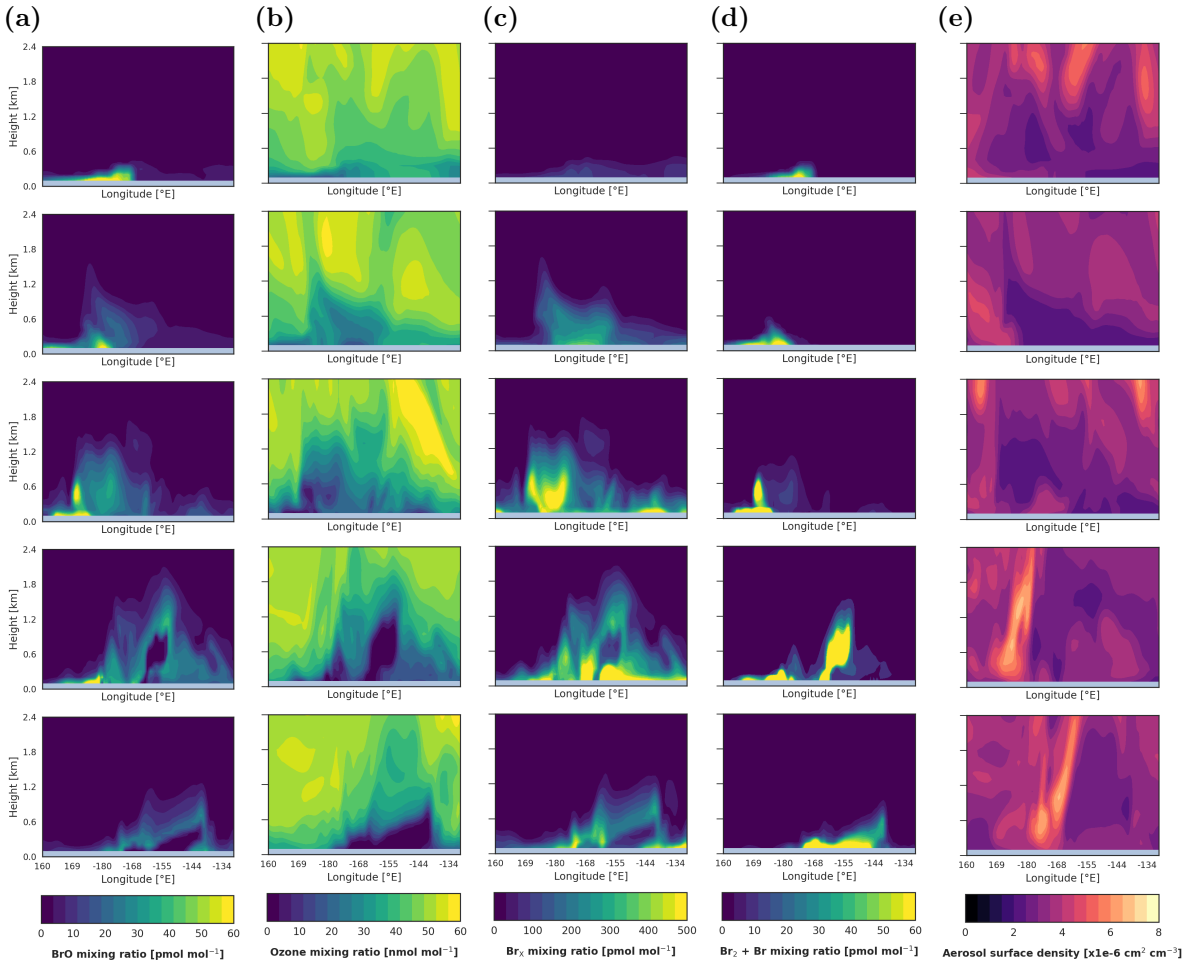

Figure 9.8: *Vertical cross section of different trace gases and aerosol density. The area shaded in light blue is the landmass as assumed by the model. Note that the resolution of the topography in the simulation is limited as discussed in chapter 8. From left to right: (a) BrO mixing ratio, (b) O_3 mixing ratio, (c) Br_x (excluding BrO) mixing ratio, (d) the sum of mixing ratios of Br_2 and Br and (e) the aerosol surface density. The cross sections are taken along the white line in Figure 9.7a. From top to bottom respectively are simulations covering five consecutive days: 17 March 2019 at 23:30 UTC, 18 March 2019 at 23:15 UTC, 19 March 2019 at 22:55 UTC, 20 March 2019 at 22:35 UTC and 21 March 2019 at 22:15 UTC.*

influence of the actual BrO scale height on the AMF is limited as discussed in section 7.5. It is therefore possible that the influence of the boundary layer height on the BrO VCD is overestimated in the model. Another explanation could be a slight overestimation of bromine formation at the surface, leading to an overestimated destruction of ozone in the area. The "gap" in the plume is surrounded by a large area of depleted ozone, especially towards the north. This also limits horizontal diffusion of ozone rich air, in turn limiting the supply of ozone. If surface bromine emissions in the days prior were slightly overestimated in a shallower boundary layer, this reduced ozone levels do impede upon the release of bromine from the surface in the deeper boundary layer, where more ozone would be available to sustain a larger column (see section 8.3). The high Br_x mixing ratio above the ground indicates strong bromine release from the surface. The maximum of the Br_x concentration is found near the sea level pressure minimum, inside the depressed boundary layer. While there are areas of less depleted ozone to the south of the plume, these are all outside the polar cyclone, which is likely causing low horizontal and vertical diffusion coefficients.

Interestingly, the aerosol surface density shows a sudden decrease beginning at the west of the low pressure system. The low aerosol surface density in the area of enhanced reactive bromine could explain the quantitative mismatch between model and satellite observation, since a low aerosol surface density would result in decreased emissions of reactive bromine from halide ladden surface. This holds especially true for air masses above the boundary layer with no contact to the surface. There, reactive bromine concentrations can only be sustained (and induce the release of new bromine) from heterogeneous reactions on aerosols as described in section 2.2.3. Since the high wind speeds in the low pressure system likely lead to blowing snow conditions, it would be possible that additional SSA production from blowing snow in the model could increase BrO production on aerosols and therefore decrease the underestimation of BrO VCDs on 18 March.

On 19 March, the plume has stabilized and Figure 9.8a shows enhanced BrO concentrations above 1000 m over a wide area along the cross section. The Br_x mixing ratio shows a very similar pattern with a distinct maximum again at the minimum of the pressure gradient along the cross section. A very shallow boundary layer is also seen in that area with a boundary layer height below 100 m. The boundary layer height again shows a gradient following the pressure gradient. However, with a decreasing horizontal pressure gradient, wind speeds are also decreasing as discussed above, which explains why the boundary layer remains more shallow and stays below 300 m almost along the complete cross section. Another localized maximum of reactive bromine concentration is found near 140° W, yet here it coincides with a deepened boundary layer, extending up to 300 m.

The higher vertical extent of reactive bromine coincides with a decreased vertical gradient in the potential temperature, with potential temperatures below 250 K extending above 1 km. There are different explanations for this correlation. As discussed in section 2.2.2, release of bromine seems to be favored by cold temperatures and Sander et al. (2006) found that recycling of BrO on aerosols is also most efficient at low temperatures. However, the aerosol surface density is still low over large parts of the area of enhanced reactive bromine

mixing ratios, so it is questionable if this potential influence on reaction dynamics by the temperature causes this correlation. Since satellite observations and model predictions agree very well on this date, it is also possible that the increased vertical lifting indicated by the decrease in potential temperature agreement is enough to explain the correlation between reactive bromine mixing ratios and potential temperature.

This is also the first day where a full depletion of ozone concentrations is predicted by the model in a small area to the east end of the low pressure system. Interestingly, this coincides with a strong increase in the mixing ratios of all reactive bromine species shown in Figure 9.8. This is in contrast to later days where BrO concentrations are depressed in regions of depleted ozone as discussed below. More generally it can be observed that the reactive bromine lofted above the boundary layer also leads to a strong decrease of ozone concentrations even above 1 km height.

On 20 March and 21 March, the sea level pressure gradient vanishes almost completely over the period of two days. As seen in Figure 9.6d, this also leads to a decrease of wind speeds and a more shallow, stable boundary layer. While the weak pressure gradient present on 20 March still coincides with a gradient in the boundary layer height (up to 400 m), the latter stabilizes on 21 March and decreases below 100 m along most of the cross section. A similar trend can also be seen in all bromine mixing ratios (see Figure 9.8) and the potential temperature cross sections.

Interestingly, the potential temperature gradient becomes even weaker on 20 March compared to previous days although the cyclonic activity is decreasing. This seems to correspond to a further increase in vertical lifting, since BrO and Br_x show enhanced mixing ratios as high as 2 km, extending even far above the deeper parts of the boundary layer here. This is mirrored by a decrease of the ozone concentrations. The aerosol surface density also shows an increase. It could be reasoned that this is a necessity to sustain such high BrO concentrations so far above the surface. In Figure 9.8a an interesting structure in form of a large "bubble" of very low BrO mixing ratio can be seen, which is extending up to heights of 1 km. This structure is mirrored closely by a "bubble" of completely depleted ozone concentrations. An inspection of the Br mixing ratio in Figure 9.8d shows that there is a large reservoir of reactive bromine components, therefore this structure of low BrO mixing ratio is likely caused by a lack of ozone. It is possible that this strong depletion of ozone was caused by the large structure of strongly increased Br_x seen on the day before in the vertical cross section (see Figure 9.8c) and which is advected there. A comparison with the wind fields (see Figure 9.6d) seems to support this. On the day after, 21 March, the potential temperature stabilize compared to the surroundings and with it a large fraction of the reactive bromine has vanished in the model. Ozone is fully depleted over the surface for a large part of the cross section. From 160° W up to 140° W this depletion extends up to 600 m. As on the day before, BrO concentrations are extremely low in that area while Br and Br_2 mixing ratios remain high, indicating again that ozone is the limiting factor in the formation of new BrO. Mixing ratios of Br_x also strongly decreased in comparison to prior days.

On 22 March, there are no longer enhanced BrO VCDs measured by the satellite and only very small enhancements in BrO predicted by the model as discussed above. Proceeding from the vertical cross sections of the trace gases on 21 March (see Figure 9.8), this seems intuitively clear: ozone above the surface where reactive bromine concentrations are still comparatively high (see Figure 9.8d) is completely destroyed. This then strongly inhibits the release of new bromine from a potentially bromide laden surface, leading to a net removal of activated bromine from the atmosphere (usually over the course of hours, see section 2.1). This seems particularly plausible if one takes the very shallow boundary layer into account that formed on 21 March (see Figure 9.7d).

The strong decrease of reactive bromine seems to be coincidental with the increase in the vertical potential temperature gradient and the vanishing of the pressure gradient. A vertically very extended BrO plume on 20 March was in large parts reduced below 800 m on 21 March, although the aerosol surface density heavily increased compared to 19 March (see Figure 9.8e). It is likely that the calm meteorological condition that followed the normalizing of the sea level pressure severely decreased the vertical (and horizontal) mixing of air masses. In particular the missing influx of fresh ozone to the surface inhibits the formation of new BrO and therefore the release of new bromine from the surface. On the other hand, BrO VCDs are strongly reduced if reactive bromine is not mixed into the free troposphere which is potentially resulting in larger columns and can extend the lifetime of activated bromine in the atmosphere.

This leads to the conclusion that the increased vertical lifting and the generally decreased atmospheric stability associated with the low pressure system exerted a favorable influence on the formation and the lifetime of atmospheric reactive bromine. For example, it is conceivable that the occluded front formed by the low pressure system is lifting and mixing air masses enriched in reactive bromine into the free troposphere while simultaneously bringing fresh ozone to the surface as proposed by Sihler (2012). Likewise, a horizontal transport and mixing of activated bromine into regions of yet undepleted ozone is also consistent with the predictions by the model. A similar horizontal transport of fresh ozone would also allow the formation of higher BrO VCDs and increase the lifetime of BrO plumes.

There are a few more interesting observations to be made. First of all, the combined mixing ratio of the BrO precursors Br and Br_2 shows two interesting distinct patterns. In some cases, the maximum mixing ratio of Br is found at the minimum of the BrO mixing ratios such as on 20 March or 21 March. It was discussed that this is likely due to low ozone levels limiting the formation of new BrO. On the other hand, there are days such as 17 March or 19 March when the maximum mixing ratio of BrO and its precursors Br and Br_2 coincide while simultaneously no Br is found in regions of medium to low BrO concentrations. As discussed in section 2.1, the rate limiting step for the BrO explosion is usually the BrO self-reaction((R2)). With lower BrO mixing ratios, the rate of this reaction, which is quadratic in the BrO concentration, is likely lower than the rate producing new BrO from the reaction of Br with O_3. However, if the BrO mixing ratio is very high, the production of Br is increased and potentially faster than the reaction linear in the Br concentration, which seems as the

most likely explanation for this observation.

The ODE observed here also shows no strong dependence on the surface temperature. Enhanced BrO VCDs are only found above surfaces below 270 K, but other than that there seems to be no clear trend towards colder temperatures (see section 2.2.2). However, this is in agreement with Swanson et al. (2020), as they reported no dependence on surface temperatures (other than that ice should not melt, so below 273 K) for events associated with low pressure systems and high wind speeds.

It is interesting to see that the BrO plume consistently coincides with the cold air mass at the 850 hPa isobar and seems to move with it. An influence of the temperature on bromine emissions from or recycling on aerosols in the model seems unlikely, as the aerosol surface density is low at the location of the BrO plume as discussed before. The most likely explanation for this is that the potential temperature gradient at 850 hPa indicates a region of high vertical lifting or an occluded front. This can then extend atmospheric bromine lifetime through mixing with air masses undepleted in ozone on the one hand and increase the supply of fresh ozone to the surface on the other hand, thereby allowing more bromine to be released from the snow-pack via the bromine explosion reaction as discussed before.

In conclusion, the high degree of agreement between model and satellite observation allows the following inferences. First of all, the increase of vertical lifting of reactive bromine from the surface as well as the stronger vertical mixing caused by such meso-scale weather events exerts a high influence on the the formation of the high BrO VCD observed from satellites in relation with such events as proposed first by Sihler (2012). Conversely, the influence of additional SSA from blowing snow on these events does seem to be limited, especially if the findings of Marelle et al. (2021) are taken into account, which showed that bromine release from blowing snow can only have a very minor influence (discussed in more detail in section 2.1.1). Therefore it also seems likely that the strong correlations between aerosols from blowing snow and BrO VCDs in such weather events (reported for example by Choi et al. (2018)) are more indicative of the increased vertical mixing related to the low pressure systems which are also associated with the increased surface wind speeds causing the blowing snow conditions.

It should be emphasized again that the ODE investigated in this case study exhibits "low pressure, high wind, thicker mixed layers and a decreased stability of the boundary layer" (Swanson et al., 2020) and therefore provides a textbook example of the "unstable" set of meteorological conditions favoring the occurrence of ODEs identified by Swanson et al. (2020) (see also section 2.2.4). As discussed previously in sections 2.1.1 and 2.2.4, up until recently the consensus was that blowing snow induced bromine release is the cause of the correlation between ODEs and these conditions (e.g. Yang et al., 2008; Choi et al., 2018; Swanson et al., 2020). However, the fact that blowing snow induced initial bromine release is not implemented in the model, yet it is capable to reproduce the observations with high accuracy, casts doubt on the importance of blowing snow induced bromine emissions in association with low pressure systems. If the most distinct examples of blowing snow induced ozone depletion events might actually be traced back to an increased mixing of bromine and

ozone rich air masses, then it also seems more likely that other cases of enhanced BrO VCDs associated with high wind speeds and a less stable boundary layer (Swanson et al., 2020) are due to an increase of (turbulent) diffusion and mixing. This matches recent studies by Marelle et al. (2021) and Swanson et al. (2022) which reported that the importance of blowing snow emissions is likely overestimated. The findings of this case study then also provide a more probable alternative explanation for the association of this specific set of meteorological conditions with ODEs as identified by Swanson et al. (2020).

This case study also demonstrated that a high enough mixing ratio of reactive bromine close to the ground can be enough to cause the very high BrO VCDs observed from the satellite under favorable meteorological conditions. It therefore lends further credibility to the conjectures formulated in section 8.3. A general increase of mixing ratios of reactive bromine at the surface would therefore also increase the probability for such ODEs related to high wind speeds and a decreased boundary layer stability to occur. Similarly, it was seen that ozone can be the limiting factor for the continued release of bromine as discussed in section 8.3. This would imply the existence of a seasonal trend for ODEs associated with this set of conditions in low pressure systems, since early in the season mixing ratios of reactive bromine are generally lower and day length is shorter (cf. section 8.3).

Finally, it should be made clear again that the results here do not rule out that blowing snow sourced SSA could improve the model performance. While agreement between simulated and observed BrO VCD is generally quite high, the model underestimates the BrO VCD by a approximately a factor of 2 on 18 March. Coincidentally, the aerosol surface density is very low on that day as discussed above. Additional bromine released from bromine explosion reactions on SSA sourced by blowing snow could therefore lead to an improved agreement on that day. This also agrees with recent model results from a study by Swanson et al. (2022) using a very similar model setup, from which they concluded that additional aerosol production from blowing snow improves model performance for some events (see also section 2.1.1). However, the results of this case study demonstrate that these are not a necessary condition for the occurrence of ODEs in the context of meso scale weather events.

9.3 Case study III - early ozone depletion event enabled by calm meteorological conditions

In this section an area of enhanced BrO near Hudson Bay on 14 January 2019 is investigated. The event occurred very early in the year and it likely provides an example of an event developed in "closed reaction chamber" with very low wind speeds and a shallow boundary layer. It will be discussed that this probably allowed a sufficiently strong enhancement of BrO to develop during the short day length of the winter which could be measured by satellite.

The TROPOMI observations of tropospheric BrO and results from the WRF-CHEM model are presented in Figure 9.9. Unfortunately the WRF-CHEM model only provides

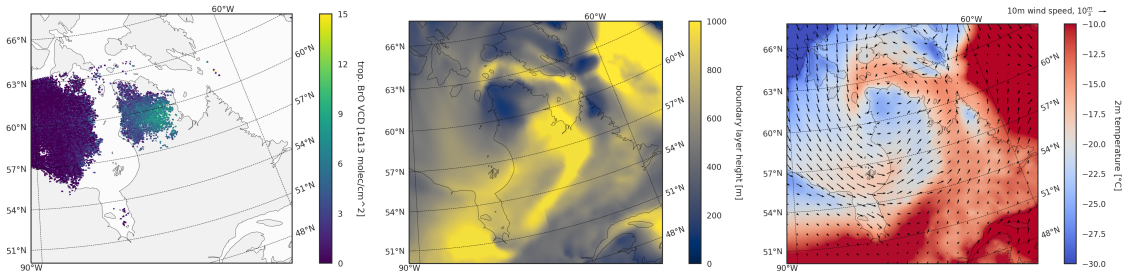

Figure 9.9: *Satellite observations and WRF meteorological simulations for the ODE showing from left to right: TROPOMI tropospheric BrO VCD, atmospheric boundary layer height and* 2 m *air temperature combined with* 10 m *wind speed. The satellite observation was made on 14 January 2019 at approximately 9:30 UTC.*

meteorological parameters and no predictions regarding the halogen chemistry. The reason for this is that the model requires a spin-up time before it can produce reliable predictions. This spin-up time is short for the weather forecast module of the model (due to its nudging to ERA5 data among other reasons, cf. section 6.2), but it requires a longer period of time for the halogen chemistry module, which is why significant results are only available from the beginning of February onwards. Due to the high SZA even at these comparatively lower latitudes this early in the year, the sensitivity of the satellite is also restricted, which is why large parts of the satellite measurement seen in Figure 9.9 are masked as possibly not sensitive to the boundary layer from the sensitivity classification. This filter also prevents an observation of the area of enhanced BrO in the days before or after 14 January 2019, as most pixels there are classified as not sensitive.

The TROPOMI measurements show an area of slightly enhanced BrO VCDs around $5\,\mathrm{molec\,cm^{-2}}$ to $8\,\mathrm{molec\,cm^{-2}}$ over the Ungava Peninsula to the east of Hudson Bay. The boundary layer in that region is generally shallow with layer heights below 150 m in the area, but it shows an increase near the eastern coast towards Ungava Bay. This also coincides with low surface temperatures (below $-20\,^{\circ}\mathrm{C}$) and slow wind speeds ranging from $1\,\mathrm{m\,s^{-1}}$ to $4\,\mathrm{m\,s^{-1}}$.

As mentioned several times by now, the main mechanism responsible for the release of large amounts of reactive bromine and the formation of large BrO mixing ratios is the bromine explosion reaction cycle. However, it requires both sunlight and an initial enhanced mixing ratio of reactive bromine to produce significant BrO concentrations (see Sections 2.1 and 2.1.1). As discussed for the case of the ODE observed at the beginning of February in section 9.1, the short day lengths during Arctic winter and in early Arctic spring put stronger requirements on the initial seed mixing ratio of atmospheric bromine. There are only a few hours each day during which the bromine explosion reaction can proceed efficiently, so in order to produce large enough quantities of BrO observable from satellite, the initial mixing ratios at the start of the day is probably higher compared to later in the year.

The BrO plume observed here most likely developed between sunrise at 4:30 UTC and time of observation at 9:30 UTC. Although the enhanced BrO VCD is observed over land,

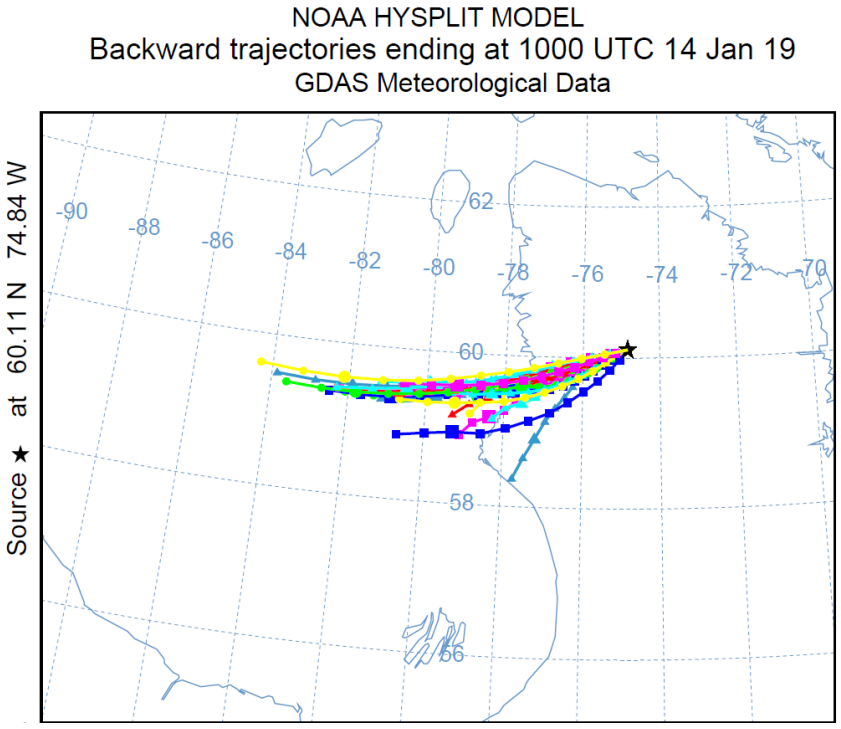

Figure 9.10: *Backward trajectories of air masses demonstrating the likely origin of the BrO enriched air mass seen in Figure 9.1a calculated using the HYSPLIT model (Stein et al., 2015). The different lines represent the different endpoint layer heights of the air mass, ranging from* 600 m *to* 10 m *final layer height. The trajectories are calculated backwards in hourly time steps beginning at 10 UTC on 14 January 2019.*

it is likely that the initial bromine release was taking place near the coast over (FY) sea ice (see also section 2.2.1). Under the assumption that the BrO enriched air mass was merely transported to the area, a backwards trajectory was performed. It was assumed that the BrO plume most likely stayed inside the boundary layer, as the low surface temperature and slower wind speeds suggest a stable boundary layer with decreased mixing. Therefore layer heights of the BrO plume between 500 m and 50 m were assumed for the trajectory calculations and the result is shown in Figure 9.10. The trajectory calculation shows that the source of the BrO most likely lies westwards over Hudson Bay very close to the shore. Interestingly, while this area is masked by the surface sensitivity classifier for most parts, a few pixels farther westwards indeed indicate enhanced BrO columns there too.

This area close to the shore shows a similarly depressed boundary layer height below 150 m together with slow wind fields and a low surface temperature. It seems likely that this served as "closed" reaction chamber allowing the accumulation of relatively high mixing ratios of reactive bromine, probably even during the night via release from the snow-pack via oxidation as discussed in section 9.1. This bromine enriched air mass then got transported to a (comparatively) deepened boundary layer over the land, allowing the formation of a larger BrO column which was detected by the satellite.

It should be emphasized that this ODE is observed very early in the year amidst Arctic winter. The SZA at the location of the BrO plume is around 85°. It is likely that this event would have gone undetected if not for the superior SNR and spatial resolution of TROPOMI, since previous implementation of the retrieval algorithm were limit to measurements below 80° SZA in order to ensure a sufficient statistics for the column separation algorithm (see chapter 7). It could also be possible that a high concentration of NO_x caused the release of bromine (see section 2.1.1), since for example N_2O_5 is very stable in these cold temperatures early in the year. However, since there is almost no human activity in the region and no oil fields are found nearby, this possibility seems unlikely. Unfortunately, no model data is available and there are also no air quality measuring stations near the site of enhanced bromine in order to rule out this possibility completely.

This event also seems to support the conjecture that calm meteorological conditions are favorable for ODEs early in the season. It might also indicate the significance of initial release mechanisms, for example bromine release from the snow-pack via ozone oxidation, possibly even during the dark (see Reaction (R25)). Furthermore, it could be very interesting to save the model run not in hourly intervals but instead in smaller intervals to determine how long it takes for the bromine explosion reaction mechanism to become dominant in comparison to other release mechanisms.

It would also be interesting to further determine sea ice thickness, since thin sea ice can indicate conditions of high salinity at the surface. This would allow a further assessment of potential sources for bromine release for ODEs such as this one or the one studied in section 9.1. There are several existing algorithms capable of retrieving sea ice thickness from satellite-based measurements, for example utilizing the Microwave Imaging Radiometer with Aperture Synthesis(MIRAS) on board the Soil Moisture and Ocean Salinity (SMOS)

satellite (e.g. Mu et al., 2018).

9.4 Summary

In this chapter, three different ODEs were investigated with the aid of meteorological and chemical simulations by the WRF-CHEM model (see section 6.2).

In section 9.1 a large BrO plume in early February was studied that was not predicted by the model. The event originated in an area linked to calm meteorological conditions and a shallow boundary layer. This was followed by a horizontal transport of enhanced BrO concentrations into a deeper and more mixed boundary layer, over which a large BrO VCD was measured by the satellite but not predicted by the model. It was shown that the mismatch between model and observation stems most likely from a wrong assumption in the ozone oxidation of surface bromide (see Reaction (R32)), which is the main mechanisms causing an ODE in the model in the absence of prior concentrations of reactive bromine.

The second case study was presented in section 9.2 and investigated an event in conjunction with a polar cyclone. The WRF-CHEM model matched the BrO VCDs measured via satellite with surprising accuracy. It was shown that increased (vertical) mixing and frontal lifting is in large parts responsible for the formation of enhanced BrO VCDs in these unstable meteorological conditions. Furthermore, this also demonstrated that blowing snow sourced SSA and blowing snow induced bromine emissions can only play a minor role for the plume formation in such meso scale weather systems. However, the possibility remains that additional aerosol formation from blowing snow could improve the agreement between model and observations even further.

The third event investigated in this chapter occurred in the middle of January (see section 9.3). It was shown that this event most likely also developed in a shallow boundary layer under conditions of low wind speeds before being transported towards the coast into a higher boundary layer.

The results of all case studies also reinforce the proposed seasonal trend in the initial bromine release mechanism and the influence of meteorological conditions on ODEs (see section 8.3). The events early in the year, in the middle of January (section 9.3) and early February (section 9.1), were shown to be enabled by initially very calm meteorological conditions. This allowed an accumulation of a large enough concentration of reactive bromine to be detected later after being transported to a slightly deepened boundary layer. In contrast, the event later in the year towards the end of March (section 9.2) was correlated to decreased atmospheric stability and high wind speeds causing increased mixing of air masses rich in reactive bromine with air masses not depleted in ozone.

10 | Investigation of area size distribution of BrO explosions

The spatial expansion of ODEs is subject to large fluctuations. Ground-based measurements detected depleted ozone concentrations both extending over a range of approximately 1200 km and isolated to one measurement station, i.e. located to an area extended over less than 150 km in length (Jones et al., 2013). Yet, precise knowledge of the typical area covered by an ODE could deepen the understanding of the underlying processes and allow an estimate of their wider influence on the cryosphere. For example, it could indicate if ODEs are in general short-lived events restricted to a local emission source and localized meteorological conditions such as temperature inversion leading to a stratified boundary layer, where the necessary conditions for the bromine explosion are fulfilled or rather larger, sustained events merely observed episodically when meteorological conditions transport them to observation sites (Jones et al., 2013).

The latter could even point towards emission from a few specific regions predisposed to the release of bromine by some combination of meteorological, chemical and surface conditions (Hollwedel et al., 2004; Sihler, 2012; Seo et al., 2020).

Some studies give an estimate of the spatial extent of ODEs (e.g. Ridley et al., 2003, 2007; Bottenheim et al., 2009; Jones et al., 2013), however a systematic investigation of their expansion is very difficult. Ground-based studies are limited by the relatively low density of research and measurement stations in the Arctic even in the coastal regions let alone over the Arctic ocean. Aircraft or ship measurements only allow the coverage of a smaller spatial extent while being limited by the duration of the respective campaign.

In contrast, satellite observations provide (better than-)daily coverage of the Arctic region. Although the temporal sampling is limited compared to ground-based observations, an investigation of the spatial extent of enhanced tropospheric BrO is possible. Yet to date, the size or shape of BrO explosions was investigated in passing only in the context of case studies on a very small number of events (or a single event) (e.g Begoin et al., 2010; Sihler, 2012; Blechschmidt et al., 2016; Choi et al., 2018).

This chapter presents a first-time detailed investigation of the spatial expansion of enhanced tropospheric BrO. The retrieval algorithm used in this thesis (see chapter 7) is especially suited for such an analysis, since it allows to utilize the high spatial resolution

of TROPOMI without any biases introduced by for example coarser stratospheric models as used in other algorithms for the separation of stratospheric and tropospheric column. This in turn allows also for the investigation of events as small as the approximate $20\,\mathrm{km}^2$ resolution of TROPOMI.

For this, the stratospheric and tropospheric BrO columns are first used to decide on a per-pixel basis if a significant tropospheric enhancement is present. Then, using methods from image processing, graph theory and topology, the area of each connected area of enhanced BrO is determined following section 10.1. In section 10.2, the resulting distribution of the area size as well as the shape of observed regions is discussed. Using an ellipse parametrization, a typical spatial length and width of an event is determined and compared to ground-based observations. This also allows further investigations of the initial bromine release and the corresponding seasonal trend in mechanisms and meteorological conditions leading to enhanced tropospheric columns.

10.1 Measurement of area size of ODEs using image processing techniques

This section describes the method for the derivation of the size of enhanced tropospheric BrO plumes.

First this requires a criterion to decide if an observed structure is indeed significantly enhanced tropospheric BrO. Here, a pixel is defined to contain an elevated tropospheric BrO column if the difference of total BrO column and stratospheric BrO column $S_{\mathrm{total}} - S_{\mathrm{strat}}$ is larger than both, $2\,\sigma$ with σ as standard deviation of the stratospheric mode as described in section 7.3, and the detection limit for tropospheric BrO as derived in section 7.5 expressed as SCD, i.e.

$$S_{\mathrm{total}} \geq S_{\mathrm{strat}} + \max\{2\,\sigma,\ 3\,\mathrm{molec\,cm^{-2}} \cdot A_{\mathrm{BL}}\}\,. \tag{10.1}$$

Using this criterion, the regions of enhanced tropospheric BrO and the encompassing area is determined orbitwise in the following fashion for the period between 1 February 2019 and 15 May 2019:

(i) As a preprocessing step, a median filter (Huang et al., 1979) is applied on all relevant data fields in order to reduce image noise. This filter is especially good in preserving edges of existing structures (Arias-Castro and Donoho, 2009), making it a good choice for determining spatially connected regions in images as relevant for this analysis. The filter uses a 5×5 footprint, meaning it takes all pixels in a 5×5 region around the pixel of interest and replaces this pixel with the median of the pixels in the footprint. An example of the result of median filtering on daily averaged tropospheric BrO VCDs can be seen in Figure 10.1.

(ii) The significance criterion Eq. (10.1) is applied to the data, resulting in a binary image of pixels containing significantly elevated tropospheric BrO. In Figure 10.2, the results

of the thresholding is shown for a single orbit. It can be seen that median filtering already reduced a lot of noise from the data. However, there a still a few structures which are "disconnected" from the large BrO enhancements, resulting of the application of the significance criterion to noisy data. Since it is very unlikely that these enhanced BrO plumes are uncorrelated to the large plume, these need to be dealt with in order to reduce false detection of small scale events later.

(iii) To improve the image for further analysis, methods from morphological image analysis are applied on the binary image. First, a morphological closing is performed to fill small "holes" in structures and close "gaps" between closely neighboured structures, followed by a morphological opening[1] to further reduce unstructured noise (e.g. Serra, 1982; Vincent, 1993; Jähne, 1993; Salembier et al., 1998; Soille et al., 1999).

(iv) The amounts of pixels enclosed in each separate region of enhanced tropospheric BrO is determined using a connected component labeling algorithm (Fiorio and Gustedt, 1996; Wu et al., 2005; Jähne, 2012). The encompassing area of an event is then calculated using the typical TROPOMI pixel size[2] (see section 5.1.2) $A_{\text{pixel}} = 24.5\,\text{km}^2$. The resulting detected events are depicted in Figure 10.4 for all orbits of a given day.

There are of course uncertainties regarding the determined size of any particular event resulting from the described method. The number of enhanced pixels and therefore the total area covered by a BrO plume might be underestimated due to the surface sensitivity classification. The application of a morphological closing should limit these by filling "holes" in the binary image, but it will not be able to close gaps larger than 5 (or 3 pixel, depending on the criterion, see below), since otherwise the closing operation in itself would introduce errors by artifically enlarging BrO plumes (see also the discussion in section 10.2). Additionally, ODEs which extend over a larger region might not be fully contained in the swath of one satellite overpass and their real size therefore is also underestimated. Furthermore, the assumption of a constant pixel size also biases towards a smaller area, since especially the pixels towards the edge of the swath cover a wider area than the pixels in the middle of the swath (cf. section 5.1.2). Finally, it is also possible that areas of depleted surface ozone are larger than the ones exhibiting enhanced tropospheric BrO VCDs, for example if the boundary layer is very shallow (see sections 2.2.4 and 8.3), which would also result in an underestimation of the spatial extent of the ODE.

On the other hand, the actual number of events, especially larger events might be slightly overestimated, since events can last for several days. Consequently, they will get registered

[1] A morphological closing is defined as the *erosion* of the *dilation* of an image by a structuring element, i.e. it first expands borders of structures according to the footprint of the structuring element, followed by a reduction using the same footprint. This reduction "preserves structures", for example gaps closed by the previous dilation are kept closed. A morphological opening inverts this and first performs an erosion followed by a dilation. This operation removes very small structures, like single pixel or very thin lines in the image, which have not been connected to a slightly larger structure by the closing performed previously. A detailed treatment is found in Soille et al. (1999).

[2] Since the analysis uses data from 2019, the slightly larger pixel size of $24.5\,\text{km}^2$ is used.

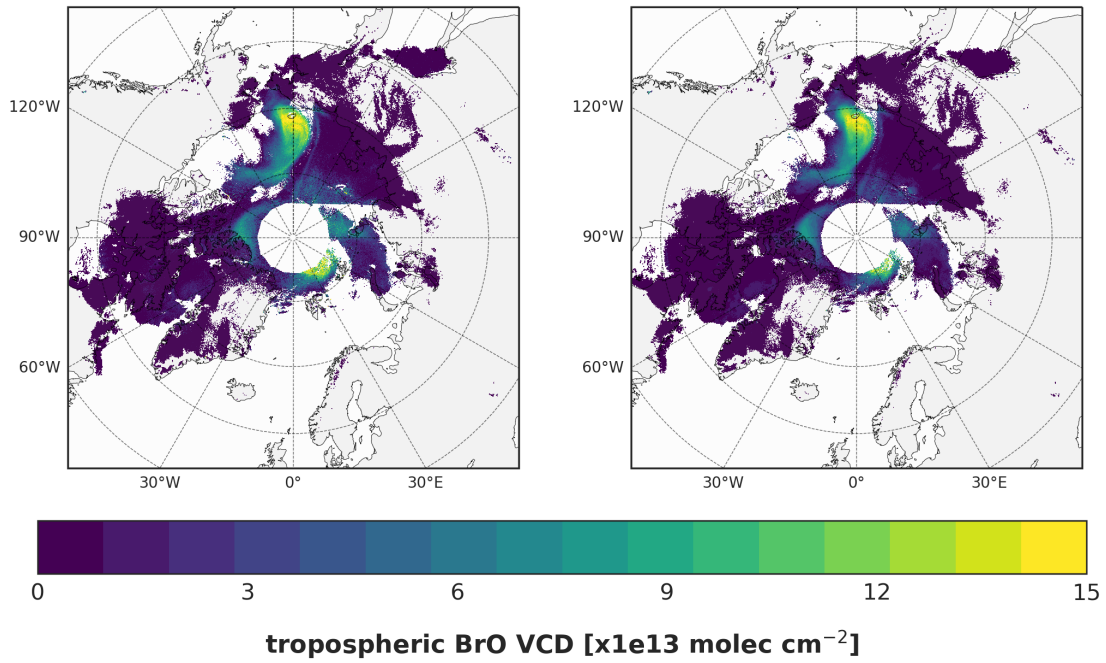

Figure 10.1: *Daily averaged tropospheric BrO VCD on March 19 2019 (left) and the same dataset after application of a median filter with* 5×5 *footprint (right). The filtered image is visible smoother, noise is reduced. Notice that some gaps masked previously as possibly obscured from the surface sensitivity classification have been slightly reduced.*

by the proposed algorithm as separate event on a measurement the next day. Therefore, events with a larger lifetime might also introduce bias. Lastly, a morphological opening which was chosen too large could result in the removal of small, "thin" events with a line-like shape. Nevertheless, the large number of events detected during the observation period (between approximately 1000 and 2000 depending on the significance criterion) give a high confidence in the statistical analysis.

To minimize errors from the choice of filter methods and significance criterion, three analyses with different combinations of filters and significance criterion were performed as described in the following. However, it is found that the influence of the specific choice of criterion and filter is small, as discussed in the next section.

(I) A $2\,\sigma$ significance criterion is used with a large image morphing footprint of 5×5. This larger footprint strongly reduces noise but biases against small-scale events, which might get filtered as noise (see Figure 10.3c).

(II) A $2\,\sigma$ significance criterion is used with a small image morphing footprint of 3×3. A smaller footprint might lead to branches of larger events being detected as seperate disjoint event, therefore resulting in a larger number of small-scale events. However, this also results in a higher accuracy for the detection of very small events (< 3 pixel, see Figure 10.3d).

(III) A $3\,\sigma$ significance criterion is used combined with a small image morphing footprint

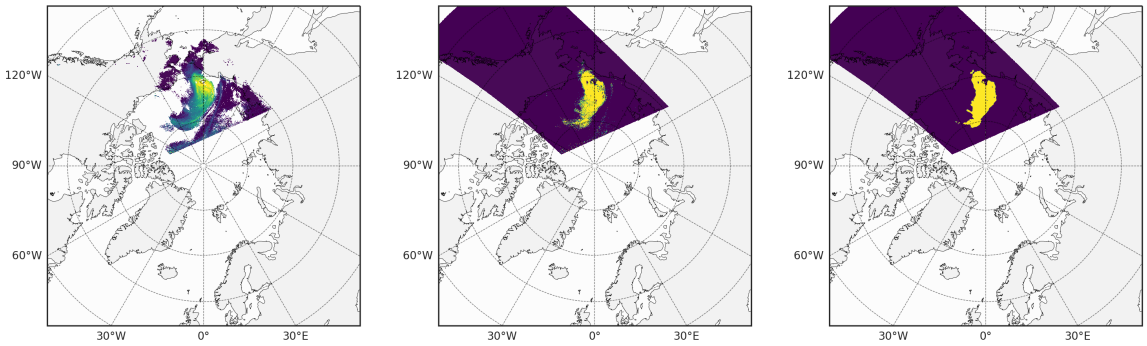

Figure 10.2: *Tropospheric BrO VCD measured in one overpass on 19 March 2019 (left). The application of the binary criterion Eq. (10.1) identifies regions of elevated tropospheric BrO (marked in yellow here for visualization purpose) without the median filter applied before (middle) and with filtering (right).*

of 3×3. This combines the reduced image distortion of a small morphing footprint with an improved filtering of elevated pixels surrounding larger events. In return however, only strong tropospheric BrO elevations (corresponding to a mean tropospheric VCD of approximately 5.5×10^{13} molec cm^{-2}) are registered as enhanced pixels (see Figure 10.3e).

In the following, the different criteria will be abbreviated according to above enumeration as I, II and III. These analyses allow for the first-time a detailed investigation of the spatial extent and shape of ODEs in the Arctic and their correlation to levels of tropospheric BrO enhancements. The connected areas showing BrO columns above the significance threshold will be denoted as *events* for the sake of brevity from here on, however one should keep in mind that an ozone depletion event can have a larger spatial extent as discussed above.

10.2 Analysis of spatial parameters of BrO plumes

This section will present a statistical analysis of the spatial expansion of BrO events. Depending on the criteria, the previously presented method detected a different number of disjoint events: (I) 1664 events, (II) 2664 events and (III) 1428. Of course, some of these might be the same plume measured a day later on the next overpass. Note that it can be presumed that for (I), the larger morphological opening identifies more potential events as possible noise while the morphological closing might connect close but disjoint events to one larger single event. Therefore less events are registered compared to (II). The stronger significance criterion of (III) also leads to a lower number of detected events, though for obviously different reasons there.

The range of the determined area is shown as a boxplot in Figure 10.5. In general it agrees well between the different criterions. The median for the two smaller morphing criteria is similar with (II) 7963 km^2 and (III) 6689 km^2. However, the larger morphing footprint (I) is systematically different resulting in 13 414 km^2 due to more regions with a

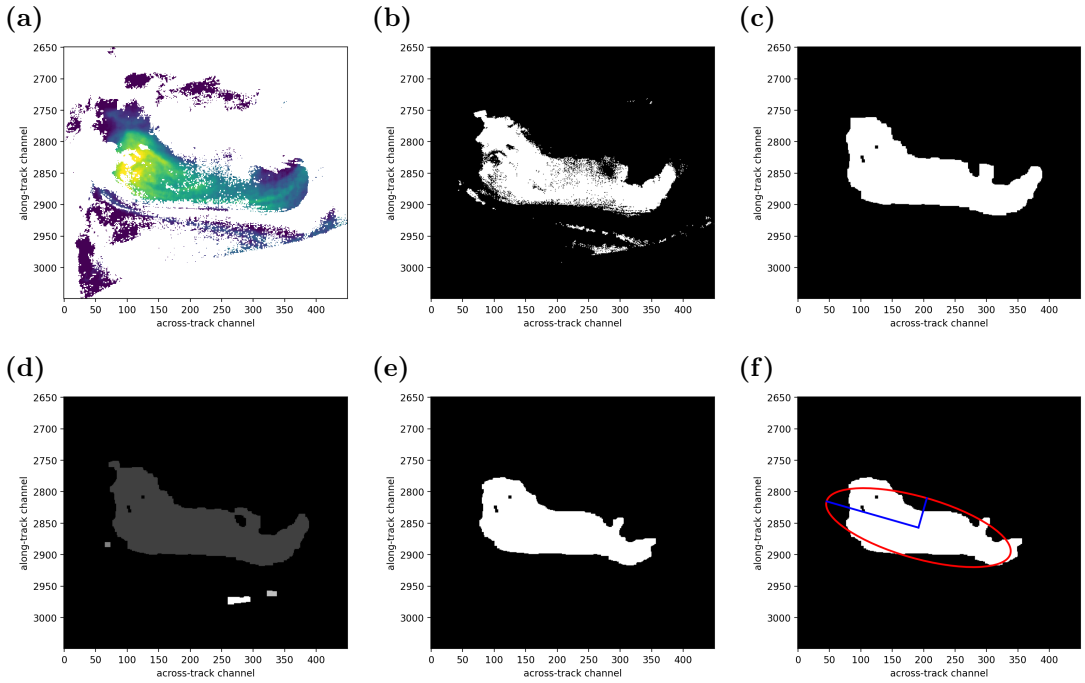

Figure 10.3: *Different significance criteria and morphing footprints visualized on the example of an extended tropospheric BrO plume measured in one overpass on 19 March 2019. Each grayscale images depicts significantly elevated pixels in white or grey, based on the corresponding significance criterion. (a) tropospheric BrO plume with possibly obscured pixels marked as white, (b) application of the 2σ significance criterion without morphological operations, (c) 2σ significance combined with a 5×5 footprint morphological operation, (d) 2σ significance and a 3×3 footprint, note that the large plume is detected as one large and three small disjoint events, (e) 3σ significance and a 3×3 footprint, (f) ellipse (red) and semi-major as well as semi-minor axis (blue) of the ellipse that has the same second moments as the significant region for the settings applied in (e).*

substantially higher area than the other two analyses. This could be due to the smaller footprint leading to more "splitted" events (cf Figure 10.3d) where a branch of the enhanced region is labeled as extra event instead of the region getting connected to the larger area via the morphological closing. Another reason might be the larger footprint artificially enhancing the size of events, for example by connecting disjoint events in close proximity or by registering "noise" in close proximity to an area as part of that region. This is also supported by the reduced number of small area sizes for (I) compared to the other settings, although this might also be ascribed to the larger footprint of the morphological opening (filtering).

In Figure 10.6, a histogram of the spatial area of tropospheric enhanced BrO VCDs is shown for all three different combinations of significance criterion as well as filter methods applied. Here it can also be seen that the trend of the observed event size is the same for all three combinations, suggesting that the overall results of the study will not be influenced strongly by the specific choice of significance criterion or filter method used. This assumption holds for for all further analyses, as seen for example even better in Figure 10.7. Nevertheless

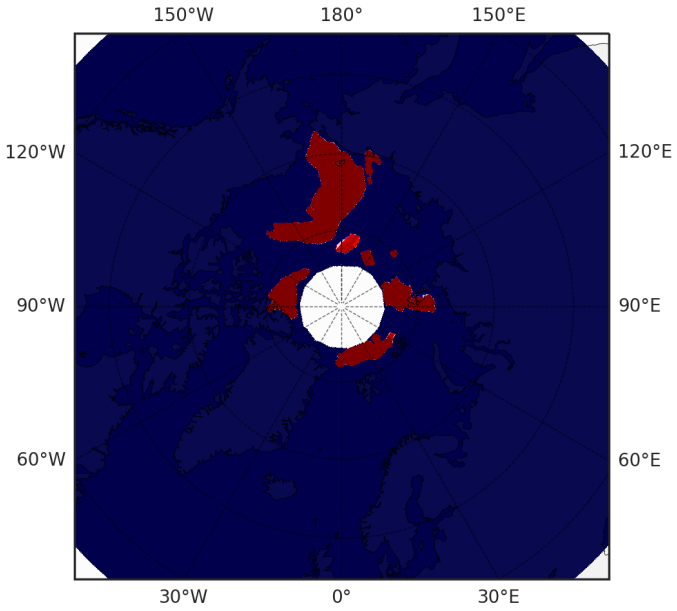

Figure 10.4: *Connected component analysis on the 19th of March 2019. The red pixels denote regions detected as events. Note that there are some artifacts at the edges of the events due to spatial averaging in the gridding routine. No averaging is used for the analyses presented here.*

the results for all three different settings will still be shown for most analyses.

Past observation of the spatial dimensions of ODEs expressed this not as area of enhanced BrO (or depleted ozone) but rather as a distance over which enhanced BrO (or depleted ozone) was measured. Further comparison therefore requires an accurate estimate of the spatial extent of ODEs from the determined area. This in turn necessitates to decide on the shape the area in which enhanced BrO is observed in order to calculate the extent from the surface area. While there is no consensus regarding the general shape of tropospheric BrO plumes, individual satellite observations have shown that many plumes exhibit a tear- or comma-shape (Blechschmidt et al., 2016). Therefore, as an ansatz, the shape is approximated via an ellipse that has the same second moments as the detected region (e.g. Hu, 1962; Jähne, 2012). This is demonstrated in Figure 10.3f.

The numerical eccentricity ϵ of the fitted ellipse then allows to decide on the elongation of the observed shape and the deviation from a circle[3]. The statistical analysis (see Figure 10.7) shows a clear trend towards long and thin ellipse shapes of events, with most events exceeding eccentricities of 0.6. In Figure 10.8 it can be seen that there is also a strong Spearman rank correlation between the size of an event and the corresponding eccentricity. While some smaller events also show small eccentricity, events covering a larger surface area are almost always exhibiting a very thin ellipse shape with high eccentricity.

[3]The numerical eccentricity is defined as $\epsilon = \sqrt{1 - \frac{b^2}{a^2}}$ with a and b the lengths of the semi-major and semi-minor axis, respectively. A numerical eccentricity ϵ of 0 would describe a circle while an eccentricity close to 1 describes a very narrow and long ellipse where the (semi-)major axis is far longer than the (semi-)minor axis.

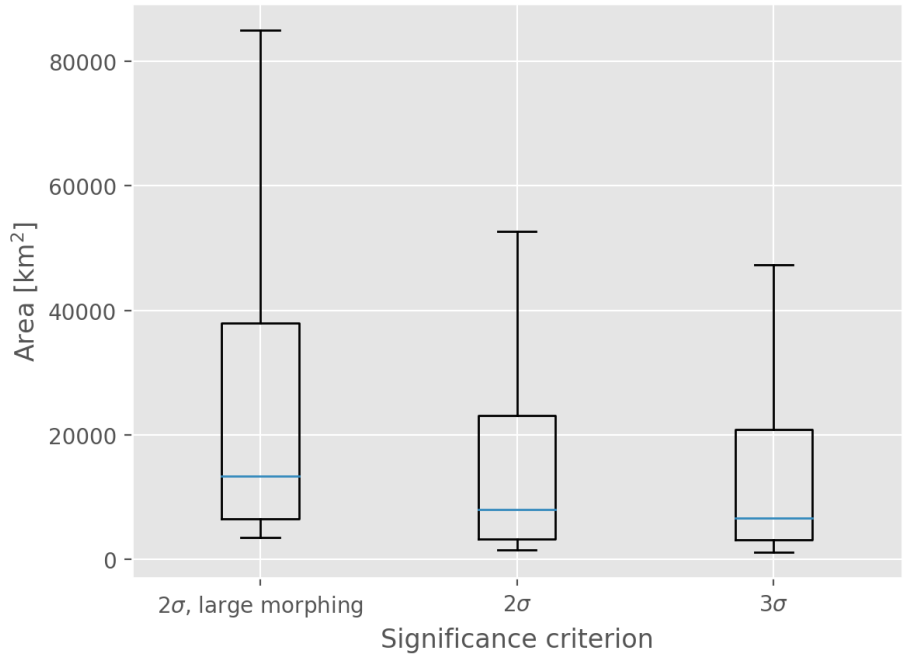

Figure 10.5: *Boxplot of the surface area covered by ODEs for three different combinations of significance criterion and morphological operations: 2 σ significance criterion and large morphing footprint (left), 2 σ significance criterion and small morphing footprint (middle) and 3 σ significance criterion and small morphing footprint (right).*

This trend is of course also seen in a comparison between the major and minor axis lengths depicted in Figure 10.9. While many events extend up to 1000 km in length, the width is below 400 km for almost all.

These observations allow the following interpretation regarding the transport processes underlying ODEs. While (turbulent) diffusion will lead to a circular expansion of the initial BrO plume emitted in the BrO explosion reaction, wind fields will transport BrO (mostly) in one direction, "smearing out" the circular BrO plume and giving the observed events an ellipse like form. This is supported in part by the Spearman rank correlation of approximately 0.3 between the median 10 m wind speeds in the detected regions and major axis length of the event, i.e. the region over which it was supposedly transported, as seen in Figure 10.10. It can be seen that extended events are often accompanied by higher wind speeds. However, it remains unclear why the correlation is much weaker than the one between eccentricity and area size. This could point towards other influencing factors, e.g. the formation of BrO along extended coastlines (with increased turbulent mixing), which would also lead to very narrow forms of the area without association with transportation.

The BrO explosion reaction cycle strongly depends on the presence of light (see section 2.1). Under the right condition (e.g. large enough ozone concentration, enough releasable bromide present) the formation of BrO begins with the first sunlight, as it is also seen in the WRF-CHEM model (see chapters 8 and 9). Since TROPOMI measures during early afternoon (13:30 h mean local solar time, cf. section 5.1.1), the initial tropospheric BrO

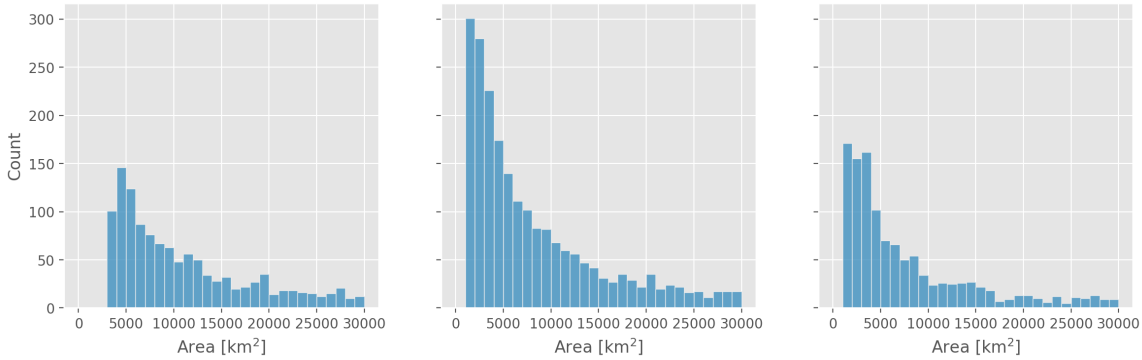

Figure 10.6: *Histogram of the surface area covered by ODEs for the three different combinations of significance criterion and morphological operations: 2σ significance criterion and large morphing footprint (left), 2σ significance criterion and small morphing footprint (middle) and 3σ significance criterion and small morphing footprint (right).*

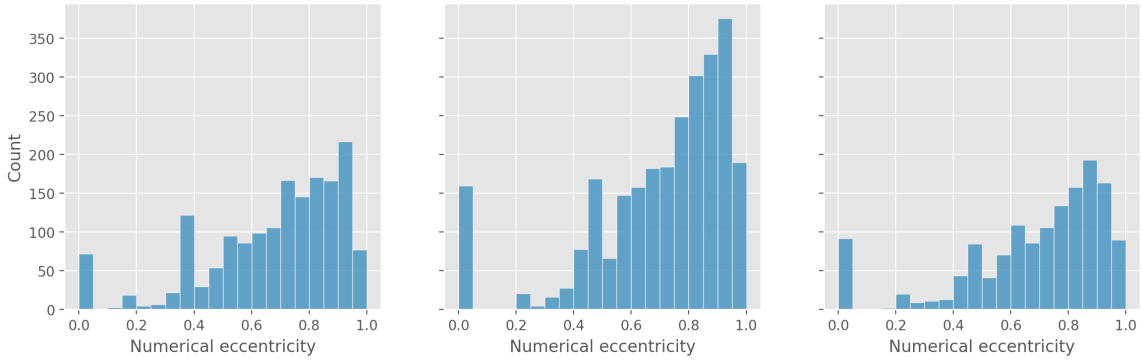

Figure 10.7: *Histogram of the numerical eccentricity of ellipses parametrizing the shape of events for the three different combinations of significance criterion and morphological operations: 2σ significance criterion and large morphing footprint (left), 2σ significance criterion and small morphing footprint (middle) and 3σ significance criterion and small morphing footprint (right).*

plume will not be measured in many cases, but rather a plume which has already evolved and was transported for a few hours, explaining the large fraction of events exhibiting a high numerical eccentricity. This interpretation would also explain the strong correlation between the area of an event and the eccentricity (see Figure 10.8). Some events could be measured either early during the initial release or during conditions of very low surface wind speed, explaining why for small events also eccentricities of 0.5 or lower are observed often. Yet most events measured from the satellite extend over a wider area, probably due to transport. If the location of the bromine emission does not change (i.e. the bromine is emitted from the same source), advection of the enhanced BrO will result in a higher eccentricity. This should even hold if the advected bromine leads to additional bromine release along its path. Additionally, a comparison between the minor and major axis lengths (see Figure 10.11) of events could then give indications to the typical size of emission areas. The minor axis extent will then only be affected by (turbulent) diffusion, the major axis extent

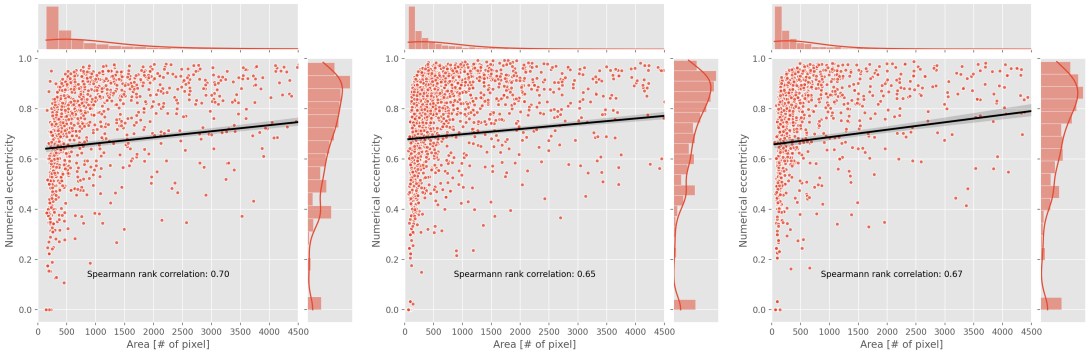

Figure 10.8: *Comparison of area size (expressed as number pixels with enhanced BrO) and corresponding eccentricity of the ellipse parametrizing the enhanced region. Shown is from left to right the corresponding combination of significance criterion and morphological operations: 2 σ significance and a 5×5 footprint (left), 2 σ significance and a 3×3 footprint (middle) and 3 σ significance and a 3×3 footprint (right).*

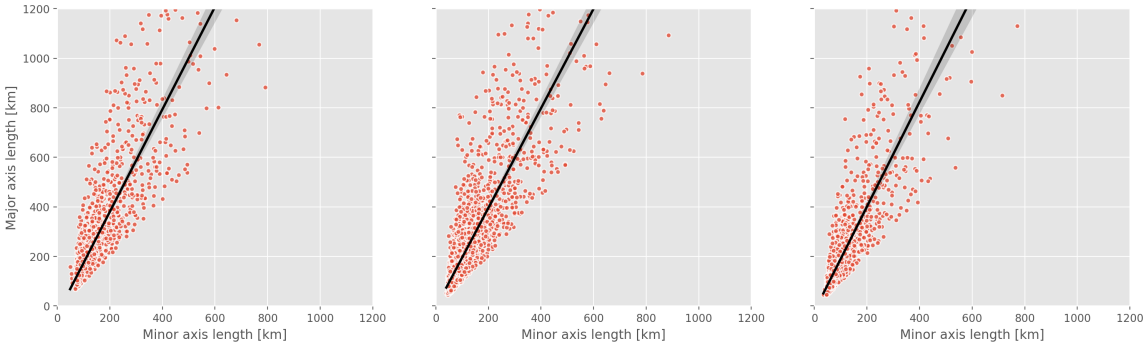

Figure 10.9: *Comparison of major and minor axis length derived from the ellipse parametrization of the detected regions for three different combinations of significance criterion and morphological operations: (I) 2 σ significance criterion and large morphing footprint (left), (II) 2 σ significance criterion and small morphing footprint (middle) and (III) 3 σ significance criterion and small morphing footprint (right).*

on the other hand will reflect the transportation of the BrO plume.

Another possible explanation for the observed high eccentricity of events could be the influence of weather fronts, which have been conjectured before to sustain a high plume lifetime and BrO plumes with a larger spatial extent (e.g. Begoin et al., 2010; Sihler, 2012; Blechschmidt et al., 2016), for example due to mixing of BrO enriched and ozone enriched air masses (see section 9.2). Such mixing processes along an extended front would result in a very thin BrO plume, which would also register as an ellipse with a very high eccentricity.

Although the histogram in Figure 10.7 shows a clear trend towards eccentricities of 0.4 or higher, there is a small number of events exhibiting an eccentricity of exactly or near 0. Comparisons with the area of the corresponding events (see Figure 10.8) demonstrate that all these circular events encompass a very small area. There are two different explanations for these special events:

(i) The events exhibiting an eccentricity of exactly 0 could result from noise in the image

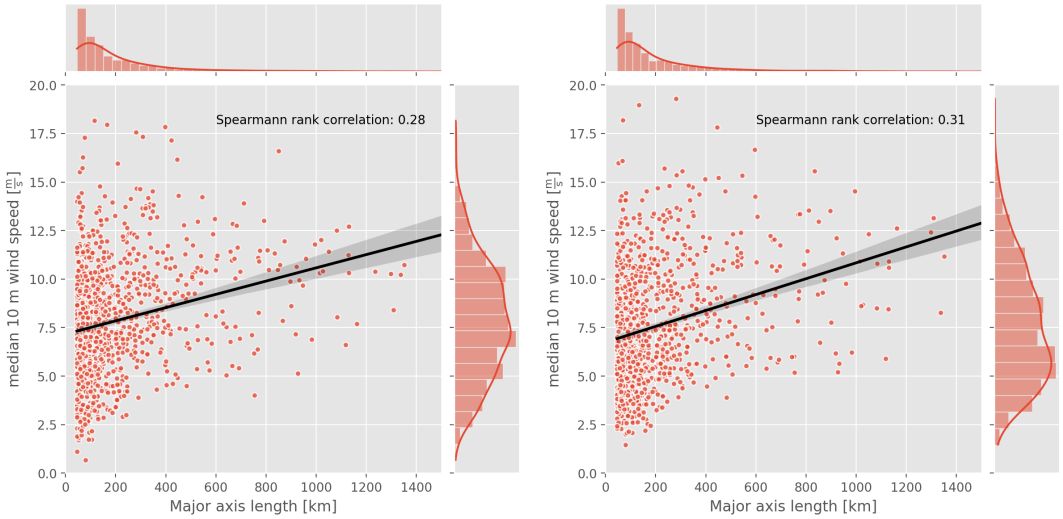

Figure 10.10: *Comparison of major axis length and median wind speed in the detected regions for the 3 σ significance criterion (III). Shown is from left to right: wind speed at the time of measurement (left) and median wind speed 8 hours before the measurement (right).*

not removed by the median filter. Neighboring "noisy" pixel might get picked up by the morphological operations and extended to a small, connected region. Since the footprint of the morphological closing is symmetric, such an extension of a small number of close pixel would result in a perfectly symmetric event, explaining the eccentricity of exactly 0 and the large gap between these events and other observed events, all with an eccentricity of 0.2 or above. One could argue that the morphological opening (which is acting as a noise filter after the closing operation) is responsible for this gap in the observed eccentricity, however an opening with a symmetric footprint would rather filter out very thin, line-like shapes, therefore reducing events with very large eccentricities close to 1.

(ii) Instead of noise causing these circular events, these could also reflect ODEs observed right at the beginning of the release of reactive bromine. It could be possible that the necessary conditions for bromine release only occur very localized, especially at the beginning of the season, were also the amount of reactive bromine is very limited (see section 8.3). However, this still does not explain why there is such a large gap in the measured eccentricities between the events with an eccentricity at 0 and all other events with eccentricities of 0.2 or higher. Yet, the measured BrO VCD would be lower for most events observed early in their development, which would result in some or most pixel in these events not being classified as elevated above the significance criterion. The morphological operations would then either filter them out as noise or "round out" the fractured event, giving it a circular form. This might also explain the small amount of observed eccentricities between 0.0 and 0.35, since small events with a circular-like shape (an eccentricity close to 0) could be wrongly expanded by the morphological closing to a symmetric shape. It should also be taken into account

that especially shallow boundary layers could lead to many pixels not containing high enough VCDs to be detected as relevant as discussed in section 10.1. This could especially affect the initial bromine release early in the season, which is favored by a shallow boundary layer (see sections 2.2.4 and 9.3).

The first point might indicate an underestimation of the actual size of small ODEs due to residual noise in the image even after the filtering processes. For this reason in further analyses the smallest events are assumed to be described by the 10th percentile of the observed spatial extent.

However, the second explanation discussed above could point towards an overestimation of the spatial extent of the smallest ODEs by the method presented here. Yet, events observed initially over a small area are unlikely to play a significant role in the depletion of ozone over larger spatial extents. A manual sighting of tropospheric BrO VCDs for all orbits from February until mid of May for the years 2019 and 2020 yielded some small-scale tropospheric BrO enhancements extending only over a small number of pixels. Yet, not a single one of these events subsequently developed to an event with either a large lifetime or covering a larger area[4], making it impossible to discriminate between such observations and noise. There it should also be taken into account that the early afternoon orbit of TROPOMI could miss the smallest events, since most observed BrO plumes will have already been extended in size as discussed before.

The presented investigation also allows the estimation of the smallest spatial extent of early events and the spatial extent of emission sources. The large number of events allows to reduce the error from noise as well as of waning events already reduced in size by taking the 10th percentile of the minor axis length (see also Figure 10.11b) as estimate for the smallest spatial extent. Following the above interpretation of the shape of events, using the minor axis length should also reduce the influence of transport from wind fields. Nevertheless, the estimated size should be seen as an upper bound, as it is possible that the size of small ODEs is overestimated either through the specific measurement time of TROPOMI or from the applied filter methods as discussed before. The upper bound for the smallest extent of BrO explosion can then be estimated as (I) 61 km, (II) 40 km and (III) 38 km.

Previously only Jones et al. (2013) were able to accurately determine a lower bound for the size of ODE of 150 km, however they were limited by the sparse distribution of the ozone monitors[5] used. The spatial extent of areas of enhanced BrO determined via satellite is far smaller, although they are still well above the spatial resolution of TROPOMI.

In previous discussion, it was established that very specific environmental conditions are probably necessary to allow the development of a significant ODE, especially early in Arctic spring when the amount of atmospheric reactive bromine is still very low (see sections 2.2

[4]Meaning that these enhanced pixels were no longer depicting enhanced tropospheric BrO the next day nor did the small BrO plume get spread out over a larger number of pixels.

[5]The authors established a network of 10 ozone monitors over 1200 km for this. Since some ODEs were only observed at a single ozone monitor, they concluded that it is limited to a region of approximately 150 km in diameter.

and 8.3). Therefore one could have expected that even smaller initial bromine releases are possible, possibly even smaller than the spatial resolution of TROPOMI. Even in large scale temperature inversions it would be possible that a temperature threshold is reached localized to a small scale, allowing for an increasing release of bromine (see section 2.2.2). On the other hand, enhanced BrO in a shallow boundary layer would also be hard to detect from satellite as discussed previously, which might bias towards larger events. Nevertheless, the resulting upper bound for the initial BrO release is still significantly smaller than previous measurements suggest and it indicates a localized trigger, such as local temperature minima in the presence of inversions.

Interestingly the extent of the smallest events stays almost constant over time (see Figure 10.14a). This might also indicate that different causes are responsible for the smallest events depending on the time of the year. Early on in February, the illuminated area along the coast, especially over FY ice, where most BrO events begin, is restricted, possibly resulting in small events. Later on, when vast regions of depleted ozone are the norm, the small events might result from bromine surface emissions over localized pockets of not (strongly) depleted tropospheric ozone mixing ratios (cf. section 8.3).

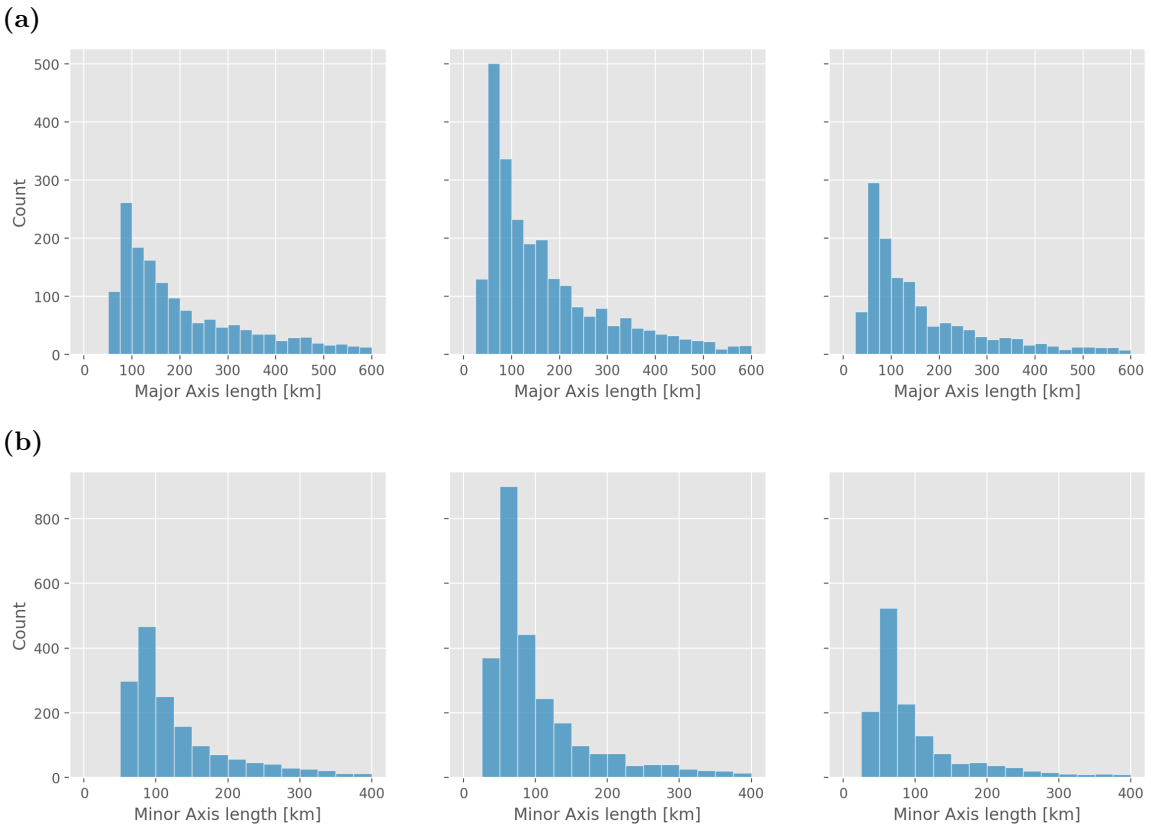

Figure 10.11: *Histograms of ellipse major (a) and minor (b) axis lengths. Shown is from left to right for each case the three different combinations of significance criterion and morphological operations: 2σ significance and a 5×5 footprint (left), 2σ significance and a 3×3 footprint (middle) and 3σ significance and a 3×3 footprint (right).*

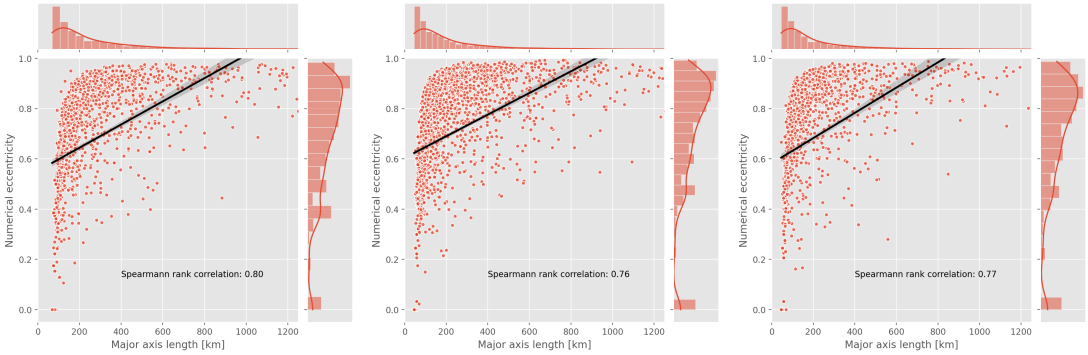

Figure 10.12: *Comparison of the major axis length and corresponding eccentricity of the ellipse parametrizing the region of enhanced tropospheric BrO. Shown is from left to right the corresponding combination of significance criterion and morphological operations: 2σ significance and a 5×5 footprint (left), 2σ significance and a 3×3 footprint (middle) and 3σ significance and a 3×3 footprint (right).*

Aircraft measurement reported ozone depleted air masses stretching over 900 km (Ridley et al., 2003, 2007) and Jones et al. (2013) even reported simultaneously measuring ozone depletion over a length of more than 1200 km. While the 75th percentile of the major axis length is approximately 60 km for all significance settings (see also Figure 10.11a), the analyses also showed events extended over more than 1500 km early in March. Interestingly, almost all events extending over more than 600 km are very narrow with an eccentricity of more than 0.6, see Figure 10.12. Following the previous interpretation of the origin of the elongated shapes of events, this means that these are all either transported events or events along meteorological fronts.

This further contradicts the hypothesis that BrO events in general are short lived episodic events (Hopper et al., 1994, 1998) and strengthens the view that ODEs can be sustained events emerging over sea ice, which get transported by wind.

In Figure 10.13, the 90th percentile and the 20th percentile of BrO VCDs measured respectively for each distinct BrO plume detected by the algorithm are plotted against the corresponding area size. It can be seen that there is a weak trend for the largest BrO VCD to increase with an increasing area size, with a Spearman rank correlation of approximately 0.3 for all settings (I)-(III) (see Figure 10.13a). On the other hand, there is no correlation at all between the area size and the smallest BrO VCDs of an event, with correlations approximately 0 (see Figure 10.13b).

The weak correlation between event size and the 90th percentile of the BrO enhancement might be explained by the fact that stronger BrO enhancements are somewhat self-limiting: a larger BrO concentration increases the depletion of ozone. This might be putting a constraint on the maximum BrO VCD due to the amount of available ozone to sustain the BrO reaction cycle and increase the atmospheric lifetime of a BrO plume. However, a transport of a BrO enriched air mass to a region with undepleted ozone levels could in turn increase the lifetime and slightly increase the maximum BrO VCDs. This would also explain why the observed

Figure 10.13: *Comparison of area size (expressed as number of pixels with enhanced BrO VCDs) and the tropospheric BrO VCD (a) 90th percentile and (b) the 20th percentile for each detected BrO plume. Shown is from left to right for each case the three different combinations of significance criterion and morphological operations: 2 σ significance and a 5×5 footprint (left), 2 σ significance and a 3×3 footprint (middle) and 3 σ significance and a 3×3 footprint (right). Note that there are a few VCDs below the significance criterion in (b). These are VCDs at the edges of events which got added to the region mask by the morphological closing.*

trend is rather weak, since fresh ozone can also be brought in contact with activated bromine, for example via turbulent diffusion at the upper edge of the planetary boundary layer or from vertical uplifting of BrO enriched air masses at meteorological fronts as discussed previously in chapter 9.

In the last chapters it was discussed that the confusion regarding the different initial release mechanisms (cf. section 2.1.1) and the meteorological conditions associated with enhanced BrO columns (cf. section 2.2.4) might be explained by a seasonal trend (see sections 8.3, 9.2 and 9.3). Early in the season, calm conditions favor the initial release of bromine from the snowpack while later in the season high wind speeds and synoptic scale weather events increase the turbulent mixing of air masses. Consequently, it could be expected that such a trend would be reflected in the satellite measurements of enhanced BrO columns, for example in the event size or the VCDs of events over the season. To investigate this, the connected regions detected above the significance threshold for the BrO VCD were arranged into bins of 15 days each, from the beginning of February to mid of

May, see Figure 10.14.

First of all, it becomes apparent that the number of events detected by the algorithm increases significantly over the season. It stays almost constant for the first 45 days, from the beginning of February until mid of March, where the algorithm detects approximately 100 events each 15 days. Then the number of events strongly increases reaching a peak of almost 1000 events in the time between mid of April and the beginning of May, from where on it starts to decrease again. This also fits the trends predicted by the model, where the areas of enhanced BrO columns strongly increase from mid of March to the beginning of May (cf. section 8.3). This can probably be attributed to a combination of generally increased mixing ratios of activated bromine as well as to more bromine explosions taking place in a less shallow boundary layer, resulting in increased column densities as discussed in section 8.3.

Likewise, the increase of the major axis length for the largest events agrees with previous interpretations. An increase in day length also allows an increased sustenance of bromine explosions, for example either due to an increased time frame for reactions at the surface or by recycling on aerosols. This then also results in an increase of the spatial expanse of the largest areas showing enhanced BrO columns. Towards the end of March and beginning of April, the abundance of (surface) ozone above bromide rich surfaces becomes the limiting factor for the formation of BrO and horizontal transport at the surface will quickly advect bromine enriched air towards regions where surface ozone is depleted from previous bromine explosions, limiting the extent of the largest events. It should also be taken into account that the number of events detected later in the season is larger. Although weather events occuring on a synoptic scale (approximately 1000 km) are expected to increase vertical mixing and sustain reactive bromine even above the boundary layer (see section 9.2 and Sihler (e.g. 2012); Blechschmidt et al. (e.g. 2016)), the frequency of enhanced BrO associated with such events is probably not high enough to influence the statistics during end of March and April.

No similar trend can be seen for the median and minimal extent of events detected by the algorithm. When taking into account that presumably the release mechanisms and meteorological conditions relevant for bromine activation strongly differ early and late in Arctic spring, this is surprising. One explanation would be the effect of temperature inversions, which might cause low temperatures on a small spatial scale as discussed before. It is possible that the algorithm presented here is unable to detect such small scale events or that the very shallow boundary layers necessary for the initial formation of reactive bromine from snow-pack emissions implicate that BrO can only be detected when its advected to regions with a less stratified boundary layer.

Figure 10.14b shows the median as well as the 90th and 20th percentile BrO VCDs of each event resampled into bins of 15 days. The 90th percentile should be seen as estimation of the largest VCD reached in plumes and the 20th percentile as the smallest VCD respectively. It can be seen that the median, the largest and the smallest BrO VCDs all decrease slightly over the season. This is also somewhat surprising. If ambient levels of activated bromine increase over the season and in late March and April ODEs are favored by higher wind speeds and

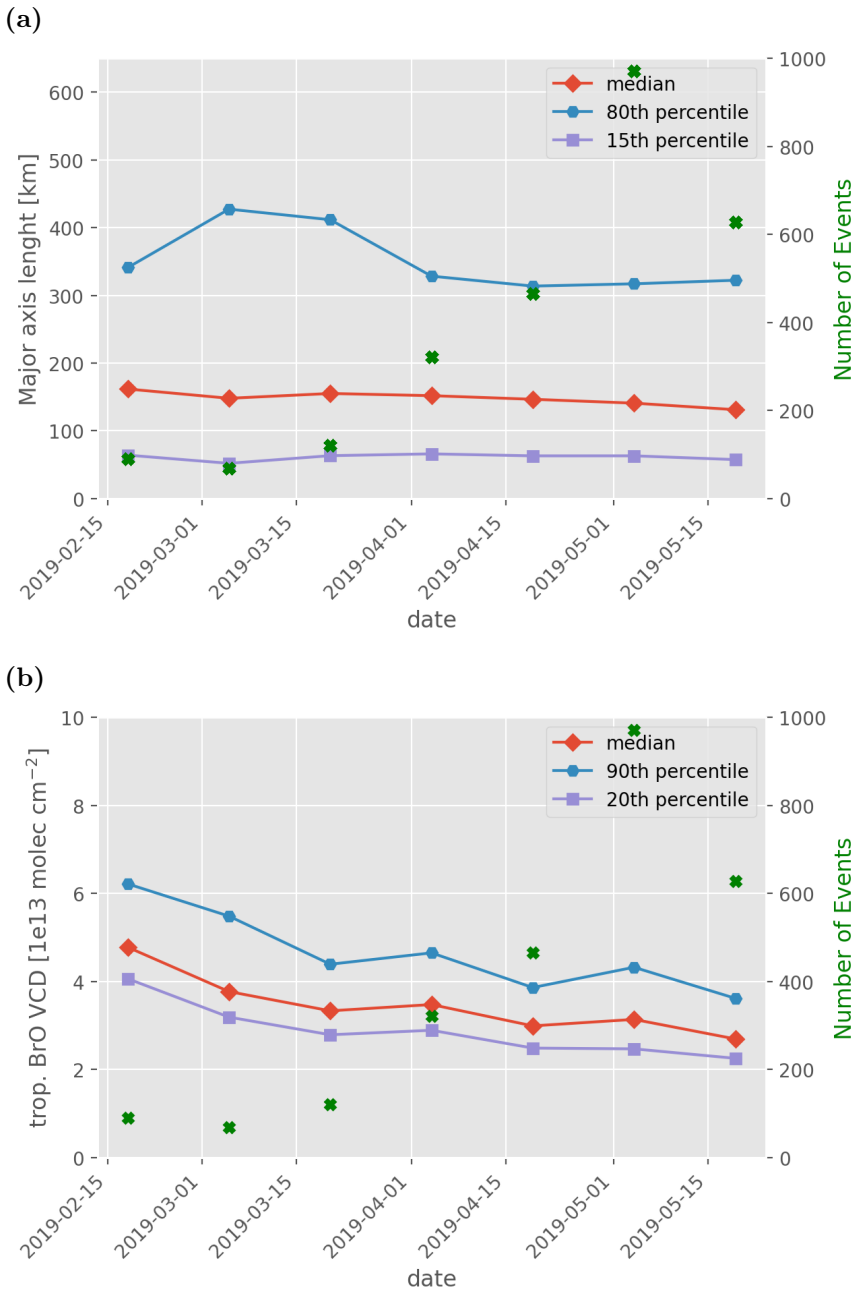

Figure 10.14: *Temporal resampling of the detected events in steps of 15 days. For each bin, the median, the 80th (90th) percentile and the 15th (20th) percentile of the major axis length (a) and the mean tropospheric BrO VCD (b) of the respective regions is shown, derived from a 3σ significance criterion and a 3×3 morphing footprint. The number of events for each resampling step are shown in green.*

increased vertical mixing, one would expect that in the deeper boundary layers also higher BrO columns could be measured. However, the influence of the larger number of detected events on the statistics should be taken into account as discussed before. This might bias towards more extreme events with larger columns for the 80th percentile early in the season. Yet this does not explain the decrease in the median and smallest VCDs. It should be taken into account that later in the season there are vast areas over the Arctic ocean which are effectively void of ozone for longer time periods (see section 8.3 and e.g. Bottenheim et al. (2009)). If large parts of the ozone above bromide rich surfaces is already depleted, then the likelihood for advected reactive bromine to trigger additional bromine release is decreased. This would then inhibit the build up of very large BrO mixing ratios. Additionally, this might also indicate that aerosols, while having a strong influence in the sustenance of an ODE, might not provide such a large reservoir of bromide as previously thought (e.g. Yang et al., 2008; Choi et al., 2018). Furthermore, this could also indicate a decreasing amount of bromine available for release, for example because the replenishment of bromide from the sea ice to the snow-pack slows down (see section 2.2.1) which would then also result in a decreasing bromide concentration in aerosols.

10.3 Summary

This chapter presented results of a statistical analysis of spatial parameters of ODEs. Connected areas of significantly elevated BrO were automatically detected using techniques from image processing, resulting in the detection of more than 2000 ODEs over the time period of one Arctic spring.

The events were assumed to be of a general elliptic shape. It was found that most events resemble the shape of a very long and thin ellipsis with very high eccentricity. Additionally, a trend towards a higher eccentricity could be established for an increased spatial extent of ODEs. From a weak correlation between the 10 m wind speed and the major axis length of the ellipsis parametrization of events it was concluded that advection has an influence on the shape and spatial expansion of BrO plumes sourced by bromine explosions.

The median major axis length of the events amounts to 200 km, covering an area of approximately 7500 km^2. It was also possible to improve the lower boundary for the spatial extent of initial bromine releases. The smallest 10th percentile of events stretches over approximately 40 km, almost a 5-fold decrease to the previous estimate of the smallest events.

A seasonal trend in the number of areas exhibiting a BrO VCD above the detection limit was established with a strong increase from mid of March onwards and a decrease after beginning of May. A similar trend was seen in the size of the largest BrO plumes, however the median and smallest event extents do not change over the season. In contrast, the BrO VCDs decrease monotonically over Arctic spring.

Part IV

Conclusions and Outlook

11 | Conclusions

Halogen activation in polar spring can severely affect the atmospheric chemistry in the Artic. This thesis investigates the phenomenon of ozone depletion events (ODEs) in Arctic spring on the basis of observations of bromine monoxide (BrO) in conjunction with a three-dimensional chemistry and meteorology model. The abundance of BrO, which is used as indicator of tropospheric halogen activation, was derived using differential optical absorption spectroscopy (DOAS). The model data is produced from a novel WRF-CHEM model based on the implementation by Herrmann et al. (2022). The main focus of this work was the improvement of a retrieval algorithm capable of determining tropospheric BrO vertical column densities (VCDs) from satellite without using external (model) input. This updated and improved algorithm was applied to measurements of the TROPospheric Monitoring Instrument (TROPOMI), which features and unprecedented signal-to-noise ratio and spatial resolution. In contrast to other satellite retrievals of tropospheric BrO, the algorithm developed for this thesis is capable of fully utilizing TROPOMI's high spatial resolution. Observations made with the help of this retrieval are then used in conjunction with predictions of the WRF-CHEM model to advance the understanding of bromine release mechanisms and their complicated relationships to meteorological conditions.

In order to correlate satellite measurements of BrO to model data, a satellite retrieval of tropospheric BrO VCDs was developed based on Sihler et al. (2012). The algorithm presented in this work is capable of separating measured total BrO column density into stratospheric and tropospheric partial columns. Unlike other retrievals, the method applied in this thesis does not depend on extensive stratospheric chemistry models or climatological data. This independence on external data distinguishes the retrieval for further comparison with an atmospheric chemistry and weather model and allows to fully exploit the high spatial resolution of TROPOMI. An additional important property of the algorithm is that it allows to discriminate between measurements which are sensitive for near-surface layers, where most reactive bromine is expected to reside, and measurements for which the lower troposphere is likely obscured. The algorithm also provides an accurate estimation of the retrieval error on a per-pixel basis.

The tropospheric BrO columns retrieved from TROPOMI observations were compared to different simulations of the WRF-CHEM model corresponding to differing assumptions on the bromide reservoir above sea ice and in the snow-pack on land. The model is able to predict almost all ODEs indicated by satellite observations of enhanced BrO columns. There

is also very good agreement between the tropospheric BrO VCDs measured from TROPOMI and VCDs predicted by the simulations for these events both in a quantitative sense and in size, shape and location. However, the model shows slightly enhanced BrO VCDs all over the Arctic not picked up by the satellite, indicating a minor overestimation of the amount of released bromine, though it is possible that a shallow boundary layer and horizontal heterogeneities may obfuscate activated bromine chemistry from the satellite. Nevertheless, the correlation between satellite observations and simulations is high for all model setups. Agreements are shown to improve with the assumption of a finite bromide source directly releasable from the surface.

Furthermore, the model was compared to ground-based ozone measurements at different measurement stations, which showed similar results with overall high correlations. The varying performance of the two simulations with differing amounts of bromide releasable from multi-year (MY) sea ice indicated that MY sea ice emissions might be of greater importance than previously assumed, which is in agreement with the more recent literature.

The excellent accordance of model and observations gave confidence in the model predictions. Furthermore it allowed to choose the simulation with overall best agreement for further investigations. Model predictions of surface concentrations of ozone and reactive bromine species were investigated with respect to possible seasonal trends. The model shows a strong increase of mixing ratios of reactive bromine during polar spring, especially in the boundary layer, close to the surface. It was conjectured that this could also imply a trend in the influence of meteorological conditions on ODEs, explaining the two disjoint sets of meteorological conditions identified in the literature (e.g. Swanson et al., 2020). Early in the season, when the time period with sufficient radiation is short and activated bromine concentrations are low, the importance of (slow) initial release mechanisms such as snow-pack release could be increased, favored by calm meteorological conditions and a shallow boundary layer. Later on, the vastly increased mixing ratios of reactive bromine combined with a depletion of surface ozone over large areas covered by sea ice could increase the influence of meteorological conditions leading to additional (vertical) mixing or vertical lifting and increasing the replenishment of ozone from transportation, such as weather fronts and low pressure systems.

The existence of such trends in meteorological conditions and the influence on initial bromine release was further investigated in case studies using satellite observations in conjunction with model predictions and backward trajectories. It could be shown that early in the year in January and February, ODEs are likely sourced by reactive bromine emitted in a shallow boundary layer during calm meteorological conditions, allowing the build up of large quantities of activated bromine from snow-pack emissions, possibly even overnight. Furthermore, it could be demonstrated that an assumed light dependence of the Br_2 emission from snow via the ozone oxidation of bromide is incorrect, which in particular affects events in early polar spring. Because that reaction is one of the main triggers for ODEs in many models of tropospheric halogen chemistry, this discovery can lead to substantial improvements for future models. Another ODE occurring in late March was observed in

association with a polar cyclone. It was shown that the formation of the large BrO plume was favored by an increase of vertical lifting of activated bromine released at the surface and stronger mixing of fresh ozone. This is in contradiction to previous studies of ODEs in cyclonic activities, which attributed the increased BrO columns and longer lifetime of the plume to increased bromine emissions from blowing snow. The results further shed doubt on the importance of blowing snow as mechanism for initial bromine release, it is however possible that additional blowing snow sourced aerosols could improve agreement between model and measurements.

Additionally, a first-time investigation of the spatial extent and shape of ODEs based on one year of tropospheric BrO VCDs measured by TROPOMI was performed. It was found that most areas of enhanced tropospheric BrO columns resemble a long, thin ellipsis in shape. By using an ellipsis for the statistical analysis of the extent of the events, it was possible to determine the median surface area over which an ODE occurs as approximately $7500\,\mathrm{km}^2$. Furthermore, it can be established that the smallest events extend over 40 km or less. This also enabled an estimate for the smallest emission sources and localized meteorological conditions favoring bromine activation and represents a significant improvement over previous estimates determined from ground-based measurements (Jones et al., 2013). A significant correlation between the shape of the ellipsis and the area covered by an ODE was found with an increase in area size together with an increasing eccentricity of the ellipsis. Likewise a moderate correlation between surface wind speed and the length of the ellipsis parameterization of an ODE was established, supporting the proposal by Sihler et al. (2012) that boundary layer meteorology has a significant impact on the distribution and occurrence of ODEs.

In conclusion, based on investigations performed for this thesis, a seasonal trend in the dependence of bromine release on environmental conditions could be proposed. In early polar spring, calm meteorological conditions favor bromine release and the occurrence of ODEs. In contrast, later in the season during March and April, ozone represents the limiting factor for BrO formation and high wind speeds associated with low pressure systems enable the mixing of air masses, which extends the lifetime of BrO plumes. Furthermore, in case studies it could be demonstrated that the typical bromine release mechanism from ozone oxidation of bromide in the snow-pack employed in numerous model for tropospheric BrO chemistry is unfit to predict ODEs in early February at high solar zenith angles.

12 | Outlook

Due to strong assumptions regarding the stratospheric bromine chemistry, the applicability of the column separation utilized for the retrieval algorithm presented in this thesis is restricted to the Arctic region. In contrast, the AMF algorithm and the corresponding surface sensitivity classifier is neither limited to the Arctic region nor to retrievals of BrO. In principle it can be applied to any DOAS retrieval investigating boundary layer trace gases above bright surfaces, such as e.g. iodine monoxide (IO) retrievals in the polar troposphere, in coastal regions or over the open ocean. Since it was acknowledged recently that the relative importance of IO for ozone depletion might have been underestimated (Benavent et al., 2022), this could provide another application for the surface sensitivity algorithm. There are also several opportunities to improve the AMF algorithm as well as the associated surface sensitivity classifier. The latter currently utilizes a rather crude geometric approximation of the parameter range sensitive to boundary layer trace gases. Compared to methods from machine learning, this gives a high degree in explainability, but in order to guarantee a low false-positive rate, many possibly sensitive measurements are discarded too. More sophisticated machine learning classifiers, such as support vector machines (e.g. Hearst et al., 1998), Naive Bayes (e.g. Zhang, 2004) or neural networks could all lead to a substantial decrease of wrongly discarded measurements while simultaneously providing better control of the allowed false-positive rate. Since the RT model is capable of providing a large set of training data, it would also be interesting to investigate if the proxy based approach for the AMF calculation could be improved upon with a neural network. This could allow for a more complex relationship between the parameters compared to the assumed multilinear relation.

The tropospheric BrO retrieval improved in this thesis is also applicable to measurements performed by other satellite instruments such as GOME-2 or OMI. The vastly improved performance compared to previous implementations facilitates investigations of large datasets covering a longer time period. However, the results of the area size study performed in this thesis indicate that the spatial resolution of GOME-2 might be too coarse for an investigation regarding the initial bromine release.

The column separation algorithm strongly depends on the similarity of the profile shape between stratospheric ozone and bromine monoxide. The arctic winter/spring 2019/2020 was exceptionally cold in the polar stratosphere, resulting in a stable polar vortex up until early April and unprecedented stratospheric ozone depletion similar to Antarctic deple-

tion levels (Weber et al., 2021; Grooß and Müller, 2021). A stable polar vortex limits the amount of available measurements from the retrieval (see chapter 7) since the utilized parameterization does not longer represent a good approximation for stratospheric dynamics and chemistry affecting BrO. Likewise, generally depleted stratospheric ozone levels could lead to an underestimation of the stratospheric fraction of the BrO column. According to Grooß and Müller (2021), the frequency of extreme Arctic winters and the extension of low temperatures into spring could be increased as a result of warming in North Pacific sea surface temperatures, which would in turn decrease the precision of the column separation algorithm applied in this thesis. This indicates the necessity to further improve the stratospheric correction scheme used in this thesis to enable also the evaluation of measurements inside the polar vortex. This requires a more sophisticated parameterization scheme. In principle, this could also lead towards an applicability of the column separation algorithm in the Antarctic region.

In addition to further applications of the retrieval algorithm developed in this thesis, this work pointed towards several other directions for future research:

- The seasonal dependency of both the relative importance of initial release mechanisms as well as meteorological conditions should be investigated in more detail. An analysis of long-term data using the tropospheric BrO retrieval developed in this thesis, resolved on a monthly basis, could provide valuable insight into seasonal trends in the relationship between meteorological parameters and ODEs. Because of the limitations of satellite observations regarding the observation of enhanced BrO mixing ratios in very shallow boundary layers, the current knowledge could also be improved upon by ground-based measurements covering at least one complete polar spring. In the best case scenario, one could use measurements taken directly above the sea ice, which could potentially enable the measurement of initial release of reactive bromine from the snow-pack. One suggestion for this was a large network of drones deployed directly above the (first-year) sea ice (Platt, 2022).

  Although there are already studies performed on long-term datasets, they either did not investigate potential seasonal trends (e.g. Nasse et al., 2019; Swanson et al., 2020) or were severely limited in their significance (Seo et al., 2019).

- The case studies presented in chapter 9 could be improved with an estimate of sea ice thickness which could also be measured space-borne, for example by SMOS (e.g. Mu et al., 2018). Low sea ice thickness can indicate higher salinity on the surface, which could lead to an increase of bromide in the snow-pack. It is possible that this might limit bromine release from the surface in particular very early in polar spring. Since WRF already supports the data assimilation of sea ice thickness data from SMOS, it should also be possible to add this to the model.

- The statistical analysis of the size and shape of ODEs could be substantially improved by tracking individual events for longer periods, i.e. different overpasses and days.

This would allow an estimation of the lifetime of atmospheric BrO plumes, which could greatly improve the significance of the results derived in this study. For example, a larger lifetime of events together with the observed shape and extent of events could allow the conclusion that few small regions where BrO is observed regularly in other studies are enough to explain the vast areas of depleted ozone in Arctic spring, as BrO is emitted in these regions and then transported over the whole region. Calculation of backward trajectories would also help in such an investigation. It might also be possible that, although no trend could be established in the spatial extent of all but the biggest ODEs, events are generally less sustained early in the season since the conditions necessary for sufficiently high bromine release do only persist for a short time.

Using the current algorithm for the detection of areas with significantly enhanced BrO VCDs, there are several possibilities to achieve this. The standard method to track objects across a series of several images applies the calculation of the optical flow (e.g. Zhang and Chanson, 2018). Another possibility is based upon recent methods from topological data analysis and utilizes "flows" of persistent homology classes (Gonzalez-Diaz et al., 2018), which could allow the calculation of an initial emission strength of BrO associated with ODEs.

- Based on the relation between size and shape of ODEs and wind speed, it could be interesting to apply the method presented in Beirle et al. (2019) to BrO plumes. Beirle et al. (2019) calculated the divergence of the NO_x advection to determine the emission source as well as the emission strength of NO_x. It should be investigated if this is applicable in a similar way to BrO fluxes and if this could allow to pinpoint the emission source of an initial BrO plume or estimate initial release flux of reactive bromine.

Additionally, there are several aspects regarding the WRF-CHEM model setup that could be further improved:

- The results of this thesis clearly demonstrate that the assumed solar zenith angle (SZA) dependence of the bromine release from the snow-pack via ozone oxidation can lead to a strong underestimation of bromine produced in an ODE, especially early in the season. An adjustment of the relative emission strength in the presence of sunlight or a complete independence from sunlight should therefore be considered.

- It could prove beneficial to save the model results with an increased temporal resolution, e.g. every 5 minutes, for the study of specific events previously identified from the satellite observations. This would allow a detailed investigation of the relative influence of the different release mechanisms. Especially early in the season, this could provide very valuable insights. It could allow the determination of a "critical" mixing ratio of atmospheric bromine from which on the bromine explosion dominates.

Likewise, it might enable the specification of necessary restrictions on meteorological conditions early in the season allowing the accumulation of such a critical mixing ratio.

- Additional sea salt aerosol release from blowing snow combined with the limited bromide resource could further improve the current model implementation. Case studies performed in this thesis revealed that even ODEs associated with very high wind speeds and typical blowing snow conditions are predicted very well by the model, but especially early on in the life time of such an event the model underestimates the produced BrO. Here additional sea salt aerosols could improve the agreement of model and observations while the limited bromide resource might help preventing a strong overestimation as reported by Swanson et al. (2022) in their similar model without bromide limitation.

- The importance of bromine recycling on aerosols, especially during conditions of high wind speeds and in Arctic cyclones, suggests that full coupling of atmospheric bromine to the aerosol module MOSAIC in the simulations, such that the size and the pH value of the aerosol is influenced by the bromine chemistry, could yield improvements. Especially an accurate modeling of the pH value could be of interest, as this would also allow a more accurate implementation of a bromine release mechanism from blowing snow, releasing bromine only from heterogeneous reactions and not constantly from every aerosol particle.

It is expected that the frequency of ODEs is going to increase over the next decades (see e.g. Hollwedel et al., 2004; Bougoudis et al., 2020) due to a an increased replacement of perennial ice by younger sea ice (Nghiem et al., 2012) as a result of global warming. Coincidentally, it is also speculated that a changing climate will lead to an increase of extreme Arctic cyclones (e.g. Vavrus, 2013), which are associated with very large BrO columns and depleted ozone mixing ratios even above the boundary layer in the free troposphere. The results of this work established that the frequency increase of ODEs could be even more drastic than expected from the decrease of sea ice age alone. More emissions of reactive bromine from an increase of bromide in the surface could increase the levels of reactive bromine early in the season, in turn increasing the likelihood for ODEs associated with higher wind speeds and more extreme weather events earlier in the season. This could increase the impact of halogen chemistry on the oxidative capacity in high latitudes and may lead to substantial depletion of tropospheric concentrations of O_3. It also implies a change in the seasonal trend conjectured in this thesis towards a decreasing time span of the importance of shallow boundary layers and calm meteorological conditions, which might already be discernible in today's long-term datasets.

Appendix

A | Bibliography - Own Contribution

Parts of this thesis have been published in:

Herrmann, M., Schöne, M., Borger, C., Warnach, S., Wagner, T., Platt, U., and Gutheil, E.: Ozone depletion events in the Arctic spring of 2019: A new modeling approach to bromine emissions, Atmospheric Chemistry and Physics Discussions, 2022, 1–39, doi:10.5194/acp-2022-334.

B | Bibliography

Aaboe, S., Breivik, L., Sørensen, A., Eastwood, S., and Lavergne, T.: Global Sea Ice Edge (OSI-402-c) and Type (OSI-403-c) Product User's Manual–v2. 2. TechnicalReportSAF, Tech. rep., OSI/CDOP2/MET-Norway/TEC/MA/205, EUMETSAT OSI SAF–Ocean and Sea Ice, 2017.

Abbatt, J., Oldridge, N., Symington, A., Chukalovskiy, V., McWhinney, R., Sjostedt, S., and Cox, R.: Release of gas-phase halogens by photolytic generation of OH in frozen halide- nitrate solutions: an active halogen formation mechanism?, The Journal of Physical Chemistry A, 114, 6527–6533, 2010.

Abbatt, J. P.: Heterogeneous reaction of HOBr with HBr and HCl on ice surfaces at 228 K, Geophysical research letters, 21, 665–668, 1994.

Abbatt, J. P. D., Thomas, J. L., Abrahamsson, K., Boxe, C., Granfors, A., Jones, A. E., King, M. D., Saiz-Lopez, A., Shepson, P. B., Sodeau, J., Toohey, D. W., Toubin, C., von Glasow, R., Wren, S. N., and Yang, X.: Halogen activation via interactions with environmental ice and snow in the polar lower troposphere and other regions, Atmospheric Chemistry and Physics, 12, 6237–6271, https://doi.org/10.5194/acp-12-6237-2012, 2012.

Acarreta, J., De Haan, J., and Stammes, P.: Cloud pressure retrieval using the O2-O2 absorption band at 477 nm, Journal of Geophysical Research: Atmospheres, 109, 2004.

Aguzzi, A. and Rossi, M. J.: Heterogeneous hydrolysis and reaction of BrONO2 and Br2O on pure ice and ice doped with HBr, The Journal of Physical Chemistry A, 106, 5891–5901, 2002.

Anderson, P. S. and Neff, W. D.: Boundary layer physics over snow and ice, Atmospheric Chemistry and Physics, 8, 3563–3582, https://doi.org/10.5194/acp-8-3563-2008, 2008.

Andreae, M. O., Hegg, D. A., and Baltensperger, U.: Sources and Nature of Atmospheric Aerosols, pp. 45–89, Springer Netherlands, Dordrecht, 2009.

Angot, H., Dastoor, A., De Simone, F., Gårdfeldt, K., Gencarelli, C. N., Hedgecock, I. M., Langer, S., Magand, O., Mastromonaco, M. N., Nordstrøm, C., et al.: Chemical cycling and deposition of atmospheric mercury in polar regions: review of recent measurements

and comparison with models, Atmospheric Chemistry and Physics, 16, 10 735–10 763, 2016.

Anlauf, K., Mickle, R., and Trivett, N.: Measurement of ozone during polar sunrise experiment 1992, Journal of Geophysical Research: Atmospheres, 99, 25 345–25 353, 1994.

Arias-Castro, E. and Donoho, D. L.: Does median filtering truly preserve edges better than linear filtering?, The Annals of Statistics, 37, 1172–1206, 2009.

Artiglia, L., Edebeli, J., Orlando, F., Chen, S., Lee, M.-T., Arroyo, P. C., Gilgen, A., Bartels-Rausch, T., Kleibert, A., Vazdar, M., et al.: A surface-stabilized ozonide triggers bromide oxidation at the aqueous solution-vapour interface, Nature Communications, 8, 700, 2017.

Atkinson, H. M., Huang, R.-J., Chance, R., Roscoe, H. K., Hughes, C., Davison, B., Schönhardt, A., Mahajan, A. S., Saiz-Lopez, A., Hoffmann, T., et al.: Iodine emissions from the sea ice of the Weddell Sea, Atmospheric Chemistry and Physics, 12, 11 229–11 244, 2012.

Atkinson, R., Baulch, D. L., Cox, R. A., Crowley, J. N., Hampson, R. F., Hynes, R. G., Jenkin, M. E., Rossi, M. J., and Troe, J.: Evaluated kinetic and photochemical data for atmospheric chemistry: Volume III - gas phase reactions of inorganic halogens, Atmospheric Chemistry and Physics, 7, 981–1191, https://doi.org/10.5194/acp-7-981-2007, 2007.

Banerjee, A., Fyfe, J. C., Polvani, L. M., Waugh, D., and Chang, K.-L.: A pause in Southern Hemisphere circulation trends due to the Montreal Protocol, Nature, 579, 544–548, 2020.

Barrie, L., Bottenheim, J., Schnell, R., Crutzen, P., and Rasmussen, R.: Ozone destruction and photochemical reactions at polar sunrise in the lower Arctic atmosphere, Nature, 334, 138, 1988.

Bartels-Rausch, T., Jacobi, H.-W., Kahan, T. F., Thomas, J. L., Thomson, E. S., Abbatt, J. P., Ammann, M., Blackford, J. R., Bluhm, H., Boxe, C., et al.: A review of air–ice chemical and physical interactions (AICI): liquids, quasi-liquids, and solids in snow, Atmospheric chemistry and physics, 14, 1587–1633, 2014.

Begoin, M., Richter, A., Weber, M., Kaleschke, L., Tian-Kunze, X., Stohl, A., Theys, N., and Burrows, J. P.: Satellite observations of long range transport of a large BrO plume in the Arctic, Atmospheric Chemistry and Physics, 10, 6515–6526, https://doi.org/10.5194/acp-10-6515-2010, 2010.

Beirle, S., Sihler, H., and Wagner, T.: Linearisation of the effects of spectral shift and stretch in DOAS analysis, Atmospheric Measurement Techniques, 6, 661–675, 2013.

Beirle, S., Lampel, J., Lerot, C., Sihler, H., and Wagner, T.: Parameterizing the instrumental spectral response function and its changes by a super-Gaussian and its derivatives, Atmospheric Measurement Techniques, 10, 581–598, https://doi.org/10.5194/amt-10-581-2017, 2017.

Beirle, S., Borger, C., Dörner, S., Li, A., Hu, Z., Liu, F., Wang, Y., and Wagner, T.: Pinpointing nitrogen oxide emissions from space, Science Advances, 5, eaax9800, https://doi.org/10.1126/sciadv.aax9800, 2019.

Benavent, N., Mahajan, A. S., Li, Q., Cuevas, C. A., Schmale, J., Angot, H., Jokinen, T., Quéléver, L. L., Blechschmidt, A.-M., Zilker, B., et al.: Substantial contribution of iodine to Arctic ozone destruction, Nature Geoscience, pp. 1–4, 2022.

Bertram, T. H. and Thornton, J. A.: Toward a general parameterization of N_2O_5 reactivity on aqueous particles: the competing effects of particle liquid water, nitrate and chloride, Atmospheric Chemistry and Physics, 9, 8351–8363, https://doi.org/10.5194/acp-9-8351-2009, 2009.

Blechschmidt, A.-M., Richter, A., Burrows, J., Kaleschke, L., Strong, K., Theys, N., Weber, M., Zhao, X., and Zien, A.: An exemplary case of a bromine explosion event linked to cyclone development in the Arctic, Atmospheric Chemistry and Physics, 16, 1773–1788, 2016.

Bock, H.-H.: Clustering methods: a history of k-means algorithms, Selected contributions in data analysis and classification, pp. 161–172, 2007.

Boersma, K., Eskes, H., Veefkind, J., Brinksma, E., Van Der A, R., Sneep, M. v., Van Den Oord, G., Levelt, P., Stammes, P., Gleason, J., et al.: Near-real time retrieval of tropospheric NO 2 from OMI, Atmospheric Chemistry and Physics, 7, 2103–2118, 2007.

Boersma, K. F., Eskes, H. J., Dirksen, R. J., van der A, R. J., Veefkind, J. P., Stammes, P., Huijnen, V., Kleipool, Q. L., Sneep, M., Claas, J., Leitão, J., Richter, A., Zhou, Y., and Brunner, D.: An improved tropospheric NO_2 column retrieval algorithm for the Ozone Monitoring Instrument, Atmospheric Measurement Techniques, 4, 1905–1928, https://doi.org/10.5194/amt-4-1905-2011, 2011.

Boersma, K. F., Eskes, H. J., Richter, A., De Smedt, I., Lorente, A., Beirle, S., van Geffen, J. H. G. M., Zara, M., Peters, E., Van Roozendael, M., Wagner, T., Maasakkers, J. D., van der A, R. J., Nightingale, J., De Rudder, A., Irie, H., Pinardi, G., Lambert, J.-C., and Compernolle, S. C.: Improving algorithms and uncertainty estimates for satellite NO_2 retrievals: results from the quality assurance for the essential climate variables (QA4ECV) project, Atmospheric Measurement Techniques, 11, 6651–6678, https://doi.org/10.5194/amt-11-6651-2018, 2018.

Bognar, K., Zhao, X., Strong, K., Chang, R.-W., Frieß, U., Hayes, P., McClure-Begley, A., Morris, S., Tremblay, S., and Vicente-Luis, A.: Measurements of tropospheric bromine monoxide over four halogen activation seasons in the Canadian High Arctic, Journal of Geophysical Research: Atmospheres, 125, e2020JD033 015, 2020.

Bogumil, K., Orphal, J., Homann, T., Voigt, S., Spietz, P., Fleischmann, O., Vogel, A., Hartmann, M., Kromminga, H., Bovensmann, H., Frerick, J., and Burrows, J.: Measurements of molecular absorption spectra with the SCIAMACHY pre-flight model: instrument characterization and reference data for atmospheric remote-sensing in the 230–2380 nm region, Journal of Photochemistry and Photobiology A: Chemistry, 157, 167–184, https://doi.org/https://doi.org/10.1016/S1010-6030(03)00062-5, atmospheric Photochemistry, 2003.

Borger, C., Beirle, S., Dörner, S., Sihler, H., and Wagner, T.: Total column water vapour retrieval from S-5P/TROPOMI in the visible blue spectral range, Atmospheric Measurement Techniques, 13, 2751–2783, https://doi.org/10.5194/amt-13-2751-2020, 2020.

Bottenheim, J., Gallant, A., and Brice, K.: Measurements of NO_y species and O_3 at 82° N latitude, Geophysical Research Letters, 13, 113–116, 1986.

Bottenheim, J., Netcheva, S., Morin, S., and Nghiem, S.: Ozone in the boundary layer air over the Arctic Ocean: measurements during the TARA transpolar drift 2006–2008, Atmospheric Chemistry and Physics, 9, 4545–4557, 2009.

Bottenheim, J. W., Fuentes, J. D., Tarasick, D. W., and Anlauf, K. G.: Ozone in the Arctic lower troposphere during winter and spring 2000 (ALERT2000), Atmospheric Environment, 36, 2535–2544, 2002.

Bougoudis, I., Blechschmidt, A.-M., Richter, A., Seo, S., Burrows, J. P., Theys, N., and Rinke, A.: Long-term time series of Arctic tropospheric BrO derived from UV–VIS satellite remote sensing and its relation to first-year sea ice, Atmospheric Chemistry and Physics, 20, 11 869–11 892, https://doi.org/10.5194/acp-20-11869-2020, 2020.

Bougoudis, I., Blechschmidt, A.-M., Richter, A., Seo, S., and Burrows, J. P.: Simulating tropospheric BrO in the Arctic using an artificial neural network, Atmospheric Environment, 276, 119 032, 2022.

Brimblecombe, P. and Clegg, S.: The solubility and behaviour of acid gases in the marine aerosol, Journal of Atmospheric Chemistry, 7, 1–18, 1988.

Buat-Menard, P., Morelli, J., and Chesselet, R.: Water-soluble elements in atmospheric particulate matter over tropical and equatorial Atlantic, Journal de Recherches Atmospheriques, 8, 661–673, 1974.

Burd, J. A., Peterson, P. K., Nghiem, S. V., Perovich, D. K., and Simpson, W. R.: Snowmelt onset hinders bromine monoxide heterogeneous recycling in the Arctic, Journal of Geophysical Research: Atmospheres, 122, 8297–8309, 2017.

Burrows, J. P., Platt, U., and Borrell, P.: The remote sensing of tropospheric composition from space, Springer Science & Business Media, 2011.

Cady, G. H.: Reaction of Fluorine with Water and with Hydroxides, Journal of the American Chemical Society, 57, 246–249, 1935.

Cao, L., Sihler, H., Platt, U., and Gutheil, E.: Numerical analysis of the chemical kinetic mechanisms of ozone depletion and halogen release in the polar troposphere, Atmos. Chem. Phys, 14, 377, 2014.

Cao, L., Platt, U., and Gutheil, E.: Role of the boundary layer in the occurrence and termination of the tropospheric ozone depletion events in polar spring, Atmospheric Environment, 132, 98–110, 2016.

Capderou, M.: Orbit and Ground Track of a Satellite, Satellites: Orbits and Missions, pp. 175–263, 2005.

Capderou, M.: Handbook of satellite orbits: From kepler to GPS, Springer Science & Business, 2014.

Chan, K. L., Valks, P., Heue, K.-P., Lutz, R., Hedelt, P., Loyola, D., Pinardi, G., Van Roozendael, M., Hendrick, F., Wagner, T., et al.: Global Ozone Monitoring Experiment-2 (GOME-2) Daily and Monthly Level 3 Products of Atmospheric Trace Gas Columns, Earth System Science Data Discussions, pp. 1–49, 2022.

Chance, K.: Analysis of BrO measurements from the global ozone monitoring experiment, Geophysical Research Letters, 25, 3335–3338, 1998.

Chen, Q., Sherwen, T., Evans, M., and Alexander, B.: DMS oxidation and sulfur aerosol formation in the marine troposphere: a focus on reactive halogen and multiphase chemistry, Atmospheric Chemistry and Physics, 18, 13 617–13 637, 2018.

Chipperfield, M. P., Bekki, S., Dhomse, S., Harris, N. R., Hassler, B., Hossaini, R., Steinbrecht, W., Thiéblemont, R., and Weber, M.: Detecting recovery of the stratospheric ozone layer, Nature, 549, 211–218, 2017.

Choi, S., Wang, Y., Salawitch, R., Canty, T., Joiner, J., Zeng, T., Kurosu, T., Chance, K., Richter, A., Huey, L. G., et al.: Analysis of satellite-derived Arctic tropospheric BrO columns in conjunction with aircraft measurements during ARCTAS and ARCPAC, Atmospheric Chemistry and Physics, 12, 1255–1285, 2012.

Choi, S., Theys, N., Salawitch, R., Wales, P., Joiner, J., Canty, T., Chance, K., Suleiman, R., Palm, S., Cullather, R., et al.: Link between Arctic tropospheric BrO explosion observed from space and sea-salt aerosols from blowing snow investigated using ozone monitoring instrument BrO data and GEOS-5 data assimilation system, Journal of Geophysical Research: Atmospheres, 123, 6954–6983, 2018.

Cicerone, R. J., Stolarski, R. S., and Walters, S.: Stratospheric ozone destruction by man-made chlorofluoromethanes, Science, 185, 1165–1167, 1974.

Clémer, K., Van Roozendael, M., Fayt, C., Hendrick, F., Hermans, C., Pinardi, G., Spurr, R., Wang, P., and De Mazière, M.: Multiple wavelength retrieval of tropospheric aerosol optical properties from MAXDOAS measurements in Beijing, Atmospheric Measurement Techniques, 3, 863–878, 2010.

Compernolle, S., Argyrouli, A., Lutz, R., Sneep, M., Lambert, J.-C., Fjæraa, A. M., Hubert, D., Keppens, A., Loyola, D., O'Connor, E., et al.: Validation of the Sentinel-5 Precursor TROPOMI cloud data withCloudnet, Aura OMI O2–O2, MODIS, and Suomi-NPP VIIR, 2021.

Crutzen, P.: A review of upper atmospheric photochemistry, Canadian Journal of Chemistry, 52, 1569–1581, 1974.

Crutzen, P. J.: The influence of nitrogen oxides on the atmospheric ozone content, Quarterly Journal of the Royal Meteorological Society, 96, 320–325, 1970.

Crutzen, P. J. and Zimmermann, P. H.: The changing photochemistry of the troposphere, Tellus A: Dynamic Meteorology and Oceanography, 43, 136–151, 1991.

Custard, K., Thompson, C., Pratt, K., Shepson, P. B., Liao, J., Huey, L., Orlando, J., Weinheimer, A., Apel, E., Hall, S., et al.: The NO x dependence of bromine chemistry in the Arctic atmospheric boundary layer, Atmospheric Chemistry and Physics, 15, 10 799–10 809, 2015.

Custard, K., Raso, A., Shepson, P., Staebler, R., and Pratt, K.: Production and release of molecular bromine and chlorine from the Arctic coastal snowpack, ACS Earth and Space Chemistry, 1, 142–151, 2017.

Deb, P., Orr, A., Hosking, J. S., Phillips, T., Turner, J., Bannister, D., Pope, J. O., and Colwell, S.: An assessment of the Polar Weather Research and Forecasting (WRF) model representation of near-surface meteorological variables over West Antarctica, Journal of Geophysical Research: Atmospheres, 121, 1532–1548, 2016.

Deschamps, P., Fouquart, Y., Tanré, D., Herman, M., Lenoble, J., Buriez, J., Dubuisson, P., Parol, F., Vanbauce, C., Grassl, H., et al.: Study on the effects of scattering on the monitoring of atmospheric constituents, Rep. 3838, ESA contract no. 9740/91/NL/BI, 1994.

Deutschmann, T., Beirle, S., Frieß, U., Grzegorski, M., Kern, C., Kritten, L., Platt, U., Prados-Román, C., Puķı, J., Wagner, T., et al.: The Monte Carlo atmospheric radiative transfer model McArtim: Introduction and validation of Jacobians and 3D features, Journal of Quantitative Spectroscopy and Radiative Transfer, 112, 1119–1137, 2011.

Domine, F., Sparapani, R., Ianniello, A., and Beine, H. J.: The origin of sea salt in snow on Arctic sea ice and in coastal regions, Atmospheric Chemistry and Physics, 4, 2259–2271, https://doi.org/10.5194/acp-4-2259-2004, 2004.

Domine, F., Taillandier, A. S., Simpson, W. R., and Severin, K.: Specific surface area, density and microstructure of frost flowers, Geophysical Research Letters, 32, 2005.

Eguchi, N. and Yoshida, Y.: A high-level cloud detection method utilizing the GOSAT TANSO-FTS water vapor saturated band, Atmospheric Measurement Techniques, 12, 389–403, 2019.

Emmons, L. K., Walters, S., Hess, P. G., Lamarque, J.-F., Pfister, G. G., Fillmore, D., Granier, C., Guenther, A., Kinnison, D., Laepple, T., et al.: Description and evaluation of the Model for Ozone and Related chemical Tracers, version 4 (MOZART-4), 2010.

Errera, Q. and Fonteyn, D.: Four-dimensional variational chemical assimilation of CRISTA stratospheric measurements, Journal of Geophysical Research: Atmospheres, 106, 12 253–12 265, 2001.

ESA: ESA S-5P Mission description, URL https://sentinel.esa.int/web/sentinel/missions/sentinel-5p/mission-objectives, a.

ESA: ESA S-5P Orbit description, URL https://sentinels.copernicus.eu/web/sentinel/missions/sentinel-5p/orbit, b.

Eskes, H., van Geffen, J., Boersma, K., Sneep, M., ter Linden, M., Richter, A., Beirle, S., and Veefkind, J.: High spatial resolution nitrogen dioxide tropospheric column observations derived from Sentinel-5P TROPOMI observations,, Atmos Meas. Tech., submitted, 2022.

EUMETSAT: GOME-2 Level 1 Product Generation Specification, URL https://www-cdn.eumetsat.int/files/2020-04/pdf_ten_990011-eps-gome-pgs.pdf, 2011.

Falk, S. and Sinnhuber, B.-M.: Polar boundary layer bromine explosion and ozone depletion events in the chemistry-climate model EMAC v2. 52: implementation and evaluation of AirSnow algorithm., Geoscientific Model Development, 11, 2018.

Fan, S.-M. and Jacob, D. J.: Surface ozone depletion in Arctic spring sustained by bromine reactions on aerosols, Nature, 359, 522, 1992.

Fang, X., Pyle, J. A., Chipperfield, M. P., Daniel, J. S., Park, S., and Prinn, R. G.: Challenges for the recovery of the ozone layer, Nature Geoscience, 12, 592–596, 2019.

Farman, J. C., Gardiner, B. G., and Shanklin, J. D.: Large losses of total ozone in Antarctica reveal seasonal ClOx/NOx interaction, Nature, 315, 207–210, 1985.

Fernandez, R. P., Carmona-Balea, A., Cuevas, C. A., Barrera, J. A., Kinnison, D. E., Lamarque, J.-F., Blaszczak-Boxe, C., Kim, K., Choi, W., Hay, T., et al.: Modeling the

sources and chemistry of polar tropospheric halogens (Cl, Br, and I) using the CAM-Chem global chemistry-climate model, Journal of Advances in Modeling Earth Systems, 11, 2259–2289, 2019.

Fickert, S., Adams, J. W., and Crowley, J. N.: Activation of Br2 and BrCl via uptake of HOBr onto aqueous salt solutions, Journal of Geophysical Research: Atmospheres, 104, 23 719–23 727, https://doi.org/10.1029/1999JD900359, 1999.

Finch, D. P., Palmer, P. I., and Zhang, T.: Automated detection of atmospheric NO_2 plumes from satellite data: a tool to help infer anthropogenic combustion emissions, Atmospheric Measurement Techniques, 15, 721–733, https://doi.org/10.5194/amt-15-721-2022, 2022.

Fiorio, C. and Gustedt, J.: Two linear time union-find strategies for image processing, Theoretical Computer Science, 154, 165–181, 1996.

Fleischmann, O. C., Hartmann, M., Burrows, J. P., and Orphal, J.: New ultraviolet absorption cross-sections of BrO at atmospheric temperatures measured by time-windowing Fourier transform spectroscopy, Journal of Photochemistry and Photobiology A: Chemistry, 168, 117–132, https://doi.org/https://doi.org/10.1016/j.jphotochem.2004.03.026, 2004.

Frey, M. M., Norris, S. J., Brooks, I. M., Anderson, P. S., Nishimura, K., Yang, X., Jones, A. E., Nerentorp Mastromonaco, M. G., Jones, D. H., and Wolff, E. W.: First direct observation of sea salt aerosol production from blowing snow above sea ice, Atmospheric Chemistry and Physics, 20, 2549–2578, 2020.

Frieß, U., Hollwedel, J., König-Langlo, G., Wagner, T., and Platt, U.: Dynamics and chemistry of tropospheric bromine explosion events in the Antarctic coastal region, Journal of Geophysical Research: Atmospheres, 109, 2004.

Frieß, U., Monks, P., Remedios, J., Rozanov, A., Sinreich, R., Wagner, T., and Platt, U.: MAX-DOAS O4 measurements: A new technique to derive information on atmospheric aerosols: 2. Modeling studies, Journal of Geophysical Research: Atmospheres, 111, 2006.

Frieß, U., Sihler, H., Sander, R., Pöhler, D., Yilmaz, S., and Platt, U.: The vertical distribution of BrO and aerosols in the Arctic: Measurements by active and passive differential optical absorption spectroscopy, Journal of Geophysical Research: Atmospheres, 116, 2011.

George, I. J. and Anastasio, C.: Release of gaseous bromine from the photolysis of nitrate and hydrogen peroxide in simulated sea-salt solutions, Atmospheric Environment, 41, 543–553, 2007.

Gong, S., Barrie, L., and Blanchet, J.-P.: Modeling sea-salt aerosols in the atmosphere: 1. Model development, Journal of Geophysical Research: Atmospheres, 102, 3805–3818, 1997.

Gonzalez-Diaz, R., Jimenez, M.-J., and Medrano, B.: Topological tracking of connected components in image sequences, Journal of Computer and System Sciences, 95, 134–142, 2018.

Graham, R. M., Hudson, S. R., and Maturilli, M.: Improved performance of ERA5 in Arctic gateway relative to four global atmospheric reanalyses, Geophysical Research Letters, 46, 6138–6147, 2019.

Grainger, J. F. and Ring, J.: Anomalous Fraunhofer Line Profiles, Nature, 193, 762, https://doi.org/10.1038/193762a0, 1962.

Grebel, J. E., Pignatello, J. J., and Mitch, W. A.: Effect of halide ions and carbonates on organic contaminant degradation by hydroxyl radical-based advanced oxidation processes in saline waters, Environmental science & technology, 44, 6822–6828, 2010.

Greenblatt, G. D., Orlando, J. J., Burkholder, J. B., and Ravishankara, A.: Absorption measurements of oxygen between 330 and 1140 nm, Journal of Geophysical Research: Atmospheres, 95, 18 577–18 582, 1990.

Grooß, J.-U. and Müller, R.: Simulation of record Arctic stratospheric ozone depletion in 2020, Journal of Geophysical Research: Atmospheres, 126, e2020JD033 339, 2021.

Halfacre, J. W., Knepp, T. N., Shepson, P. B., Thompson, C. R., Pratt, K. A., Li, B., Peterson, P. K., Walsh, S. J., Simpson, W. R., Matrai, P. A., Bottenheim, J. W., Netcheva, S., Perovich, D. K., and Richter, A.: Temporal and spatial characteristics of ozone depletion events from measurements in the Arctic, Atmospheric Chemistry and Physics, 14, 4875–4894, https://doi.org/10.5194/acp-14-4875-2014, 2014.

Halfacre, J. W., Shepson, P. B., and Pratt, K. A.: pH-dependent production of molecular chlorine, bromine, and iodine from frozen saline surfaces, Atmospheric Chemistry and Physics, 19, 4917–4931, 2019.

Hausmann, M. and Platt, U.: Spectroscopic measurement of bromine oxide and ozone in the high Arctic during Polar Sunrise Experiment 1992, Journal of Geophysical Research: Atmospheres, 99, 25 399–25 413, 1994.

Hearst, M. A., Dumais, S. T., Osuna, E., Platt, J., and Scholkopf, B.: Support vector machines, IEEE Intelligent Systems and their applications, 13, 18–28, 1998.

Herrmann, M., Cao, L., Sihler, H., Platt, U., and Gutheil, E.: On the contribution of chemical oscillations to ozone depletion events in the polar spring, Atmospheric Chemistry and Physics, 19, 10 161–10 190, https://doi.org/10.5194/acp-19-10161-2019, 2019.

Herrmann, M., Sihler, H., Wagner, T., Platt, U., and Gutheil, E.: 3D simulations of tropospheric ozone depletion events using WRF-Chem, Atmospheric Chemistry and Physics Discussions, 2020, 1–35, https://doi.org/10.5194/acp-2020-952, 2020.

Herrmann, M., Sihler, H., Frieß, U., Wagner, T., Platt, U., and Gutheil, E.: Time-dependent 3D simulations of tropospheric ozone depletion events in the Arctic spring using the Weather Research and Forecasting model coupled with Chemistry (WRF-Chem), Atmospheric Chemistry and Physics, 21, 7611–7638, 2021.

Herrmann, M., Schöne, M., Borger, C., Warnach, S., Wagner, T., Platt, U., and Gutheil, E.: Ozone depletion events in the Arctic spring of 2019: A new modeling approach to bromine emissions, Atmospheric Chemistry and Physics Discussions, 2022, 1–39, https://doi.org/10.5194/acp-2022-334, 2022.

Herrmann, M. M.: Modellierung des troposphärischen Ozonabbaus im arktischen Frühling, Ph.D. thesis, 2021.

Hersbach, H. and Dee, D.: ERA5 reanalysis is in production, ECMWF Newsletter, 147, 2016.

Heue, K.-P., Brenninkmeijer, C., Baker, A., Rauthe-Schöch, A., Walter, D., Wagner, T., Hörmann, C., Sihler, H., Dix, B., Frieß, U., et al.: SO 2 and BrO observation in the plume of the Eyjafjallajökull volcano 2010: CARIBIC and GOME-2 retrievals, Atmospheric Chemistry and Physics, 11, 2973–2989, 2011.

Holla, R., Schmitt, S., Frieß, U., Pöhler, D., Zingler, J., Corsmeier, U., and Platt, U.: Vertical distribution of BrO in the boundary layer at the Dead Sea, Environmental chemistry, 12, 438–460, 2015.

Hollwedel, J., Wenig, M., Beirle, S., Kraus, S., Kühl, S., Wilms-Grabe, W., Platt, U., and Wagner, T.: Year-to-year variations of spring time polar tropospheric BrO as seen by GOME, Advances in Space Research, 34, 804–808, 2004.

Hönninger, G. and Platt, U.: Observations of BrO and its vertical distribution during surface ozone depletion at Alert, Atmospheric Environment, 36, 2481–2489, 2002.

Hönninger, G., Leser, H., Sebastian, O., and Platt, U.: Ground-based measurements of halogen oxides at the Hudson Bay by active longpath DOAS and passive MAX-DOAS, Geophysical research letters, 31, 2004.

Hopper, J., Peters, B., Yokouchi, Y., Niki, H., Jobson, B., Shepson, P., and Muthuramu, K.: Chemical and meteorological observations at ice camp SWAN during Polar Sunrise Experiment 1992, Journal of Geophysical Research: Atmospheres, 99, 25 489–25 498, 1994.

Hopper, J., Barrie, L., Silis, A., Hart, W., Gallant, A., and Dryfhout, H.: Ozone and meteorology during the 1994 Polar Sunrise Experiment, Journal of Geophysical Research: Atmospheres, 103, 1481–1492, 1998.

Hörmann, C., Sihler, H., Bobrowski, N., Beirle, S., Penning de Vries, M., Platt, U., and Wagner, T.: Systematic investigation of bromine monoxide in volcanic plumes from space

by using the GOME-2 instrument, Atmospheric Chemistry and Physics, 13, 4749–4781, 2013.

Hörmann, C., Sihler, H., Beirle, S., Penning de Vries, M., Platt, U., and Wagner, T.: Seasonal variation of tropospheric bromine monoxide over the Rann of Kutch salt marsh seen from space, Atmospheric Chemistry and Physics, 16, 13 015–13 034, 2016.

Hu, M.-K.: Visual pattern recognition by moment invariants, IRE transactions on information theory, 8, 179–187, 1962.

Huang, J. and Jaeglé, L.: Wintertime enhancements of sea salt aerosol in polar regions consistent with a sea ice source from blowing snow, Atmospheric Chemistry and Physics, 17, 3699–3712, 2017.

Huang, J., Jaeglé, L., and Shah, V.: Using CALIOP to constrain blowing snow emissions of sea salt aerosols over Arctic and Antarctic sea ice, Atmospheric Chemistry and Physics, 18, 16 253–16 269, 2018.

Huang, J., Jaeglé, L., Chen, Q., Alexander, B., Sherwen, T., Evans, M. J., Theys, N., and Choi, S.: Evaluating the impact of blowing-snow sea salt aerosol on springtime BrO and O 3 in the Arctic, Atmospheric Chemistry and Physics, 20, 7335–7358, 2020.

Huang, T., Yang, G., and Tang, G.: A fast two-dimensional median filtering algorithm, IEEE transactions on acoustics, speech, and signal processing, 27, 13–18, 1979.

Hulst, H. C. and van de Hulst, H. C.: Light scattering by small particles, Courier Corporation, 1981.

Irie, H., Kanaya, Y., Akimoto, H., Iwabuchi, H., Shimizu, A., and Aoki, K.: First retrieval of tropospheric aerosol profiles using MAX-DOAS and comparison with lidar and sky radiometer measurements, Atmospheric Chemistry and Physics, 8, 341–350, 2008.

Jacobi, H.-W., Kaleschke, L., Richter, A., Rozanov, A., and Burrows, J. P.: Observation of a fast ozone loss in the marginal ice zone of the Arctic Ocean, Journal of Geophysical Research: Atmospheres, 111, 2006.

Jacobi, H.-W., Morin, S., and Bottenheim, J. W.: Observation of widespread depletion of ozone in the springtime boundary layer of the central Arctic linked to mesoscale synoptic conditions, Journal of Geophysical Research: Atmospheres, 115, 2010.

Jähne, B.: Spatio-temporal image processing: theory and scientific applications, Springer, 1993.

Jähne, B.: Digitale Bildverarbeitung und Bildgewinnung, Springer-Verlag, 2012.

Joiner, J., Bhartia, P. K., Cebula, R. P., Hilsenrath, E., McPeters, R. D., and Park, H.: Rotational Raman scattering (Ring effect) in satellite backscatter ultraviolet measurements, Applied Optics, 34, 4513–4525, 1995.

Jones, A., Anderson, P., Wolff, E., Turner, J., Rankin, A., and Colwell, S.: A role for newly forming sea ice in springtime polar tropospheric ozone loss? Observational evidence from Halley station, Antarctica, Journal of Geophysical Research: Atmospheres, 111, 2006.

Jones, A., Wolff, E., Brough, N., Bauguitte, S.-B., Weller, R., Yela, M., Navarro-Comas, M., Ochoa, H., and Theys, N.: The spatial scale of ozone depletion events derived from an autonomous surface ozone network in coastal Antarctica, Atmospheric Chemistry and Physics, 13, 1457–1467, 2013.

Jones, A. E., Weller, R., Wolff, E. W., and Jacobi, H. W.: Speciation and rate of photochemical NO and NO2 production in Antarctic snow, Geophysical Research Letters, 27, 345–348, https://doi.org/10.1029/1999GL010885, 2000.

Jones, A. E., Weller, R., Anderson, P. S., Jacobi, H. W., Wolff, E. W., Schrems, O., and Miller, H.: Measurements of NOx emissions from the Antarctic snowpack, Geophysical Research Letters, 28, 1499–1502, https://doi.org/10.1029/2000GL011956, 2001.

Jones, A. E., Anderson, P. S., Begoin, M., Brough, N., Hutterli, M. A., Marshall, G. J., Richter, A., Roscoe, H. K., and Wolff, E. W.: BrO, blizzards, and drivers of polar tropospheric ozone depletion events, Atmospheric Chemistry and Physics, 9, 4639–4652, 2009.

Jones, A. E., Anderson, P. S., Wolff, E. W., Roscoe, H. K., Marshall, G. J., Richter, A., Brough, N., and Colwell, S. R.: Vertical structure of Antarctic tropospheric ozone depletion events: characteristics and broader implications, Atmospheric Chemistry and Physics, 10, 7775–7794, 2010.

Kaleschke, L., Richter, A., Burrows, J., Afe, O., Heygster, G., Notholt, J., Rankin, A., Roscoe, H., Hollwedel, J., Wagner, T., et al.: Frost flowers on sea ice as a source of sea salt and their influence on tropospheric halogen chemistry, Geophysical research letters, 31, 2004.

Kattawar, G., Young, A. T., and Humphreys, T. J.: Inelastic scattering in planetary atmospheres. I-The Ring effect, without aerosols, The Astrophysical Journal, 243, 1049–1057, 1981.

King, M. D.: Determination of the scaled optical thickness of clouds from reflected solar radiation measurements, Journal of the Atmospheric Sciences, 44, 1734–1751, 1987.

Kleipool, Q., Ludewig, A., Babić, L., Bartstra, R., Braak, R., Dierssen, W., Dewitte, P.-J., Kenter, P., Landzaat, R., Leloux, J., Loots, E., Meijering, P., van der Plas, E., Rozemeijer, N., Schepers, D., Schiavini, D., Smeets, J., Vacanti, G., Vonk, F., and Veefkind, P.: Prelaunch calibration results of the TROPOMI payload on-board the Sentinel-5 Precursor satellite, Atmospheric Measurement Techniques, 11, 6439–6479, https://doi.org/10.5194/amt-11-6439-2018, 2018.

Koo, J.-H., Wang, Y., Kurosu, T., Chance, K., Rozanov, A., Richter, A., Oltmans, S., Thompson, A., Hair, J., Fenn, M., et al.: Characteristics of tropospheric ozone depletion events in the Arctic spring: analysis of the ARCTAS, ARCPAC, and ARCIONS measurements and satellite BrO observations, Atmospheric Chemistry and Physics, 12, 9909–9922, 2012.

Koop, T., Kapilashrami, A., Molina, L. T., and Molina, M. J.: Phase transitions of sea-salt/water mixtures at low temperatures: Implications for ozone chemistry in the polar marine boundary layer, Journal of Geophysical Research: Atmospheres, 105, 26 393–26 402, 2000.

Kreher, K., Keys, J., Johnston, P., Platt, U., and Liu, X.: Ground-based measurements of OClO and HCl in austral spring 1993 at Arrival Heights, Antarctica, Geophysical research letters, 23, 1545–1548, 1996.

Kwok, R., Cunningham, G., Wensnahan, M., Rigor, I., Zwally, H., and Yi, D.: Thinning and volume loss of the Arctic Ocean sea ice cover: 2003–2008, Journal of Geophysical Research: Oceans, 114, 2009.

Kwok, R., Kacimi, S., Webster, M., Kurtz, N., and Petty, A.: Arctic Snow Depth and Sea Ice Thickness From ICESat-2 and CryoSat-2 Freeboards: A First Examination, Journal of Geophysical Research: Oceans, 125, e2019JC016 008, https://doi.org/10.1029/2019JC016008, e2019JC016008 2019JC016008, 2020.

Latsch, M., Richter, A., Eskes, H., Sneep, M., Wang, P., Veefkind, P., Lutz, R., Loyola, D., Argyrouli, A., Valks, P., Wagner, T., Sihler, H., van Roozendael, M., Theys, N., Yu, H., Siddans, R., and Burrows, J. P.: Intercomparison of Sentinel-5P TROPOMI cloud products for tropospheric trace gas retrievals, Atmospheric Measurement Techniques Discussions, 2022, 1–43, https://doi.org/10.5194/amt-2022-122, 2022.

Lehrer, E., Hönninger, G., and Platt, U.: A one dimensional model study of the mechanism of halogen liberation and vertical transport in the polar troposphere, Atmos. Chem. Phys., 4, 2427–2440, 2004.

Lewis, E. R., Lewis, R., and Schwartz, S. E.: Sea salt aerosol production: mechanisms, methods, measurements, and models, vol. 152, American geophysical union, 2004.

Liao, J., Huey, L. G., Tanner, D., Brough, N., Brooks, S., Dibb, J. E., Stutz, J., Thomas, J., Lefer, B., Haman, C., et al.: Observations of hydroxyl and peroxy radicals and the impact of BrO at Summit, Greenland in 2007 and 2008, Atmospheric Chemistry and Physics, 11, 8577–8591, 2011.

Lieb-Lappen, R. M. and Obbard, R. W.: The role of blowing snow in the activation of bromine over first-year Antarctic sea ice, Atmospheric Chemistry and Physics, 15, 7537–7545, https://doi.org/10.5194/acp-15-7537-2015, 2015.

Light, B., Maykut, G. A., and Grenfell, T. C.: Effects of temperature on the microstructure of first-year Arctic sea ice, Journal of Geophysical Research: Oceans, 108, https://doi.org/10.1029/2001JC000887, 2003.

Lopez-Hilfiker, F. D., Constantin, K., Kercher, J. P., and Thornton, J. A.: Temperature dependent halogen activation by N_2O_5 reactions on halide-doped ice surfaces, Atmospheric Chemistry and Physics, 12, 5237–5247, https://doi.org/10.5194/acp-12-5237-2012, 2012.

Loyola, D., Lutz, R., Argyrouli, A., and Spurr, R.: S5P/TROPOMI ATBD Cloud Products, German Aerospace Center, 2021.

Loyola, D. G., Gimeno García, S., Lutz, R., Argyrouli, A., Romahn, F., Spurr, R. J., Pedergnana, M., Doicu, A., Molina García, V., and Schüssler, O.: The operational cloud retrieval algorithms from TROPOMI on board Sentinel-5 Precursor, Atmospheric Measurement Techniques, 11, 409–427, 2018.

Ludewig, A., Kleipool, Q., Bartstra, R., Landzaat, R., Leloux, J., Loots, E., Meijering, P., van der Plas, E., Rozemeijer, N., Vonk, F., and Veefkind, P.: In-flight calibration results of the TROPOMI payload on board the Sentinel-5 Precursor satellite, Atmospheric Measurement Techniques, 13, 3561–3580, https://doi.org/10.5194/amt-13-3561-2020, 2020.

Marchuk, G., Mikhailov, G., Nazaraliev, M., Dacbinjan, R., Kargin, B., and Elepov, B.: Monte Carlo methods in atmospheric optics, Applied Optics, 20, 1981.

Marelle, L., Thomas, J. L., Ahmed, S., Tuite, K., Stutz, J., Dommergue, A., Simpson, W. R., Frey, M. M., and Baladima, F.: Implementation and impacts of surface and blowing snow sources of Arctic bromine activation within WRF-Chem 4.1. 1, Journal of advances in modeling earth systems, 13, e2020MS002 391, 2021.

Martin, R. V., Chance, K., Jacob, D. J., Kurosu, T. P., Spurr, R. J., Bucsela, E., Gleason, J. F., Palmer, P. I., Bey, I., Fiore, A. M., et al.: An improved retrieval of tropospheric nitrogen dioxide from GOME, Journal of Geophysical Research: Atmospheres, 107, ACH–9, 2002.

Matveev, V., Peleg, M., Rosen, D., Tov-Alper, D. S., Hebestreit, K., Stutz, J., Platt, U., Blake, D., and Luria, M.: Bromine oxide—ozone interaction over the Dead Sea, Journal of Geophysical Research: Atmospheres, 106, 10 375–10 387, 2001.

McClure-Begley, A., Petropavlovskikh, I., and Oltmans, S.: NOAA Global Monitoring Surface Ozone Network, 1973–2014, National Oceanic and Atmospheric Administration, Earth Systems Research Laboratory Global Monitoring Division, Boulder, CO, doi, 10, V57P8WBF, 2014.

McConnell, J., Henderson, G., Barrie, L., Bottenheim, J., Niki, H., Langford, C., and Templeton, E.: Photochemical bromine production implicated in Arctic boundary-layer ozone depletion, Nature, 355, 150, 1992.

McElroy, M. B., Salawitch, R. J., Wofsy, S. C., and Logan, J. A.: Reductions of Antarctic ozone due to synergistic interactions of chlorine and bromine, Nature, 321, 759–762, 1986.

McNaught, A. D., Wilkinson, A., et al.: Compendium of chemical terminology, vol. 1669, Blackwell Science Oxford, 1997.

McNeill, V. F.: Atmospheric aerosols: clouds, chemistry, and climate, Annual review of chemical and biomolecular engineering, 8, 427–444, 2017.

Moore, C. W., Obrist, D., Steffen, A., Staebler, R. M., Douglas, T. A., Richter, A., and Nghiem, S. V.: Convective forcing of mercury and ozone in the Arctic boundary layer induced by leads in sea ice, Nature, 506, 81, 2014.

Morin, S., Hönninger, G., Staebler, R., and Bottenheim, J.: A high time resolution study of boundary layer ozone chemistry and dynamics over the Arctic Ocean near Alert, Nunavut, Geophysical research letters, 32, 2005.

Morin, S., Marion, G. M., von Glasow, R., Voisin, D., Bouchez, J., and Savarino, J.: Precipitation of salts in freezing seawater and ozone depletion events: a status report, Atmospheric Chemistry and Physics, 8, 7317–7324, https://doi.org/10.5194/acp-8-7317-2008, 2008.

Mozurkewich, M.: Mechanisms for the release of halogens from sea-salt particles by free radical reactions, Journal of Geophysical Research: Atmospheres, 100, 14 199–14 207, 1995.

Mu, L., Yang, Q., Losch, M., Losa, S. N., Ricker, R., Nerger, L., and Liang, X.: Improving sea ice thickness estimates by assimilating CryoSat-2 and SMOS sea ice thickness data simultaneously, Quarterly Journal of the Royal Meteorological Society, 144, 529–538, 2018.

Munro, R., Eisinger, M., Anderson, C., Callies, J., Corpaccioli, E., Lang, R., Lefebvre, A., Livschitz, Y., and Albinana, A. P.: GOME-2 on MetOp, in: Proc. of The 2006 EUMETSAT Meteorological Satellite Conference, Helsinki, Finland, vol. 12–16 June 2006, ISBN 92-9110-076-5, EUMETSAT, p. 48, 2006.

Munro, R., Lang, R., Klaes, D., Poli, G., Retscher, C., Lindstrot, R., Huckle, R., Lacan, A., Grzegorski, M., Holdak, A., Kokhanovsky, A., Livschitz, J., and Eisinger, M.: The GOME-2 instrument on the Metop series of satellites: instrument design, calibration, and level 1 data processing – an overview, Atmospheric Measurement Techniques, 9, 1279–1301, https://doi.org/10.5194/amt-9-1279-2016, 2016.

Nasse, J.-M.: Halogens in the coastal boundary layer of Antarctica, Ph.D. thesis, Ruperto-Carola University, Heidelberg, 2019.

Nasse, J.-M., Eger, P. G., Pöhler, D., Schmitt, S., Frieß, U., and Platt, U.: Recent improvements of long-path DOAS measurements: impact on accuracy and stability of short-term and automated long-term observations, Atmospheric Measurement Techniques, 12, 4149–4169, 2019.

Nghiem, S. V., Rigor, I. G., Richter, A., Burrows, J. P., Shepson, P. B., Bottenheim, J., Barber, D. G., Steffen, A., Latonas, J., Wang, F., et al.: Field and satellite observations of the formation and distribution of Arctic atmospheric bromine above a rejuvenated sea ice cover, Journal of Geophysical Research: Atmospheres, 117, 2012.

Noxon, J.: Nitrogen dioxide in the stratosphere and troposphere measured by ground-based absorption spectroscopy, Science, 189, 547–549, 1975.

Obbard, R. W., Roscoe, H. K., Wolff, E. W., and Atkinson, H. M.: Frost flower surface area and chemistry as a function of salinity and temperature, Journal of Geophysical Research: Atmospheres, 114, 2009.

Oltmans, S.: Surface ozone measurements in clean air, Journal of Geophysical Research: Oceans, 86, 1174–1180, https://doi.org/10.1029/JC086iC02p01174, 1981.

Oltmans, S., Schnell, R., Sheridan, P., Peterson, R., Li, S.-M., Winchester, J., Tans, P., Sturges, W., Kahl, J., and Barrie, L.: Seasonal surface ozone and filterable bromine relationship in the high Arctic, Atmospheric Environment (1967), 23, 2431–2441, 1989.

O'Neill, B.: Elementary differential geometry, Academic Press, New York, 1966.

Oum, K., Lakin, M., and Finlayson-Pitts, B.: Bromine activation in the troposphere by the dark reaction of O3 with seawater ice, Geophysical Research Letters, 25, 3923–3926, 1998.

Palmer, P. I., Jacob, D. J., Chance, K., Martin, R. V., Spurr, R. J., Kurosu, T. P., Bey, I., Yantosca, R., Fiore, A., and Li, Q.: Air mass factor formulation for spectroscopic measurements from satellites: Application to formaldehyde retrievals from the Global Ozone Monitoring Experiment, Journal of Geophysical Research: Atmospheres, 106, 14 539–14 550, 2001.

Perner, D. and Platt, U.: Detection of nitrous acid in the atmosphere by differential optical absorption, Geophysical Research Letters, 6, 917–920, 1979.

Perovich, D. K. and Richter-Menge, J. A.: Surface characteristics of lead ice, Journal of Geophysical Research: Oceans, 99, 16 341–16 350, 1994.

Peterson, P., Simpson, W., Pratt, K., Shepson, P., Frieß, U., Zielcke, J., Platt, U., Walsh, S., and Nghiem, S.: Dependence of the vertical distribution of bromine monoxide in the lower troposphere on meteorological factors such as wind speed and stability, Atmospheric Chemistry and Physics, 15, 2119–2137, 2015.

Peterson, P. K., Pöhler, D., Sihler, H., Zielcke, J., General, S., Frieß, U., Platt, U., Simpson, W. R., Nghiem, S. V., Shepson, P. B., et al.: Observations of bromine monoxide transport in the Arctic sustained on aerosol particles, Atmospheric Chemistry and Physics, 17, 7567–7579, 2017.

Peterson, P. K., Hartwig, M., May, N. W., Schwartz, E., Rigor, I., Ermold, W., Steele, M., Morison, J. H., Nghiem, S. V., and Pratt, K. A.: Snowpack measurements suggest role for multi-year sea ice regions in Arctic atmospheric bromine and chlorine chemistry, Elementa: Science of the Anthropocene, 7, 2019.

Pfeilsticker, K., Arlander, D., Burrows, J., Erle, F., Gil, M., Goutail, F., Hermans, C., Lambert, J.-C., Platt, U., Pommereau, J.-P., et al.: Intercomparison of the influence of tropospheric clouds on UV-visible absorptions Detected during the NDSC Intercomparison Campaign at OHP in June 1996, Geophysical research letters, 26, 1169–1172, 1999.

Platt, U.: Air monitoring by differential optical absorption spectroscopy, Encyclopedia of Analytical Chemistry: Applications, Theory and Instrumentation, pp. 1–28, 2006.

Platt, U.: personal communication, 2022.

Platt, U. and Hönninger, G.: The role of halogen species in the troposphere, Chemosphere, 52, 325–338, https://doi.org/https://doi.org/10.1016/S0045-6535(03)00216-9, naturally Produced Organohalogens, 2003.

Platt, U. and Janssen, C.: Observation and role of the free radicals NO3, ClO, BrO and IO in the troposphere, Faraday Discussions, 100, 175–198, 1995.

Platt, U. and Lehrer, E.: Arctic tropospheric ozone chemistry, ARCTOC, Final Report of the EU-Project No, Tech. rep., EV5V-CT93-0318, Heidelberg, 1996.

Platt, U. and Lehrer, E.: Arctic tropospheric ozone chemistry, ARCTOC, no. 64 in Air pollution research report, European Commission Directorate-General, Science, Research and Development, Luxembourg, 1997.

Platt, U. and Stutz, J.: Differential Optical Absorption Spectroscopy, Springer Berlin, Heidelberg, https://doi.org/10.1007/978-3-540-75776-4, 2008.

Platt, U., Meinen, J., Pöhler, D., and Leisner, T.: Broadband cavity enhanced differential optical absorption spectroscopy (CE-DOAS)–applicability and corrections, Atmospheric Measurement Techniques, 2, 713–723, 2009.

Pöhler, D., Vogel, L., Frieß, U., and Platt, U.: Observation of halogen species in the Amundsen Gulf, Arctic, by active long-path differential optical absorption spectroscopy, Proceedings of the National Academy of Sciences, 107, 6582–6587, 2010.

Prados-Román, C.: Aircraft-borne spectroscopic limb measurements of trace gases absorbing in the UV-A spectral range: investigations of bromine monoxide in the Arctic troposphere, Ph.D. thesis, 2010.

Prados-Roman, C., Butz, A., Deutschmann, T., Dorf, M., Kritten, L., Minikin, A., Platt, U., Schlager, H., Sihler, H., Theys, N., et al.: Airborne DOAS limb measurements of

tropospheric trace gas profiles: case studies on the profile retrieval of O 4 and BrO, Atmospheric Measurement Techniques, 4, 1241–1260, 2011.

Pratt, K. A., Custard, K. D., Shepson, P. B., Douglas, T. A., Pöhler, D., General, S., Zielcke, J., Simpson, W. R., Platt, U., Tanner, D. J., et al.: Photochemical production of molecular bromine in Arctic surface snowpacks, Nature Geoscience, 6, 351, 2013.

Puķīte, J., Kühl, S., Deutschmann, T., Platt, U., and Wagner, T.: Extending differential optical absorption spectroscopy for limb measurements in the UV, Atmospheric Measurement Techniques, 3, 631–653, 2010.

Rankin, A. M., Wolff, E. W., and Martin, S.: Frost flowers: Implications for tropospheric chemistry and ice core interpretation, Journal of Geophysical Research: Atmospheres, 107, AAC 4–1–AAC 4–15, https://doi.org/10.1029/2002JD002492, 2002.

Raso, A. R., Custard, K. D., May, N. W., Tanner, D., Newburn, M. K., Walker, L., Moore, R. J., Huey, L. G., Alexander, L., Shepson, P. B., et al.: Active molecular iodine photochemistry in the Arctic, Proceedings of the National Academy of Sciences, 114, 10 053–10 058, 2017.

Rhodes, R. H., Yang, X., Wolff, E. W., McConnell, J. R., and Frey, M. M.: Sea ice as a source of sea salt aerosol to Greenland ice cores: a model-based study, Atmospheric Chemistry and Physics, 17, 9417–9433, 2017.

Richardson, C.: Phase relationships in sea ice as a function of temperature, Journal of Glaciology, 17, 507–519, 1976.

Richter, A. and Wagner, T.: The Use of UV, Visible and Near IR Solar Back Scattered Radiation to Determine Trace Gases, pp. 67–121, Springer Berlin Heidelberg, Berlin, Heidelberg, https://doi.org/10.1007/978-3-642-14791-3_2, 2011.

Richter, A., Wittrock, F., Eisinger, M., and Burrows, J. P.: GOME observations of tropospheric BrO in northern hemispheric spring and summer 1997, Geophysical Research Letters, 25, 2683–2686, https://doi.org/https://doi.org/10.1029/98GL52016, 1998.

Richter, A., Wittrock, F., Ladstätter-Weißenmayer, A., and Burrows, J.: GOME measurements of stratospheric and tropospheric BrO, Advances in Space Research, 29, 1667–1672, 2002.

Ridley, B., Zeng, T., Wang, Y., Atlas, E., Browell, E., Hess, P., Orlando, J., Chance, K., and Richter, A.: An ozone depletion event in the sub-arctic surface layer over Hudson Bay, Canada, Journal of atmospheric chemistry, 57, 255–280, 2007.

Ridley, B. A., Atlas, E., Montzka, D., Browell, E. V., Cantrell, C., Blake, D., Blake, N., Cinquini, L., Coffey, M. T., Emmons, L., et al.: Ozone depletion events observed in the high latitude surface layer during the TOPSE aircraft program, Journal of Geophysical Research: Atmospheres, 108, TOP–4, 2003.

Rodgers, C. D.: Inverse methods for atmospheric sounding: theory and practice, vol. 2, World scientific, 2000.

Roscoe, H., Brooks, B., Jackson, A., Smith, M., Walker, S., Obbard, R., and Wolff, E.: Frost flowers in the laboratory: Growth, characteristics, aerosol, and the underlying sea ice, Journal of Geophysical Research: Atmospheres, 116, 2011.

Roscoe, H., Brough, N., Jones, A., Wittrock, F., Richter, A., Van Roozendael, M., and Hendrick, F.: Characterisation of vertical BrO distribution during events of enhanced tropospheric BrO in Antarctica, from combined remote and in-situ measurements, Journal of Quantitative Spectroscopy and Radiative Transfer, 138, 70–81, 2014.

Rosengren, M.: ERS-1 - An earth observer that exactly follows its chosen path, 1988.

Rowland, F. S. and Molina, M. J.: Stratospheric sink for chlorofluoromethanes: chlorine atom-catalysed destruction of ozone, Nature, 249, 810–812, 1974.

Rozanov, V. V. and Rozanov, A. V.: Differential optical absorption spectroscopy (DOAS) and air mass factor concept for a multiply scattering vertically inhomogeneous medium: theoretical consideration, Atmospheric Measurement Techniques, 3, 751–780, https://doi.org/10.5194/amt-3-751-2010, 2010.

Saiz-Lopez, A. and von Glasow, R.: Reactive halogen chemistry in the troposphere, Chemical Society Reviews, 41, 6448–6472, 2012.

Saiz-Lopez, A., Mahajan, A. S., Salmon, R. A., Bauguitte, S. J.-B., Jones, A. E., Roscoe, H. K., and Plane, J. M.: Boundary layer halogens in coastal Antarctica, Science, 317, 348–351, 2007.

Salawitch, R., Canty, T., Kurosu, T., Chance, K., Liang, Q., da Silva, A., Pawson, S., Nielsen, J., Rodriguez, J., Bhartia, P., et al.: A new interpretation of total column BrO during Arctic spring, Geophysical Research Letters, 37, 2010.

Salembier, P., Oliveras, A., and Garrido, L.: Antiextensive connected operators for image and sequence processing, IEEE Transactions on Image Processing, 7, 555–570, 1998.

Sander, R. and Crutzen, P. J.: Model study indicating halogen activation and ozone destruction in polluted air masses transported to the sea, Journal of Geophysical Research: Atmospheres, 101, 9121–9138, 1996.

Sander, R. and Morin, S.: Introducing the bromide/alkalinity ratio for a follow-up discussion on" Precipitation of salts in freezing seawater and ozone depletion events: a status report", by Morin et al., published in Atmos. Chem. Phys., 8, 7317–7324, 2008, Atmospheric Chemistry and Physics, 10, 7655–7658, 2010.

Sander, R., Keene, W., Pszenny, A., Arimoto, R., Ayers, G., Baboukas, E., Cainey, J., Crutzen, P., Duce, R., Hönninger, G., et al.: Inorganic bromine in the marine boundary layer: a critical review, Atmospheric Chemistry and Physics, 3, 1301–1336, 2003.

Sander, R., Burrows, J., and Kaleschke, L.: Carbonate precipitation in brine–a potential trigger for tropospheric ozone depletion events, Atmospheric Chemistry and Physics, 6, 4653–4658, 2006.

Sander, R., Baumgaertner, A., Gromov, S., Harder, H., Jöckel, P., Kerkweg, A., Kubistin, D., Regelin, E., Riede, H., Sandu, A., Taraborrelli, D., Tost, H., and Xie, Z.-Q.: The atmospheric chemistry box model CAABA/MECCA-3.0, Geoscientific Model Development, 4, 373–380, https://doi.org/10.5194/gmd-4-373-2011, 2011.

Schroeder, W., Steffen, A., Scott, K., Bender, T., Prestbo, E., and Ebinghaus, R.: First international arctic atmospheric mercury research workshop, Atmospheric environment (1994), 37, 2551–2555, 2003.

Schroeder, W. H., Anlauf, K., Barrie, L., Lu, J., Steffen, A., Schneeberger, D., and Berg, T.: Arctic springtime depletion of mercury, Nature, 394, 331–332, 1998.

Seabrook, J., Whiteway, J., Staebler, R., Bottenheim, J., Komguem, L., Gray, L., Barber, D., and Asplin, M.: LIDAR measurements of Arctic boundary layer ozone depletion events over the frozen Arctic Ocean, Journal of Geophysical Research: Atmospheres, 116, 2011.

Seo, S.: Retrieval and analysis of tropospheric bromine monoxide enhancements in polar regions using satellite measurements, Ph.D. thesis, Universität Bremen, 2020.

Seo, S., Richter, A., Blechschmidt, A.-M., Bougoudis, I., and Burrows, J. P.: First high-resolution BrO column retrievals from TROPOMI, Atmospheric Measurement Techniques, 12, 2913–2932, https://doi.org/10.5194/amt-12-2913-2019, 2019.

Seo, S., Richter, A., Blechschmidt, A.-M., Bougoudis, I., and Burrows, J. P.: Spatial distribution of enhanced BrO and its relation to meteorological parameters in Arctic and Antarctic sea ice regions, Atmospheric Chemistry and Physics, 20, 12 285–12 312, 2020.

Serdyuchenko, A., Gorshelev, V., Weber, M., Chehade, W., and Burrows, J. P.: High spectral resolution ozone absorption cross-sections - Part 2: Temperature dependence, Atmospheric Measurement Techniques, 7, 625–636, https://doi.org/10.5194/amt-7-625-2014, 2014.

Serra, J.: Image analysis and mathematical morphology, 1982.

Sihler, H.: Halogen activation in the polar troposphere, Ph.D. thesis, Heidelberg, Univ., Diss., 2012, https://doi.org/10.11588/heidok.00013663, online publiziert: 2012, 2012.

Sihler, H., Platt, U., Beirle, S., Marbach, T., Kühl, S., Dörner, S., Verschaeve, J., Frieß, U., Pöhler, D., Vogel, L., Sander, R., and Wagner, T.: Tropospheric BrO column densities in the Arctic derived from satellite: retrieval and comparison to ground-based measurements, Atmospheric Measurement Techniques, 5, 2779–2807, https://doi.org/10.5194/amt-5-2779-2012, 2012.

Sihler, H., Dörner, S., Pozzer, A., Frieß, U., Platt, U., and Wagner, T.: Meteorology and vertical structure of plumes of enhanced bromine monoxide as detected by satellite remote sensing during Arctic spring, in: EGU General Assembly Conference Abstracts, p. 15426, 2014.

Sihler, H., Beirle, S., Dörner, S., Gutenstein-Penning de Vries, M., Hörmann, C., Borger, C., Warnach, S., and Wagner, T.: MICRU: an effective cloud fraction algorithm designed for UV–vis satellite instruments with large viewing angles, Atmospheric measurement techniques, 14, 3989–4031, 2021.

Simpson, W., Glasow, R. v., Riedel, K., Anderson, P., Ariya, P., Bottenheim, J., Burrows, J., Carpenter, L., Frieß, U., Goodsite, M. E., et al.: Halogens and their role in polar boundary-layer ozone depletion, Atmospheric Chemistry and Physics, 7, 4375–4418, 2007a.

Simpson, W. R., Alvarez-Aviles, L., Douglas, T. A., Sturm, M., and Domine, F.: Halogens in the coastal snow pack near Barrow, Alaska: Evidence for active bromine air-snow chemistry during springtime, Geophysical research letters, 32, 2005.

Simpson, W. R., Carlson, D., Hönninger, G., Douglas, T. A., Sturm, M., Perovich, D., and Platt, U.: First-year sea-ice contact predicts bromine monoxide (BrO) levels at Barrow, Alaska better than potential frost flower contact, Atmospheric Chemistry and Physics, 7, 621–627, https://doi.org/10.5194/acp-7-621-2007, 2007b.

Simpson, W. R., Brown, S. S., Saiz-Lopez, A., Thornton, J. A., and von Glasow, R.: Tropospheric halogen chemistry: Sources, cycling, and impacts, Chemical reviews, 115, 4035–4062, 2015.

Sinnhuber, B.-M., Arlander, D., Bovensmann, H., Burrows, J., Chipperfield, M., Enell, C.-F., Frieß, U., Hendrick, F., Johnston, P., Jones, R., et al.: Comparison of measurements and model calculations of stratospheric bromine monoxide, Journal of Geophysical Research: Atmospheres, 107, ACH–11, 2002.

Sjostedt, S. and Abbatt, J.: Release of gas-phase halogens from sodium halide substrates: heterogeneous oxidation of frozen solutions and desiccated salts by hydroxyl radicals, Environmental Research Letters, 3, 045 007, 2008.

Skamarock, W. C., Klemp, J. B., Dudhia, J., Gill, D. O., Barker, D. M., Wang, W., and Powers, J. G.: A description of the Advanced Research WRF version 3. NCAR Technical note-475+ STR, https://doi.org/10.5065/D68S4MVH, 2008.

Sneep, M., Ityaksov, D., Aben, I., Linnartz, H., and Ubachs, W.: Temperature-dependent cross sections of O2–O2 collision-induced absorption resonances at 477 and 577 nm, Journal of Quantitative Spectroscopy and Radiative Transfer, 98, 405–424, 2006.

Sneep, M., De Haan, J., Stammes, P., Wang, P., Vanbauce, C., Joiner, J., Vasilkov, A., and Levelt, P.: Three-way comparison between OMI and PARASOL cloud pressure products, Journal of Geophysical Research: Atmospheres, 113, 2008.

Snyder, J. P.: Map projections: A working manual, U.S. Government Printing Office, https://doi.org/10.3133/pp1395, 1987.

Soille, P. et al.: Morphological image analysis: principles and applications, vol. 2, Springer, 1999.

Solberg, S., Schmidbauer, N., Semb, A., Stordal, F., and Hov, Ø.: Boundary-layer ozone depletion as seen in the Norwegian Arctic in spring, Journal of Atmospheric Chemistry, 23, 301–332, 1996.

Solomon, S., Garcia, R. R., Rowland, F. S., and Wuebbles, D. J.: On the depletion of Antarctic ozone, Nature, 321, 755–758, 1986.

Solomon, S., Schmeltekopf, A. L., and Sanders, R. W.: On the interpretation of zenith sky absorption measurements, Journal of Geophysical Research: Atmospheres, 92, 8311–8319, 1987.

Spurr, R. J.: VLIDORT: A linearized pseudo-spherical vector discrete ordinate radiative transfer code for forward model and retrieval studies in multilayer multiple scattering media, Journal of Quantitative Spectroscopy and Radiative Transfer, 102, 316–342, 2006.

Steffen, K. and deMaria, T.: Surface Energy Fluxes of Arctic Winter Sea Ice in Barrow Strait, Journal of Applied Meteorology, 35, 2067–2079, https://doi.org/10.1175/1520-0450(1996)035<2067:SEFOAW>2.0.CO;2, 1996.

Stein, A., Draxler, R. R., Rolph, G. D., Stunder, B. J., Cohen, M., and Ngan, F.: NOAA's HYSPLIT atmospheric transport and dispersion modeling system, Bulletin of the American Meteorological Society, 96, 2059–2077, 2015.

Stull, R. B.: An introduction to boundary layer meteorology, vol. 13, Springer Netherlands, https://doi.org/10.1007/978-94-009-3027-8, 1988.

Stutz, J. and Platt, U.: Numerical analysis and estimation of the statistical error of differential optical absorption spectroscopy measurements with least-squares methods, Applied Optics, 35, 6041–6053, 1996.

Stutz, J., Thomas, J. L., Hurlock, S., Schneider, M., Von Glasow, R., Piot, M., Gorham, K., Burkhart, J. F., Ziemba, L., Dibb, J. E., et al.: Longpath DOAS observations of surface BrO at Summit, Greenland, Atmospheric Chemistry and Physics, 11, 9899–9910, 2011.

Swanson, W. F., Graham, K. A., Halfacre, J. W., Holmes, C. D., Shepson, P. B., and Simpson, W. R.: Arctic reactive bromine events occur in two distinct sets of environmental conditions: A statistical analysis of 6 years of observations, Journal of Geophysical Research: Atmospheres, 125, e2019JD032 139, 2020.

Swanson, W. F., Holmes, C. D., Simpson, W. R., Confer, K., Marelle, L., Thomas, J. L., Jaeglé, L., Alexander, B., Zhai, S., Chen, Q., Wang, X., and Sherwen, T.: Comparison of model and ground observations finds snowpack and blowing snow both contribute to Arctic tropospheric reactive bromine, Atmospheric Chemistry and Physics Discussions, 2022, 1–38, https://doi.org/10.5194/acp-2022-44, 2022.

Tang, J. and McConnell, J.: Surface ozone depletion in Arctic spring sustained by bromine reactions on aerosols, Geophysical Research Letters, 23, 2633–2636, 1996.

Tarasick, D. and Bottenheim, J.: Surface ozone depletion episodes in the Arctic and Antarctic from historical ozonesonde records, Atmospheric Chemistry and Physics, 2, 197–205, 2002.

Thalman, R. and Volkamer, R.: Temperature dependent absorption cross-sections of O2–O2 collision pairs between 340 and 630 nm and at atmospherically relevant pressure, Phys. Chem. Chem. Phys., 15, 15 371–15 381, https://doi.org/10.1039/C3CP50968K, 2013.

The New York Times Editorial Board: The World Solved the Ozone Problem. It Can Solve Climate Change., URL https://www.nytimes.com/2019/12/07/opinion/sunday/ozone-climate-change.html, 2019.

Theys, N., Van Roozendael, M., Dils, B., Hendrick, F., Hao, N., and De Maziere, M.: First satellite detection of volcanic bromine monoxide emission after the Kasatochi eruption, Geophysical Research Letters, 36, 2009.

Theys, N., Van Roozendael, M., Hendrick, F., Yang, X., De Smedt, I., Richter, A., Begoin, M., Errera, Q., Johnston, P., Kreher, K., et al.: Global observations of tropospheric BrO columns using GOME-2 satellite data, Atmospheric Chemistry and Physics, 11, 1791–1811, 2011.

Tilstra, L., Tuinder, O., Wang, P., and Stammes, P.: Surface reflectivity climatologies from UV to NIR determined from Earth observations by GOME-2 and SCIAMACHY, Journal of Geophysical Research: Atmospheres, 122, 4084–4111, 2017.

Tørseth, K., Aas, W., Breivik, K., Fjæraa, A. M., Fiebig, M., Hjellbrekke, A.-G., Lund Myhre, C., Solberg, S., and Yttri, K. E.: Introduction to the European Monitoring and Evaluation Programme (EMEP) and observed atmospheric composition change during 1972–2009, Atmospheric Chemistry and Physics, 12, 5447–5481, 2012.

Toyota, K., McConnell, J. C., Lupu, A., Neary, L., McLinden, C. A., Richter, A., Kwok, R., Semeniuk, K., Kaminski, J. W., Gong, S.-L., Jarosz, J., Chipperfield, M. P., and

Sioris, C. E.: Analysis of reactive bromine production and ozone depletion in the Arctic boundary layer using 3-D simulations with GEM-AQ: inference from synoptic-scale patterns, Atmospheric Chemistry and Physics, 11, 3949–3979, https://doi.org/10.5194/acp-11-3949-2011, 2011.

Toyota, K., McConnell, J. C., Staebler, R. M., and Dastoor, A. P.: Air–snowpack exchange of bromine, ozone and mercury in the springtime Arctic simulated by the 1-D model PHANTAS - Part 1: In-snow bromine activation and its impact on ozone, Atmospheric Chemistry and Physics, 14, 4101–4133, https://doi.org/10.5194/acp-14-4101-2014, 2014.

Tuckermann, M., Ackermann, R., Gölz, C., Lorenzen-Schmidt, H., Senne, T., Stutz, J., Trost, B., Unold, W., and Platt, U.: DOAS-observation of halogen radical-catalysed arctic boundary layer ozone destruction during the ARCTOC-campaigns 1995 and 1996 in Ny-Ålesund, Spitsbergen, Tellus Series B Chemical and Physical Meteorology B, 49, 533, https://doi.org/10.3402/tellusb.v49i5.16005, 1997.

Van Geffen, J., Eskes, H., Boersma, J., and Veefkind, J.: TROPOMI ATBD of the total and tropospheric NO2 data products, Report S5P-KNMI-L2-0005-RP, version 2.2.0, 2021-06-16, URL https://sentinel.esa.int/documents/247904/2476257/Sentinel-5P-TROPOMI-ATBD-NO2-data-products.

Van Geffen, J., Boersma, K. F., Eskes, H., Sneep, M., Ter Linden, M., Zara, M., and Veefkind, J. P.: S5P TROPOMI NO 2 slant column retrieval: Method, stability, uncertainties and comparisons with OMI, Atmospheric Measurement Techniques, 13, 1315–1335, 2020.

Van Geffen, J., Eskes, H., Compernolle, S., Pinardi, G., Verhoelst, T., Lambert, J.-C., Sneep, M., Ter Linden, M., Ludewig, A., Boersma, K. F., et al.: Sentinel-5P TROPOMI NO 2 retrieval: impact of version v2. 2 improvements and comparisons with OMI and ground-based data, Atmospheric Measurement Techniques, 15, 2037–2060, 2022.

Vandaele, A., Hermans, C., Simon, P., Carleer, M., Colin, R., Fally, S., Mérienne, M., Jenouvrier, A., and Coquart, B.: Measurements of the NO2 absorption cross-section from 42,000 cm^{-1} to 10,000 cm^{-1} (238–1000 nm) at 220 K and 294 K, Journal of Quantitative Spectroscopy and Radiative Transfer, 59, 171–184, https://doi.org/https://doi.org/10.1016/S0022-4073(97)00168-4, atmospheric Spectroscopy Applications 96, 1998.

Vasilkov, A., Joiner, J., Haffner, D., Bhartia, P., and Spurr, R.: What do satellite backscatter ultraviolet and visible spectrometers see over snow and ice? A study of clouds and ozone using the A-train, Atmospheric Measurement Techniques, 3, 619–629, 2010.

Vassilvitskii, S. and Arthur, D.: k-means++: The advantages of careful seeding, in: Proceedings of the eighteenth annual ACM-SIAM symposium on Discrete algorithms, pp. 1027–1035, 2006.

Vavrus, S. J.: Extreme Arctic cyclones in CMIP5 historical simulations, Geophysical Research Letters, 40, 6208–6212, 2013.

Veefkind, J., Aben, I., McMullan, K., Förster, H., de Vries, J., Otter, G., Claas, J., Eskes, H., de Haan, J., Kleipool, Q., van Weele, M., Hasekamp, O., Hoogeveen, R., Landgraf, J., Snel, R., Tol, P., Ingmann, P., Voors, R., Kruizinga, B., Vink, R., Visser, H., and Levelt, P.: TROPOMI on the ESA Sentinel-5 Precursor: A GMES mission for global observations of the atmospheric composition for climate, air quality and ozone layer applications, Remote Sensing of Environment, 120, 70–83, https://doi.org/https://doi.org/10.1016/j.rse.2011.09.027, the Sentinel Missions - New Opportunities for Science, 2012.

Veefkind, J. P., De Haan, J. F., Sneep, M., and Levelt, P. F.: Improvements to the OMI O 2–O 2 operational cloud algorithm and comparisons with ground-based radar–lidar observations, Atmospheric Measurement Techniques, 9, 6035–6049, 2016.

Vincent, L.: Grayscale area openings and closings, their efficient implementation and applications, in: First Workshop on Mathematical Morphology and its Applications to Signal Processing, pp. 22–27, 1993.

Von Glasow, R. and Crutzen, P.: Model study of multiphase DMS oxidation with a focus on halogens, Atmospheric Chemistry and Physics, 4, 589–608, 2004.

Wagner, T.: Satellite observations of atmospheric Halogen Oxides, URL http://www.ub.uni-heidelberg.de/archiv/539, 2000.

Wagner, T. and Platt, U.: Satellite mapping of enhanced BrO concentrations in the troposphere, Nature, 395, 486–490, 1998.

Wagner, T., Chance, K., Frieß, U., Gil, M., Goutail, F., Hönninger, G., Johnston, P., Karlsen-Tørnkvist, K., Kostadinov, I., Leser, H., Petritoli, A., Richter, A., Van Roozendael, M., and Platt, U.: Correction of the Ring effect and I_0-effect for DOAS observations of scattered light, URL http://satellite.mpic.de/pdf_dateien/RING4.pdf, 1999.

Wagner, T., Leue, C., Wenig, M., Pfeilsticker, K., and Platt, U.: Spatial and temporal distribution of enhanced boundary layer BrO concentrations measured by the GOME instrument aboard ERS-2, Journal of Geophysical Research: Atmospheres, 106, 24 225–24 235, 2001.

Wagner, T., Von Friedeburg, C., Wenig, M., Otten, C., and Platt, U.: UV-visible observations of atmospheric O4 absorptions using direct moonlight and zenith-scattered sunlight for clear-sky and cloudy sky conditions, Journal of Geophysical Research: Atmospheres, 107, AAC–3, 2002.

Wagner, T., Dix, B. v., Friedeburg, C. v., Frieß, U., Sanghavi, S., Sinreich, R., and Platt, U.: MAX-DOAS O4 measurements: A new technique to derive information on atmospheric aerosols—Principles and information content, Journal of Geophysical Research: Atmospheres, 109, 2004.

Wagner, T., Ibrahim, O., Sinreich, R., Frieß, U., von Glasow, R., and Platt, U.: Enhanced tropospheric BrO over Antarctic sea ice in mid winter observed by MAX-DOAS on board the research vessel Polarstern, Atmospheric Chemistry and Physics, 7, 3129–3142, https://doi.org/10.5194/acp-7-3129-2007, 2007.

Wagner, T., Beirle, S., and Deutschmann, T.: Three-dimensional simulation of the Ring effect in observations of scattered sun light using Monte Carlo radiative transfer models, Atmospheric Measurement Techniques, 2, 113–124, https://doi.org/10.5194/amt-2-113-2009, 2009a.

Wagner, T., Deutschmann, T., and Platt, U.: Determination of aerosol properties from MAX-DOAS observations of the Ring effect, Atmospheric Measurement Techniques, 2, 495–512, 2009b.

Wang, C., Graham, R. M., Wang, K., Gerland, S., and Granskog, M. A.: Comparison of ERA5 and ERA-Interim near-surface air temperature, snowfall and precipitation over Arctic sea ice: effects on sea ice thermodynamics and evolution, The Cryosphere, 13, 1661–1679, 2019.

Wang, P., Stammes, P., Van Der A, R., Pinardi, G., and Van Roozendael, M.: FRESCO+: an improved O 2 A-band cloud retrieval algorithm for tropospheric trace gas retrievals, Atmospheric Chemistry and Physics, 8, 6565–6576, 2008.

Wang, S. and Pratt, K. A.: Molecular Halogens Above the Arctic Snowpack: Emissions, Diurnal Variations, and Recycling Mechanisms, Journal of Geophysical Research: Atmospheres, 122, 11,991–12,007, https://doi.org/https://doi.org/10.1002/2017JD027175, 2017.

Warnach, S.: Bromine monoxide in volcanic plumes, Ph.D. thesis, Dissertation, Heidelberg University, 2022, Heidelberg, https://doi.org/10.11588/heidok.00031910, 2022.

Warren, S. G., Brandt, R. E., and Grenfell, T. C.: Visible and near-ultraviolet absorption spectrum of ice from transmission of solar radiation into snow, Applied optics, 45, 5320–5334, 2006.

Weber, M., Arosio, C., Feng, W., Dhomse, S. S., Chipperfield, M. P., Meier, A., Burrows, J. P., Eichmann, K.-U., Richter, A., and Rozanov, A.: The unusual stratospheric Arctic winter 2019/20: Chemical ozone loss from satellite observations and TOMCAT chemical transport model, Journal of Geophysical Research: Atmospheres, 126, e2020JD034 386, 2021.

Weller, R.: Airchemistry at Neumayer station, Antarctica during the year 2016, https://doi.org/10.1594/PANGAEA.882136, 2017.

Wennberg, P.: Atmospheric chemistry: Bromine explosion, Nature, 397, 299, 1999.

Wesely, M.: Parameterization of surface resistances to gaseous dry deposition in regional-scale numerical models, Atmospheric Environment (1967), 23, 1293–1304, 1989.

Wessel, S., Aoki, S., Winkler, P., Weller, R., Herber, A., Gernandt, H., and Schrems, O.: Tropospheric ozone depletion in polar regions A comparison of observations in the Arctic and Antarctic, Tellus B: Chemical and Physical Meteorology, 50, 34–50, 1998.

Wikipedia: Sun-synchronous orbit — Wikipedia, The Free Encyclopedia, URL http://en.wikipedia.org/w/index.php?title=Sun-synchronous%20orbit&oldid=1106648377, 2022.

Wofsy, S. C., McElroy, M. B., and Yung, Y. L.: The chemistry of atmospheric bromine, Geophysical Research Letters, 2, 215–218, 1975.

Wren, S. N., Donaldson, D., and Abbatt, J.: Photochemical chlorine and bromine activation from artificial saline snow, Atmospheric Chemistry and Physics, 13, 9789–9800, 2013.

Wu, K., Otoo, E., and Shoshani, A.: Optimizing connected component labeling algorithms, in: Medical Imaging 2005: Image Processing, vol. 5747, pp. 1965–1976, SPIE, 2005.

Yang, X., Pyle, J. A., and Cox, R. A.: Sea salt aerosol production and bromine release: Role of snow on sea ice, Geophysical Research Letters, 35, n/a–n/a, https://doi.org/10.1029/2008GL034536, l16815, 2008.

Yang, X., Pyle, J. A., Cox, R. A., Theys, N., and Van Roozendael, M.: Snow-sourced bromine and its implications for polar tropospheric ozone, Atmospheric Chemistry and Physics, 10, 7763–7773, https://doi.org/10.5194/acp-10-7763-2010, 2010.

Yang, X., Neděla, V., Runštuk, J., Ondrušková, G., Krausko, J., Vetráková, L., and Heger, D.: Evaporating brine from frost flowers with electron microscopy and implications for atmospheric chemistry and sea-salt aerosol formation, Atmospheric Chemistry and Physics, 17, 6291–6303, 2017.

Yang, X., Frey, M. M., Rhodes, R. H., Norris, S. J., Brooks, I. M., Anderson, P. S., Nishimura, K., Jones, A. E., and Wolff, E. W.: Sea salt aerosol production via sublimating wind-blown saline snow particles over sea ice: parameterizations and relevant microphysical mechanisms, Atmospheric Chemistry and Physics, 19, 8407–8424, https://doi.org/10.5194/acp-19-8407-2019, 2019.

Yang, X., Blechschmidt, A.-M., Bognar, K., McClure-Begley, A., Morris, S., Petropavlovskikh, I., Richter, A., Skov, H., Strong, K., Tarasick, D. W., et al.: Pan-Arctic surface ozone: modelling vs. measurements, Atmospheric Chemistry and Physics, 20, 15 937–15 967, 2020.

Yang, X., Strong, K., Criscitiello, A. S., Santos-Garcia, M., Bognar, K., Zhao, X., Fogal, P., Walker, K. A., Morris, S. M., and Effertz, P.: Surface snow bromide and nitrate at Eureka, Canada in early spring and implications for polar boundary layer chemistry, EGUsphere, pp. 1–30, 2022.

Zaveri, R. A., Easter, R. C., Fast, J. D., and Peters, L. K.: Model for simulating aerosol interactions and chemistry (MOSAIC), Journal of Geophysical Research: Atmospheres, 113, 2008.

Zhang, G. and Chanson, H.: Application of local optical flow methods to high-velocity free-surface flows: Validation and application to stepped chutes, Experimental Thermal and Fluid Science, 90, 186–199, 2018.

Zhang, H.: The optimality of naive Bayes, Aa, 1, 3, 2004.

Zhao, X., Strong, K., Adams, C., Schofield, R., Yang, X., Richter, A., Friess, U., Blechschmidt, A.-M., and Koo, J.-H.: A case study of a transported bromine explosion event in the Canadian high arctic, Journal of Geophysical Research: Atmospheres, 121, 457–477, 2016.

Zielcke, J.: Observations of reactive bromine, iodine and chlorine species in the Arctic and Antarctic with differential optical absorption spectroscopy, Ph.D. thesis, Ruperto-Carola University, Heidelberg, 2015.

Zuidema, P. and Evans, K. F.: On the validity of the independent pixel approximation for boundary layer clouds observed during ASTEX, Journal of Geophysical Research: Atmospheres, 103, 6059–6074, 1998.

C | Lists

List of Figures

List of Tables

D | Medium bromide simulation time-series

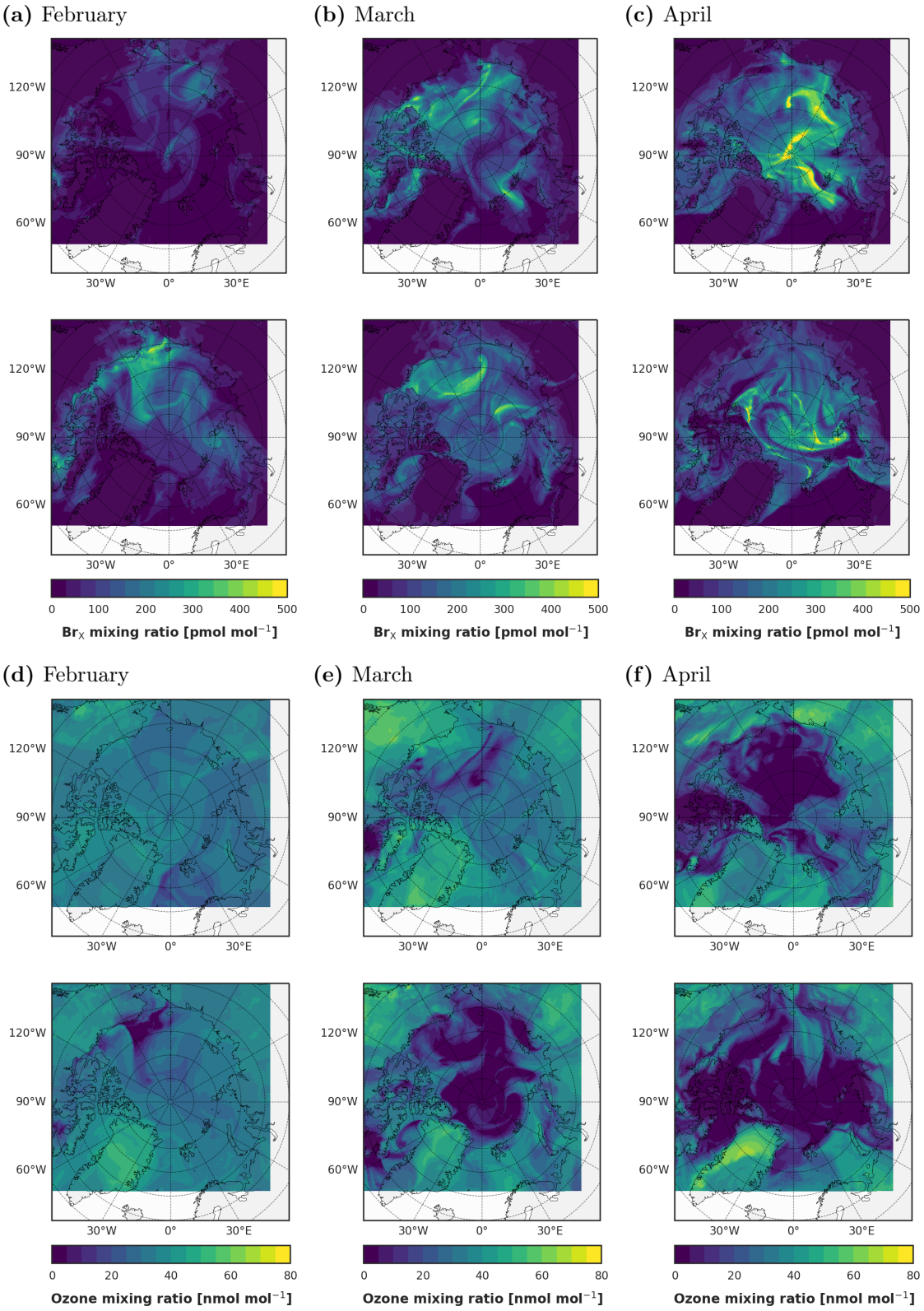

Figure D.1: *Seasonal overview of simulated surface Br_X concentrations from February to April (a) - (c) and surface O_3 concentrations from February to April (d) - (f) from the medium bromide simulation. In the top, the 5th of the corresponding month is shown. In the bottom, the 20th of the corresponding month is shown. The simulation time is always 22:00 UTC.*

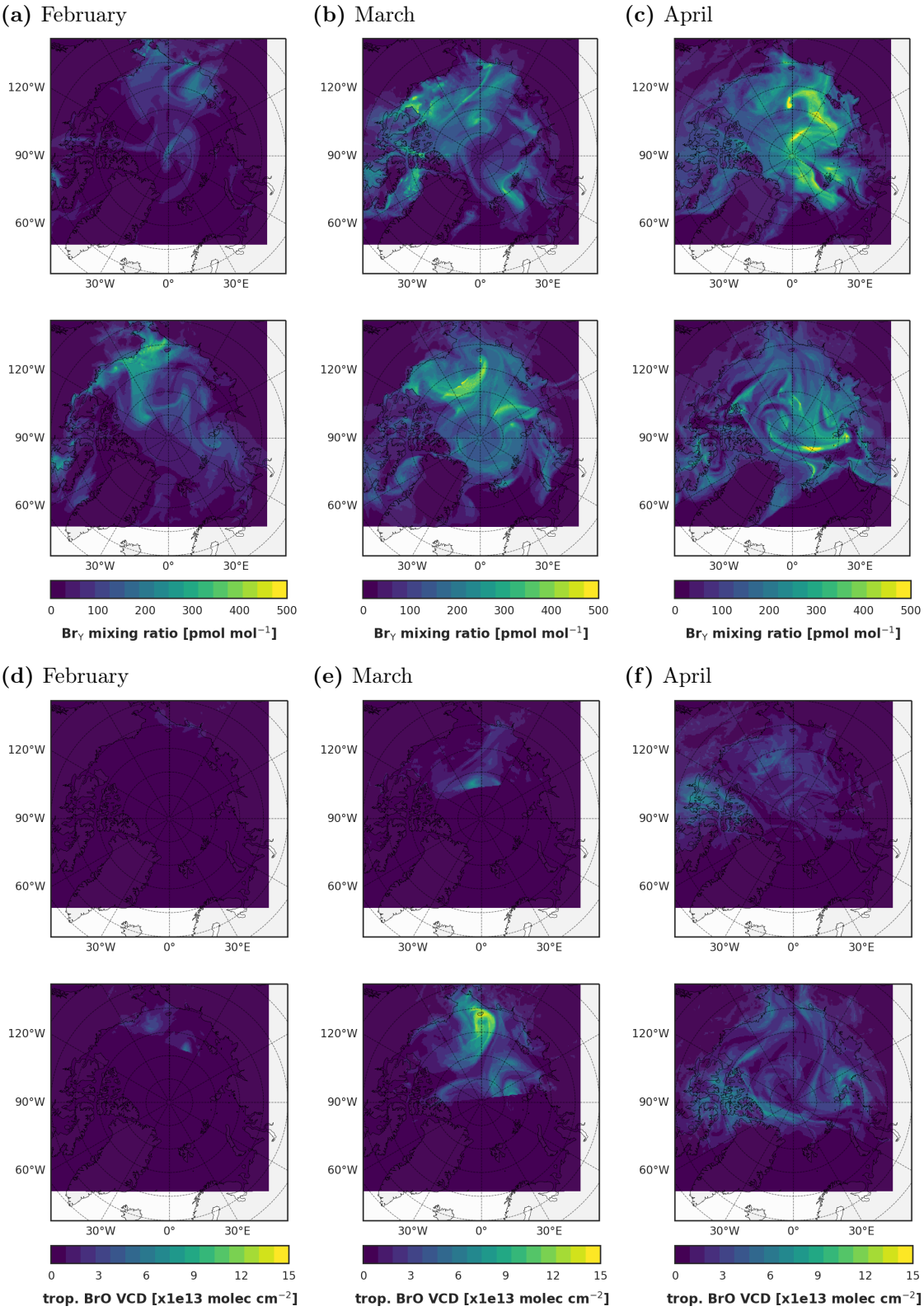

Figure D.2: *Seasonal overview of simulated surface Br_Y concentrations from February to April (a) - (c) and tropospheric BrO VCDs from February to April (d) - (f) from the medium bromide simulation. In the top, the 5th of the corresponding month is shown. In the bottom, the 20th of the corresponding month is shown. The simulation time is always 22:00 UTC.*

Acknowledgements - Danksagung

Diese Doktorarbeit wurde zu gleichen Teilen in zwei verschiedenen Arbeitsgruppen, an zwei verschiedenen Instituten verfasst und unter der Begleitung von zwei Betreuern verfasst. An erster Stelle möchte ich daher zu gleichen Teilen meinem Doktorvater Professor Ulrich Platt sowie Professor Thomas Wagner vom MPIC in Mainz danken. Beide Betreuer haben mir großzügige Freiheiten in der Ausgestaltung meiner Arbeit gestattet und mir die Teilnahme an einer großen Zahl an internationalen Konferenzen ermöglicht. Die zahlreichen gemeinsamen Diskussionen haben stark dazu beigetragen, diese Arbeit zu formen und das Ziel nicht aus den Augen zu verlieren. Prof. Ulrich Platt hatte dank seines riesigen Erfahrungsschatzes in der Bromchemie und der Fernerkundung immer viele prägnante Vorschläge und Ideen zur Verbesserung und Weiterführung der Arbeit beizutragen, wofür ich sehr dankbar bin. Für seine ungeheure Motivationskraft und seine große Geduld bin ich besonders Prof. Thomas Wagner sehr dankbar. Thomas hat es immer geschafft aus einer überbordernden Menge meiner unausgegorener Ideen die Wichtigen auszuwählen, auch wenn es nicht die waren, die mir in diesem Moment wichtig erschienen. Ohne seinen Rat würde ich wohl noch immer an einer Parameterisierung der Clusteranalyse feilen.

Nicht zuletzt bin ich sowohl Prof. Ulrich Platt als auch Prof. Thomas Wagner sehr dankbar für das entgegengebrachte Vertrauen, mir als "fachfremder" Person aus der theoretischen Physik dieses spannende Projekt anzuvertrauen und mir somit die Gelegenheit zu geben, meinen Horizont zu erweitern.

Vielen Dank an Prof. Thomas Leisner für die Übernahme der Zweitbegutachtung. Ebenso möchte ich mich bei Prof. Hans-Christian Schultz-Coulon und Prof. Carlo Ewerz für ihre Teilnahme an meiner Prüfungskommission bedanken.

Einen ganz besonderer Dank möchte ich auch an Dr. Holger Sihler sowie Dr. Steffen Beirle aussprechen. Holger hat mir mit viel Geduld und Empathie sowohl die Satellitenfernerkundung als auch das "saubere" Programmieren nahe gebracht und war stets bereit, mir meine unzähligen Fragen zu seinen vergangenen Arbeiten zu beantworten. Außerdem wäre ohne seine Leistung bei der Erschaffung der Methode zur Bestimmung von troposphärischem BrO diese Arbeit nicht möglich gewesen. Steffens Ideenreichtum sowie sein Beharren auf mögichen Verbesserungen des Algorithmus haben maßgeblich zu dieser Arbeit beigetragen. Außerdem danke ich Steffen auch für das von ihm ins Leben gerufene "TecSem", welches mir

viele neue Ansätze im Programmieren nahegebracht hat und einen wundervollen Ideenaustausch erlaubt hat.

Ebenso möchte ich mich vielmals bei Dr. Maximilian Herrmann bedanken. Zum einen war er stets bereit mit mir in die Wirrungen der arktischen Bromfreisetzung abzusteigen und meine unzähligen Fragen über das von ihm entwickelte Model für die Bromchemie in der Artkis zu beantworten. Zum anderen bin ich sehr dankbar für die uns verbindende Freundschaft, seinen Zuspruch bei Zweifeln an meiner Arbeit sowie die gemeinsame Kooperation an veröffentlichten Aufsätzen und Vorträgen. Ohne das von ihm entwickelte Model der Bromchemie wäre diese Arbeit deutlich ärmer an Erkenntnissen.

Mein Dank gilt ebenso Christian Borger und Dr. Simon Warnach für ihre Unterstützung bei allem was mit Satelliten zu tun hatte. Die von ihnen bereitgestellte Infrastruktur für die Auswertung der Satellitenspektren hat diese Arbeit immens beschleunigt. Außerdem waren beide stets bereit die teils merkwürdigen Fragen eines ehemaligen Theoretikers zu beantworten. Besonders zu Dank verpflichtet bin ich auch Christian für die Kollegialität in Zeiten von Corona und vielen gemeinsamen Gesprächen über Skype, egal ob es ums Programmieren, um die Entwicklung von Satellitenalgorithmen oder den neuesten Tratsch aus Mainz geht, den man als Heidelberger allzu häufig verpasst. Ebenso möchte ich mich bei Simon für seinen Beistand gerade in schwierigen Zeiten meiner Promotion bedanken. Er stand mir nicht nur mit Rat und Tat zur Seite wenn es um die physikalische Interpretation mancher Ergebnisse ging sondern half mir auch beim Umschiffen von so mancher Kommunikationshürde.

Meinen Kollegen Dr. Jonas Kuhn und Leon Kuhn danke ich für gute Diskussionen über Fachliches und darüber hinaus. Jonas half mir bei vielen konzeptionellen Fragen zu DOAS schnell und präzise aus und war auch sonst ein toller Gesprächspartner, sei es über die Energiewende, den Kapitalismus oder einfach nur das allgemeine Universitätsleben. Bei Leon möchte ich mich für spannende Diskussionen rund ums Programmieren bedanken, teils geführt zu den ungewöhnlichsten Zeiten.

Mein Dank gebührt auch Dr. Steffen Ziegler für seine Hilfestellungen bei der Durchführung und Auswertung der McArtim-Simulationen und seine Ideen bei allen meteorologischen Fragestellungen. Ebenso zu Dank verpflichtet bin ich Rüdiger Sörensen für die “Nothilfe” des Clusters in Mainz und der Unterstützung bei der Arbeit mit diesem.

I would like to thank the complete group of “Satellites” in Mainz for their warm welcome, wonderful discussions, feedback and ideas in the weekly “SatSem” and fun board game nights. In particular I want to thank Vinod Kumar for interesting discussions regarding topics of machine learning as well as teaching me about India. I also want to thank Sebastian

Donner for fun discussions during lunch and coffee breaks.

Ebenso möchte ich der gesamten DOAS Gruppe in Heidelberg danken. In den wöchentlichen Gruppensitzungen konnte ich mein Wissen über die Atmosphärenphysik vertiefen, ebenso war aber auch eine Vertiefung zu Themen der erneuerbaren Energien und der Verkehrswende stets ein spannender Diskussionspunkt. Besonders hervorzuheben sind hier auch die Diskussionen zu Halogenen mit Dr. Udo Frieß und Dr. Jan-Markus Nasse sowie die schönen Gespräche mit meinem Bürokollege Dr. Lukas Tirpitz.

Ich möchte mich vielmals bei Prof. Eva Gutheil für die gute Zusammenarbeit sowie die Bereitstellung der Simulationsergebnisse und des WRF-CHEM Models bedanken.

Besonders dankbar bin ich Thomas Wagner, Christian Borger, Maximilian Herrmann, Simon Warnach, Bianca Lauster, Lukas Hahn und Alexandra Winizuk für ausführliche Korrekturen der Doktorarbeit und wunderbare Verbesserungsvorschläge.

Ich möchte Dr. Sascha Leonhardt für seine wertvolle Freundschaft und seinen guten Rat danken, der mich durch die Zeit des Doktorats gebracht hat. Ebenso möchte ich mich bei Lukas Hahn und Arnulf Barth bedanken. Die regelmäßigen Kaffeetreffen waren eine Gelegenheit gemeinsam über die Promotion und weitere Wirdigkeiten des Lebens zu lamentieren. Ich bedanke mich bei Lukas für seine Weisheiten was den Stellenwert der Geschwindigkeit angeht und bei Arnulf für tolle Gespräche über Gott und die Welt, bei denen man keine Angst haben muss mal daneben zu liegen. Danke euch beiden für eure fortwährende Freundschaft.

Vielen Dank an all die anderen Menschen die mich in den letzten Jahren begleitet haben und mir in den letzten Monaten dieser Arbeit Zerstreuung geschenkt haben. Danke an Max und Ella für die wöchentlichen Brettspielabende und an Jan-Marco für die sportliche Begleitung während der Corona Einschränkungen. Ebenso möchte ich mich bei Daniel für viele ausdauernde und horizonterweiternde Diskussionen bedanken und bei Robert für all die Gespräche über Vereinspolitik und seine Ratschläge zum maschinellen Lernen.

Ich möchte mich vielmals bei meiner Mutter Angela und meinem Vater Gerhard bedanken. Vielen Dank für eure fortwährende Unterstützung in diesen vielen Jahren des Studiums. Ihr beide habt so manche Last von meinen Schultern genommen und mir neue Kraft für die Promotion gegeben.

Zuletzt möchte ich mich bei Alexandra bedanken. Ohne deine Unterstützung und deine unerschöpfliche Geduld mit mir wäre diese Arbeit nie vollendet worden. Danke das du da bist.

GESAMTFAKULTÄT FÜR MATHEMATIK,
INGENIEUR- UND NATURWISSENSCHAFTEN

COMBINED FACULTY OF MATHEMATICS,
ENGINEERING AND NATURAL SCIENCES

RUPRECHT-KARLS-
UNIVERSITÄT
HEIDELBERG

Eidesstattliche Versicherung gemäß § 8 der Promotionsordnung für die Gesamtfakultät für Mathematik, Ingenieur- und Naturwissenschaften der Universität Heidelberg / Sworn Affidavit according to § 8 of the doctoral degree regulations of the Combined Faculty of Mathematics, Engineering and Natural Sciences at the Heidelberg University

1. Bei der eingereichten Dissertation zu dem Thema / The thesis I have submitted entitled

   ……

   handelt es sich um meine eigenständig erbrachte Leistung / is my own work.

2. Ich habe nur die angegebenen Quellen und Hilfsmittel benutzt und mich keiner unzulässigen Hilfe Dritter bedient. Insbesondere habe ich wörtlich oder sinngemäß aus anderen Werken übernommene Inhalte als solche kenntlich gemacht. / I have only used the sources indicated and have not made unauthorised use of services of a third party. Where the work of others has been quoted or reproduced, the source is always given.

3. Die Arbeit oder Teile davon habe ich wie folgt/bislang nicht[1)] an einer Hochschule des In- oder Auslands als Bestandteil einer Prüfungs- oder Qualifikationsleistung vorgelegt. / I have not yet/have already[1)] presented this thesis or parts thereof to a university as part of an examination or degree.

   Titel der Arbeit / Title of the thesis:……

   Hochschule und Jahr / University and year:……

   Art der Prüfungs- oder Qualifikationsleistung / Type of examination or degree:……

4. Die Richtigkeit der vorstehenden Erklärungen bestätige ich. / I confirm that the declarations made above are correct.

5. Die Bedeutung der eidesstattlichen Versicherung und die strafrechtlichen Folgen einer unrichtigen oder unvollständigen eidesstattlichen Versicherung sind mir bekannt. / I am aware of the importance of a sworn affidavit and the criminal prosecution in case of a false or incomplete affidavit

Ich versichere an Eides statt, dass ich nach bestem Wissen die reine Wahrheit erklärt und nichts verschwiegen habe. / I affirm that the above is the absolute truth to the best of my knowledge and that I have not concealed anything.

…….. ……..……

Ort und Datum / Place and date — Unterschrift / Signature

[1)] Nicht Zutreffendes streichen. Bei Bejahung sind anzugeben: der Titel der andernorts vorgelegten Arbeit, die Hochschule, das Jahr der Vorlage und die Art der Prüfungs- oder Qualifikationsleistung. / Please cross out what is not applicable. If applicable, please provide: the title of the thesis that was presented elsewhere, the name of the university, the year of presentation and the type of examination or degree.

The German text is legally binding.